Aix-Marseille Université
ED 353 – Sciences pour l'ingénieur : Mécanique, Physique, Micro et Nanoélectronique
Laboratoire de Mécanique et d'Acoustique - CNRS - UPR 7051

A thesis submitted for the degree of doctor of Philosophy

Discipline: Engineering sciences
Speciality: Acoustics

Quentin MESNILDREY

Towards a Better Understanding of the Cochlear Implant – Auditory Nerve Interface:

from intracochlear electrical recordings to psychophysics.

Jury members:

Johannes Frijns	Leiden University Medical Center	Reviewer
Jan Wouters	University of Leuven	Reviewer
Patrick Boyle	Advanced Bionics ®	Examiner
Etienne Gaudrain	CRNL CNRS - UMR 5292	Examiner
Frédéric Venail	University Hospital Montpellier	Examiner
Philippe Herzog	LMA CNRS - UPR 7051	PhD Supervisor
Olivier Macherey	LMA CNRS - UPR 7051	PhD Supervisor

11 January 2017

Towards a Better Understanding of the Cochlear Implant – Auditory Nerve Interface:

from intracochlear electrical recordings to psychophysics

Vers une Meilleure Compréhension de l'Interface entre l'Implant Cochléaire et le Nerf Auditif :

mesures électriques intracochléaires et psychophysique.

Keywords:

Cochlear implant, auditory nerve, interactions, selectivity, neurostimulation, speech, vocoder, impedance, psychophysics.

Mots clés :

Implant cochléaire, nerf auditif, interactions, sélectivité, stimulation neurale, parole, vocoder, impédance, psychophysique.

Affiliations:

LMA, CNRS, UPR 7051, Aix-Marseille Univ, Centrale Marseille, F-13453 Marseille Cedex 13.

Postal address:

Laboratoire de Mécanique et d'Acoustique
CNRS - UPR 7051
4 impasse Nikola Tesla
CS 40006
13453 Marseille Cedex 13

Remerciements

Mes premiers remerciements sont évidemment adressés à Olivier pour son encadrement sans faille durant cette thèse et les deux stages qui ont précédés. Merci pour ta volonté de me faire apprendre et avancer professionellement. Merci de m'avoir guidé tout au long de ce projet, sauf peut-être dans les rues de Szeged où j'aurais mieux fait de suivre mon instinct.

Un grand merci à Philippe pour avoir pris part à ce projet exotique, nous avoir offert ton expertise et d'avoir enrichit ce projet par ton regard extérieur.

J'en profite pour remercier sincèrement les rapporteurs de mon jury de thèse Johannes Frijns et Jan Wouters, ainsi que les examinateurs Frédéric Venail, Paddy Boyle et Etienne Gaudrain pour avoir évalué mon travail avec interêt et rigeur.

Ce projet de thèse a permis de faire naitre plusieurs collaborations qui je l'espère perdureront. Je remercie sincèrement le CHU de Montpellier, particulièrement Frédéric Venail et les membres du service ORL, Marielle Sicard, Jean-Pierre Piron, Maxime Balcon pour leur accueil et leur disponibilité.

Merci à Advanced Bionics ®(Paddy Boyle, Leo Litvak, Kanthaiah Koka, Idryck Akhoun, Florian Sadreux) pour leur soutien, technique dans premier temps, puis financier qui a permis de bon déroulement de mon travail expérimental.

J'ai eu par ailleurs l'occasion d'être intégré à une autre collaboration, de plus longue date celle-ci, entre Marseille (Olivier) et le MRC-CBU de Cambridge (Bob Carlyon, John Deeks, Alan Archer Boyd, Stefano Cosentino, Francois Guerit). Je remercie tout ce groupe pour nos échanges réguliers entre les plages de Marseille et les pubs de Cambridge et plus particulièrement Alan pour son accueil et son aide lors des expériences que j'ai eu la chance de mener au sein de leur laboratoire.

Mais rien n'aurait pu exister sans la disponibilité et la patience de tous les participants implantés et normo-entendants.

Cette période à Marseille a aussi été animée par quelques personnages grandioses que je tiens à remercier: la famille psychoacoustique au complet (Olivier, Gaston, Jacques, Sabine, Sophie, Guy, Michèle) avec qui j'ai eu la chance de passer quatre années mémorables, comme à la maison. S'il ne fait pas officiellement partie des encadrants de ma thèse je tiens ici à remercier particulièrement Gaston pour avoir partagé ton amour de la "vraie" science expérimentale, originale, curieuse et rigoureuse mais aussi pour ta générosité à tous les niveaux, *Dank u zeer*. En parlant de générosité, un immense merci à Jacques, champion du monde et des environs. Merci pour ta disponibilité, ton sens du partage et d'avoir communiqué ton amour de la plus belle région du monde, je suis presque convaincu...

Merci à Etienne pour nos discussions sans fin au comptoir du champ de mars, alternant entre design de protocoles expérimentaux et l'age d'or des Stones.. Lennie pour avoir partagé un peu de ton karma et ta passion des pique-niques qu'ils soient gargantuesques ou messneriens, mais aussi, Gaultier, Thomas, Pierre-Yvon, Simon, Soizic, Adrien, Gaëtan, et bien d'autres.

Je remercie bien évidemment ma famille qui a accepté mon exil de terre normande pour la côte d'Azur tout en me soutenant depuis le début. Merci à mes amis hors-labo de Marseille ou d'ailleurs et tout particulièrement la smala de Poitiers (JC, Stan, Quentin, Théo, Max, Arthur). Enfin, merci à Margaux pour à peu prêt tout..mais surtout pour ta patience infinie et ton soutien essentiel durant cette période intense. Une aventure se termine et des milliers d'autres nous attendent, *vamos !*

Abstract

Cochlear implants (CIs) are limited by the lack of spatial selectivity of the electrical stimulation. Multipolar strategies have been proposed to improve this spatial selectivity but, so far, have not yielded consistent benefits for speech intelligibility. The present project aims to better understand the CI-auditory nerve interface and provide relevant information for the design of alternative stimulation strategies.

In chapter 2, vocoder simulations of CIs were used to assess the effect of electrode configuration on speech intelligibility in normal hearing subjects. We found that interactions limited the spectral resolution of monopolar configuration to 8 functional channels and that the presence of several peaks of excitation in bipolar or tripolar configurations may be deleterious for speech intelligibility.

The phased-array strategy is a possible way to limit the presence of these multiple peaks of excitation. It aims to focus the electrical field near one electrode while minimizing the residual voltage elsewhere. However, it relies on several assumptions that may not hold. In particular, it assumes that the cochlear medium is purely resistive and that the voltage produced near a stimulating electrode can be extrapolated from measures made on other electrodes. In chapter 3, we performed impedance measurements in a group of CI listeners. We show that for the majority of electrodes tested, the hypothesis of resistivity is valid up to 46 kHz. However, 18% of our recordings showed an additional capacitive behavior at low frequency that may relate to a partial polarization of the measurement electrodes. Finally, we introduce a simple equivalent electrical model that can describe the impedance of stimulating electrodes. This model shows a better fit than previous attempts made in the CI field and provides an estimation of the voltage near the stimulating electrode without the need to extrapolate.

Another factor to consider in the design of spatially-selective strategies is neural survival as there may be no use in focusing the electrical field in a region where there is no neuron to excite. In Chapter 4, we investigated whether the sensitivity to polarity may provide a psychophysical correlate of neural survival. Detection thresholds (T-levels) for partial-tripolar biphasic stimuli were measured in 16 CI subjects. Consistent with previous studies, we showed that the electrode-to-modiolus distance, estimated from CT (computerized tomography) images, accounted for a significant part of the within-subject variance in T-levels. We also showed that the polarity effect defined as the difference in T-level between cathodic and anodic stimulation was correlated within subjects with T-levels even when the effect of EMD was partialed out. This suggests that part of the variance in T-levels that is not explained by the EMD is

explained by polarity sensitivity. We also showed that the polarity effect averaged across the electrode array correlated across subjects with a measure of spectro-temporal modulation perception. These two results suggest that the sensitivity to polarity at threshold may reflect neural survival.

While Chapter 3 focused on estimating the electrical field at the level of the electrode array, the neural elements that have to be excited are located a few millimeters away from the electrodes. In Chapter 5, we evaluate what would be needed to infer the voltage at the level of the neurons based on measures made at the level of the electrodes. Electrical field recordings in CIs showed that more than 2 mm away from a stimulating electrode, the voltage measured on the electrodes could provide a reasonable approximation of the voltage at the modiolar wall. In contrast, in the near-field region, computational modeling is necessary to account for across-electrode and across-subject differences.

The implications of this thesis for clinical follow-up, diagnostic of dead regions, and improvement of focusing strategies are described in chapter 6.

Résumé

Introduction

L'implant cochléaire (IC) est une prothèse neuronale implantée chirurgicalement permettant la restauration partielle de sensations auditives pour les patients atteints de surdité neuro-sensorielle sévère à profonde. L'IC se compose d'une partie externe qui capte le son et l'analyse à travers un processeur multi-canaux. Dans chaque bande fréquentielle, l'enveloppe temporelle des signaux est extraite et convertie en un code de stimulation électrique. Ce code est ensuite transmis à une partie interne. Les informations de chaque canal servent à moduler en amplitude des trains d'impulsions électriques qui sont ensuite transmis à différentes électrodes implantées à l'intérieur de la cochlée permettant d'initier la génération de potentiels d'action au niveau des fibres nerveuses.

De nombreuses études ont permis de démontrer la capacité de cet appareil à restaurer une reconnaissance de la parole correcte dans un environnement silencieux. Malheureusement, les performances de patients implantés sont rapidement limitées dans des environnements sonores plus complexes, en présence de bruit ou d'autres locuteurs. L'une des raisons principales provient du fait que dans le mode de stimulation classique, *monopolaire* (MP), à l'activation d'un canal, le courant électrique circule entre une électrode intracochléaire donnée et une électrode de retour située au niveau du muscle temporal. Du fait des propriétés électriques de l'oreille interne, le champ électrique créé dans la cochlée se diffuse alors largement. Lorsque plusieurs électrodes sont activées, les champs électriques produits se chevauchent créant des interférences qui perturbent la transmission de l'information sonore.

Plusieurs études ont montré qu'il est possible de limiter l'étalement spatial du champ électrique en utilisant plusieurs électrodes par canal (Kral et al., 1998; Bierer and Middlebrooks, 2002; Snyder et al., 2004). Ces modes de stimulation dits "multipolaires" consistent à superposer plusieurs champs électriques de manière contrôlée pour focaliser le champ global à un endroit souhaité. Par exemple, le mode dit *bipolaire* (BP) utilise une autre électrode dans la cochlée comme électrode de retour limitant ainsi l'étendue de la diffusion du courant. De la même manière le mode *tripolaire* (TP) utilise cette fois trois électrodes par canal. Le courant électrique circule alors entre l'électrode centrale et deux électrodes de retour de part et d'autre.

Malheureusement, les différents modes multipolaires proposés n'ont jusque là pas montré de bénéfice homogène entre études, en terme de reconnaissance de la parole.

Ce projet de doctorat a pour objectif de mieux comprendre l'interface entre l'implant cochléaire et le nerf auditif afin de fournir des indices utiles à l'implémentation d'une nouvelle stratégie de stimulation incluant à la fois une stimulation spatialement focalisée et par ailleurs optimisée en fonction de paramètres spécifiques au patient. Pour cela, nous avons suivi une approche multi-disciplinaire mêlant psychophysique, mesures électriques in vitro et chez le patient implanté.

Simulation acoustique

Interactions

La simulation acoustique, ou *vocoder*, est un outil de recherche permettant de reproduire les étapes principales du traitement de signal appliqué par le processeur de l'implant pour ainsi tester leur influence sur la perception de sujets normo-entendants. De la même manière que dans l'IC, des filtres d'analyse découpent le signal d'entrée en différents canaux fréquentiels, les enveloppes temporelles de chacune de ces sous-bandes sont ensuite extraites avant d'être appliquées sur des porteuses acoustiques. En simulation acoustique, il ne s'agit plus de trains d'impulsions électriques mais de signaux acoustiques, ici, des bandes de bruit. L'étape de synthèse consiste à filtrer ces bruits modulés avant de sommer les différents canaux et de les présenter à un sujet entendant. La plupart des vocoders classiques font appel aux mêmes filtres pour l'analyse et la synthèse afin de s'assurer que le contenu fréquentiel du signal d'origine ne soit pas transposé. Pour comprendre l'influence des interactions entre électrodes sur la perception de la parole, leur effet peut être simulé en utilisant des filtres de synthèses plus larges que ceux d'analyse, imposant ainsi un chevauchement de l'information contenue dans différents canaux (Bingabr et al., 2008; Strydom and Hanekom, 2011a).

Dans le chapitre 2, plusieurs filtres de synthèse ont été créés sur la base de la théorie de la fonction d'activation neuronale (Rattay, 1989) de manière à simuler le profil d'excitation produit par différents modes de stimulation. La reconnaissance de la parole de sujets normo-entendants a été testée pour ces différentes simulations.

Dans une première expérience, les modes MP et BP ont été simulés. De manière similaire à ce qui a été observé chez l'IC, les scores de reconnaissance de la parole montrent une amélioration en fonction du nombre de canaux jusqu'à 8 canaux actifs. Au-delà, le recouvrement des filtres de synthèse détériore la transmission de l'information et les performances saturent, voire diminuent pour le mode BP, illustrant l'influence des interactions entre canaux. Une seconde expérience a permis de confirmer que, pour le mode BP, cette saturation provient bien de la superposition des différents filtres plutôt que de la forme discontinue du filtre lui-même. Enfin, une troisième expérience a révélé que la corrélation des signaux interagissant a aussi une importance. Lorsque les signaux proviennent de deux canaux distants spectralement, ceux-ci vont transmettre des modulations très différentes que le sujet ne va pas parvenir à séparer. A l'inverse, pour des canaux adjacents, les modulations transmises sont relativement bien corrélées, induisant un effet moins délétère. Pour une transmission efficace de l'information sonore, il semble donc crucial de générer un champ électrique unimodal présentant un seul pic sélectif au niveau d'un canal donné.

Porteuse acoustique (étude complémentaire)

Cette première étude a été l'occasion de pointer une possible limitation de la simulation acoustique. Comme évoqué précédemment, des bandes de bruit peuvent être utilisées comme porteuses acoustiques afin de simuler un étalement spatial de la stimulation. Cependant, ces bandes de bruit contiennent des modulations intrinsèques à leur enveloppe temporelle. Lors de la modulation en amplitude effectuée par le simulateur, ces modulations s'ajoutent à celles que l'on souhaite transmettre. En stimulation électrique, cette perturbation n'existe pas. Une solution pour pallier à ce problème est d'utiliser des sons purs comme porteuses acoustiques. Ceux-ci ont une enveloppe temporelle plate, parfaitement adaptée à la transmission exacte des modulations. Cependant ces signaux sont spectralement restreints et ne permettent donc pas de simuler l'étalement de l'excitation comme précédemment.

Pour se rapprocher davantage de ce qui est fait dans l'IC, nous nous sommes penchés, dans l'étude présentée dans l'appendice 7.1, sur l'utilisation d'autres signaux acoustiques. Hilkhuysen and Macherey (2014) ont introduit une classe de signaux acoustiques appelés *Pulse-spreading-harmonic-complexes* ou PSHCs. Ces signaux, construits en sommant des sous-séries de complexes harmoniques (pour plus de détails, voir l'annexe 7.2) présentent un spectre large bande et une forme d'onde pulsatile à cadence fixe et dont l'enveloppe temporelle peut être optimisée de manière à minimiser les fluctuations intrinsèque après filtrage cochléaire. Hilkhuysen and Macherey (2014) ont par ailleurs montré dans une tâche de détection de modulation chez des sujets normo-entendants, que l'utilisation de PSHCs comme porteuse acoustique induit de meilleures performances que d'autres signaux large bande. Ce résultat corrobore l'idée que le PSHC est d'avantage adapté à la transmission de modulations que les bandes de bruit. Dans cette étude, nous avons testé l'influence de la porteuse acoustique sur la reconnaissance de la parole en comparant des vocoders à sinus, bruit large bande et PSHC. Ces vocoders comprenaient 6 canaux fréquentiels et, cette fois-ci, les filtres d'analyse et de synthèse ont été choisis volontairement similaires pour se focaliser sur la capacité des porteuses acoustiques à transmettre les modulations en limitant les interactions. Les résultats obtenus montrent que les performances des sujets étaient en moyenne les meilleures avec les sons purs, intermédiaires avec les PSHCs et enfin moins bonnes avec le bruit. Ces résultats étendent les résultats de Hilkhuysen and Macherey (2014) à la transmission des modulations de la parole et font du PSHC une alternative intéressante du point de vue temporel et spectral pour la simulation de l'IC.

Mesures d'impédance

Pour limiter les interactions électriques dans la cochlée, il est nécessaire de connaitre les propriétés électriques de l'appareil et de l'oreille interne. Le champ électrique produit par une électrode dans la cochlée peut être mesuré au niveau des autres électrodes inactives. On obtient ainsi une estimation de l'étalement spatial le long du faisceau. En généralisant cette mesure à l'ensemble des combinaisons d'électrodes, on obtient la matrice d'impédance, Z. En inversant Z, il est théoriquement possible de calculer le courant avec lequel activer chaque électrode pour créer un champ de potentiel arbitraire. Ce problème inverse est le principe de la strategie *Phased Array* (PA) proposée par van den Honert and Kelsall (2007). Malheureusement cette technique est potentiellement limitée par plusieurs facteurs : (1) comme toute stratégie multi-polaire, elle suppose la parfaite résistivité du milieu cochléaire, (2) la valeur du potentiel à la surface d'une électrode active (ie. la diagonale de Z) ne peut être estimée directement à cause de la polarisation de l'interface avec le fluide cochléaire au passage du courant, et enfin, (3) une focalisation parfaite au niveau des électrodes n'implique pas nécessairement une sélectivité optimale au niveau des neurones.

Dans le chapitre 3 nous nous sommes tout d'abord intéressés aux points (1) et (2) énoncés précédemment. Divers protocoles de mesures ont été développés pour l'implant HiRes 90k (Advanced Bionics) et le système de stimulation Bionic Ear Data Collection System (BEDCS, Litvak (2003)) et de nombreuses mesures électriques ont été réalisées in vitro ainsi que chez 8 patients adultes implantés.

Hypothèses fondamentales

La stimulation multipolaire est basée sur certaines hypothèses fondamentales concernant la diffusion électrique dans les tissus biologiques. Il est notamment nécessaire que le milieu dans son intégralité soit purement résistif pour que les chemins de courant n'introduisent pas de déphasage. De précédentes études se sont intéressées à cet aspect (Suesserman and Spelman, 1993a; Vanpoucke et al., 2004a), démontrant ainsi la résistivité du milieu jusqu'à 12.5-kHz. Cependant, les stimuli électriques utilisés dans les ICs sont en général des créneaux biphasiques dont le spectre contient des composantes au delà de 12.5-kHz. Compte tenu de l'importance de cette hypothèse, un protocole de mesures de spectroscopie d'impédance sur la gamme [0.2-46.4]-kHz a été mis au point. Des mesures préliminaires in vitro ont permis de révéler la présence d'une capacité parasite, C_p, intrinsèque à l'appareil. Couplée à l'impédance de charge de l'électrode, l'ensemble agit comme un filtre passe-bas dont l'effet est identifiable à l'analyse des diagrammes d'amplitude et de phase.

In vivo, la présence de C_p pourrait masquer la présence éventuelle d'un effet capacitif des tissus biologiques. Pour surmonter ce problème, des mesures de spectroscopie similaires ont été réalisées chez le patient en changeant l'espacement entre l'électrode de stimulation et celle de mesure avec l'hypothèse que la présence de tissus capacitifs induirait une augmentation du déphasage à haute fréquence avec la distance. Les données ainsi mesurées n'ont révélé aucune tendance de ce type suggérant que l'oreille interne peut être considérée purement résistive sur la gamme de fréquence étudiée. Cependant pour 18% des configurations testées un autre phénomène a pu être identifié à basse fréquence ($< 1\ kHz$) montrant un déphasage plus ou moins marqué associé à une augmentation de l'amplitude. Ceci pourrait s'expliquer par une polarisation partielle des électrodes de mesure due à un transfert de charge au niveau de l'électronique de l'appareil et/ou via le passage du courant à proximité. L'effet de ces deux phénomènes pourrait par ailleurs être amplifié par une réduction de la surface "utile" des électrodes (ex : fibrose).

Comme évoqué précédemment, la présence de C_p agit comme un filtre passe-bas. Ceci a un effet particulièrement important sur les transitoires des stimuli impulsionnels. Par conséquent, nous avons pu observer (in vitro et in vivo) que lorsque deux champs électriques présentant des transitoires légèrement différents se superposent, il y a émergence d'artefacts qui peuvent être particulièrement problématiques pour la stimulation multipolaire.

Polarisation

L'interprétation de la mesure du potentiel électrique au niveau d'une électrode en réponse à l'activation d'une autre électrode se fait de manière directe et l'amplitude mesurée quantifie ainsi la décroissance du champ électrique entre ces deux points. Cependant, au niveau d'une électrode active, l'interface entre le métal et le fluide cochléaire se polarise du fait du passage du courant. Ce phénomène induit une distorsion du signal mesuré sur cette électrode. Malgré l'importance fondamentale de cette donnée, il n'est donc pas possible de mesurer directement le potentiel à la surface d'une électrode active.

Pour séparer l'influence de l'interface de la résistance entre l'électrode et la masse, de précédentes études ont modélisé ce phénomène à l'aide d'un circuit électrique équivalent simple du type R-C (Vanpoucke et al., 2004b; Tykocinski et al., 2005). Les mesures d'impédance de contact avec un haut échantillonnage temporel réalisées dans notre étude nous ont permis de discuter de la véracité d'un tel modèle. Ici, nous proposons un modèle phénoménologique plus réaliste dérivé d'études animales et in vitro mais comportant le même nombre de paramètres. En particulier, ce modèle tient compte de la présence de C_p introduite précédemment. L'interface électrode-fluide est, quant à elle, modélisée par une résistance d'accès, R_a, en série avec un élément à phase constante (CPE). R_a représente la résistance du chemin entre l'électrode et la masse, et le CPE modélise le transfert de charges à l'interface (i.e, polarisation).

Pour l'ensemble des patients testés, ce modèle a permis de décrire précisément les données mesurées et d'estimer les différents paramètres à la fois dans le domaine temporel et dans le domaine spectral. L'estimation rigoureuse de R_a est cruciale à plusieurs niveaux. D'un point de vue clinique, l'estimation des impédances constitue un critère de désactivation d'électrode lorsqu'elles sont trop élevées et définissent aussi le niveau de stimulation maximum des sources de courant. Une estimation plus précise permettrait donc potentiellement un meilleur suivi des patients. Connaitre R_a nous donne aussi accès à la diagonale de la matrice d'impédance Z. En prenant en compte les estimations de ce modèle, il devient alors possible d'appliquer la stratégie PA de manière plus efficace pour focaliser le champ électrique au niveau des électrodes. Cependant, comme énoncé précédemment, la création d'un stimulus sélectif au niveau des électrodes n'est pas synonyme d'une meilleure sélectivité et/ou efficacité de la stimulation au niveau des neurones. Le chemin entre la surface des électrodes et la position des fibres nerveuses résiduelles constitue un enjeu majeur pour l'optimisation des stratégies de stimulation.

L'interface électrode-neurones

Pour aboutir à une stimulation sélective efficace il est nécessaire de s'assurer de l'état de la population neuronale. De précédentes études ont modélisé les paramètres principaux de la périphérie du système auditif par *l'interface électrode-neurones* (Cohen et al., 2006; Bierer, 2010; Long et al., 2014). Cette interface tient compte de l'électrode, de la distance de l'électrode à la position supposée des neurones et enfin de l'état de la population neuronale. La bonne compréhension de cette interface et la capacité de quantifier l'influence des différents paramètres sur la performance des sujets implantés pourrait permettre l'optimisation sujet-spécifique de la stimulation. Dans le chapitre 4, la distance électrode-neurones a été estimée via l'analyse des scanners CT, et des tests de parole et de détection de modulation spectro-temporelles (SMRT, Aronoff and Landsberger (2013)) ont été réalisés.

Afin d'aller plus loin dans la description de la réceptivité de la population neuronale nous nous sommes intéressés à l'effet de la polarité de la stimulation sur les seuils de détection. En effet, des études animales et des modèles de simulation ont montré qu'un stimulus de polarité positive (anodique) stimule plus facilement l'axone central tandis qu'un stimulus de polarité négative (cathodique) stimule préférentiellement la périphérie du neurone. Malgré la nécessité d'équilibrer les charges électriques pour des raisons de sécurité chez l'humain, il est possible d'induire cet effet de polarité en utilisant diverses formes de stimuli (Macherey et al., 2006). Ici, les seuils de détection de 16 patients implantés ont été mesurés en utilisant les stimuli suivants :

1. CA : impulsion biphasique présentant deux phases successives, cathodique-anodique de même amplitude. Dans ce cas, chaque phase peut stimuler les neurones.

2. ACA : impulsion triphasique composée d'une phase centrale de polarité cathodique et d'amplitude donnée, précédée et suivie d'une phase de polarité anodique et d'amplitude deux fois plus faible pour respecter l'équilibre de charges. La stimulation ACA devrait faciliter la stimulation de la périphérie.

3. CAC : impulsion triphasique composée cette fois-ci d'une phase centrale de polarité anodique, précédée et suivie d'une phase de polarité cathodique et d'amplitude deux fois plus faible. La stimulation CAC devrait faciliter la stimulation de l'axone central.

Macherey et al. (2006) ont démontré une plus grande sensibilité à la polarité anodique chez l'humain au niveau de confort. Cette plus grande sensibilité pourrait en partie s'expliquer par le fait que la périphérie des neurones est la première partie susceptible de dégénérer. Cette dégénérescence peut entrainer la perte de l'axone central ou aboutir à des fibres nerveuses unimodales, ne présentant que la portion de l'axone central. Nous nous demandons dans ce chapitre, si l'analyse de la différence entre seuils cathodiques et anodiques, notée Δ_{C-A} pourrait nous informer sur l'état de dégénérescence de la partie périphérique des neurones. Plus la valeur de Δ_{C-A} est élevée, plus la probabilité que les axones périphériques au voisinage de l'électrode testée soient dégénérés est grande. A l'inverse, une valeur faible, voire négative, supposerait que les axones périphériques sont présents et peuvent être stimulés.

En analysant les données inter-sujet, normalisées par la moyenne, nous avons pu observer, de manière similaire aux études précédentes de Cohen et al. (2006) et Long et al. (2014), une relation linéaire significative entre la distance aux neurones et les seuils de détection, pour tous les stimuli. Long et al. (2014) ont par ailleurs montré que lorsque la distance ne permet pas d'expliquer les variations de seuils pour un sujet, ses performances en reconnaissance de la parole ont tendance à être faibles suggérant que les variations de seuils sont aussi influencées par l'état de la population neuronale.

Les mesures de seuils de détection réalisées ici montrent des seuils anodiques plus bas pour 78% des électrodes testées ce qui corrobore les résultats de Macherey et al. (2006). Une analyse des corrélations partielles ($Distance \times \Delta_{C-A} \times Seuils$) suggère par ailleurs qu'une part de la variance inter-sujets qui ne peut pas être expliquée par la distance peut être expliquée par cet effet de polarité, quantifié par Δ_{C-A}.

Pour chaque sujet, le Δ_{C-A} moyen (noté $\bar{\Delta}_{C-A}$) a été calculé pour l'ensemble des électrodes testées. Nos résultats montrent que cette mesure global de l'effet de polarité est significativement corrélée aux performances des sujets en détection de modulations spectro-temporelles. Cette relation renforce l'hypothèse que l'estimation de Δ_{C-A} est dépendante de l'état de la population neuronale.

A l'inverse, les données recueillies n'ont pas permis de reproduire les résultats de précédentes études (Pfingst et al., 2004) suggérant que la variance inter-sujet des seuils est, elle aussi, corrélée aux performances des sujets et donc potentiellement à l'état de dégénérescence des neurones. Cependant, il semblerait que les performances en reconnaissance de la parole aient été très affectées par la durée de surdité des patients ainsi que leur expérience avec l'IC (Blamey et al., 2013). Par ailleurs, il est intéressant de noter que les patients ayant des scores de parole faibles n'ont pas nécessairement obtenu de mauvais scores en détection de modulations spectro-temporelles. Cela suggère que la durée de surdité a eu un effet plus central sur le traitement de la parole.

Diffusion du champ électrique produit par l'IC

On peut penser que la stimulation optimale consisterait à générer un champ électrique sélectif au niveau des fibres nerveuses et non au niveau des électrodes. Dans le chapitre

5 nous tentons de mieux comprendre les facteurs influençant la diffusion du champ électrique dans l'oreille interne. Dans un premier temps, un banc de mesure in vitro a été mis au point pour mesurer les champs produits par différents modes de stimulation ainsi que leur diffusion dans l'espace. In vitro, en conditions de milieu homogène, infini, la stimulation d'une électrode en mode MP génère un champ de potentiel qui peut être décrit par une loi théorique en $1/r$, r représentant la distance du point de mesure à l'électrode. La méthode CPA (pour *Contact Phased Array*) basée sur l'estimation des termes diagonaux de la matrice d'impédance à partir du modèle présenté dans cette thèse a été implémentée et testée in vitro. Dans les conditions de tests, cette stratégie CPA a abouti à une meilleure sélectivité de la stimulation que la stimulation MP. Cependant les conditions in vitro était vraisemblablement très favorables comparées à des conditions réelles in vivo.

Pour transposer la stratégie PA au niveau des neurones, il est nécessaire de comprendre les lois de diffusion du champ électrique dans la cochlée implantée. La distribution du potentiel électrique produit par une électrode peut être estimée par l'EFI (*Electrical Field Imaging*). Ici, nous avons utilisé différentes approches afin de tirer un maximum d'information de ces profils mesurés. Si qualitativement il est possible de décrire les champs diffusés le long de la rampe tympanique par une loi exponentielle décroissante, cela ne fournit que peu d'information sur la nature physique de la diffusion électrique.

Il a été possible de démontrer que, dans notre cas précis, l'influence de la géométrie de la cochlée sur la décroissance du champ de potentiel est limitée. L'un des principaux facteurs de différences inter-sujets semble être la résistance d'accès (R_a) et plus généralement le champ proche, à proximité de la surface de l'électrode. Ensuite, pour l'ensemble des électrodes et des sujets, le champ décroit à la même vitesse le long du faisceau. L'asymétrie apex/base des profils d'EFI semble s'expliquer par la présence d'un passage préférentiel du courant vers la base de la cochlée, plutôt que par sa géométrie spiralée ou encore son rétrécissement vers l'apex.

Pour évaluer l'efficacité des différents modes de stimulation MP, PA_{Ra} (stratégie multipolaire dont les termes diagonaux sont définis comme la moyenne entre les estimations de R_a et celle obtenues par extrapolation) et CPA chez l'implanté, la sélectivité au niveau neuronal a été mesurée psychophysiquement à l'aide du *niveau d'interaction* (Townshend and White, 1987). Cette mesure permet de quantifier les interactions simultanées de deux canaux adjacents au niveau du seuil de détection. Les résultats de cette étude préliminaire sur un unique sujet implanté a montré que PA_{Ra} et CPA produisent moins d'interactions que MP.

Les mesures de champs in vitro ainsi que les données chez l'IC montrent que le champ électrique dans la cochlée peut être décrit en trois zones distinctes. Au niveau d'une électrode active, la structure complexe de la cochlée n'influe que peu sur le champ électrique produit. On peut donc considérer une loi de diffusion proche du champ libre en $1/r$ jusqu'au niveau des premières électrodes voisines (1.1 mm). Au delà de cette limite les lignes de courants deviennent de plus en plus guidées à l'intérieur de la rampe tympanique, la décroissance est alors moins rapide. Au delà de cette zone de transition ($r > 2mm$), les données in vitro suggèrent une loi de champ lointain signifiant que le champ mesuré par les électrodes de l'implant est comparable à la valeur qui serait mesurée à la parois du modiolus. En considérant un modèle très simplifié d'un milieu semi-infini composé de deux zones de résistivités différentes on peut obtenir une idée de ce que serait les champs électriques au niveau de la paroi du modiolus. On constate alors que la perte de sélectivité spatiale est en grande partie due à un contraste de résistivité important entre le fluide intracochléaire et la paroi osseuse du modiolus.

De cette description, il vient une simplification du problème PA impliquant une modification des deux premières sur-diagonales et deux premières sous-diagonales de la matrice d'impédance. Cependant, si la résolution du problème inverse d'une telle stratégie apparait mathématiquement réalisable, elle requerrait une optimisation plus avancée afin d'améliorer significativement l'efficacité de la stimulation.

Conclusion et perspectives

Au cours de cette étude, différents outils de mesure et d'analyse ont été mis au point afin d'améliorer nos connaissances sur les principes fondamentaux de la stimulation électrique et en particulier de la stimulation multipolaire dans le but de générer des champs électriques sélectifs.

La simulation des interactions entre canaux a permis de mieux comprendre l'origine des interactions électriques et leur influence sur la transmission des indices essentiels à la compréhension de la parole. La combinaison des deux études de simulations acoustiques pourrait permettre la mise au point d'un simulateur plus réaliste. En prenant en compte les interactions entre canaux, un signal porteur pulsatile et présentant le minimum de fluctuations temporelles, nous sommes en mesure de penser que la simulation acoustique de l'IC se rapprocherait significativement de la stimulation électrique à la fois en termes d'indices transmis mais aussi du timbre perçu.

Les hypothèses fondamentales requises pour la faisabilité de la stimulation multipolaire ont pu être validées malgré l'identification de phénomènes parasites. La capacité parasite, C_p, propre à l'appareil est notamment responsable d'un filtrage passe-bas de tous les signaux générés. Les impulsions électriques générées présentent en réalité des transitoires exponentiels qui peuvent varier légèrement d'une électrode à l'autre. La sommation de champs peut alors faire émerger des artefacts au niveau de ces transitoires. L'utilisation de stimuli aux transitoires moins raides permettrait d'éviter ces artefacts.

Le modèle proposé pour la modélisation de l'impédance des électrodes polarisées a permis une estimation plus précise de la résistance d'accès ainsi que d'autres paramètres propres à l'interface polarisée. L'estimation de R_a a permis d'implémenter la stratégie Phased Array en prenant en compte l'estimation de la matrice d'impédance complète. Par ailleurs les mesures d'impédance sont utilisées en clinique afin de s'assurer du bon fonctionnement des électrodes. De trop hautes impédances peuvent par exemple aboutir à la désactivation d'une électrode. En plus de l'application technique, une meilleure estimation de R_a ainsi que des autres paramètres du modèle pourrait permettre un meilleur suivi clinique des patients.

L'étude de la sensibilité des neurones à la polarité de la stimulation a déjà montré l'importance de la forme des stimuli utilisés. D'un point point de vue technique, l'utilisation de stimuli plus efficaces permettrait de réduire la consommation des batteries. Par ailleurs, il semblerait que cet effet de polarité, et en particulier, l'estimation de Δ_{C-A}, puisse nous informer indirectement sur l'état de la population neuronale le long du faisceau d'électrode.

Les mesures de champs électriques in vitro et in vivo ont permis de mieux comprendre les lois de diffusion dans l'oreille interne implantée. Dans l'optique de développer une stratégie permettant la focalisation du champ électrique au niveau des neurones, il semble crucial de prendre en compte la zone de champ proche autour de chaque électrode stimulée. Par ailleurs, du fait de la courbure des lignes de courant électrique provoquée par la structure de la cochlée, il semble possible d'estimer le champ électrique à la paroi du modiolus en se limitant à une zone de deux ou trois électrodes autour d'une électrode active. Cependant, même en estimant le potentiel électrique au niveau des neurones, un travail d'optimisation sera nécessaire pour générer des stimuli efficaces.

Acknowledgements

We sincerely thank Paddy Boyle, Leo Litvak, Kanthaiah Koka, Idrick Akhoun, from Advanced Bionics for their help and support. Frédéric Venail, Marielle Sicard and Jean-Pierre Piron, from the University Hospital of Montpellier (F), for their help and their welcome. Yves Cazals, from LNIA lab, Marseille (F). Alan Archer-Boyd, John Deeks, and Bob Carlyon, from MRC-CBU (UK). All normal-hearing and CI subjects for their participation.

This PhD project was partly funded by:

- Advanced Bionics ®.
- Agence Nationale de la Recherche (French Research Agency). Project DAIMA, Grant No. ANR-11-PDOC-0022.
- Ministère de l'enseignement supérieur et de la Recherche.

All experiments carried out with normal-hearing subjects and cochlear implant users were approved by the local ethics committee.

Table of contents

Chapter 1

General Introduction

1.1 Human auditory system

In humans, the perception of sound involves many complex stages and several transformations of the original acoustic stimuli from the outer ear to the brain. Sound is initially a pressure wave traveling through the air which contains a lot of information that our auditory system has to convert into cues interpretable by the brain. From a simple vibration of the air, the brain must finally be able to answer questions such as:

- *Where does the sound come from?*
- *Is it moving?*
- *Is it speech, music, noise, ... ?*
- *Do I know the speaker?*
- etc.

This complex analysis is initiated at the peripheral auditory system which is divided in three segments called the outer ear, middle ear and inner ear, as represented in figure 1.1. To reach the brain, an acoustic stimulus first enters the outer ear. It is guided into the auditory canal until it hits the tympanic membrane (or eardrum). The variation of pressure onto the membrane sets in motion a group of three small bones called the ossicles and composing the middle ear. The presence of these three bones enables to convert the vibration of the air into a mechanical motion. The last element of the ossicles, named the stapes, can then transmit its motion to the inner ear via the oval window of the cochlea with sufficient energy.

The cochlea is the most complex organ of the peripheral auditory system. Its bony structure consists of a conical cavity dug into the petrous part of the temporal bone. This tube coils for approximately 2.5 turns around a central core named the modiolus. The dimensions of the human cochlea have been accurately measured in Erixon et al. (2008) and the main information is reported in table 1.1.

	First turn			Second turn			Third turn		
	mean	s.d.	n	mean	s.d.	n	mean	s.d.	n
Length (mm)	22.6	0.83	65	12.4	0.63	63	6.1	1.40	58
Width (mm)	6.8	0.46	71	3.8	0.25	68	2.1	0.52	60
Height (mm)	2.1	0.2	73	1.2	0.17	67	0.6	0.18	60

Table 1.1: Average length, width and height of the 1^{st}, 2^{nd} and 3^{rd} turn of the human cochlea, data from Erixon et al. (2008).

This bony cavity contains three different chambers (see cross section view, figure 1.2). The scala vestibuli (SV) and scala tympani (ST) are filled with perilymph and are separated by the scala media (SM) filled with endolymph. Both endolymph and perilymph are saline physiological fluids with slightly different ionic compositions. The scala

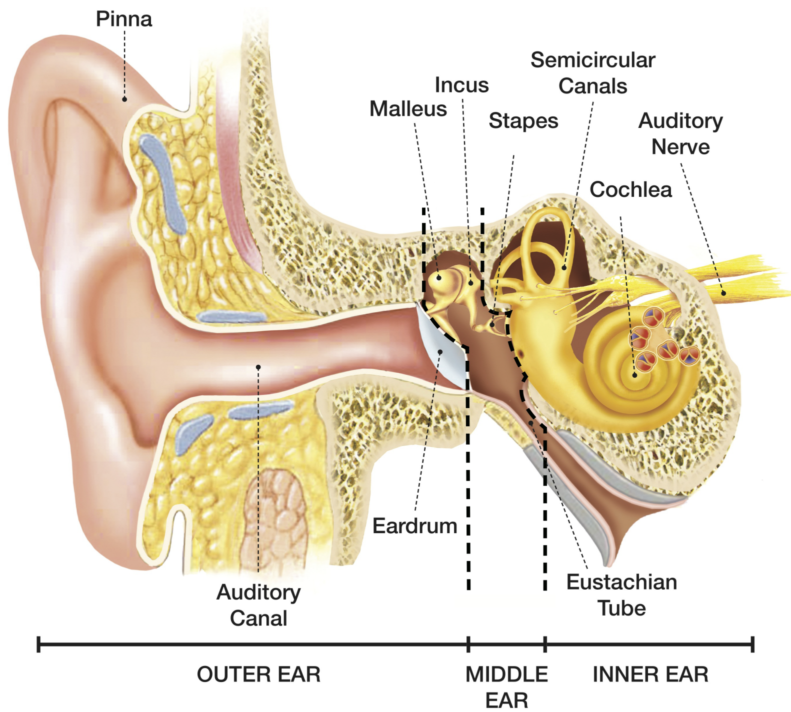

Figure 1.1: Schematic representation of the human auditory system

tympani and scala media are separated by a thin flexible membrane called the basilar membrane on which lies the organ of Corti (see figures 1.2 and 1.3). The movement of the stapes on the oval window convert the mechanical vibration back into a pressure wave traveling through the fluids of the cochlea. The displacement of the fluid induces the vibration of the basilar membrane and, consequently, of the organ of Corti. When the vibration is sufficiently large in magnitude at a given location, small sensitive hair cells which are distributed along the cochlea upon the organ of Corti are compressed against a stationary membrane called the tectorial membrane (TM, see figure 1.3). The bending of the hair cells initiates the release of neurotransmitters triggering the generation of electrical action potentials which can then travel through the auditory nerve fibers to the brainstem and to the higher stages of the auditory system before being processed by the brain. Figure 1.2 and 1.3 represent cross section views of the human cochlea obtained from scanning electron micrography and showing the elements described previously, involved in the conversion of acoustic stimuli into electrical stimuli.

The cochlea not only transduces a mechanical stimulus into electrical action potentials, it also realizes a crucial signal frequency analysis. The pressure wave initiated at the base of the cochlea potentially contains a wide spectrum of frequency components. Because of the mechanical properties of the basilar membrane, high frequency components yield a maximum of vibration of the membrane toward its basal extremity where it is stiff and thin while low frequency components travel along the cochlea and

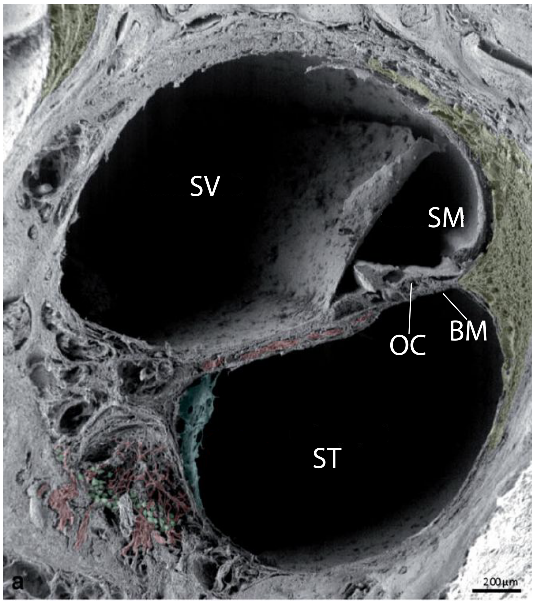

Figure 1.2: Scanning electron micrograph. Cross section of the cochlea showing: the three chambers, scala tympani (ST), vestibuli (SV) and media (SM), the basilar membrane (BM), the Organ of Corti (OC). Adapted from Rask-Andersen et al. (2012).

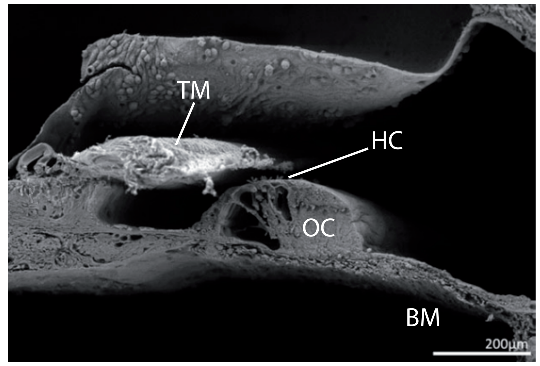

Figure 1.3: Scanning electron micrograph of the Organ of Corti (OC) and basilar membrane (BM) showing the interface between the hair cells (HC) and the tectorial membrane (TM). Adapted from Rask-Andersen et al. (2012).

create a maximum of vibration toward the apex where the membrane is composed of longer fibers and is more flexible. As a result, the action potentials generated at different locations along the cochlea code for specific frequencies. This place-frequency mapping is known as cochlear *tonotopy*. It was first demonstrated by von Békésy in the 1940s, theorized by the so called Greenwood function (equation 1.1, Greenwood (1990), f is the frequency in Hertz, x is the position on the basilar membrane from the apex expressed in mm, $A = 165.4$, $a = 0.06$ and $k = 0.88$) and then further investigated by Stakhovskaya et al. (2007).

$$f = A \cdot 10^{a \cdot x} - k \tag{1.1}$$

Whenever a component of this complex chain is damaged or missing, the auditory perception is no longer possible. In the present project we are mostly interested in sensorineural deafness which is most often due to an inability to generate action potentials at the level of the inner ear due to missing or profoundly-damaged hair cells. This type of deafness represents 90% of clinical cases and is mainly caused by:

- Age (presbycusis)
- Genetics
- Infection of the inner ear
- Trauma

- Ear surgery
- Meningitis
- Meniere's disease
- Ototoxic drugs
- Sudden hearing loss

1.2 Cochlear implant

Since the early eighties, in the case of severe to profound hearing loss, the implantation of a cochlear implant (CI) remains the only way to restore some auditory perception. Today five different brands commercialize their cochlear implant devices and, over the years, more than 400.000 people have undergone CI surgery.

1.2.1 How does it work?

A CI is a neural prosthesis which provides an auditory percept by generating action potentials in the remaining auditory nerve fibers using direct electrical stimulation. The main stages of the sound processing by a cochlear implant are represented in figure 1.4. The device consists of an external part responsible for signal processing and an internal part surgically implanted. The external part is provided with a microphone which receives the acoustic stimulus. The electrical signal passes through pre-processing stages which apply different treatments such as gain control, noise reduction algorithm, etc. The main processor then aims to mimic the analysis stages that a healthy ear would normally do. An analysis filter bank divides the original signal into a dozen frequency channels with center frequencies ranging from approximately 200 Hz to 8 kHz, depending on the device. In each channel, the low frequency envelope fluctuations are extracted either using the Hilbert transform or half-wave rectification and then low-pass filtering. Each channel thus contains the temporal variations of a specific part of the spectrum which supposedly reproduces the role of both the basilar membrane and the hair cells. One important difference between acoustic stimulation and electrical stimulation concerns the amplitude dynamics. Acoustic stimuli span an amplitude dynamic range of approximately 100 dB while the electrical dynamic range can be dramatically reduced to 15-20 dB (Nelson et al., 1996). As a result the CI processor has to apply an amplitude compression on the channel outputs. This information is finally used to generate stimulation codes. The encoded information of each channel is sent to an internal receiver located in the temporal muscle using a radio-frequency transmitter. The stimulation codes are used to amplitude modulate electrical current pulse trains. The electrical waveforms that are clinically used are trains of charge-balanced biphasic pulses with rates up to thousands of pulses per second (*pps*). Those modulated pulse trains are finally sent to different electrodes implanted in the scala tympani. Low-frequency channels are connected to apical electrodes while high-frequency channels are connected to basal electrodes in order to respect the tonotopy of the cochlea.

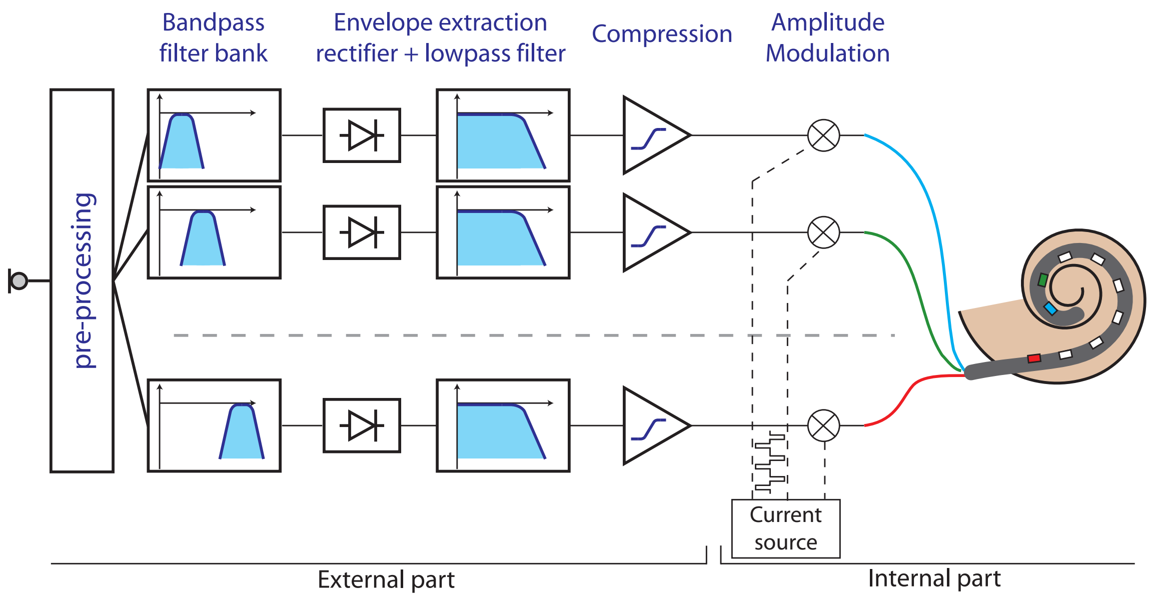

Figure 1.4: Schematic representation of the sound processing by a cochlear implant.

Such signal processing transmits strongly degraded information to the auditory nerve. Still, this device has proven its efficiency to create an auditory perception and even restore access to speech recognition in silence in the case of profound deafness. This success can be attributed to the fact that the human brain can still retrieve a sufficient amount of information from greatly spectrally and temporally degraded speech (Shannon et al., 1995; Zeng and Galvin III, 1999; Loizou et al., 2000).

1.2.2 Main limitations

Despite a continuous fast technical improvement over the past twenty years, the cochlear implant is still far from restoring normal hearing to profoundly deaf people. It suffers from several limitations that prevent optimal performance. The following paragraphs present some of the main limitations of contemporary clinical devices.

Frequency range

Because of the limited electrode array length ($\approx 20\ mm$, depending on the devices) and the risk of traumatic implantation toward the very apex (Gstoettner et al., 1999), a full insertion along the entire cochlear length is usually impossible. As a result, the location of a given electrode does not necessarily correspond to the tonotopic mapping of a healthy cochlea. Matching the frequency range of the analysis filter bank to the insertion depth would dramatically reduce spectral information especially in the low frequency range. A lack of low frequency cues can strongly deteriorate the performance of CI users in terms of speech perception. Instead, the entire frequency range is compressed into a smaller tonotopic region (Baskent and Shannon, 2005). As a result, low frequency information is likely to be sent to a region where nerve fibers normally code for higher frequencies. Fortunately, several studies demonstrated the capacity of the brain to rearrange and interpret the spectral content of speech even with compressed or wrapped frequency maps (Fu and Shannon, 1999; Rosen et al., 1999; Shannon et al., 2002; Baskent and Shannon, 2003). The ability of CI users to compensate for this compression is also dependent on the duration of deafness. Indeed, when the auditory cortex does not receive sound information for a long period, those regions can be reallocated for the treatment of other stimuli such as visual stimuli. This ability of the brain is known as cross-modal plasticity (Lomber et al., 2010; Campbell and Sharma, 2014; Sharma et al., 2015). After cochlear implantation, the ability to process spectrally-degraded auditory inputs requires the reversibility of those brain changes.

Spectral/spatial resolution

Typical electrode arrays carry between 12 and 22 stimulating contacts which enable to analyze input sounds through 12 to 22 frequency bands while a healthy ear contains hundreds of "analysis channels". The low number of electrodes thus limits the spectral resolution of electrical stimulation. Spectral resolution of cochlear implants has been investigated in many studies, for instance, by testing speech recognition as a function of the number of channels (Fishman et al., 1997; Friesen et al., 2001; Fu and Nogaki, 2005). Those studies consistently reported that the performance in speech recognition improves with the number of electrodes up to a saturation point where the scores plateau. Figure 1.5, adapted from Friesen et al. (2001), represents the percent correct of vowels recognition with a signal-to-noise ratio of +15 dB, for CI users as a function of the number of electrodes compared to normal hearing (NH) listeners performance listening to a channel vocoder. Those results suggest that when the number of electrodes is higher than 8-10, CI users no longer benefit from stimulating additional electrodes.

The fact that NH listeners do benefit from a larger number of channels up to 100% scores suggested that this limitation is specific to electrical stimulation and not to the sound processing *per se*. Indeed, activating an electrode generates an electrical field within the cochlea and the electrical properties of the inner ear tend to facilitate the spread of current along the scala tympani. As a consequence, when stimulating electrodes are close, individual electrical fields overlap as represented schematically in figure 1.6. These electrical interactions deteriorate the transmission of sound information at the level of the nerve fibers. This poor spectral resolution is a major issue for CI performance in complex sound environments such as speech recognition in noise or with multiple speakers, but also for music appreciation.

This topic has been the subject of many research projects for a long time. Several features have progressively been added to the CI device in order to reduce channel interactions. First, several studies reported that lower detection thresholds can be achieved by placing the electrodes close to the modiolus where neural fibers lie (Shepherd et al., 1993; Cohen et al., 2006). This can be done utilizing pre-curved electrode arrays or

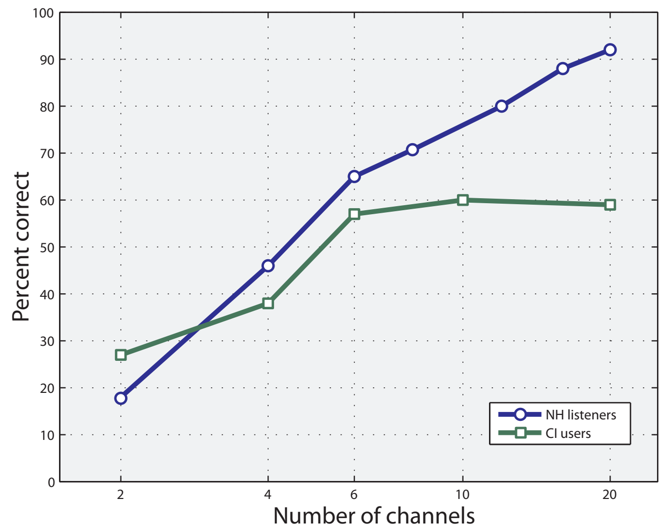

Figure 1.5: Vowels recognition (% correct) as a function of the number of electrodes for CIs or vocoder channels for NH listeners. Adapted from Friesen et al. (2001)

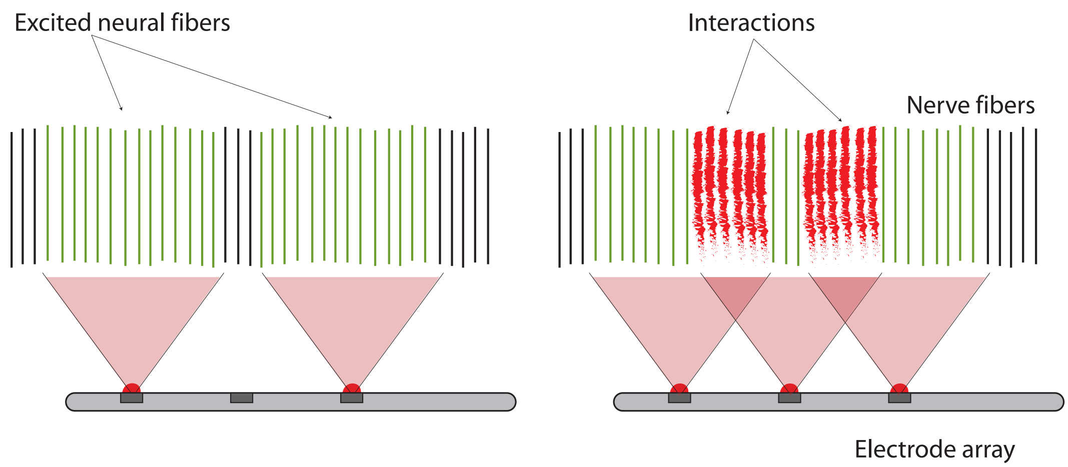

Figure 1.6: Schematic representation of electrode interactions

inserting the array with a positioner. A decrease in current level and a closer distance were assumed to narrow the neural excitation pattern. However, numerous studies also showed that this reduction in current level was no longer present at suprathreshold levels (Shepherd et al., 1993; Saunders et al., 2002; Cohen et al., 2006; Davis et al., 2015). A potential benefit of a small electrode to neurons distance in terms of spatial selectivity is thus not clear. Moreover, such insertion procedures are likely to damage cochlear fine structure of the modiolus and neural elements and may increase the risk of tip fold over (Shepherd et al., 1993; Glueckert et al., 2005; Coordes et al., 2013; Jeyakumar et al., 2014; Pile and Simaan, 2013). Another approach to reduce channel interactions consists in trying to control interactions instead of avoiding them. In the clinical stimulation strategies, each electrode transmits the information extracted from one spectral band. In this so-called monopolar mode, electrical current actually runs between one intracochlear electrode and a remote reference, thus creating an electrical field in the cochlea centered around the stimulating electrode. In contrast, multipolar strategies stimulate several electrodes simultaneously for each channel in order to limit the lateral spread along the scala tympani (figure 1.7). However, most of these strategies require multiple current sources and thus cannot be achieved in all devices. Besides, existing multi-electrode strategies have not shown a significant benefit in terms of speech perception (Lehnhardt et al., 1992; Zwolan et al., 1996; Pfingst et al., 1997; Kileny et al., 1998; Mens and Berenstein, 2005). Alternative multipolar strategies designed to create focused stimulation are the main topic of the present work and will be reviewed and discussed in detail in the next chapters.

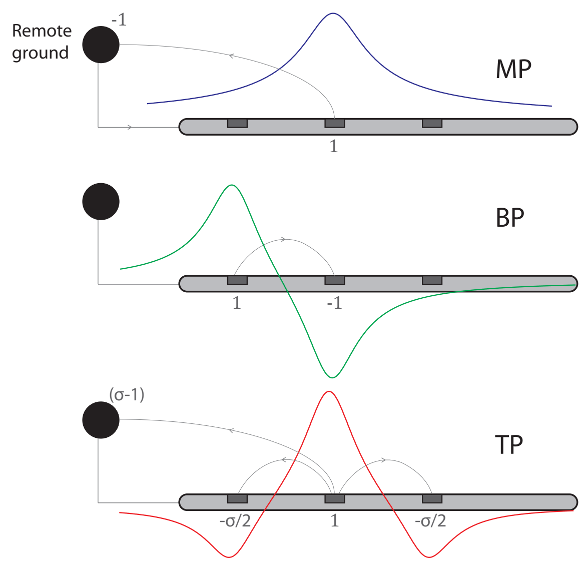

Figure 1.7: Schematic representation of the relative current weights and the resulting electrical field produced by monopolar (MP), bipolar (BP) and tripolar (TP) stimulation modes.

Neural population.

Previous paragraphs demonstrated that the transmission of sound information to the auditory nerve fibers is affected by technical issues. However, overcoming these issues might not be sufficient to improve CI performance without taking into account the target of the electrical stimulation: neural fibers.

In a healthy ear, auditory nerve fibers (ANFs) are secondary cells which do not produce action potentials on their own. They are used to convey the action potentials initiated at the hair cell synapse to the cochlear nucleus. However, cochlear implant stimulation can create action potentials in the absence of hair cells by forcing the cell membrane to depolarize at some location. It is thus important to understand the organization of the neural population in the inner ear.

ANFs are bipolar cells made of two capillary sections, the peripheral axon and the central axon linked by the cell body called the spiral ganglion cell (SGC) or *soma*. In human, the peripheral axons are connected to the synapse of the hair cells in the Organ of Corti. They run through the thin bony extension named the osseous spiral lamina (OSL) up to a porous bony cavity of the modiolus called Rosenthal's canal where SGCs from different nerve fibers aggregate. After the soma, central axons are clustered to form the cochlear nerve which leaves the modiolus towards the brainstem.

Neural processes are fragile structures which can easily be harmed or even destroyed. When hair cells are damaged or non existent, no action potentials travel through the nerve fibers. This inactivity can lead to the progressive degeneration of peripheral processes (Leake and Hradek, 1988; Shepherd and Javel, 1997; Stankovic et al., 2004; Glueckert et al., 2005). Even though the degeneration of peripheral processes is relatively slow in human and does not necessarily induce the degeneration of the central axon (Felder et al., 1997; Teufert et al., 2006; Liu et al., 2015), this phenomenon encouraged the implantation as soon as profound deafness is diagnosed. Central axons can also be damaged after reimplantation or traumatic insertion especially with precurved arrays hugging the modiolus as previously mentioned (Glueckert et al., 2005; Coordes et al., 2013; Pile and Simaan, 2013; Jeyakumar et al., 2014). It is thus very common that the implanted cochlea has an inhomogeneous neural population with either few available nerve fibers or "dead-regions" along the cochlea where no fibers can be stimulated (Schuknecht, 1964; Moore et al., 2000). When an intracochlear electrode faces such a dead-region, current level probably needs to be set much higher to stimulate available fibers further away and produce an auditory percept (Khan et al., 2005b). This can have unfortunate consequences. First, the available neural population is more likely to be stimulated by another electrode which would yield strong channel interactions. Secondly, this reallocation can increase the frequency mismatch mentioned earlier.

Subjects' background

All research studies experience an important variability across subjects. The main limitations previously mentioned may also vary from one subject to another and are expected to strongly influence CI users performance. Although etiology itself has not been identified as the most prominent factor influencing CI outcomes (Lazard et al., 2012), it can be included in the more general concept of subjects *background*. Indeed, etiology is likely to play an important role in subjects outcome since it is influent at both the peripheral and more central levels of the auditory system. From a peripheral point of view, etiology can, for instance, result in different cochlear anatomies and induce different electrode positioning. The cause of deafness together with the duration of deafness may also be responsible for differences in the neural survival populations across subjects. On the other hand, from a higher level point of view, etiology is also indirectly related to the brain's ability to interpret spectro-temporally degraded sounds. Indeed, auditory deprivation not only induces neural degeneration of the peripheral processes, but has also been identified as an influencing factor of CI performance due to reorganization processes at the level of the auditory cortex (Lazard et al., 2012; Blamey et al., 2013; Campbell and Sharma, 2014). As previously mentioned, after cochlear implantation, the brain changes induced by cross-modal plasticity have to be reversed. This process, referred to as auditory rehabilitation, is highly subject-dependent and is likely to be influenced by the duration of deafness which may explain why patients with several years of experience with either acoustic or electric hearing are likely to perform better than people deprived of auditory inputs for a long period. The importance of the social environment and support has also been suggested as potentially helpful to facilitate auditory rehabilitation (Moore and Shannon, 2009). Finally some subjective parameters have been proposed to explain why people with the same device and comparable etiology can perform differently. For instance, patients with a strong musical experience are likely to benefit from a better functioning of their auditory processes in challenging conditions (Fuller et al., 2014).

1.3 Motivations and Outline

1.3.1 Approach and objectives of the present research project

Past decades of research have already proven the ability of the cochlear implant to partially restore the sense of hearing to profoundly-deaf people. Unfortunately, commonly-used stimulation strategies suffer from limiting factors which strongly restrain CI users' performance in challenging conditions. Some alternative techniques have been recently proposed to improve CI outcome. Optical stimulation of neural tissues has been proposed as an alternative to electrical stimulation (Wells et al., 2005; Izzo et al., 2006; Wenzel et al., 2009) but may require the presence of healthy hair cells which limits its relevance for the treatment of sensorineural deafness (Thompson et al., 2015). Other approaches, such as neurotrophic-induced nerve growth (Shibata et al., 2012), optogenetic stimulation (Hernandez et al., 2014; Jeschke and Moser, 2015) or intraneural electrode arrays (Middlebrooks and Snyder, 2007) are currently studied. Despite promising results, such approaches still represent too much of a challenge for a short-term perspective. In the present project we aim to tackle some limitations of the electrical stimulation that could yield a significant improvement of CI performance whilst remaining achievable either with present technology or in a very near future.

First, channel interactions, introduced in the previous section represent one of the main issues of electrical stimulation. The activation of a given electrode creates an electrical field that will widely spread along the scala tympani due to the conductive properties of cochlear fluids. As a result, if another electrode is activated, both electrical fields will overlap and distort the sound information conveyed in each channel. Paradoxically, electrical interactions can also be used in a controlled way to improve spatial selectivity. This idea was used in alternative stimulation strategies, referred to as *multipolar strategies*. Bipolar (BP) and tripolar (TP) (cf figure 1.7) are the most common multipolar strategies. In BP stimulation, each channel is associated with a pair of intracochlear electrodes activated with the same amplitude and opposite polarities. In the same way, for TP stimulation, three adjacent electrodes are required for each channel. The middle one is activated with a given amplitude and polarity while flanking electrodes are activated with half the amplitude and the opposite polarity. For both BP and TP, the linear summation of the different electrical fields theoretically limits the spread along the scala tympani. The concept of multipolar stimulation was extended to the entire array in the *Phased Array* (PA) strategy (van den Honert and Kelsall, 2007). In this specifically advanced technique, all electrodes are required to create a unimodal highly-focused electrical field. Unfortunately, the benefit for CI users performance of focused stimulation has not been clearly demonstrated. The first main aspect of the present project, addressed in Chapters 2 and 3 is thus to identify the possible weaknesses of focused stimulation strategies to understand these inconsistent results and also to investigate ways to improve them.

Besides technical limitations, present devices hardly account for subject-specific parameters. While this lack of subject-specificity might not strongly affect CI outcome using the classic MP stimulation, it might become more and more influent with spatially-focused stimulation strategies. Across-subject variability can arise from different stages of the processing chain of the auditory system, from the lowest level (e.g. electrode position) to the highest level (e.g. subject experience, brain plasticity). A second aspect of the present project aims to investigate ways to adapt a stimulation strategy to each subject based on the identification of the most prominent factors in the periphery of the auditory system (Chapter 4). In particular we attempt to provide a measure of the quality of the electrode−auditory nerve interface and to assess what features have a significant influence on psychophysical outcomes and, thus, would need to be taken into account in an optimized strategy.

The present work is essentially motivated by the fact that we now have numerous tools available to investigate those weaknesses and provide hints for the design of alternative stimulation strategies that could improve electrical hearing quality and restore speech recognition in noise and music appreciation for all CI users. To investigate both aspects, we followed a multidisciplinary approach involving electrical engineering, anatomical and physiological analysis and psychophysics. Next sections introduce the different problematics addressed in this PhD project and presented in this manuscript.

1.3.2 Simulating channel interactions in a vocoder.

Acoustic (or vocoder) simulations of cochlear implants have been used in numerous studies over the years to assess the impact of signal processing on the transmission of sound cues (Shannon et al., 1995; Friesen et al., 2001; Shannon et al., 2002; Stone et al., 2008; Fuller et al., 2014). The first stages of signal analysis realized in a cochlear implant processor can be easily reproduced on a computer and tested with normal hearing listeners. As illustrated in figure 1.8, vocoder stimulation and electrical stimulation with a cochlear implant differ on three main aspects: first, the carrier signal used to transmit the envelope fluctuations extracted in each channel (electrical pulse trains vs. pressure wave), second, the spread of excitation, and finally, the mechanism of the generation of action potentials.

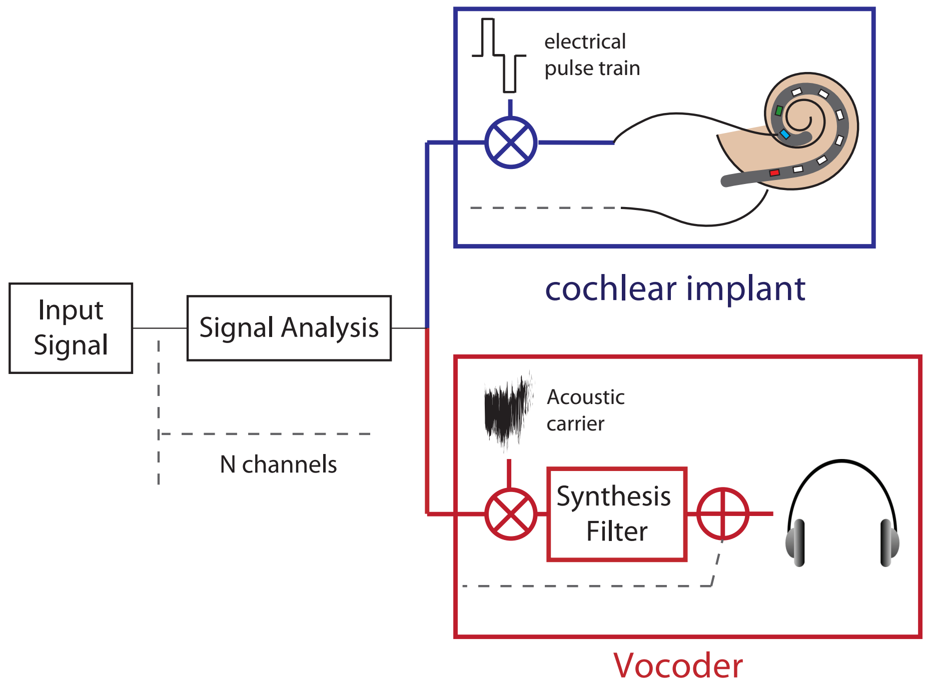

Figure 1.8: Schematic illustration of the principle of acoustic simulation and cochlear implant stimulation.

Although acoustic simulations will never be perfectly comparable to the cochlear implant stimulation, we attempt to improve the realism of these simulations to build a more reliable and complete research tool and use them to test several hypotheses. Chapter 2 and an additional study presented in appendix 7.1 aimed to improve acoustic simulations of cochlear implant and to provide a better understanding of the limitations of multipolar strategies. Both of these studies have been published in Hearing Research and JASA, respectively (Mesnildrey and Macherey, 2015; Mesnildrey et al., 2016).

To investigate the transmission of spectrally-degraded sound information, classic vocoders generally analyze the input signal through a bank of non-overlapping adjacent bandpass filters and use the same filters in the synthesis stage. However, as previously mentioned, one main characteristic of present cochlear implant devices is the superimposition of signals from different spectral bands. To simulate these channel interactions, one can use broadband carriers such as white noise bands to carry signal modulations and apply wider synthesis filters to impose an overlap between several bands (Bingabr et al., 2008; Strydom and Hanekom, 2011a). Theoretically, controlling the shape and the number of synthesis filters enable to both quantify the amount of interactions and identify which parts of the spectrum are affected by them. Chapter 2 presents a model of synthesis filters designed to simulate the spread of excitation in an implanted ear using a noise-vocoder. Synthesis filter shapes were calculated based on the activating function theory (Rattay, 1989) to mimic the neural excitation pattern produced by MP, BP and other virtual stimulation modes. Speech recognition was tested in normal hearing listeners with those different filters to understand the influence of spectral interactions on the transmission of speech cues and explain the results from the literature obtained in CIs using BP stimulation mode.

1.3.3 Optimal acoustic carrier for CI simulations. *(A complementary study)*

The previous acoustic simulation study led us to discuss the relevance of using wide-band noise carriers in CI simulations in an additional study. As this study is somewhat disconnected from the rest of this thesis, I have chosen to present it in Appendix 7.1.

Different carrier signals can, and have been used in vocoder studies. Noise bands present the advantage of being broadband signals, it is thus possible to filter those bands to simulate a specific excitation pattern as described in chapter 2 and in other studies (Qin and Oxenham, 2003; Fu and Nogaki, 2005; Strydom and Hanekom, 2011a). However, a broadband noise strongly differs from an electrical pulse train in the temporal domain. First, it is not pulsatile, and second it contains intrinsic modulations that will add to the original modulations conveyed in each channel. Pure tones centered in each analysis band have also been used in the past (Whitmal et al., 2007; Crew et al., 2012). Contrary to noise bands, pure-tones have perfectly flat envelopes which enables to convey the exact temporal modulations but they are also spectrally restricted and cannot simulate the wide spread of excitation of CIs.

Hilkhuysen and Macherey (2014) introduced a signal named *Pulse Spreading Harmonic Complex* (PSHC). The generation of PSHCs, described in Appendix 7.2, theoretically enables to create pulsatile acoustic signals optimized to elicit minimum intrinsic fluctuations after auditory filtering. Hilkhuysen and Macherey (2014) confronted optimized PHSC signals to other broadband signals (pseudo-random noise and low-noise noise) in a modulation detection task with normal hearing listeners. Modulation detection thresholds were significantly lower for PSHC signals suggesting that other signals contain more intrinsic fluctuations.

In this additional study, PSHCs, pure tones and broadband noises were used as carrier signals in vocoder simulations. Speech Reception Thresholds (SRT) were measured in a group of naive normal hearing listeners. Based on modulation detection results reported in Hilkhuysen and Macherey (2014) PSHC was hypothesized to yield better speech recognition performance than broadband noises but worse than pure-tones. With its temporal and spectral properties, PSHCs could represent a relevant alternative to other carrier signals commonly used in the literature and thus further improve the reliability of vocoder simulations of CIs.

1.3.4 Impedance measurements and electrical properties of the implanted ear.

Even though the general concepts of electrical diffusion have been known for a long time, some aspects require further clarification to be able to efficiently control electrical interactions within the cochlea using multipolar strategies. In Chapter 3, different electrical recordings were carried out in CI users using the Advanced Bionics HiRes 90k device to better understand the electrical properties of both the device and the biological medium. An in vitro setup was also developed to provide a baseline for the analysis of CI data and facilitate their interpretation.

In this chapter, intracochlear recordings were carried out to assess some of the most fundamental assumptions required for multipolar stimulation. Spelman et al. (1982); Suesserman and Spelman (1993a); Vanpoucke et al. (2004a) reported that the electrical diffusion through the variety of biological media composing the cochlea was not frequency dependent. This observation suggests that the entire inner ear can be considered as purely resistive. However, those studies were limited to frequencies up to 12.5 kHz while clinical pulses contain higher frequency components. Given the importance of this assumption, further measurements were made in the present study, in both the spectral and temporal domain to evaluate this hypothesis at higher frequencies.

While BP and TP stimulation attempt to restrict the electrical spread using one or two electrodes, in the PA strategy, all electrodes are simultaneously activated with different amplitudes and polarities so that the overall electrical field is highly focused in the vicinity of a specific electrode.

To be able to compute the optimal contribution of all electrodes, the PA strategy requires the estimation of the electrical field produced by each electrode.

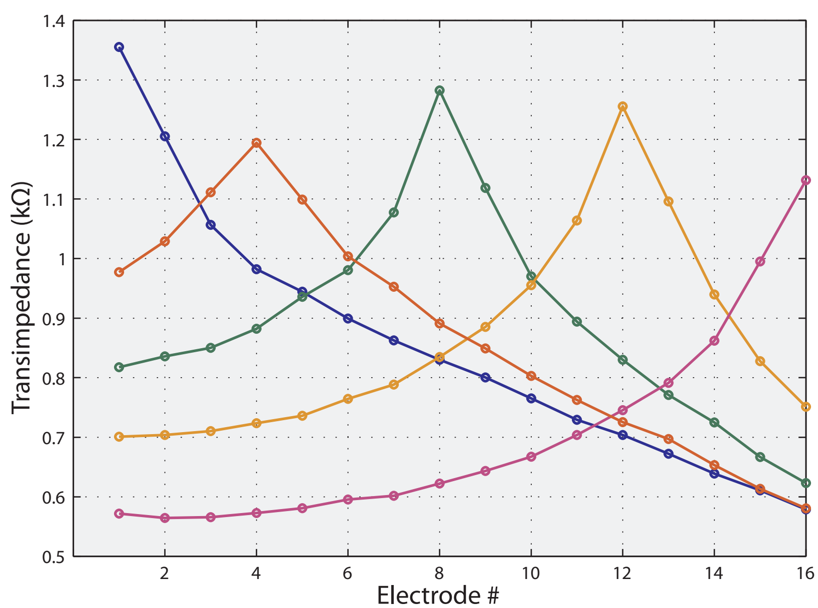

Figure 1.9: Transimpedance pattern recorded in one CI subject. Peak values estimated using linear extrapolation. Subset shown for clarity.

This can be easily measured by activating one electrode and record the voltage on all available inactive electrodes of the array (figure 1.9). Once normalized by the input current amplitude, these data are referred to as the *transimpedance matrix*, Z. Considering the vector of current amplitude, I_e, applied to each electrode, the resulting voltage is given by the generalized Ohm's law (equation 1.2). It is thus possible to quantify the amplitude of interacting electrical fields at the level of a given electrode. The inverse problem expressed in equation 1.3 can then be computed to estimate the relative currents to apply on each electrode to generate the specific voltage distribution V_d at the level of the electrodes. Figure 1.10 represents the relative weights of each electrode to achieve a single focused voltage peak at electrode 8.

$$V = Z.I_e \tag{1.2}$$

$$I_e = Z^{-1}.V_d \tag{1.3}$$

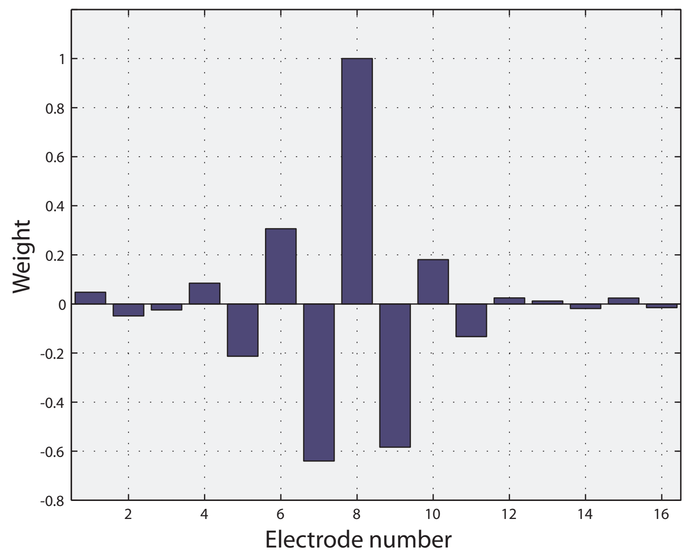

Figure 1.10: Current weights computed from CI data to generate one focused voltage peak at electrode 8

.

Unfortunately, when an electrode is stimulated, its interface with the inner ear fluids polarizes. The recorded waveform thus comprises several components: (1) the interface impedance, (2) the resistance between the stimulating contact and the ground (referred to as the *access resistance*), which is the value of interest, and (3) the impedance due to the device electronics. This prevents the direct measurement of the electrical peak voltage at the surface of the contact. Figure 1.11 illustrates the charge reorganization at the electrode-fluid interface.

This means that the diagonal terms of the matrix Z, (i.e. the most prominent voltage peaks) cannot be directly measured which is a major issue for the PA strategy. To overcome this issue in the original strategy, diagonal terms were estimated using linear extrapolation from measures on adjacent electrodes. However, it is known that the electrical potential decreases very quickly in the vicinity of the electrode surface. As a result, the extrapolated values may strongly underestimate the actual contact impedance.

Being able to accurately estimate the access resistance represents a challenge for

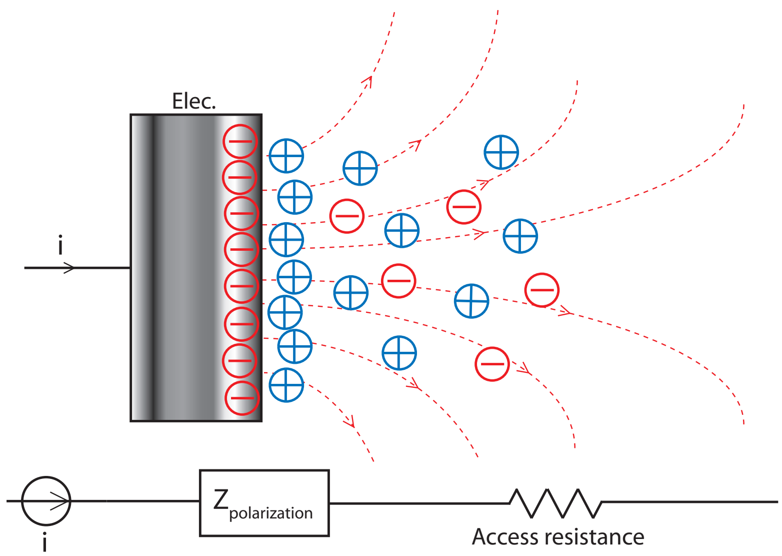

Figure 1.11: Charge reorganization at the electrode-fluid interface. Current lines are depicted by dotted lines.

various industrial or medical applications and has thus been the topic of many research projects. To isolate the access resistance from polarized impedances, several studies used equivalent electrical circuits. However, in the field of cochlear implant and specifically in humans, few studies attempted to model this phenomenon (Vanpoucke et al., 2004b; Tykocinski et al., 2005). Moreover, studies on this topic relied on simple models which, as we will see, cannot accurately describe the electrode impedance.

Chapter 3 presents an alternative phenomenological model for polarized electrodes' impedance based on high resolution temporal and spectral voltage recordings.

1.3.5 Electrode-neuron interface and psychophysics

Being able to focus electrical stimuli at the level of a given electrode does not guarantee an improvement of CI users' performance in speech recognition. Indeed, the electrical stimuli generated at the surface of the electrodes do not necessarily represent what is actually present at the level of the nerve fibers. To further improve electrical stimulation, several studies highlighted the importance of characterizing the electrode-neuron interface by modeling the chain of elements that are supposed to affect electrical stimulation from the electrode itself to the initiation of action potentials (Bierer, 2010; Goldwyn et al., 2010; Long et al., 2014). These studies classically include the electrode position, the electrical diffusion from the electrode surface to the neurons and, finally, the excitability of the neuron population itself. As such, they model the most peripheral sources of subjects' performance variability.

Chapter 4 attempts to describe the electrode-neuron interface for each patient using CT scans, electrical intracochlear recordings and psychophysics. The most basic model of the electrode-neuron interface is based on the estimation of the distance between the electrodes and the closest neurons using CT scans. A small electrode-to-neurons distance is generally associated with lower detection thresholds. However, the distance itself cannot account for CI users' performance (Saunders et al., 2002; Long et al., 2014). Long et al. (2014) measured the electrode position, detection thresholds and speech recognition performance in CI users and demonstrated that subjects for which distance poorly explains the variation of thresholds across the array had lower speech recognition scores than those for which the distance model was more representative of across-electrode threshold variations. They hypothesized that this result might reveal the importance of neural survival. In the study presented in chapter 4, similar measures as in Long et al. (2014) were made in CI users but the neural responsiveness was further investigated by measuring the *polarity effect*. This *polarity effect* relies on the assumption that peripheral and central processes of the neurons exhibit different sensitivity to stimulus polarity. Herein, we thus try to assess whether the difference in neural responsiveness as a function of stimulus polarity might provide further information on the state of neural survival and thus better explain psychophysical outcomes. If so, this would enable to include another prominent subject-specific factor for the design of alternative spatially-focused stimulation strategies.

1.3.6 Electrical diffusion in the implanted cochlea

As previously mentioned, the electrical field generated by an intracochlear electrode can be estimated at a dozen of discrete locations by measuring transimpedances. However, to achieve optimized stimulation at the level of the neural fibers one may need more accurate information on the diffusion of electrical currents in the inner ear. In Chapter 5, we took a closer look at the diffusion of electrical stimuli generated by a cochlear implant. We investigated this aspect using both in vitro and in vivo measurements and tried to identify potential ways to further enhance spatially selective stimulation with the Phased Array strategy. In particular we evaluate what would be needed to infer the voltage distribution at the level of the modiolar wall from recordings made on the electrodes. Finally, we discuss our findings in the perspective of developing a remote electrical focusing technique.

1.3.7 Conclusion

This thesis was written so that each chapter can be read independently. Finally, Chapter 6 summarizes the outcomes of the different experiments and discusses the approach used in this project. In particular, we discuss the different recording and analysis tools developed for the present work and their possible implications in the field of cochlear implants. We also expose potential ways to integrate the main insights in the design of alternative cochlear implant stimulation strategies which would be both spatially selective and subject-specific.

These main perspectives are addressed on two different time scales. Some features may be integrated in existing devices without further technical modifications. This may be beneficial since it would be applicable to most CI users and may eventually lead to improved hearing. On the other hand, some features appear to be much more complicated to handle with contemporary devices. However, interesting hints will be highlighted for the perspective of improving future devices.

Chapter 2

Acoustic Simulations of the Spread of Excitation: Effect on Speech Intelligibility.

Adapted from:
Mesnildrey, Q., and Macherey, O. (2015). "Simulating the dual-peak excitation pattern produced by bipolar stimulation of a cochlear implant: Effects on speech intelligibility", Hear. Res. 319, 32–47.

Abstract

Several electrophysiological and psychophysical studies have shown that the spatial excitation pattern produced by bipolar stimulation of a cochlear implant (CI) can have a dual-peak shape. The perceptual effects of this dual-peak shape were investigated using noise-vocoded CI simulations in which synthesis filters were designed to simulate the spread of neural activity produced by various electrode configurations, as predicted by a simple cochlear model.

Experiments 1 and 2 tested speech recognition in the presence of a concurrent speech masker for various sets of single-peak and dual-peak synthesis filters and different numbers of channels. Similarly as results obtained in real CIs, both monopolar (MP, single-peak) and bipolar (BP+1, dual-peak) simulations showed a plateau of performance above 8 channels. The benefit of increasing the number of channels was also lower for BP+1 than for MP. This shows that channel interactions in BP+1 become especially deleterious for speech intelligibility when a simulated electrode acts both as an active and as a return electrode for different channels because envelope information from two different analysis bands are being conveyed to the same spectral location.

Experiment 3 shows that these channel interactions are even stronger in wide BP configuration (BP+5), likely because the interfering speech envelopes are less correlated than in narrow BP+1.

Although the exact effects of dual- or multi-peak excitation in real CIs remain to be

determined, this series of experiments suggest that multipolar stimulation strategies, such as bipolar or tripolar, should be controlled to avoid neural excitation in the vicinity of the return electrodes.

2.1 Introduction

Most contemporary cochlear implants (CIs) stimulate the auditory nerve by delivering current pulses to individual intra-cochlear electrodes with reference to a far-field ground. This so-called monopolar (MP) configuration produces a broad spread of excitation across the auditory nerve array. Consequently, different electrodes excite overlapping neural populations and limit the number of independent information channels that can be transmitted to CI listeners. Specifically, these interactions are believed to be responsible for the inability of many patients to benefit from more than about eight electrodes (Fishman et al., 1997; Friesen et al., 2001; Fu and Nogaki, 2005). To overcome this limitation, several multi-electrode configurations have been proposed and tested. Animal studies have shown that the spread of excitation can be reduced using bipolar (BP) or tripolar (TP) stimulation where current pulses are delivered between two or three closely-spaced intra-cochlear electrodes (Kral et al., 1998; Bierer and Middlebrooks, 2002; Snyder et al., 2004, 2008; Bierer, 2010). Paradoxically, attempts to use these spatially "focused" configurations in CI users have produced inconsistent results. Using psychophysical forward masking, Kwon and van den Honert (2006) observed no difference between the widths of the patterns produced by MP and BP stimuli in a group of six CI subjects whereas Boëx et al. (2003) found a small advantage for BP in the two subjects they tested. Although Nelson and Kreft (2008) reported forward-masked tuning curves that were narrower for BP than for MP, these tuning curves were measured in different subjects for the two configurations. Given these two groups of subjects also had different implant types and electrode designs, it remained unclear whether the difference in tuning was due to the difference in electrode configuration or to some other factors. More recent data comparing forward-masked tuning curves did not find any difference between MP and BP although the same subjects were tested in both configurations (Bingabr et al., 2014). Spatial selectivity of TP stimulation was recently investigated in three studies (Bierer and Faulkner, 2010; Landsberger et al., 2012; Fielden et al., 2013). Modest but significant improvements were reported for TP compared to MP although, here again, substantial inter-subject variability was noticed.

Several studies have also compared speech recognition scores obtained with MP and BP (Lehnhardt et al., 1992; Zwolan et al., 1996; Pfingst et al., 1997; Kileny et al., 1998). These studies did not find any advantage for BP and sometimes even showed better performance for MP. Rather counter-intuitively, Pfingst et al. (1997) reported that speech perception of CI listeners improved when the spacing between the electrodes of each bipolar channel increased from one to six inactive electrodes. More recently, speech processing strategies using the "partial-tripolar" configuration have shown slightly more encouraging results. Partial tripolar is identical to tripolar except that a fraction of the current returns to the extra-cochlear ground electrode. Although Mens and Berenstein (2005) did not find any advantage of using partial tripolar over MP stimulation, Srinivasan et al. (2013) reported an improvement in speech reception threshold of about 3 dB for partial tripolar in a group of five Advanced Bionics subjects.

There may be several reasons for these rather disappointing and inconsistent results.

First, as suggested by Kwon and van den Honert (2006), it is possible that MP and focused (BP or TP) stimuli produce similar spreads of excitation when compared at the same loudness. Two electrophysiological studies have underlined the importance of the current levels at which the excitation patterns generated by different configurations are compared. Smith and Delgutte (2007) measured the spread of excitation produced by MP and BP stimuli in the inferior colliculus of the cat. They observed that the patterns produced by both stimuli at levels within a 5-dB range above their respective thresholds had comparable peak amplitudes and spreads of excitation. Similarly, Schoenecker et al. (2012) equated their MP and BP stimuli so that they produced the same peak spike rate in inferior colliculus neurons and found similar tonotopic spreads of excitation for both configurations.

Second, Pfingst et al. (2001) have argued that a broad spread of excitation (i.e. using either BP with a large spacing between electrodes or MP) may provide more robust information to the central auditory system by recruiting a larger population of neurons than BP with closely-spaced electrodes. Consistent with this hypothesis, Middlebrooks (2008) showed that modulation detection thresholds, as measured electrophysiologically at the level of the auditory cortex of guinea pigs, were worse for BP than for MP. He showed that MP stimulation produced synchronous activation over a broader range of neurons than BP, thereby conveying temporally-more precise information to the auditory cortex. This suggests that, even if spatial selectivity is improved in some CI subjects, performance on speech perception tasks may not because of a concomitant decrease in modulation sensitivity.

Third, it has been shown by Kwon and van den Honert (2006) that BP stimulation produces thresholds and forward masking patterns that are more irregular across the electrode array than those produced by MP. This pattern variability may be due to differences in electrode placement or to an irregular distribution of neural survival but also to the fact that focused stimulation requires the stimulation of at least two intra-cochlear electrodes. Several computational modeling studies have shown that this can produce discrete peaks of excitation proximal to each electrode (Frijns et al., 1996; Hanekom, 2001; Litvak et al., 2007; Bonham and Litvak, 2008). For example, in BP stimulation, two main groups of neurons may be excited, close to each stimulated electrode. Such dual-peak excitation patterns have also been reported in an electrophysiological animal study (Snyder et al., 2008) and in psychophysical and electrophysiological human CI studies (Lim et al., 1989; Chatterjee et al., 2006; Undurraga et al., 2012). This dual-peak shape may also arise when measuring tuning curves. (Kral et al., 1998) reported "tip-splitted" neural tuning curves in about 30% of cats' single auditory nerve fibers subjected to BP stimulation. These tuning curves showed a maximum surrounded by two minima with a threshold difference of about 5 dB between them. Using psychophysical masking, Nelson and Kreft (2008) and Zhu et al. (2012) also observed tip-splitted tuning curves in some of their human CI subjects stimulated in BP configuration. Similarly, for TP stimulation, if the amount of current returning to the neighboring electrodes is large (e.g. at loud levels), each return electrode may produce excitation in its vicinity, potentially creating a triple-peak excitation pattern and decreasing any putative increase in spatial selectivity (Litvak et al., 2007). One potential problem of transmitting the information extracted from a given spectral channel through multi-peak auditory-nerve excitation arises when considering how electrodes are activated in a speech-coding strategy. If the aim is to maximize the number of spectral channels that are conveyed, each intra-cochlear electrode needs to serve both as the "active" electrode of one channel and as the "return" electrode of another (in bipolar) or several other (in tripolar) channel(s). Therefore, a given electrode may stimulate the same, spatially-restricted, neural population with information extracted from different frequency bands.

The main goal of the present study was to investigate the effects of such multi-peak excitation patterns on the perception of speech, focusing on the comparison between single- and dual-peak shapes. These effects were tested in normal-hearing subjects listening to noise-vocoded simulations for two main reasons. First, the performance of CI listeners is subject to an inherent variability due to several potential factors including peripheral ones such as the tonotopic distribution of residual nerve fibers or the distance between the electrodes and the fibers (Blamey et al., 2013; Long et al., 2014). These peripheral factors may explain why different electrodes in a given subject show variable degrees of spatial selectivity Bierer and Faulkner (2010). These sources of variability are not involved when testing normal-hearing subjects. Furthermore, acoustic simulations provide an accurate control of stimulation parameters that may not be easily manipulated in a real CI. Although a lot of CI simulation studies have investigated the effect of channel interactions on speech (Friesen et al., 2001; Fu and Nogaki, 2005; Bingabr et al., 2008; Strydom and Hanekom, 2011b,a) and pitch perception (Laneau et al., 2006; Crew et al., 2012), to our knowledge, none of them has included multi-peak excitation patterns. Here we present the results of three speech recognition experiments specifically designed to better understand these effects. In Experiments 1 and 2, speech perception is measured for different numbers of channels and different single- and dual-peak simulated excitation patterns. In Experiment 3, we focus on simulating the effect of electrode separation in BP stimulation and try to relate the present findings to previously published CI data Pfingst et al. (1997, 2001).

2.2 General methods

2.2.1 Subjects

17 normal hearing subjects were paid to take part in a series of three vocoded speech recognition experiments. Written informed consent was obtained from all subjects prior to data collection. The subjects first had to perform a pure-tone audiogram (Bekesy-tracking) for frequencies ranging from 125 to 8000 Hz. Their detection thresholds were

all lower than 20 dB HL.

2.2.2 Speech material and experimental platform

In all experiments, the subjects were asked to recognize speech sentences presented in different conditions. The target sentences were part of the French Matrix Test Corpus (FrMatrix) developed by Jansen et al. (2012). The FrMatrix Corpus contains 28 lists of 10 phonetically-balanced sentences. The whole corpus is built up with 10 names, 10 verbs, 10 numerals, 10 objects and 10 colors. All sentences have the exact same structure and consist of five words (one of each category) presented consecutively, e.g. "Michel achète cinq ballons jaunes" (Michel-buys-five-balls-yellow).

Target sentences were mixed with a speech masker before being processed by the vocoder. The presence of the masker was necessary to avoid ceiling effects and simulates a challenging situation for CI users. As in Deeks and Carlyon (2004), time-reversed speech maskers were used. They were constructed by randomly selecting and concatenating sentences extracted from the French Intelligibility Sentence Test corpus Luts et al. (2008). Such maskers have similar temporal and spectral properties as interfering speech but remain unintelligible, thereby reducing the influence of informational masking. Note that the speakers of the target and masker sentences were female and male, respectively, and, therefore, had different F_0s.

Two different target-to-masker ratios (TMRs) of +5 and +10 dB were tested in the following experiments. After being mixed with the masker, each stimulus was vocoded to simulate a specific electrode configuration, following the signal processing steps described in section 2.2.3. All stimuli were digitally generated on a personal computer, using Matlab (Mathworks, Natick, MA, USA), and played out via an external sound card (Saffire pro 24, Focusrite Audio Engineering Ltd, United Kingdom). The stimuli were presented monaurally through a single earpiece of a pair of HD215 Sennheiser headphones at an overall level of 65 dB SPL. Subjects sat in a sound-isolated booth and were asked to report the words they recognized via a graphical interface displayed on a computer screen. The interface consisted of a matrix of virtual response buttons comprising 5 columns of 10 words, one for each category. After a sentence was presented, the subject was asked to choose one word of each category by clicking on the virtual buttons with a computer mouse. The results were expressed in percentage of words recognized and transformed into rationalized arcsine units (rau) to homogenize the variances of the scores across conditions (Studebaker, 1985).

2.2.3 Signal processing

2.2.3.1 Vocoder processing

To simulate different electrode configurations, a noise-band vocoder was implemented based on the original study by Shannon et al. (1995). The processing steps of this

	4 Channels	8 Channels	11 Channels	15 Channels
Analysis filters cutoff frequencies (-3 dB)	250, 623, 1348, 2760, 5500 Hz	250, 406, 623, 926, 1348,1938, 2760, 3904, 5500 Hz	250, 358, 496, 671, 894,1179, 1541, 2002, 2590, 3336, 4288, 5500 Hz	250, 327, 418, 528, 658, 814,1000, 1222, 1487, 1804, 2182, 2633, 3172, 3815, 4583, 5500 Hz

Table 2.1: Cut-off frequencies (-3 dB) of the analysis filters for 4, 8, 11 and 15-channels vocoders.

vocoder are schematically illustrated in Figure 2.1. The stimuli were first passed through a bank of analysis filters (AFs; zero-phase 6th order Butterworth filters) spanning the 250-5500 Hz frequency range. For N analysis bands, this frequency range was divided into N portions equated in terms of the theoretical width of excitation along the basilar membrane, as given by Greenwood's function Greenwood (1990). The edges of each band defined the low and high cut-off (-3 dB point) frequencies of the band-pass filters and are reported in 2.1 for the different Ns tested in the three experiments.

The temporal envelopes in each analysis band were extracted by half-wave rectification and low-pass filtering using a second-order Butterworth filter with a 50-Hz cut-off frequency. The ability of all band-pass filters used in these experiments to convey modulations up to at least 50 Hz was checked prior to the tests by computing the modulation spectrum of a white noise filtered by each filter and verifying that modulations up to 50 Hz were not attenuated (Apoux and Bacon, 2008a). Each envelope was then used to amplitude-modulate a white-noise carrier. Noise carriers were preferred to pure-tone carriers because their spectral shape could be adjusted to simulate different spreads of excitation. Each amplitude-modulated noise was further filtered using a synthesis filter corresponding to a specific configuration and the level of each filter's output was scaled to equate the energy of the corresponding analysis band. Finally, the stimulus presented to the subject consisted of the sum of the N synthesized band-limited signals.

2.2.3.2 Synthesis filters' design

The synthesis filters were designed assuming that the temporal envelopes were transmitted to an imaginary array of 17 intra-cochlear electrodes. This number of electrodes corresponds to the average number of contacts present in commercially-available CIs. To minimize the frequency mismatch between the analysis and synthesis stages, these imaginary electrodes were assumed to be regularly distributed along a portion of the basilar membrane corresponding to the analysis frequency range. The characteristic frequencies corresponding to the location of these imaginary electrodes are given in table 2.2. Using Greenwood's function, Greenwood (1990), this electrode spacing was found to be equivalent to a distance between adjacent contacts of 1.13 mm, which is comparable to the spacing found in contemporary CIs. Note that although it has been suggested

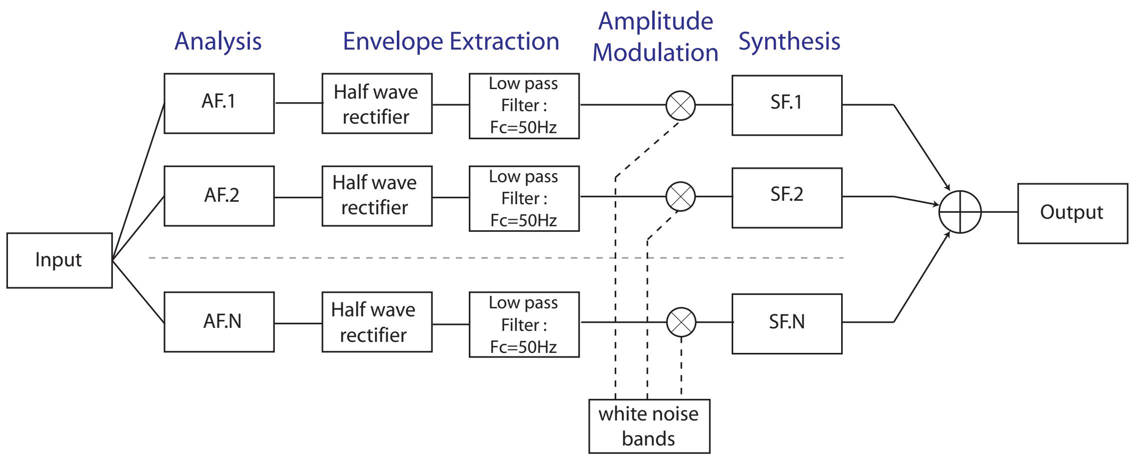

Figure 2.1: Block diagram showing the signal processing steps performed by the vocoder.

that Greenwood's function may not be valid in CI users because of uncertainties on the exact site of excitation along the nerve fibers, it provides a first approximation of the frequency-to-place mapping in human CI listeners (Stakhovskaya et al., 2007). In addition, electro-acoustic pitch comparisons performed in unilaterally-deaf implanted CI subjects with no previous experience with their CI showed pitch matches overall consistent with Greenwood's function Carlyon et al. (2010). Different electrode configurations were simulated by manipulating the shape of the synthesis filters. These filters were designed using a simple model based on the theoretical study of Rattay (1989) and on simulations by Litvak et al. (2007). In a CI, when an electrode is activated with reference to a remote ground (i.e. in monopolar configuration), an electrical field is generated in the medium surrounding this electrode. As a first approximation, let us consider the cochlea as a homogenous and infinite medium. Following Rattay (1989), the electrical potential field produced by this electrode is given by equation 2.1.

$$V = \frac{\rho.I}{4.\pi.r} \tag{2.1}$$

V is the electrical potential, ρ is the extracellular resistivity, I is the electrode current and r is the distance to the electrode.
As shown by Rattay (1989), the pattern of polarization of a nerve fiber in such a medium is effectively described by the second derivative of the electrical potential along the fiber, known as the activating function. To obtain a simple expression of this activating function, the model geometry of the electrode-neuron interface introduced by Litvak et al. (2007) is used. In this particular geometry, a rectilinear electrode array lies along the y-axis. All nerve fibers are parallel to the x-axis and belong to the plane defined by

$(\vec{x},\vec{y},z = d)$. The distance d between the electrodes and the nerve fibers is assumed to be constant and equal to 1 mm (Cohen et al., 2006). The dark thin lines in figure 2.2 show the activating functions of several nerve fibers in response to monopolar cathodic stimulation of an electrode located at $(x, y, z) = (0, 0, 0)$. Each nerve fiber is depolarized (positive values of the activating function) at a site close to the electrode and hyperpolarized (negative values of the activating function) at more remote sites. For anodic stimulation, the opposite pattern of polarization is obtained showing zones of hyperpolarization close to the electrode and of depolarization more distally (not shown). In this model, the maximum of depolarization (i.e. the maximum of the positive part of the activating function) produced by a monopolar symmetric biphasic pulse is obtained during the cathodic phase and is located, for each fiber, right above the electrode array (i.e., for $x = 0$ in figure 2.2). We refer to the maximum of depolarization across the population of nerve fibers as the MOD (Maximum of Depolarization, in $mVmm^{-2}$). It is illustrated by the dark thick line in figure 2.2 and its mathematical expression is given in equation 2.2.

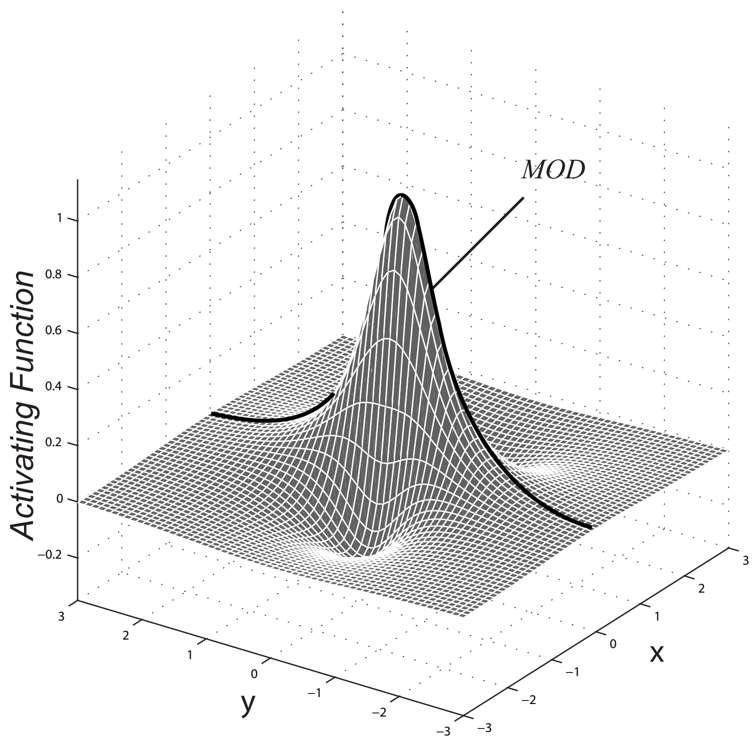

Figure 2.2: Activating functions according to the present model geometry of the electrode-neuron interface. The white thin lines represent the activating functions of different fibers for monopolar cathodic stimulation of an electrode located at the origin. The dark thick line represents the MOD across the population of nerve fibers.

$$MOD(y) = \frac{\rho.I}{4.\pi.((y - y_0)^2 + d^2)^{(3/2)}} \tag{2.2}$$

y_0 is the abscissa of the activated electrode and d is the distance between the neurons and the electrode array. It is further assumed that, at any given abscissa y, there is a group of nerve fibers with thresholds distributed uniformly over a wide range of levels. This range is assumed to be sufficiently large so that saturation of neural activity never occurs for the stimulation levels considered here. Consequently, the larger the amplitude of the depolarization, the more fibers cross their threshold and generate an action potential. The number of neural firings at a given place along the $\vec{y}$-axis in response to an electrical pulse is therefore proportional to the MOD along the $\vec{y}$-axis.

Each excitation pattern calculated with this model is a very coarse approximation of the spatial distribution of neural firings across the auditory-nerve array in response to an electrical pulse. Considering the tonotopic organization of the cochlea, each location y in the space domain can be related to a frequency f using Greenwood's function, $y = G(f)$, Greenwood (1990). Thus, we can express the spatial distribution of the number of neural firings in response to a monopolar eletrical pulse train, $N_{firings}$, as a function of the characteristic frequency of the nerve fibers f, as shown in equation 2.3.

$$N_{firings}(f) = \frac{N_0}{MOD(G(f_0))}.MOD(G(f)) \tag{2.3}$$

f_0 is the characteristic frequency of the fibers located right above the stimulating electrode, N_0 is the number of firings produced in fibers with characteristic frequency f_0, G is the Greenwood's function.

Moreover, Relkin and Doucet (1997) showed that the logarithm of the number of neural firings produced by an acoustic tone is proportional to the level of the tone expressed in dB SPL. Extrapolating this relation to a broadband signal centered on f_0, the difference in $log(N_{firings})$ produced by this signal at two different frequency locations is proportional to the difference in intensity spectrum level at these two frequencies, as shown in equation 2.4.

$$20.\log\left(\frac{N_{firings}(f)}{N_0}\right) = \beta.[L_{dB}(f) - L_{dB}(f_0)] \tag{2.4}$$

L_{dB}, is the intensity spectrum level and β is the proportionality coefficient. We want to obtain the magnitude frequency response $|H_{mp}(f)|$ of a filter centered on f_0 that would, for a broadband input, produce an output signal with the same spatial distribution of $N_{firings}$ as that produced by a monopolar electrical stimulus. Following equation 2.4, this magnitude response can be expressed as a function of the relative number of firings its output would produce at different frequencies (equation 2.5).

$$|H_{mp}(f)| = \left(\frac{N_{firings}(f)}{N_0}\right)^{1/\beta} \tag{2.5}$$

Further expressing $N_{firings}(f)$ as a function of the MOD as given in equation 2.3 leads to the magnitude frequency response of the filter shown in equation 2.6.

$$|H_{mp}(f)| = \left(\frac{MOD(G(f))}{MOD(G(f_0))}\right)^{1/\beta} = \left(\frac{d^3}{((G(f) - G(f_0))^2 + d^2)^{(3/2)}}\right)^{1/\beta} \tag{2.6}$$

$G(f_0)$ corresponds to the location of the stimulating electrode. Relkin and Doucet (1997) observed a frequency dependence for β (equal to 0.39 and 0.21 for pure tones at 1 kHz and 8 kHz, respectively). However, we chose to fix this parameter ($\beta = 1$) to obtain filter bandwidths in accordance with previous vocoder studies that simulated MP configuration. These studies used bandwidths derived from physical measurements of current spread (Bingabr et al., 2008) or from perceptual measures of electrode discrimination in CI subjects (Laneau et al., 2006) and will be discussed in section 2.3.3.

Simulating the BP excitation pattern requires the additional hypothesis that contributions of several electrodes to the electrical field add linearly (Litvak et al., 2007). During the first phase of the pulse, electrode a of the bipolar channel is stimulated cathodically. According to the present model, this produces, for each fiber, an activating function with a peak of depolarization in the vicinity of this electrode. The depolarization pattern along the $\vec{y}$-axis that would produce electrode a if it was stimulated in MP configuration is shown for $x = 0$ by the dotted lines in figure 2.3A. Electrode b, however, is stimulated anodically and produces a peak of hyperpolarization in nearby fibers. The hyperpolarization pattern along the y axis that would produce this electrode if it was stimulated on its own is shown for $x = 0$ by the dashed lines in figure 2.3A. The global polarization pattern along the y axis produced by bipolar stimulation of electrodes a and b is given by the sum of these two patterns (solid line in figure 2.3A). During the second phase of stimulation, the opposite pattern of polarization is obtained (figure 2.3B). In this case, the peak of depolarization is located proximal to Electrode b. Assuming neural excitation is only achieved by depolarizing currents, the MOD produced by a biphasic pulse in BP stimulation is given by the sum of the half-wave rectified polarization patterns produced by each phase, as shown in figure 2.3C. This pattern presents a characteristic dual-peak shape, similar to the pattern shape derived from computational models of the cochlea (Frijns et al., 1996; Hanekom, 2001; Bonham and Litvak, 2008) and observed in electrophysiological measures (Snyder et al., 2008) for electrode separations of 1 mm or more between the two electrodes of a bipolar channel. The magnitude frequency response of a BP synthesis filter is given in equation 2.7.

$$|H_{BP}(f)| = \left|\left(\frac{d^3}{((G(f) - G(f_1))^2 + d^2)^{(3/2)}}\right)^{1/\beta} - \left(\frac{d^3}{((G(f) - G(f_2))^2 + d^2)^{(3/2)}}\right)^{1/\beta}\right| \tag{2.7}$$

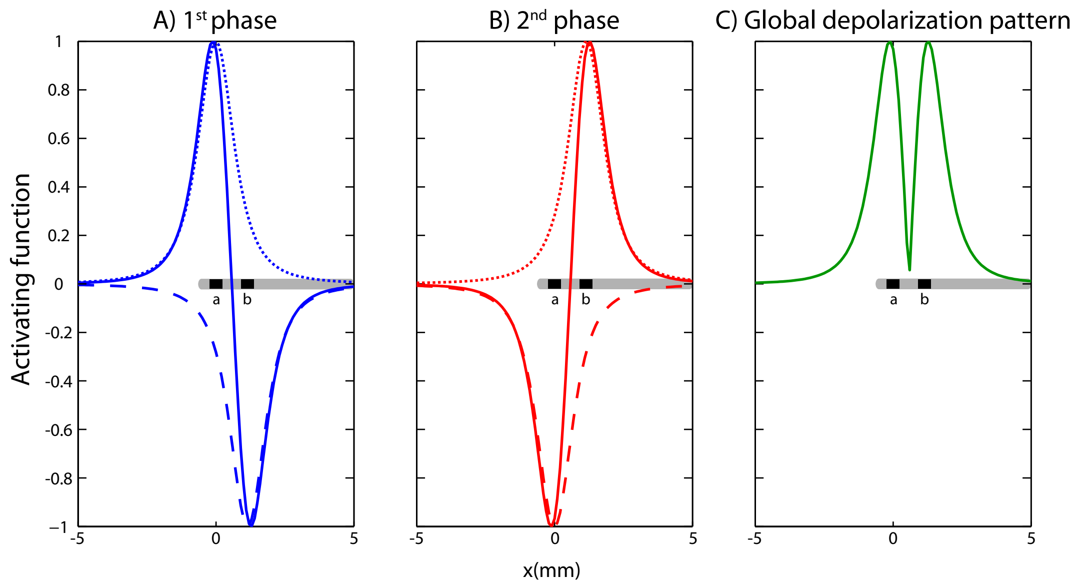

Figure 2.3: Generation of the dual-peak pattern produced by bipolar stimulation. A) Pattern of polarization produced by the first phase of a biphasic bipolar pulse. The dotted and dashed lines represent, the depolarization and hyperpolarization that would be generated by each electrode stimulated individually in monopolar configuration. The solid line shows the pattern of polarization produced by the same two electrodes stimulated bipolarly; B) Same as A) for the second phase of the biphasic pulse C) Global depolarization pattern. Black squares represent two stimulated electrodes of an electrode array.

$G(f_1)$ and $G(f_2)$ correspond to the locations of the two electrodes of the pair, d is the distance between the neurons and the electrode array. The desired shape of the synthesis filters was obtained by calculating the coefficients of a finite-impulse response filter using the fir2 function of Matlab. To avoid phase distortions, zero-phase filtering was applied using Matlab's $filtfilt$ function. The transmission of a stimulus to a particular electrode was obtained by matching the characteristic frequency of the electrode (see table 2.2) to the maximum of the excitation pattern and further applying the appropriate synthesis filter.

Electrode	1	2	3	4	5	6	7	8	9
Frequency (Hz)	282	355	440	538	654	789	947	1133	1349
Electrode	10	11	12	13	14	15	16	17	
Frequency (Hz)	1602	1898	2243	2648	3120	3673	4320	5075	

Table 2.2: Characteristic frequencies of the simulated electrodes.

2.3 Experiment 1: Comparing monopolar and bipolar simulations for different numbers of channels

2.3.1 Rationale and Methods

2.3.1.1 Rationale

Experiment 1 had two aims. One aim was to investigate how performance using the two model-based vocoders (simulating MP and BP configurations) would change as a function of the number of channels N. As previously stated, CI users' speech recognition shows a plateau of performance for values of N larger than about 8 whereas performance of normal-hearing subjects listening to noise-vocoded simulations continue to improve up to higher values of N when channel interactions are not taken into account (Friesen et al., 2001). Two recent studies that included channel interactions in their vocoder implementation found, however, that speech recognition scores also yielded an asymptote for values of N higher than 7 or 8 channels (Bingabr et al. (2008); Strydom and Hanekom (2011b). Building on these previous studies, the present experiment investigated whether the model-based vocoders used here behave similarly. Another aim of the experiment was to compare speech recognition scores for MP and BP vocoders. As previously mentioned, several studies performed in real CI listeners reported similar or better performance with MP than with BP and we wished to investigate whether our simulations would show the same trend.

2.3.1.2 Experimental conditions

Exp. 1 measured speech recognition for three synthesis filter shapes designed to simulate three configurations referred to as Monopolar (MP), Bipolar-plus-1 (BP+1) and Control (CTRL). These three filter shapes were evaluated using different numbers N of analysis/synthesis channels (4, 8 and 15 channels), leading to nine conditions in total [1]. Speech recognition was measured for these nine conditions at two different TMRs (+5dB and +10dB).

The synthesis filters of MP and BP+1 were obtained using the model described in section 2.2.3.2 and are shown in the panels A, B, C and D of figure 2.4 for N=4 and N=8 analysis/synthesis channels. BP+1 refers to bipolar stimulation with a spacing of one electrode between the two active contacts. This particular spacing was chosen both because it reflects a configuration that can be used with most CI patients without exceeding the compliance range of the implanted current sources and also because it

[1] For MP, the stimulation was assumed to be applied to the imaginary electrodes numbered 3, 7, 11 and 15 for N = 4; 2, 4, 6, 8, 10, 12, 14, and 16 for N = 8; and 2, 3, 4, 5, 6, 7, 8, 9, 10, 11, 12, 13, 14, 15 and 16 for N = 15. For BP, the stimulation was assumed to be applied to electrode couples (2,4), (6,8), (10,12) and (14,16) for N = 4; (1,3), (3,5), (5,7), (7,9), (9,11), (11,13), (13,15), (15,17) for N = 8; (1,3), (2,4), (3,5), (4,6), (5,7), (6,8), (7,9), (8,10), (9,11), (10,12), (11,13), (12,14), (13,15), (14,16), (15,17) for N = 15 (c.f. Table 2.2 for the correspondence between electrode number and center frequency).

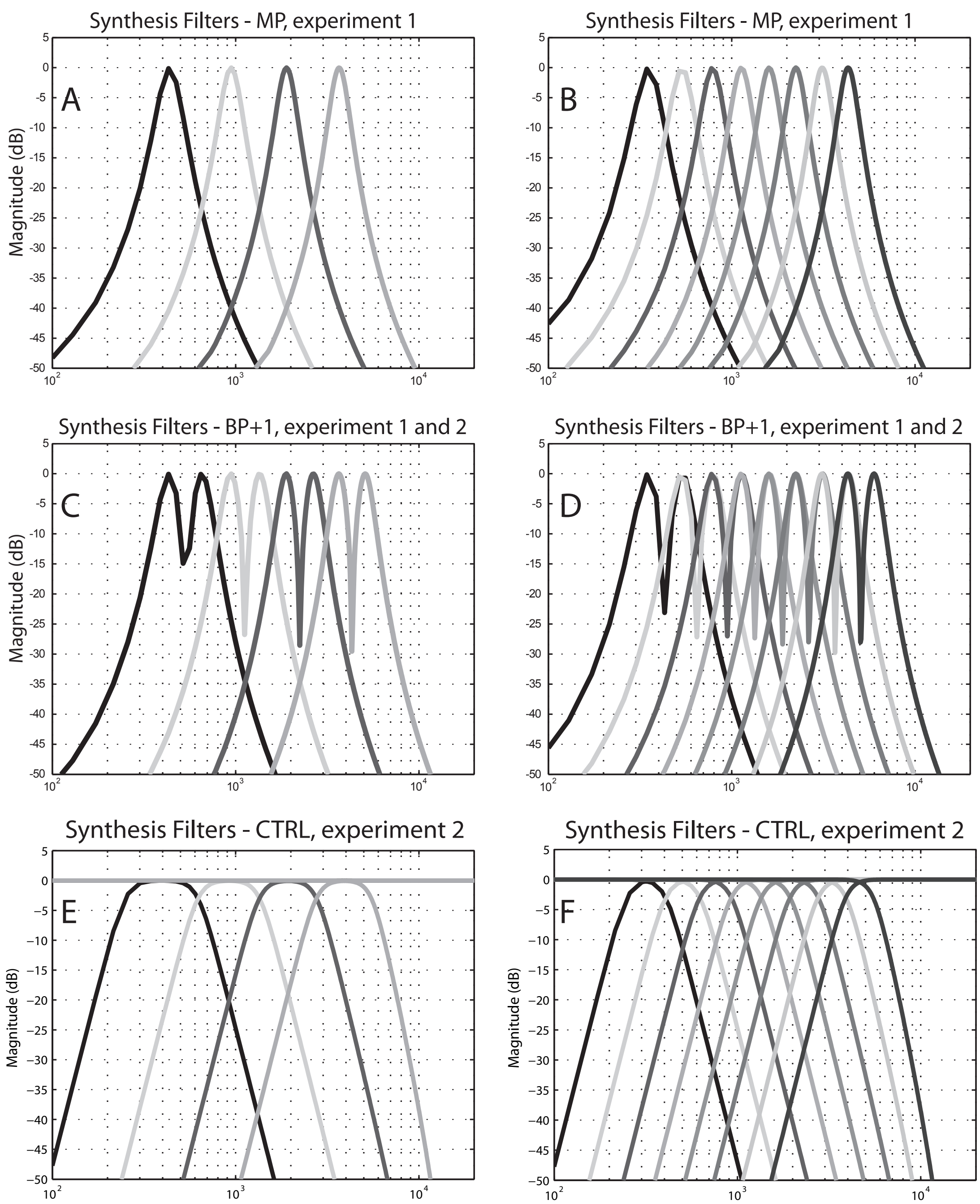

Figure 2.4: Synthesis filters used in Experiment 1 and 2: from top to bottom, MP, BP+1 and CTRL, AS, CTN, for 4 channels (left panels) and 8 channels (right panels).

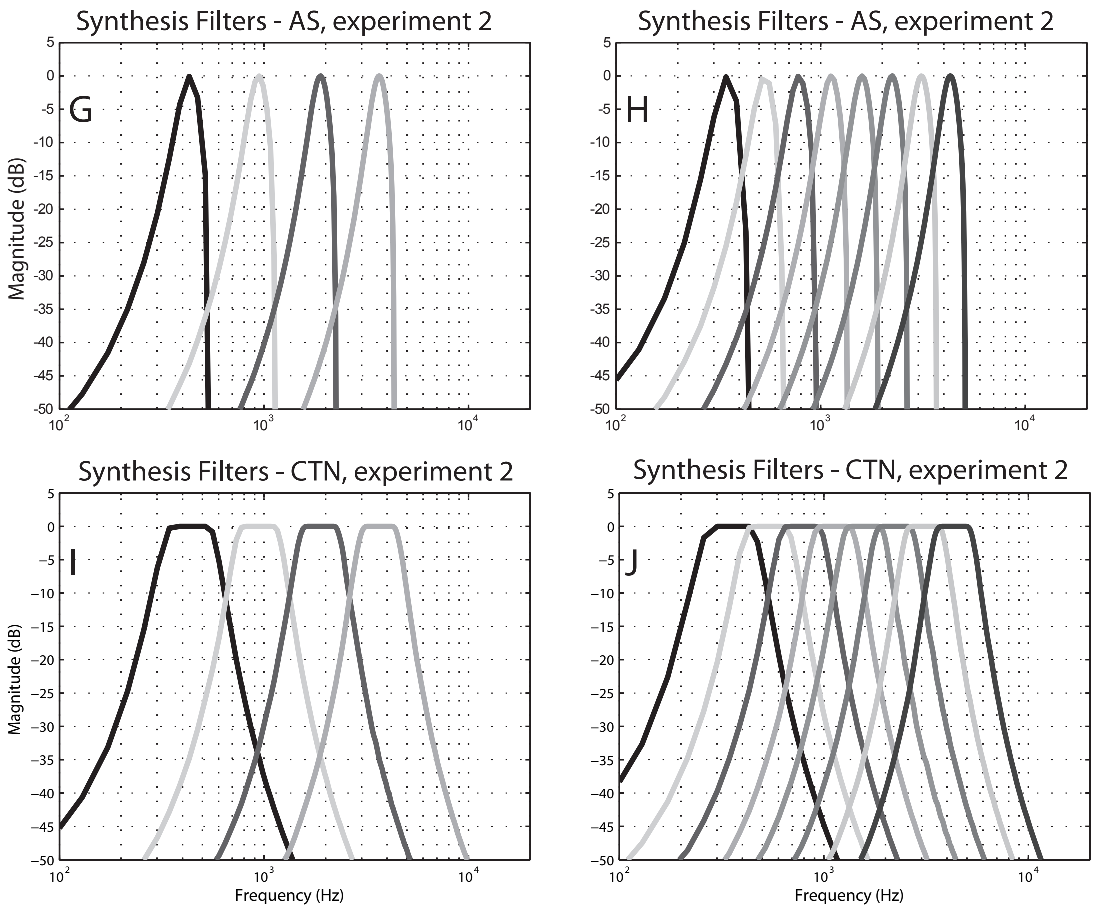

Figure 2.4 (Continued): Synthesis filters used in Experiment 1 and 2: from top to bottom, MP, BP+1 and CTRL, AS, CTN, for 4 channels (left panels) and 8 channels (right panels).

should elicit a clear dual-peak excitation pattern in normal-hearing listeners. To evaluate the presence of this dual-peak pattern after processing by the peripheral auditory system, white noises were filtered using each BP+1 synthesis filter and further passed through a gammatone filterbank with bandwidths derived from masking data obtained in normal-hearing listeners (Glasberg and Moore, 1990). The resulting excitation patterns showed a difference between the peaks and the troughs of more than 7 dB for all BP+1 synthesis filters suggesting that the dual-peak pattern should still be present after auditory filtering. The spectrum of a sentence processed by the 4-channel BP+1 filters and the resulting excitation pattern obtained at the output of the gammatone filterbank are shown in figures 2.5A and 2.5B respectively.

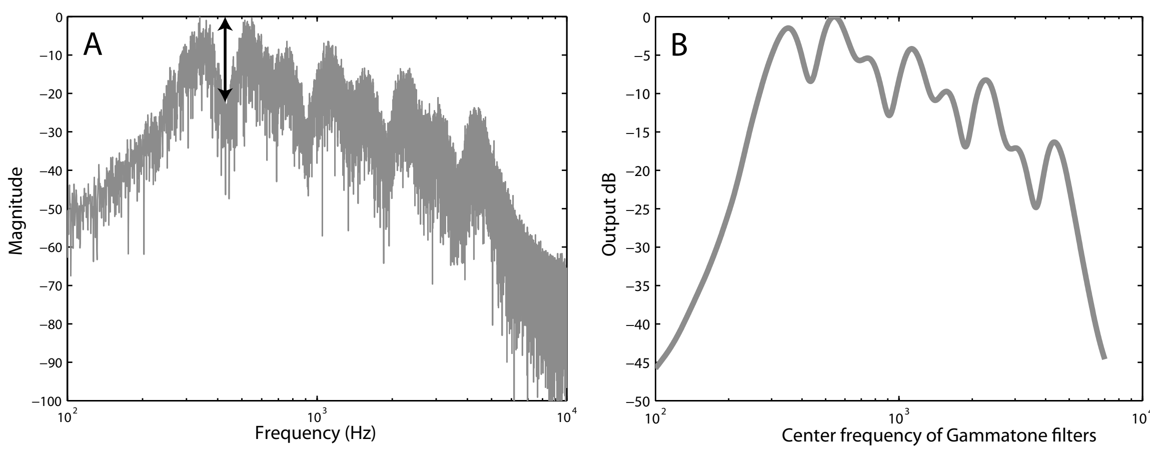

Figure 2.5: A. Spectrum of a sentence processed by the 4-channel BP+1 vocoder. B. Simulated excitation pattern of the same signal using a gammatone auditory filterbank.

Note that, when considering the two peaks of the BP+1 synthesis filters, the filters are broader than for MP and this will be specifically discussed in section 2.6.2. The CTRL configuration is a control condition in which analysis and synthesis filters are identical (6th order Butterworth filters as shown in panels E and F of figure 2.4). This condition replicates what has been used in several previous vocoder studies (e.g. Friesen et al. (2001); Qin and Oxenham (2003); Deeks and Carlyon (2004)). The bandwidth of the CTRL filters becomes narrower when N increases so that filters from adjacent channels always cross at their 3-dB attenuation points for all values of N. In contrast, for MP and BP+1, the shape of the synthesis filters does not depend on the number of channels. Thus, any increase in N will also increase the amount of channel interactions and potentially limit the benefit of having more channels. It was hypothesized that performance with the CTRL configuration would show a larger improvement as a function of N than the model-based configurations.

2.3.1.3 Subjects

Nine normal hearing subjects (7 females and 2 males) who had no previous experience with noise-vocoded speech participated in this experiment. Their age ranged from 19 to 30 years old (mean of 22.5). One of the subjects could not complete the experiment and only performed the +10 dB TMR condition.

2.3.1.4 Procedure

Recognition of noise-vocoded speech in a reversed speech background is a difficult task and training as well as fatigue effects were expected. To include sufficient training while limiting the duration of the tests, four sessions of approximately 1.5 to 2 hours each were needed, as detailed below.

1. In session 1, a pure-tone audiogram was first performed with each subject. They were then asked to practise the task with one list of unprocessed sentences in order to become familiar with the interface and with the speech material. They were subsequently trained on the nine conditions at a TMR of +10dB. To speed up the training, an initial phase of passive listening of vocoded sentences called the "pop-out" phase was included (Davis et al., 2005; Hervais-Adelman et al., 2008). In this phase, subjects had the opportunity to read the sentence on the screen at the same time as they heard it. This has been shown to produce faster training and has the effect of making the sentence perceptually "pop out". For each condition, subjects listened to two lists of pop-out followed by one list for which they had to perform the task (i.e. identify the sentences). Feedback was provided during the identification task.

2. In session 2, the TMR was fixed at +10dB and the 9 conditions were tested. Subjects first had to complete a training phase where they listened, for each condition, to two lists of pop-out followed by one list of training with feedback. For the test phase, a total of 18 lists (two lists per condition) were presented to each subject in pseudo-random order. Before a new list began, two sentences of pop-out were presented using the new processing condition. This aimed to avoid the subjects being surprised by a change in timbre when changing condition. No feedback was provided during the test phase.

3. In session 3, the exact same procedure as in session 2 was repeated except that the TMR was +5dB.

4. In session 4, all subjects completed a third list for each of the 9 conditions both at +10 and +5dB TMR.

2.3.2 Results

Figure 2.6 shows the word recognition scores averaged across three lists and eight subjects for a TMR of +10 (left panel) and +5 dB (right panel). All subjects showed a quick learning phase during the first two sessions. Recognition scores showed an average improvement of 6 points between the first (session 1) and the second training list (session 2). Paired-sample t-tests performed on the mean scores obtained by each subject for all conditions revealed that this improvement was significant ($p < 0.05$). No significant improvement was observed between the two successive test series. However, performance significantly improved (4 points on average) in the last test series.

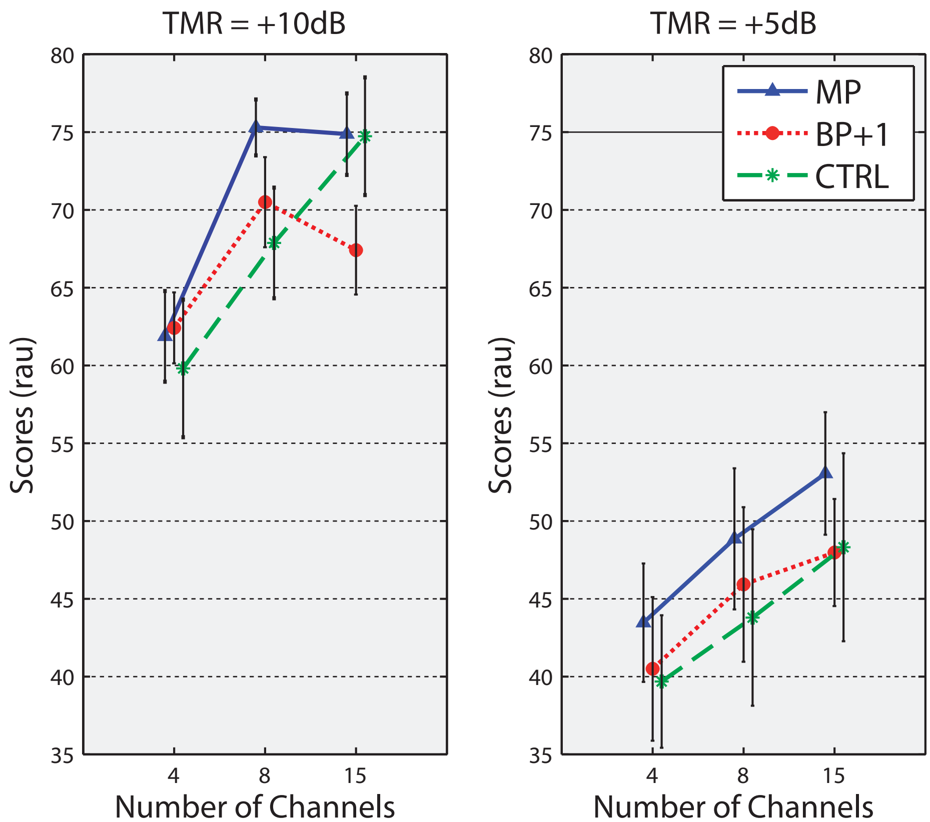

Figure 2.6: Mean word recognition scores obtained in experiment 1. Both panels show the mean results of the eight subjects who completed the experiment. Error bars indicate +/- 1 standard error.

All test data were analyzed with a three-way repeated measures (RM) ANOVA with factors "N", "synthesis filter shape", and "TMR", which all led to significant main effects. An additional two-way RM ANOVA ("$filtershape \times N$") was carried out including the nine subjects who performed the +10dB TMR condition. This analysis led to similar outcomes and is therefore not detailed here.

Not surprisingly, performance was markedly affected by the TMR ($F(1, 7) = 90.25, p < 0.001$). The recognition scores for the +10dB conditions were, on average, 22.5 points higher than for the +5dB conditions. Overall performance also improved with increases in the number of channels ($F(2, 14) = 101.75, p < 0.001$). Finally, synthesis filter shape had a significant effect on performance ($F(1.35, 9.43) = 5.91, p = 0.035$, using the Greenhouse-Geisser correction). A pairwise comparison showed that MP stimulation was overall more intelligible than BP+1 ($p = 0.002$), which is in agreement with CI data reported in the literature (Zwolan et al., 1996; Pfingst et al., 1997).

No interaction between factors was significant ($p > 0.05$) except the interaction between N and synthesis filter shape ($F(4, 28) = 4.81, p = 0.004$). This indicates that the ability to benefit from a high number of channels depended on the filter shape. For a low number of channels ($N = 4$), MP, BP+1 and CTRL were equally intelligible. All three filter shape conditions showed a significant improvement when N increased from 4 to 8 channels ($p < 0.001$). Further increasing N from 8 to 15 channels, the scores for the CTRL configuration significantly improved ($p < 0.001$), whereas those for BP+1 and MP showed a marked plateau. This plateau is in agreement with results reported for CI users and may be a direct consequence of the spread of excitation and of the channel interactions it produces (Friesen et al., 2001). It is also noteworthy that, although MP and BP+1 yielded equivalent scores for $N = 4$, the plateau in performance for BP+1 was 5 points lower than that obtained with MP.

To gain further insights into the evolution of the scores as a function of N, a second RM ANOVA was conducted on the differences between the scores obtained for $N = 4$ and $N = 15$. Here again, the analysis demonstrated a significant effect of synthesis filter shape ($F(2, 14) = 6.78, p = 0.009$) and showed that the difference in scores between $N = 4$ and $N = 15$ was significantly larger for MP than for BP+1 (p=0.015). One possible explanation for these results is that for $N = 8$ and $N = 15$ in BP+1 configuration, many simulated electrodes act as the active electrode for one channel and as the return electrode for a neighboring channel. Thus, the speech envelopes from two different analysis bands are transmitted to the same location in the cochlea, as shown in panel D of figure 2.4. The resulting channel interactions may, in this case, be more deleterious than those produced by MP.

2.3.3 Discussion

The range of speech recognition scores [40-75 rau] suggests that the plateau in performance obtained in MP and in BP+1 at +10 dB TMR was not caused by ceiling effects. It is also worth noting that, for MP stimulation at +5 dB TMR, performance continued to improve when increasing N from 8 to 15 channels ($p = 0.003$). Since this condition was more difficult than the +10dB TMR condition, subjects may have benefited from a higher number of channels before reaching asymptotic performance. This would be consistent with data showing that CI subjects can benefit from a higher number of channels in noise than in silence (Friesen et al., 2001). Our CTRL configuration showing a continuous increase in performance as a function of N confirms that when synthesis filters are narrowed at the same time as N is increased, subjects can benefit from a higher number of channels, which is also consistent with the simulation study of Friesen et al. (2001). Hence, it seems that the plateau observed for MP and BP+1 is a direct consequence of channel interactions. These results corroborate the findings of Bingabr et al. (2008) and Strydom and Hanekom (2011b) who both showed that speech recognition scores asymptote above 7 or 8 channels when simulating the spread of excitation in normal hearing subjects listening to vocoded speech.

In order to compare the shape of the model-based filters with those previously used in the literature, the 10-dB bandwidth of all filters was calculated and further converted in millimeters by applying Greenwood's function. Note that in most acoustic simulation studies, synthesis filters have constant slopes in dB/mm while in the present study, the filters' slopes vary continuously as a function of the distance from the imaginary stimulating electrode. The bandwidth values corresponding to the MP and BP+1 synthesis filters are shown in table 2.3 together with those of several previous studies. The bandwidth of the MP filter used here was derived from data collected by Laneau et al. (2006). They compared the perceptual influence of spectral smearing in CI users and in normal-hearing subjects listening to noise-vocoded speech. They found that, to match the results of CI users in an electrode discrimination task, the synthesis filters used in their noise-band vocoder had to have 10-dB bandwidths of approximately 2.3 mm in terms of cochlear distance (c.f. table 2.3). In the design of our synthesis filters, we chose the β coefficient used in equations 2.6 and 2.7 to be constant and equal to 1 so that the filter we used to simulate MP had a comparable 10-dB bandwidth of 2.17 mm. Bingabr et al. (2008) simulated the spread of excitation using synthesis filters with constant slopes in dB/mm whose values were based on physical measurements of current spread reported by Kral et al. (1998). Three slopes were tested, -3.33, -13.33, and -26.66 dB/mm, simulating respectively wide, medium and narrow spreads of excitation. They tested speech recognition by varying both the slope of their synthesis filters and the number of channels in their vocoder and found that speech intelligibility depended on both of these factors. They observed that for the medium and wide spreads (see table 2.3), speech recognition scores did not improve when increasing the number of channels from 8 to 16. It is worth noting that the filters which led to a plateau of performance in the present study (MP and BP+1) had bandwidths in between the medium and broad conditions of Bingabr et al. (2008), and that they led to a similar plateau. Recently, several vocoder studies have also used synthesis filter shapes similar to those of Bingabr et al. (2008) in order to simulate the spread of excitation produced by a CI (Churchill et al., 2014; Stafford et al., 2014). Strydom and Hanekom (2011b) followed a different approach. They simulated the effect of current spread by modulating each of their noise band carrier with a smeared envelope consisting of the weighted sum of the envelopes extracted from all frequency bands of their vocoder. These weights were assigned assuming a current decay of 7 dB/mm away from the stimulating electrode. Even though their approach was quite different from that of the present study, the extent of their spread at -10 dB was comparable to that used here and their data also showed a plateau in performance above 7 channels (c.f. table 2.3).

An important finding of Exp. 1 was that the BP+1 vocoder was less intelligible than the MP vocoder at high values of N. However, the reason for this difference remains unclear. It may be the result of the specific dual-peak shape of the BP+1 filters but it could also just be due to the fact that the BP+1 filters were broader than the MP filters. These two possible explanations are disentangled in Experiment 2.

10-dB bandwidth (mm)	
Bingabr et al. (2008)	Wide: 5.8 Medium : 1.6 Narrow: 0.75
Laneau et al. (2006)	MP[a]: 2.3
Strydom and Hanekom (2011b)	2.85
Strydom and Hanekom (2011a)	Narrow[b] : 5.4
Stafford et al. (2014)	Wide: 10 Medium: 2 Narrow: 1.17
Current Study	MP: 2.17 BP+1 (one peak): 1.84 BP+1 (overall pattern): 4.42

Table 2.3: 10-dB bandwidth of various synthesis filters, converted in spatial spread along the basilar membrane in mm. a) Synthesis filter's bandwidth that matched the performance of CI users in an electrode discrimination task. b) This refers to the condition Narrow Noise tested in Strydom and Hanekom (2011b).

2.4 Experiment 2: Effect of the dual-peak shape of the excitation pattern.

2.4.1 Rationale and Methods

As in Experiment 1, nine conditions were tested. There were three different synthesis filter shapes referred to as BP+1, Asymmetric (AS) and Continuous (CTN) and three numbers of channels (N=4, 8 and 15). These nine conditions were tested at two different TMRs (+5 and +10 dB). The corresponding synthesis filters are reported in panels C, D, G, H, I and J of figure 2.4 for N=4 and N=8. The first set of filters was the same BP+1 set as in Exp. 1 (panels C and D, in figure 2.4). The AS filters were also identical to the BP+1 filters except that the basal lobe of each filter was removed (panels G and H, in fig. 2.4). The resulting single-peak AS pattern therefore had the same shape as the most apical peak of the BP+1 dual-peak pattern. The difference between the AS condition and the MP condition of Exp. 1 was that the filters were slightly narrower for AS (10-dB bandwidth of 1.88 mm for AS compared to 2.17 mm for MP). The AS condition simulates the pattern that might ideally be obtained with asymmetric electrical pulses consisting of a short, high-amplitude phase of one polarity followed by a longer and lower-amplitude phase of opposite polarity. Computational modeling, electrophysiological and psychophysical studies have indeed shown that the amplitude of one of the two peaks of the pattern produced by BP stimulation can be attenuated by using such asymmetric shapes, thereby improving spatial selectivity (Frijns et al., 1996; Macherey et al., 2010; Undurraga et al., 2012). As a consequence, AS filters were asymmetrical and showed more spread towards the apex. Comparing the results of BP+1 and AS will also test if the transmission of the same temporal envelope to two partially distinct regions of the cochlea introduces a redundancy that helps the integration of speech cues or, conversely, if these cues are already efficiently conveyed by one electrode. The CTN filters (panels I and J, in fig. 2.4) were also based on the BP+1 shape but the trough between the two peaks of the pattern was filled, i.e., the filters showed no attenuation between the peaks. This condition aimed to investigate whether the spectral discontinuity of the BP+1 excitation pattern was deleterious for speech intelligibility. It also allowed us to test whether the worse performance obtained for BP+1 compared to MP in Exp. 1 was due to the broader synthesis filters or specifically to the dual-peak shape.

The same eight subjects who completed Exp. 1 took part. Two sessions identical to sessions (2) and (3) of Exp. 1 were necessary. The original stimuli were also identical to those used in Exp. 1 except that the masker began one second before the target. This manipulation aimed to help the subjects anticipate the time at which the target would start in order to make the task easier. Three lists were tested for each condition.

2.4.2 Results

The word recognition scores averaged across the three test lists and all subjects are illustrated in figure 2.7. Paired-sample t-tests revealed no significant difference between the BP+1 scores obtained in Experiments 1 and 2 ($p > 0.05$), suggesting that the time delay between the masker and signal onsets did not have any effect.

Similarly as in Exp. 1, all data were analyzed with a three-way repeated measures ANOVA with factors "N", "TMR" and "filter shape". Increasing the TMR from +5 to +10 dB yielded an average improvement across conditions of 22 points ($F(1, 7) = 202.88, p < 0.001$). A significant effect of N was also revealed by the analysis ($F(2, 14) = 118.55, p = 0.001$). Finally, the effect of filter shape was significant ($F(2, 14) = 10.43, p = 0.002$). Subsequent pairwise comparisons indicated that removing the second peak of the BP+1 pattern (i.e. using the AS filter shape) led to the best overall performance; AS yielded significantly better scores than both BP+1 ($p = 0.002$) and CTN ($p = 0.006$). This demonstrates that improving spatial selectivity by removing this second peak improved the intelligibility of our stimuli. Moreover, although the gap between the two peaks of excitation in the BP+1 pattern introduced a spectral discontinuity, the analysis showed no significant difference in performance between the CTN and BP+1 conditions ($p > 0.05$). This suggests that the poorer performance obtained with BP+1 in Exp. 1 compared to MP was probably due to the overall broader filters and not specifically to the dual-peak shape of the pattern.

The interaction between N and filter shape was the only significant interaction ($F(4, 28) = 2.74, p < 0.05$). All synthesis filter conditions led to equivalent performance for N=4. Performance improved for all conditions when N increased from 4 to 8 channels ($p < 0.001$ for all filter shapes). However, for $N = 8$, the scores obtained with AS were

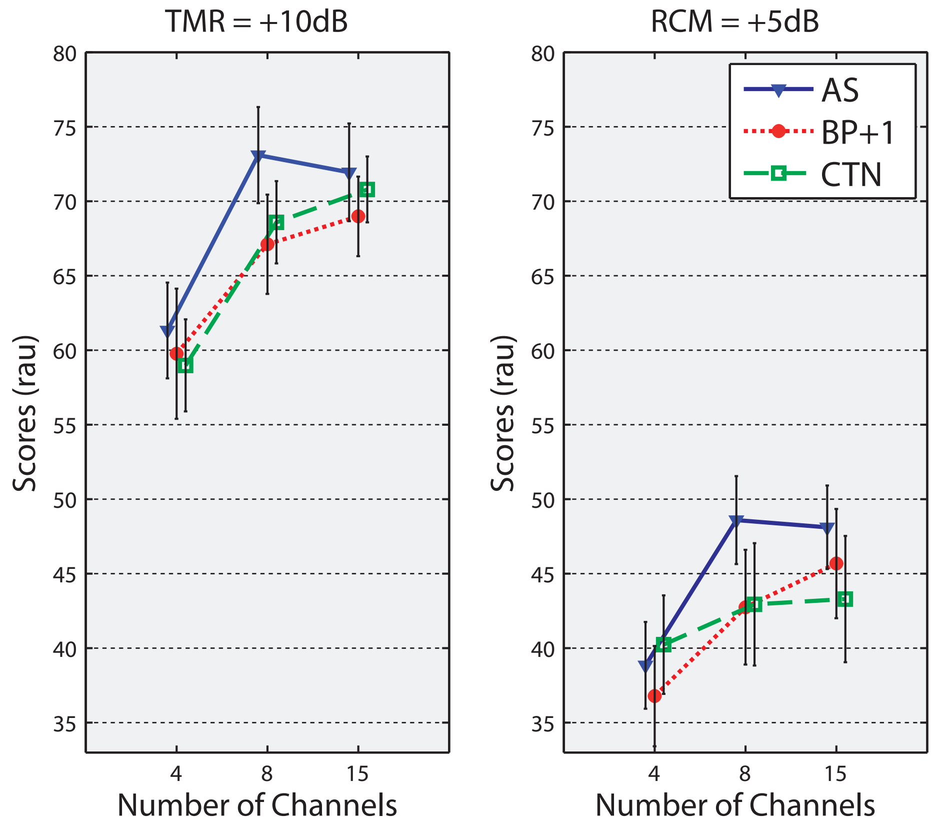

Figure 2.7: Mean word recognition scores obtained in experiment 2. Error bars indicate +/- 1 standard error.

at least 4.5 points higher than those obtained with the other filter shapes. Further increasing N from 8 to 15 channels resulted in a plateau of performance for all filter shapes. Similarly as in Exp. 1, channel interactions probably limited the performance of the subjects when stimulated with a high number of channels.

2.4.3 Discussion

Speech recognition is related to the perception of many signal features among which the overall spectral shape. It has been observed from spectral restoration (Warren et al., 1997) and acoustic CI simulation studies (Souza and Rosen, 2009) that the ability to identify a speech stimulus is better when its spectrum does not show discontinuities. In the latter, they compared the speech recognition of normal-hearing listeners obtained with tone- and noise-vocoders. It appeared that with few channels (two to five) and a low cutoff frequency (30 Hz) of the smoothing filter, tone-vocoders were less intelligible than noise-vocoders. One explanation for this poor performance was that in such conditions, pure tones are too spectrally restricted compared to noise bands, so that the neural representation of the stimuli is weaker than with noise vocoders.

The perception of individual formants as well as the transition between formants are also strongly dependent on the overall shape of the spectrum (Blumstein et al., 1982).

Considering the 8-channel condition, the comparison between BP+1 and CTN enables to investigate these effects. Indeed, since the CTN filter shape is derived from the BP+1, they have the exact same overall extent. Thus, interactions between channels occur in the same frequency regions. Consequently, acoustic stimuli in both configurations mainly differ in their overall spectral shape. Despite the irregular spectral shape induced by BP+1 pattern (see, figure 2.5), the results suggest that in both configurations the transmitted cues led to comparable performance.

The 4-and 8-channel BP+1 conditions are also reminiscent of the study by Shannon et al. (2002) who simulated the presence of dead regions in the cochlea by removing and/or reallocating channels to other intra-cochlear places. They simulated the presence of dead regions in the cochlea by removing and/or reallocating channels to other intra-cochlear places. They reported that CI users as well as normal-hearing subjects could tolerate holes in the spectrum as large as 6 mm near the base of the cochlea and as large as 3 mm near the apex. Compared to the CTN condition, BP+1 emulates the presence of a dead region within each channel, or at least, regions where fewer fibers are excited. Whereas each CTN filter generates a single-peak pattern, each BP+1 filter creates a "hole" of approximately 2.3 mm in the spectrum, corresponding to the distance between the simulated electrodes of each bipolar channel. For a single channel, the data of Shannon et al. (2002) suggest that this hole should not deteriorate speech recognition. However, when considering 8 channels of stimulation in BP+1, 8 holes of 2.3 mm are created. Although such a condition with multiple holes was not tested by Shannon et al. (2002), our results suggest that these holes may not affect the subjects' performance. This interpretation cannot be extended to the 15-channel condition since the "hole" generated by each channel contains in this case the spectral information from another channel.

To summarize, Exp. 2 shows that the discontinuity of the transmitted spectrum (i.e. the presence of two peaks in the excitation pattern) may not be deleterious *per se* for speech information transmission. One limitation of this experiment is that the size of the dip between the two peaks in the excitation pattern may be too small to have an effect and may also be different from that produced by a real CI. In order to check that this dip could, however, be perceived by the subjects, we asked six normal-hearing subjects to participate in a control experiment where they had to discriminate between noise-bands passed through single-channel synthesis filters of the BP+1 and CTN vocoders. The task was a three-interval, two-alternative forced-choice "odd-man out" task and was performed for three channels separately (the most apical, the most basal and a middle channel of the 15-channel vocoder). In addition, a level rove of $\pm 2.5\ dB$ was added to the stimuli. Despite this rove, the subjects could all easily discriminate between the BP+1 and CTN signals. This suggests that the dip in the excitation pattern produced by the BP+1 vocoder is present at the neural level. To conclude, the main factor limiting speech perception for the BP+1 vocoder seems to be the amount of overlap between channels rather than the presence of the spectral dip. The effect of this overlap is further investigated in Experiment 3.

2.5 Experiment 3: Effects of electrode spacing in bipolar stimulation.

2.5.1 Rationale and Methods

2.5.1.1 Rationale

A third simulation experiment was carried out to investigate the effect of the spacing between electrodes in BP stimulation. This experiment had several motivations. First, varying the spacing between electrodes is often necessary clinically due to the limitation of the current sources. Moreover, as previously mentioned, two narrow peaks of excitation are obtained with BP stimulation because the two electrodes generate opposite-polarity electrical fields that interfere, thereby reducing the excitation spread that each one would produce on its own. Conversely, if the two electrodes of a BP channel are far from each other, the resulting pattern resembles the pattern that would be obtained with two distant monopoles (Hanekom, 2001). Given the deleterious effects of channel interactions on speech intelligibility, a narrow BP configuration (i.e. where the two electrodes are close to each other) should provide better spatial selectivity and better speech recognition than a wide BP configuration. However, the results of Pfingst et al. (1997, 2001) suggest that narrow BP can in some cases produce worse speech recognition scores than wide BP. They proposed that wide BP led to better performance because of the wider pool of nerve fibers excited. Nevertheless, as argued below, changing the spacing between electrodes also changes the amount and the location of the channel interactions. This experiment mainly focuses on this last aspect and aimed to assess its influence on speech perception.

2.5.1.2 Experimental conditions

Except otherwise stated, the signal processing steps were identical to those described in Experiments 1 and 2 (c.f. fig. 2.1). The number of analysis/synthesis channels N was fixed and always equal to 11. The input signal was first decomposed into 11 analysis bands spanning the same frequency range as in Experiments 1 and 2 (the filter cut-off frequencies are reported in table 2.1). Five conditions similar to those tested by Pfingst et al. (2001) in CI users were simulated. The conditions included three configurations with a narrow electrode spacing (BP+1) and two configurations with a wide spacing (BP+5; c.f. figure 2.8). Note that the distance between adjacent electrodes in the CI listeners tested by Pfingst et al. (1997, 2001) was 0.75 mm whereas our imaginary array has an inter-electrode distance of 1.13 mm. Therefore, the spacing simulated here in BP+5 was slightly larger than the BP+6 spacing tested by Pfingst et al. (1997, 2001) in CI users (respectively 6.8 mm and 5.25 mm).

The envelopes extracted from the eleven analysis bands were directed to eleven adjacent synthesis channels as constrained by our imaginary electrode array and shown in figure 2.8. For the BP+5 condition, the 17 simulated electrodes of the array were required. For the BP+1 condition, 13 electrodes among the 17 were required and different analysis band-to-simulated electrode allocations were tested. As in Pfingst et al. (2001), a compression between the analysis and synthesis frequency ranges was imposed by delivering the extracted envelopes either to the eleven most apical channels or to the eleven most basal channels or to the eleven middle channels (c.f. table 2.2). Thus, three BP+1 conditions were tested (referred to as Apical, Basal, and Centered). The excitation patterns produced by these different conditions are illustrated schematically in figure 2.8.

As previously mentioned, when using a high number of channels in narrow BP configuration, the excitation patterns produced by neighboring channels overlap. This is because some electrodes are required to act both as the "active" and as the "return" electrode of two distinct channels. Let us consider the different BP+1 conditions (figure 2.8A, B, C). To convey information from 11 analysis bands, 13 adjacent electrodes are required and nine of them are used by two different stimulating channels. When the spacing is increased, interacting channels are located further away from each other. For the BP+5 condition (figure 2.8D), 17 electrodes are required but only five of them, located in the center of the array, are used by two different stimulating channels. This reduction of the amount of overlapping channels may also contribute to the better performance reported for wide BP stimulation in CI users (Pfingst et al., 1997). We may therefore expect this simulation of wide BP to provide better intelligibility than narrow BP.

In the present model, when two excitation patterns overlap, two different temporal envelopes are mixed together. The fifth condition, named NoiseBP+5 (figure 2.8.E), aimed to investigate whether the information conveyed by these portions of the spectrum still provide usable information to the subjects. In this condition, the allocation of the envelopes to specific electrodes was performed separately depending on whether the electrode was used by two different stimulating channels or not. To do so, two distinct filters were constructed from each original BP+5 filter, one filter for each lobe, referred to as SF.a for the most apical lobe and SF.b for the most basal lobe. As shown in figure 2.8, for all channels except channel 6, one electrode of each BP pair is used by different channels while the other is not. The processing steps needed to generate the NoiseBP+5 condition are illustrated in figure 2.9. For channel 6, the processing was identical to the BP+5 condition. For all other channels, the noise band modulated by the speech envelope was first filtered separately by both synthesis filters SF.a and SF.b. If the more basal electrode of the channel was also used by another channel (i.e. for channels i with i=1 to 5), the output of the filter SFi,b was replaced by a stationary white noise filtered by SFi,b to have the same spectral content and scaled to have the same energy. Similarly, if the more apical electrode of a given channel was used by another channel (i.e. for channels j with j=7 to 11), the output of the filter SFj.a was replaced by another stationary white noise filtered by SFj.a. If subjects performed better in BP+5 than in NoiseBP+5, this would suggest that they were able to extract useful information from the overlapping parts of the signal's spectrum.

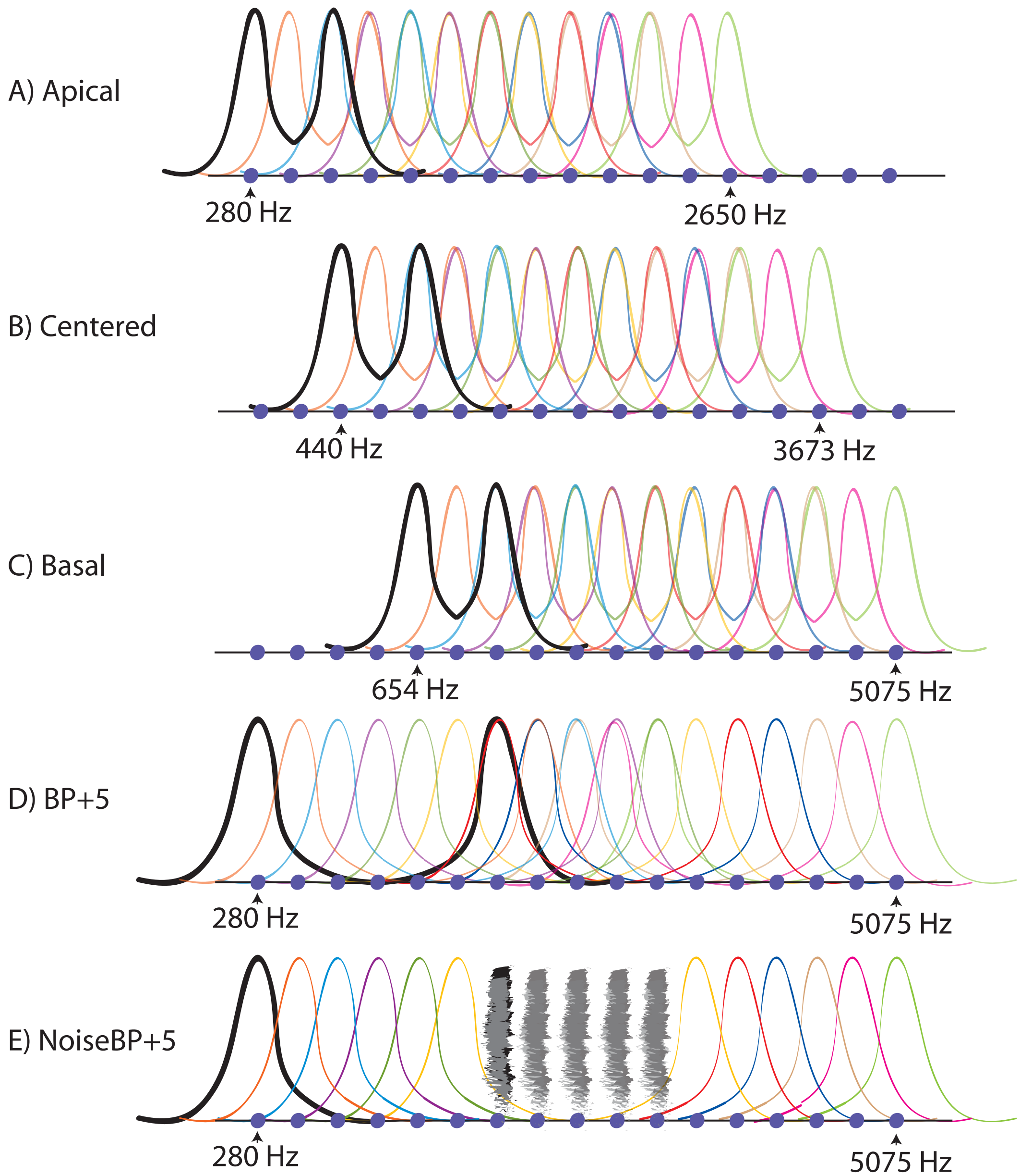

Figure 2.8: Schematic distribution of the excitation along our imaginary electrode array (illustrated by circles on a horizontal line) for the five conditions tested in experiment 3.

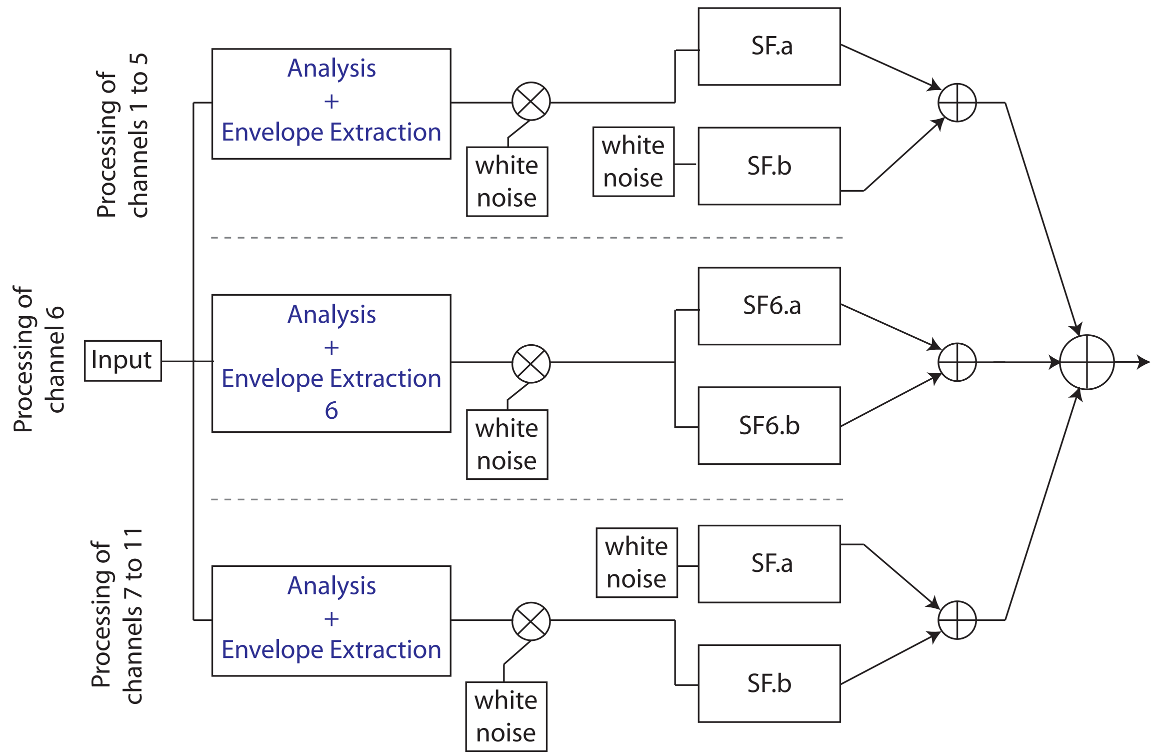

Figure 2.9: Block diagram showing the signal processing steps for the NoiseBP+5 condition.

2.5.1.3 Subjects

Eight normal hearing subjects (seven females and one male) who did not participate in Experiments 1 and 2 were recruited. Their age ranged from 21 to 23 years old (mean of 21.6).

2.5.1.4 Procedure

The five conditions ($Apical$, $Basal$, $Centered$, $BP+5$ and $NoiseBP+5$) were tested at two different TMRs, +10 dB and +5 dB using the same speech material and task as in Experiments 1 and 2. Three sessions were necessary to complete this experiment and were organized as follows.

1. In Session 1, as in Exp. 1, subjects first had to perform an audiogram and get accustomed to the test interface. The TMR was then fixed at +10 dB for the whole session. Subjects were trained with four lists of pop-out followed by two lists of speech recognition with feedback, for each of the five conditions.

2. During the second session, the TMR was fixed at +10 dB and the five conditions were tested. Subjects first listened to two lists of pop-out and performed one list of training with feedback for each condition. Then, during the actual test, three lists in total were tested per condition, presented in pseudo-random order. No

feedback was provided in the test series. Two sentences of pop-out were presented before each new list began. As in Exp. 2, the target sentence started one second after the onset of the masker.

3. The exact same procedure as in Session 2 was followed in Session 3 except that the TMR was fixed at +5dB.

2.5.2 Results and Discussion

Here again, paired-sample t-tests revealed a marked improvement (15 point on average) between the first and last training lists ($p < 0.05$) while no significant learning effect was observed across the test sessions. All eight subjects completed the experiment at +10 dB TMR but two of them performed at chance at +5 dB, hence the corresponding data were not included in the analysis and are not shown here. The word recognition scores averaged across the three lists and the eight and six subjects, respectively, for TMRs of +10 and +5 dB are shown in figure 2.10.

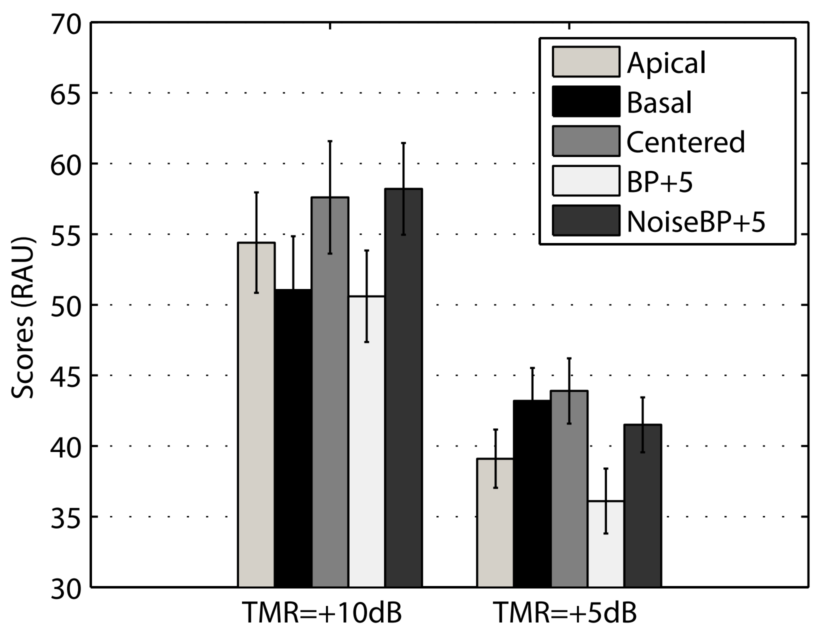

Figure 2.10: Mean word recognition scores for the five conditions tested in experiment 3. Error bars indicate +/- 1 standard error.

A two-way repeated measures ANOVA was performed with factors "Configuration" (5 levels: Apical, Basal, Centered, BP+5, NoiseBP+5) and "TMR". Changing the TMR from +5 dB to +10 dB resulted in an average improvement across conditions of 18 points. This effect of TMR was statistically significant ($F(1, 5) = 136.6, p < 0.001$). There was, however, no interaction between TMR and Configuration ($F(4, 20) = 1.86, p = 0.16$). Furthermore, given two subjects could not perform the task at the

+5dB TMR, an additional one-way repeated measures was carried out on the data obtained for the +10dB TMR only. In the following description, the results of the analyses performed on the two TMRs and on the +10 dB TMR only are referred to as overall and TMR_{10dB}, respectively. Both analyses showed a significant effect of configuration ($overall : F(4, 20) = 4.14, p = 0.013, TMR_{10dB} : F(4, 28) = 4.58, p = 0.006$), demonstrating an influence of the analysis band-to-simulated electrode mapping on speech recognition. These differences are further described and discussed in the next two subsections.

2.5.2.1 Effect of spacing between bipolar electrodes.

Pairwise comparisons showed no difference between $BP + 5$ and *Apical* ($p = 0.23$) nor between $BP + 5$ and *Basal* ($p = 0.825$). Subjects even showed better performance for *Centered* than for $BP + 5$ (overall: $p = 0.01, TMR_{10dB}, p = 0.023$). These results contrast with those obtained by Pfingst et al. (1997, 2001) in real CIs. They showed that speech recognition was poorer in their narrow BP, *Basal*condition than in wide BP. Moreover, their *Centered* and wide BP configurations yielded equivalent speech scores. The poorer performance observed here for BP+5 compared to BP+1 suggests that the channel interactions produced by these two configurations are not equally deleterious. Since the temporal envelopes are the only cues transmitted by the vocoders, it may be important for two envelopes transmitted to the same cochlear location to be partially correlated in order to convey meaningful information. Moreover, Crouzet and Ainsworth (2001) highlighted the fact that, in speech signals, temporal envelopes extracted from adjacent spectral channels are highly correlated, and that this correlation decreases when increasing the distance between channels.

When simulating BP stimulation, main interactions between channels occur when one electrode is shared between two channels. Two envelopes extracted from different analysis bands are in this case transmitted to the same cochlear location. In BP+1, these interactions occur between channels transmitting envelope information extracted from relatively "close" analysis bands (1st and 3rd, 2nd and 4th … 9th and 11th) whereas with BP+5, interfering channels are more "distant" (1st and 7th, 2nd and 8th … 5th and 11th). To estimate the correlation between these interfering envelopes, each sentence of the corpus was first passed through the analysis filter bank. The envelopes were then extracted and the correlation coefficient between all couples of interfering envelopes was calculated in the linear amplitude domain separately for BP+1 and BP+5. For BP+1, the interfering envelopes were relatively well correlated ($r = 0.65$ on average). As expected for BP+5, the correlation coefficient was much smaller ($r = 0.28$ on average), which is consistent with the study of Crouzet and Ainsworth (2001). This correlation analysis suggests that the channel interactions in BP+5 are more deleterious than in BP+1. It is therefore possible that despite the smaller number of electrodes used by two different channels in BP+5, no improvement was observed because the superimposition of poorly correlated waveforms produced modulation masking that impaired the perception of the speech modulations conveyed by the other electrodes.

This interpretation is supported by the better performance obtained in NoiseBP+5 compared to BP+5 for the +10dB TMR (overall: mean difference of 6.8 points, $p = 0.087$, TMR_{10dB}: significant mean difference of 7.6 points, $p = 0.023$). This result shows that, not only were the scores not decreased by replacing the overlapping envelopes by stationary noises, they were even improved. Only one subject performed worse with NoiseBP+5 than with BP+5 for the +5dB TMR. All other subjects seemed to benefit from the removal of speech information conveyed in the overlapped regions. This demonstrates, first, that this speech information is probably no longer available because of interactions. Second, the improvement in performance obtained when replacing these interfering speech envelopes by stationary noises suggests that these interactions even act as a more effective masker than stationary noise. This observation is consistent with the study by Apoux and Bacon (2008b) who measured consonant identification for speech signals that were restricted to a low or to a high frequency region in the presence of an off-frequency noise masker. They found that imposing a modulation on the masker deteriorated performance compared to the unmodulated case. Similar modulation masking may have been created by the overlapped envelopes of our BP+5 condition. This result may also have implications for CI processing strategies. If an electrode has an especially broad spread of excitation, it may create interactions with distant electrodes and could act as a powerful masker of the rest of the signal. The present data suggest that deactivating such an electrode should be beneficial.

2.5.2.2 Effect of frequency mismatch between the analysis and the synthesis

Results of pairwise t-tests showed that the *Centered* configuration led to better performance than the *Basal* configuration (overall: $p = 0.041$, TMR_{10dB}: $p < 0.001$) which is consistent with the results obtained by Pfingst et al. (2001) with CI listeners. However, there was no difference between the *Centered* and *Apical* configurations (overall: p=0.071, TMR_{10dB}: p=0.184), nor between the *Apical* and *Basal* configurations (overall: $p = 0.684$, TMR_{10dB}: p=0.094). The three BP+1 configurations can be analyzed in terms of the spectral compression between the analysis and synthesis frequency ranges. Both acoustic simulation and electric stimulation studies have shown that a shift of the synthesis range towards the base of the cochlea affects speech recognition (Fu and Shannon, 1999). Baskent and Shannon (2003) highlighted the fact that a tonotopic compression or expansion of the spectral map deteriorates the transmission of speech cues. More precisely, it appears that a mismatch of 3 mm of the cochlear map is a critical value above which performance in speech recognition is strongly affected. Below this value, a training period can minimize the influence of the mismatch.

The *Centered* configuration induces a maximum mismatch of up to 3.1mm while the other configurations induce a maximum mismatch of 6.2 mm either towards the base (*Basal* condition) or towards the apex (*Apical* condition). Considering the results of Baskent and Shannon (2003) the *Centered* condition may have been less affected by this spectral compression because of a smaller mismatch than in the other two conditions.

The previous results first confirm the deleterious effect of spectral compression between the analysis and the synthesis ranges. However, despite the fact that the model used here is extremely simple, the results probably do not match those obtained by Pfingst et al. (2001) for the *Basal* configuration because of a difference in the size of the frequency mismatch. The mismatch between the center frequencies of the analysis bands and the frequencies corresponding to the location of the excitation in the cochlea was quantified using equation 2.8, as defined in Pfingst et al. (2001).

$$mismatch = \frac{\sum_{n=1}^{N} \log F_e/F_t}{n} \tag{2.8}$$

Here, F_e is the frequency corresponding to the halfway location between the active and return electrodes of a BP pair. F_t is the center frequency (geometric mean of the high and low cut off frequencies) of each channel.

What clearly appears is that the amount of mismatch in the present simulations is smaller than that estimated by Pfingst et al. (2001). Among all conditions in the present experiment, the largest mismatch was 0.17 for the *Basal* condition whereas it was comprised between 0.4 and 0.86 in Pfingst et al. (2001). A larger mismatch would have probably lowered the performance of the *Basal* and *Apical* configurations tested here even more.

2.6 General Discussion

2.6.1 Model limitations

The model used to derive the shape of the MP and BP+1 synthesis filters suffers from several limitations. First, the hypothesis of an infinite homogeneous medium may underestimate the spread of excitation produced by a real CI electrode. The scala tympani resembles a fluid-filled tube that acts like a leaky transmission line. As suggested by (Briaire and Frijns, 2000), a better model of the current spread function would be a combination of the homogeneous medium model for the near-field domain (a few millimeters away from the electrode) and of a transmission line model (exponential decay) for the far-field domain (several millimeters away). The present model may therefore only be valid in the near field. Interestingly, most previous vocoder studies which simulated current spread only considered the exponential decay component (Laneau et al., 2006; Bingabr et al., 2008; Strydom and Hanekom, 2011b).

Second, the electrode-neuron geometry is very approximate and does not take into account the orientation and curvature of the fibers relative to the electrode, which has been shown to play a major role in the pattern of polarization produced by a stimulating electrode (Rattay et al., 2001). For example, the present model predicts that nerve fibers should be more sensitive to the cathodic phase of the pulse whereas it has been shown that at suprathreshold levels, the opposite is true for human CI listeners (Macherey et al., 2008).

Third, different parts of each fiber are not equally excitable. Peripheral and central processes show differences in their diameters and may not contain the same voltage-gated ion-channels. All these properties may play a role in the determination of the site and extent of excitation (Rattay et al., 2001).

Fourth, it is assumed that there is, at each place along the cochlea, an unlimited pool of excitable fibers with a uniform distribution of thresholds. This hypothesis was necessary to keep the filter shape independent from stimulation level. However, it is possible that, in real CIs, the neural population closest to the electrode is saturated at high stimulation levels. Increasing the current level would in this case recruit more remote fibers and produce a broader spread of excitation across the cochlea. Simulating such a phenomenon by, e.g., implementing level-dependent synthesis filters' slopes would be a step forward but would require knowledge about the extent of this variation.

Fifth, we did not include any effect of compression to account for the fact that the acoustic dynamic range is much greater than the typical electrical dynamic range found in CIs (Bingabr et al., 2008; Strydom and Hanekom, 2011b).

Despite these limitations, this model remains the simplest model that can exhibit a dual-peak excitation pattern in response to bipolar stimulation and should be considered as a first attempt to better understand the effects of multi-peak excitation patters on speech perception. It cannot be excluded, however, that the dual-peak shape that was simulated is different from that produced by a real CI and more research is needed to identify the implications of multi-peak excitation on speech perception by CI listeners.

2.6.2 Spatial selectivity of MP and BP configurations

Considering the two peaks of the dual-peak pattern, the spread of excitation simulated in the vocoder was broader for BP+1 than for MP (c.f. table 2.3). Simulations using BP+0 (not shown here) showed that the pattern would be narrower than for BP+1 but would still be wider than for MP when considering the two peaks (3.35 mm). Despite common acceptance that BP stimulation produces a narrower spread of excitation than MP, evidence from the literature remains sparse. Although many electrophysiological measures in animals have shown a narrower spread for BP, most of these studies compared the two configurations over a very large range of current levels and used single-pulse stimuli (e.g. Snyder et al. (2008)). As mentioned in the Introduction, recent data by Smith and Delgutte (2007) and Schoenecker et al. (2012) suggest that when the excitation spreads of MP and BP are measured at comparable levels (i.e. at levels that are not too high relative to threshold and that are equalized to produce similar peak spike rates), there is no clear difference between them. Furthermore, Schoenecker et al. (2012) showed that the response to the first pulse in a train may produce a very different excitation spread (i.e. much broader) than subsequent pulses. Given the vast majority of electrophysiological data were performed with single-pulse stimuli, generalizing their results to CI subjects fitted with a high-rate coding strategy deserves some caution. This is especially true since most psychophysical studies in human CI listeners have not shown any convincing evidence that MP and BP differ from each other in terms of excitation spread (Kwon and van den Honert, 2006; Bingabr et al., 2014). Predictions from a 3D computational model of the human cochlea also showed that the spread of excitation as calculated 10 dB above threshold was similar or even larger (depending on the type of electrode and on the electrode position) for BP+0 or BP+1 with their two peaks than for a condition meant to simulate MP Hanekom (2001). Based on a simpler model, Bonham and Litvak (2008) also argued that BP should produce a broader spread than MP when the two peaks are considered. Two previous vocoder studies (Bingabr et al., 2008; Strydom and Hanekom, 2011a) that simulated the excitation spreads of MP and BP partly based their choice of filter bandwidth on saline tank measurements reported by Kral et al. (1998). In both cases, the choice of the BP bandwidth was based on measurements corresponding to a single peak of the BP pattern. Given the difference in recognition scores observed between the AS and BP+1 conditions of Experiment 2, the present study suggests that the two peaks should be taken into account in future vocoders simulating bipolar stimulation.

2.6.3 Summary of findings

1. The excitation patterns produced by different electrode configurations were simulated using a simple model of electrical stimulation and used to design the synthesis filters of a noise-vocoder. The model predicted single- and dual-peak excitation patterns for MP and BP configurations, respectively.

2. The performance obtained with MP and BP+1 simulations showed a marked plateau when the number of channels increased above 8. MP was also more intelligible than BP+1 when the number of channels was equal or higher than 8. These effects are qualitatively consistent with previous observations made in CI users.

3. The results of Experiment 2 suggested that the spectral discontinuity introduced by the dual-peak shape of the filters was not the reason for the lower intelligibility scores obtained in BP+1 because filling this discontinuity did not result in any improvement. Interestingly, removing one of the lobes of each synthesis filter improved speech recognition scores by 5 points for the eight-channel condition.

4. Experiment 3 compared the intelligibility of narrow BP (BP+1) and wide BP (BP+5) simulation. Contrary to data obtained with CI users (Pfingst et al., 2001), no benefit was found with wide BP compared to narrow BP. One possible explanation for this discrepancy is that the frequency mismatch between the analysis and the synthesis filters of the BP+1 simulations was smaller than that of the CI users tested by Pfingst et al. It is argued that channel interactions produced by BP stimulation are more deleterious when the analysis bands from which the interacting signals are extracted are distant from each other. Replacing the parts of the spectrum corresponding to this overlap by stationary noises of equal energy improved the mean speech recognition scores by 7.6 and 5.4 points for TMRs of

+10 and +5dB, respectively. These results demonstrate that channel interactions can in some cases produce strong masking of clean parts of the speech signal.

5. Even though the outcomes of acoustic simulations cannot be directly transposed to electric hearing, the present study suggests that for multi-electrode configurations to enhance spectral resolution in CIs, the amount of current returning to neighboring electrodes needs to be controlled to avoid the emergence of multiple peaks of excitation across the auditory-nerve array (Litvak et al., 2007). This control may be achieved in two different ways or in a combination of them.

   First, as we will see in chapter 4, the neural excitation is dependent on stimuli polarity. Using asymmetric stimulus waveforms that take into account the polarity-sensitive properties of the nerve fibers has been proposed specifically for this purpose (Frijns et al., 1996; Macherey et al., 2010). These waveforms consist of a short, high-amplitude phase of one polarity followed by a longer and lower-amplitude phase of opposite-polarity. Such pulse shapes should enable to maximize the excitation near the desired electrode while minimizing excitation near other electrodes.

   Second, it may be possible to produce a highly focused electrical field by stimulating all electrodes simultaneously with in-phase and out-of-phase pulses (van den Honert and Kelsall, 2007). This "phased-array" configuration has the theoretical advantage of canceling the electrical field at all electrode sites except the desired site, thereby potentially creating a focused, single-peak excitation pattern. However, the limits of this specific stimulation strategy will be investigated in detail in chapters 3 and 5 of the present thesis.

Acknowledgments

The authors wish to thank Bom Jun Kwon and an anonymous reviewer for providing helpful and constructive comments on previous versions of this manuscript. We also thank Bob Carlyon and Jaime Undurraga for insightful comments concerning the design of these experiments, Hörtech and the ExpORL lab of KU Leuven for providing the speech materials of the FrMatrix and FIST tests and all the subjects who participated in these experiments. The current study is part of theDAIMA project, supported by the the Agence Nationale de la Recherche (F), Grant No. ANR-11-PDOC- 0022.

Chapter 3

Investigating the Electrical Properties of the Cochlear Medium.

Abstract

The Phased Array strategy (van den Honert and Kelsall, 2007) was proposed to achieve a highly-focused stimulation based on measures of the electrical spread along the electrode array. This strategy is however based on several assumptions that require verifications.

The present study aims to validate those assumptions and to better understand the electrical properties of the inner ear.

Several impedance measurements (transimpedances, contact impedances, tetrapolar measurements, and spectroscopy) were carried out in vitro and in eight CI users using the same device (HiRes 90k, Advanced Bionics) and were analyzed either in the time or in the spectral domain.

Investigating the resistivity and linearity of the inner ear revealed the presence of two parasitic phenomena. In the high frequency region ($> 30kHz$), a low-pass filtering could be clearly identified and attributed to a parasitic capacitance internal to the device. Our data show that the inner ear biological medium is not frequency dependent at high frequencies. In the low frequency region ($< 1kHz$), another phenomenon yielding an increase in impedance occurred for 18% of the recording configurations. The origin of this phenomenon, its consequences on electrical stimulation as well as possible ways to handle it are discussed.

A simple electrical model was used to describe polarized electrodes' impedance and yielded an accurate estimation of the access resistance for all patients.

3.1 Introduction

In contemporary multichannel cochlear implants (CI), spectro-temporal information of sound is sent to intra-cochlear electrodes implanted in the scala tympani (ST). The different electrodes target the residual auditory nerve fibers in their vicinity to mimic the tonotopic organization of the cochlea.

Even though many studies reported good speech recognition ability in silence, most CI users' perform poorly in noisy environment, and have difficulties to discriminate between speakers or to appreciate music. A commonly-acknowledged reason for this poor performance is the lack of spatial selectivity of electrical stimulation. In monopolar stimulation (MP), electrical current flows from a stimulating electrode and widely spreads across the conductive perilymph of the ST. It then leaves the cochlea to reach the ground electrode located in the temporal muscle. Each electrode thus presumably stimulates a large portion of the cochlea. Activating several electrodes yields interferences which distort the pattern of neural activity produced along the cochlea and deteriorate the transmission of sound information.

Several alternative multi-electrode stimulation modes have been designed to improve the spatial selectivity of electrical stimuli and thus reduce those interactions. Bipolar (BP) stimulation uses another intracochlear electrode as return electrode to reduce the current spread while in tripolar stimulation (TP), for a given electrode, two flanking electrodes act as return electrodes. Both animal data and models suggest that such strategies can enhance the spatial selectivity of the neural excitation pattern (Kral et al., 1998; Bierer and Middlebrooks, 2002; Snyder et al., 2004, 2008; Bierer et al., 2011). However, studies trying to investigate the benefits of focused stimulation strategies for speech recognition by CI listeners have shown mixed results (c.f. Section 2.1 in Chapter 2). This may be due to the fact that BP and TP stimulation produce side-lobes of neural excitation near the return electrode(s) in addition to the main peak of excitation near the so-called active electrode (Litvak et al., 2007). To efficiently control the electrical spread using multi-electrode stimulation, it appears necessary to better understand the electrical behavior of the human inner ear.

High-resolution imaging techniques have provided an accurate description of the complex anatomical organization of the human cochlea (Küçük et al., 1991; Shepherd and Colreavy, 2004; Rask-Andersen et al., 2012). These studies enabled to identify the presence of complex bony structures, fluids and soft tissues. However, the electrical properties of these different biological elements are still not known accurately and have not been directly measured in humans. Most computational models thus rely on resistivity estimations from few animal studies (Strelioff, 1973; Finley et al., 1990; Suesserman and Spelman, 1993a). Besides, both the geometry and the resistivity of biological tissues can differ from one patient to another which probably yields subject-specific patterns of electrical spread (Micco and Richter, 2006a).

For a given patient, the electrical field produced by the activation of an electrode can be measured on other inactive electrodes. In most studies, the recorded voltage is normalized by the amplitude of the current input and is expressed in terms of impedance.

In the present study, *transimpedance* measurements refer to voltage recordings made between an inactive intracochlear electrode and the remote ground in response to the activation of another intracochlear electrode with reference to the same ground. Measuring transimpedances between all stimulating-recording electrode combinations, gives the so-called impedance matrix. Using the estimation of the current spread for the design of highly-focused stimulation strategies has been proposed in early CI studies (von Compernolle, 1985; Townshend and White, 1987). More recently, van den Honert and Kelsall (2007) proposed a practical method for the implementation of such a strategy known as the Phased Array (PA) strategy. It is indeed theoretically possible to determine the current input to impose at each electrode simultaneously to generate a desired voltage vector along the electrode array by computing an inverse problem (see equations 1.2 and 1.3 in the Introduction, chapter 1). The ability of the PA strategy to produce a narrower spread of excitation than MP has been investigated in several studies which reported inconsistent results.

Computational model studies of the human cochlea (Frijns et al., 2011; Kalkman et al., 2015) suggested that PA stimulation might reduce the spread of excitation at the level of the auditory nerve. However, as pointed out by Kalkman et al. (2015) this ability to produce narrow excitation patterns might be dependent on several factors such as the electrode-to-neurons distance and the state of neural degeneration. This was corroborated psychophysically by Smith et al. (2013), who demonstrated better performance of CI listeners in a spectral ripple discrimination task using a psychophysically-optimized version of PA compared to MP. Still confronting MP and focused stimulation, Marozeau et al. (2015) used the original unmodified PA and found comparable forward masking patterns. However, they also measured the loudness summation produced by stimulating 2 MP channels or 2 PA channels, which suggested that the electrode separation required to yield independent channels was 2.4 mm for PA and 4.8 mm for MP. Their data suggested that PA can lead to a reduced current spread but not necessarily to a reduced neural spread.

Here, we evaluate potential weaknesses of the original PA strategy and propose alternatives for its optimization. First, PA relies on several assumptions that require verification.

The most fundamental assumption implicitly used in this strategy, as well as in all multi-electrode strategies (e.g. BP and TP), is that, despite the presence of different biological materials in the inner ear, the overall medium is purely resistive. This implies that stimulating an electrode with a biphasic current pulse instantly produces in the cochlea a biphasic voltage pulse whose amplitude is given by the resistance of the current pathway. It also assumes that the contribution of different electrodes add linearly within the cochlea. In experiment 1, several measurements were carried out, both in vitro and in CI users, to verify the validity of these fundamental assumptions and confirm (or not) the findings of previous animal studies (Clopton and Spelman, 1982; Suesserman and Spelman, 1993a).

A second assumption relates to voltage measurements made between active electrodes and the ground to estimate the diagonal terms of the impedance matrix. When an electrode is activated, electrical charge carriers flow to the metallic surface of the electrode. The passage of current from the electrode to the perilymph requires a transition between electrical charge carriers and ionic charge carriers. This transition consists in an important charge reorganization at the electrode-fluid interface known as the charge double layer illustrated in figure 3.1 (Gouy, 1910; Grahame, 1947; Dymond, 1976).

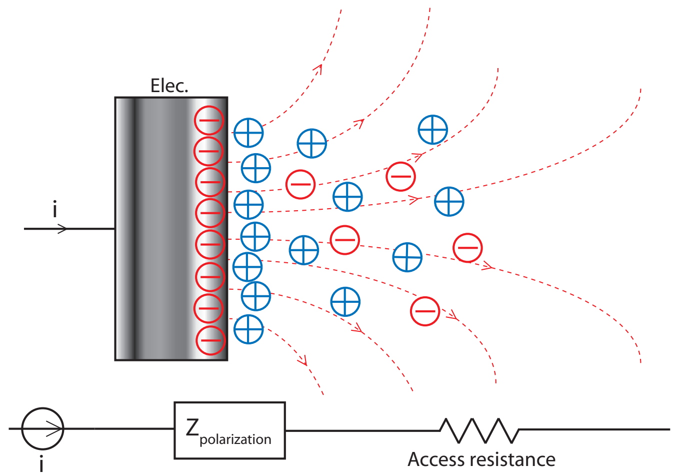

Figure 3.1: Illustration of the charge reorganization at the electrode/fluid interface

The ionic current then flows through cochlear tissues and fluids to reach the ground electrode. Voltage is measured between the active contact and the ground electrode whose area is assumed to be large enough so that it is not polarizable. Recorded waveforms are distorted by the polarized interface of the intracochlear electrode which prevents a straightforward estimation of the resistance path between the electrode surface and the ground. van den Honert and Kelsall (2007) proposed an estimation of the diagonal terms using linear extrapolation from transimpedance measurements on adjacent electrodes. However, since the impedance matrix is inverted to determine what current level to send on each electrode, a poor estimation of the diagonal terms could strongly deteriorate current focusing. In Experiment 3, electrode polarization was studied in vitro and in CI users. A simple electrical model was used to estimate contact impedance and then to infer tissue impedance. A proper estimation of tissue impedance would provide a fully-determined impedance matrix and might open new perspectives for further improvements of focused electrical stimulation.

3.2 General Methods

3.2.1 Device specifications

In vitro and in vivo experiments were carried out using the HiRes 90k device (Advanced Bionics®) connected to the HiFocus 1J electrode array which consists of 16 rectangular

($0.5 * 0.4mm^2$ surface) platinum contacts spaced by 1.1 mm and recessed in a silicon carrier. Stimulation and measurements were made using custom software implemented in Matlab (The MathWorks, Natick, MA, 2010) which served as an interface to the BEDCS software (Bionic Ear Data Collection System, Advanced Bionics®, Litvak (2003)).

3.2.2 In vitro setup

An in vitro experimental setup (figure 3.2) was designed so that the HiFocus 1J electrode array was immersed in artificial perilymph (APL). APL was initially made following Desmadryl et al. (2012) yielding a resistivity of 80 Ω.cm. However, Baumann et al. (1997) pointed out that the conductivity of human cerebrospinal fluid increases by approximately 23% between room temperature and body temperature. The present ionic solution as well as the commonly used value of 70 Ω.cm (Finley et al., 1990; Strelioff, 1973; Suesserman and Spelman, 1993a) thus probably overestimate the resistivity of the real inner ear perilymph at body temperature, supposedly around 55 Ω.cm. To carry these experiments at room temperature (≈ 20°C) while considering more realistic values of conductivity, NaCl was added to the original APL to match the conductivity of the actual perilymph at 37°C.

The electrode array was maintained vertically with a small weight attached to the apical end of the silicon carrier while the receiver and the ground electrode remained above the solution. The tank sides were covered with a stainless steel wire mesh connected to the ground with an external resistor R_e to mimic the resistive path between the inner ear and the temporal muscle.

This setup provides a controlled environment that corresponds to free field stimulation in a homogeneous medium. The possibility to vary R_e enables investigation of its influence independently from the other parameters and also provides impedance measures with orders of magnitude closer to those measured with CI users.

3.2.3 CI users

8 adult CI users took part in this experiment and were paid for their participation. All subjects were implanted with the HiFocus 1J electrode array. Subjects' details are reported in table 3.1.

3.2.4 Stimuli

The stimuli were either electrical pulses or sinusoids presented in monopolar mode with reference to the case electrode, or in bipolar mode.

Electrical pulses were symmetric and biphasic (anodic-first, unless otherwise stated) and had no interphase gap. Their phase duration ranged from 17.96 μs to 99 μs and they were presented at a current level ranging from 25 μA to 100 μA.

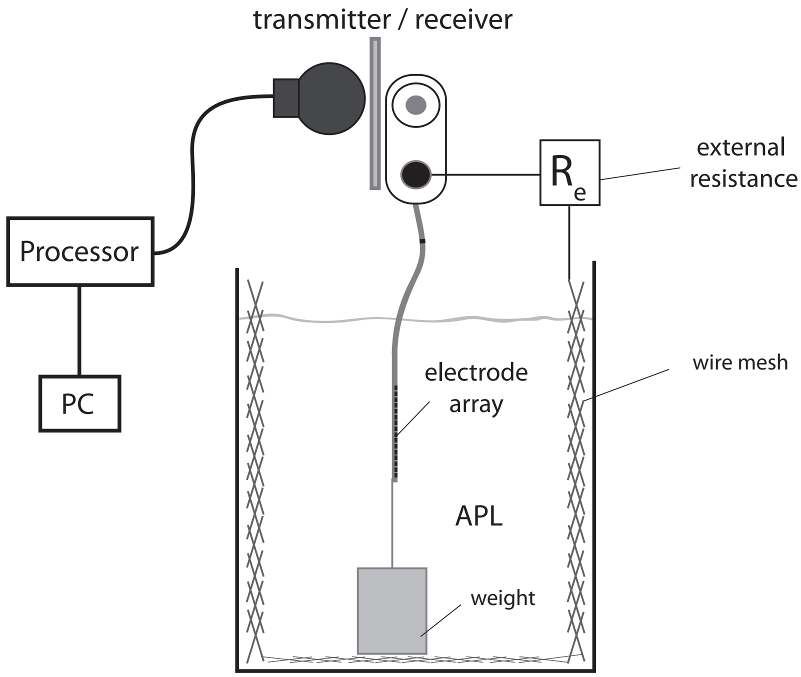

Figure 3.2: Experimental in vitro setup

One period of a sinusoid was created by concatenating either 24 or 36 monophasic pulses. The duration of these pulses was adjusted between 208 and 0.898 μs depending on the frequency of the sinusoid. Fifteen different sinusoids with frequencies logarithmically spaced in the [0.2-46.4] kHz range were tested (see details in table 3.2). Finally multi-periods stimuli could be obtained by repeating this pattern. The memory capacity of the present device is shared between the stimulating stage and the recording stage. The actual buffer duration is thus dependent on both the sampling rate, and the complexity of the stimulus (ie. the number of monophasic segments used to define it). As a result, the total duration of the sinusoidal stimuli was chosen depending on the available space in the device buffer.

In CI users, since detection thresholds for sinusoidal stimuli drop dramatically when the frequency decreases below 300 Hz (Pfingst, 1988), the stimulation level was chosen according to the subjects' most comfortable level for the 200 Hz stimulus and was kept constant at all frequencies, and for all electrodes.

3.2.5 Recording

The BEDCS software enables recording of the electrical voltage across a given pair of electrodes. Here, recordings were made between one intracochlear electrode and the large ground electrode, unless otherwise stated. Voltage waveforms were then normal-

Subject	Duration of deafness prior to CI (years)	Etiology	CI use (years)	Age
S1	20	Unknown progressive	12	38
S2	7	Unknown progressive	7	62
S3	/	Unknown progressive	11	76
S4	/	Unknown progressive	13	52
S5	/	Genetic	7	48
S6	6	Usher syndrome	13	20
S7	24	Pendred syndrome	12	39
S8	2	Unknown progressive	15	87

Table 3.1: CI subjects details (S1–S8) with duration of deafness, etiology, duration of implant use, and age.

Frequency (kHz)	Pulses per period	Phase duration (μs)	Number of periods
0.20	24	208	6
0.30	24	141	10
0.43	24	96.1	10
0.64	36	43.1	10
0.94	36	29.6	12
1.41	36	19.8	20
2.12	24	19.8	30
3.09	24	8.98	35
4.42	36	6.29	40
6.63	24	6.29	55
10.31*	36	2.69	5
15.47*	24	2.69	7
23.20*	24	1.80	7
30.93*	36	0.898	5
46.40*	24	0.898	7

Table 3.2: Details on sinusoidal stimuli. *recordings made using the up-sampling procedure (see section 3.2.5).

ized by the input current level to be expressed in Ohms.

The present device is provided with an adaptable amplifier gain (1 dB to 1000 dB) and sampling rate (9 kHz to 55.6 kHz). However, for the scope of the present study, a higher resolution was sometimes required to record fast onset and offset transients for biphasic pulses and also high frequency sinusoids (higher than 9 kHz) with a resolution of at least 15 samples per period. To achieve a higher sampling rate, the following up-sampling technique was used. With a 55.6 kHz sampling rate, samples are taken every 17.96 μs synchronized with the internal clock. To be able to measure the voltage waveform within the inter-sample time of 17.96 μs, several recordings were made by introducing small known delays. The different recordings were then concatenated offline. Given the minimal time step of 0.898 μs, the maximum sampling rate is 1.1-MHz. Additional control recordings were carried out with and without the upsampling procedure to make sure that the phase and magnitude of the recorded waveforms were identical in both cases. This provided an indirect check for this method.

For biphasic pulses, the waveforms were analyzed in the time domain while for sinusoids, amplitude and phase were obtained by fitting (nonlinear least-square fitting) delayed sine waves with a frequency equal to the input frequency (table 3.2). Magnitude and phase were plotted and analyzed with Bode diagrams. Specific stimulation or recording parameters are further described for each experiment.

3.3 Experiment 1: Resistivity and Linearity

3.3.1 Resistivity

3.3.1.1 Rationale and methods

Multipolar stimulation strategies rely on the assumption that the inner ear is purely resistive. In other words, it is assumed that a given stimulus creates an instantaneous voltage proportional to the current level. Several early animal studies demonstrated this up to 12.5 kHz (eg. Clopton and Spelman (1982); Suesserman and Spelman (1993a)). Vanpoucke et al. (2004a) assessed this assumption in human CI recipients but still on a limited frequency range (up to 12 kHz). Besides, their analysis was restricted to magnitude changes and did not consider possible frequency dependency of the phase. Since biphasic pulses present very steep transients, the spectrum of these electrical signals contains higher frequency components.

Herein, impedance spectroscopy measures were carried out with the CI device on the [0.2:46.4]-kHz frequency range to investigate a possible frequency dependency of transimpedance magnitude and phase. For each electrode, the up-sampled transimpedance on an adjacent electrode was also measured with biphasic pulses to evaluate the influence of a potential frequency dependency in the time domain.

Transimpedance spectroscopy was carried out in vitro and in vivo, between several stimulating-recording electrode couples in order to evaluate different current pathways along the entire array length.

In CI users, three stimulating electrodes, located at the apical, medial and basal part of the array were used: 1, 8 and 16. Electrode 1 was first used as the stimulating electrode while recording electrodes were separated by either one, five, ten or fifteen electrodes (i.e. electrodes 2, 6, 11, 16), resulting in a minimum and maximum spacing of 1.1-mm and 16.5-mm, respectively. Similar recordings were made using electrode 16 as the stimulating electrode and recording on electrodes 15, 11, 6, and 1. Finally electrode 8 was used as the stimulating electrode and electrodes 1, 4, 7, 9, 12, 16 as recording electrodes. We hypothesize that the presence of capacitive components along the current pathway (i.e., perilymph, bones or tissues) would be associated with an influence of the inter-electrode distance on the phase and magnitude impedance spectra. To evaluate the level dependency of spectroscopy data, additional measurements were carried out at a lower current level for a subset of electrode pairs (1-2, 8-9, and 16-15) and only three frequencies (0.64-, 2.12-, and 10.31-kHz).

3.3.1.2 Preliminary in vitro experiment: Parasitic Capacitance

To define a baseline for the analysis of CI data, transimpedance spectroscopy was first carried out in vitro for different values of R_e (2.2, 5.6 and 9.9-$k\Omega$). For each R_e, stimulation was made on electrode 1, 4, 8, 12, and 16 and voltage was recorded on an adjacent electrode (ie. electrodes 2, 5, 9, 13, and 15 respectively).

Figure 3.3 displays the Bode diagram for all 15 conditions. Different electrode conditions yielded identical patterns. One can note a slight decrease of magnitude above 30 kHz associated with a more visible phase shift. Increasing R_e enhanced this effect which is inconsistent with a purely resistive behavior and thus suggests the presence of capacitive components within the circuit comprising device electronics, platinum-iridium wires, electrodes and the APL.

Figure 3.4 shows the transimpedance waveforms measured with biphasic pulses stimuli in the same 15 conditions. The low-pass filtering mentioned above resulted in smooth exponential transients at the onsets, offsets and phase reversals.

Even though the capacitive behavior of the APL is theoretically negligible (Schwan and Calvin, 1957), complementary measures (data not shown here) were carried out to identify the location of these capacitive components. The transmitter was first connected to an experimental load board where current sources output can be displayed on an oscilloscope (i.e., without APL). Using the experimental setup shown in figure 3.2, voltage was also measured across R_e using the HZ109 differential probe (Hameg Instruments®). Similar trends were observed for both spectroscopy data and biphasic pulses which suggests that this effect is only dependent on the resistive load and not on the electrolyte per se. This capacitive behavior can thus be fully attributed to a parasitic capacitance, C_p, emerging from current sources imperfections and the proximity between individual wires and the device electronics (Barbour, 2014; Scholvin et al., 2016). To estimate the order of magnitude of C_p, the entire transimpedance matrix was measured in vitro using the up-sampling procedure for $R_e = 5.6k\Omega$. All waveforms were normalized and the exponential transients' time constants were estimated. This

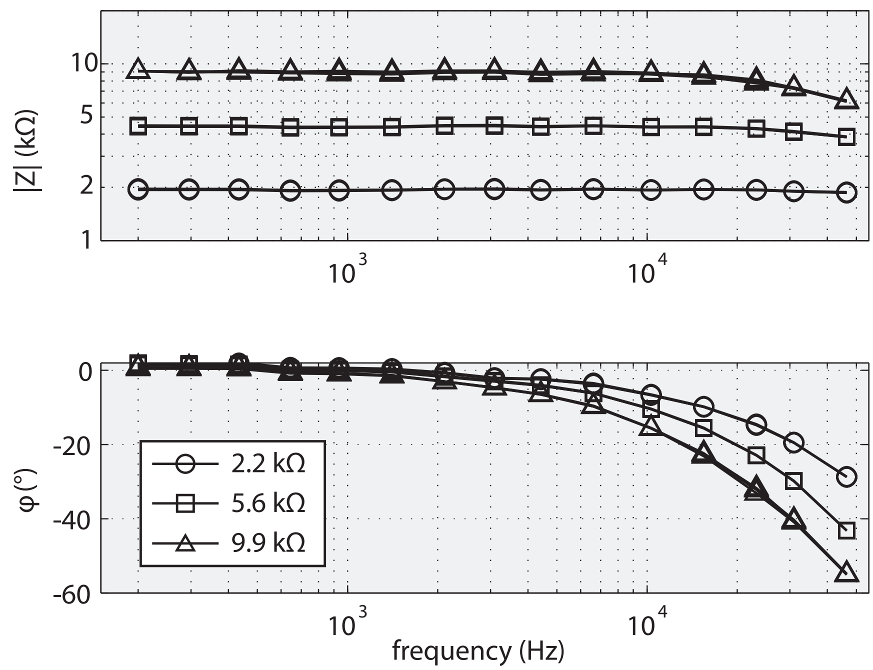

Figure 3.3: Bode diagram from transimpedance spectroscopy measured in vitro for various values of R_e. For each R_e, measurements were made for stimulating-recording pairs 1-2, 4-5, 8-9, 12-13, 16-15.

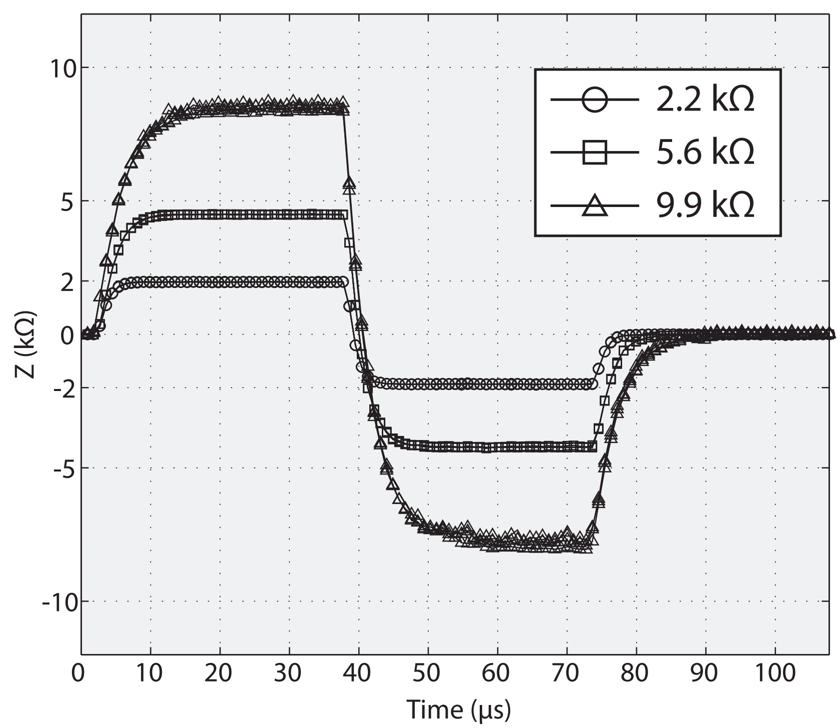

Figure 3.4: Impedance waveforms measured in vitro for biphasic pulse inputs for various values of R_e. For each R_e, measurements were made for stimulating-recording pairs 1-2, 4-5, 8-9, 12-13, 16-15.

yielded a very consistent estimation of 0.38-nF (s.d. = 0.004-nF).

Even though the ionic composition of the APL is supposedly close to that of the human perilymph, the human inner ear is composed of many different media which may not all be resistive.

3.3.1.3 Evaluating the resistivity assumption in CIs

With CI subjects, the access resistance of a given electrode is fixed and recordings can only be made on intracochlear electrodes. In this configuration, a potential capacitive behavior of the cochlear fluids and tissues would be mixed with C_p and thus difficult to identify. The presence of capacitive materials was investigated by varying the distance between the stimulating and the recording electrodes. Figure 3.5 shows a typical Bode diagram measured in one CI subject (S3) for stimulating-recording electrodes pairs 1-2, 1-6, 1-11, and 1-16.

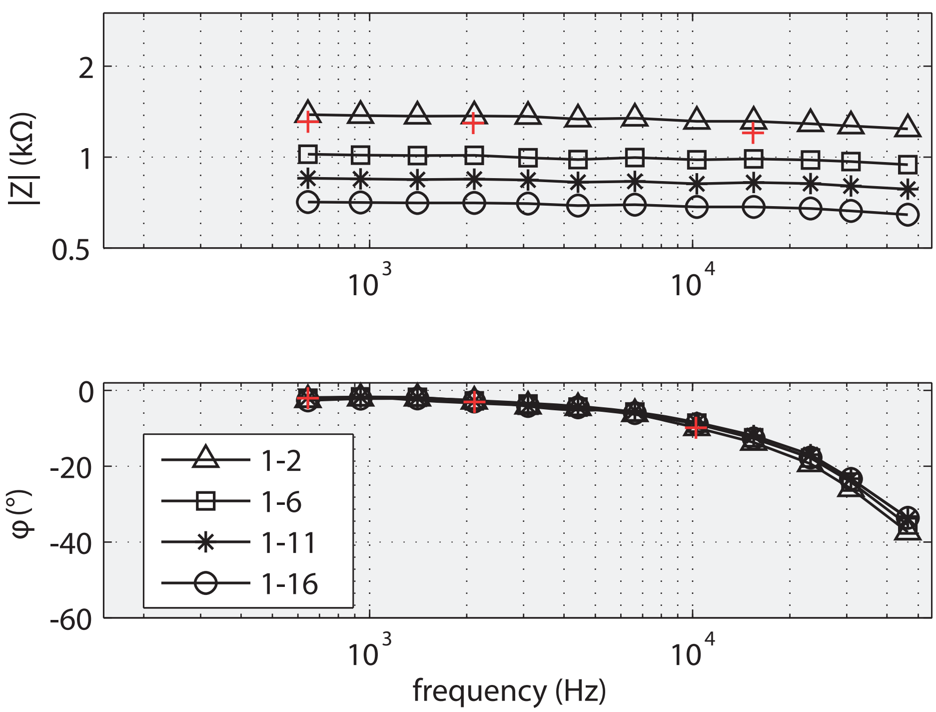

Figure 3.5: Bode diagram from transimpedance spectroscopy measured in subject S3 with an amplitude of 25-μA. Electrode 1 was used as stimulating electrode and recordings were made on electrode 2, 6, 11, and 16. The red + symbols represent the additional data recorded using electrodes 1-2 with an amplitude of 10-μA.

For all subjects, varying the stimulation level did not affect spectroscopy data (red + symbols in fig.3.5). In the high frequency range ($> 10kHz$), all spectroscopy data showed the expected phase shift comparable to what was observed in vitro. To separate the contribution of C_p from a possible capacitive behavior of biological media, the effect of longer current path on phase shift was examined by plotting $\Delta\phi_{46.4kHz}$, defined as the variation of the phase angle at 46.4 kHz as a function of electrode spacing relative to the phase angle at 46.4 kHz for a spacing of one electrode (fig 3.6). In this representation we hypothesize that an additional capacitive effect introduced by long current pathway would yield a monotonic decrease of $\Delta\phi_{46.4kHz}$ as a function of the inter-electrode distance. Herein, no such trend was observed and the maximal value for $\Delta\phi_{46.4kHz}$ remained lower than the quantization error. This suggests that the high frequency phase shift is independent of the electrode separation and that it is thus associated with C_p only. The effect of C_p is only effective at high frequency, thereby distorting biphasic current pulses at onsets, offsets and phase reversals. The voltage response can, therefore, be described by a biphasic voltage pulse with exponential transients.

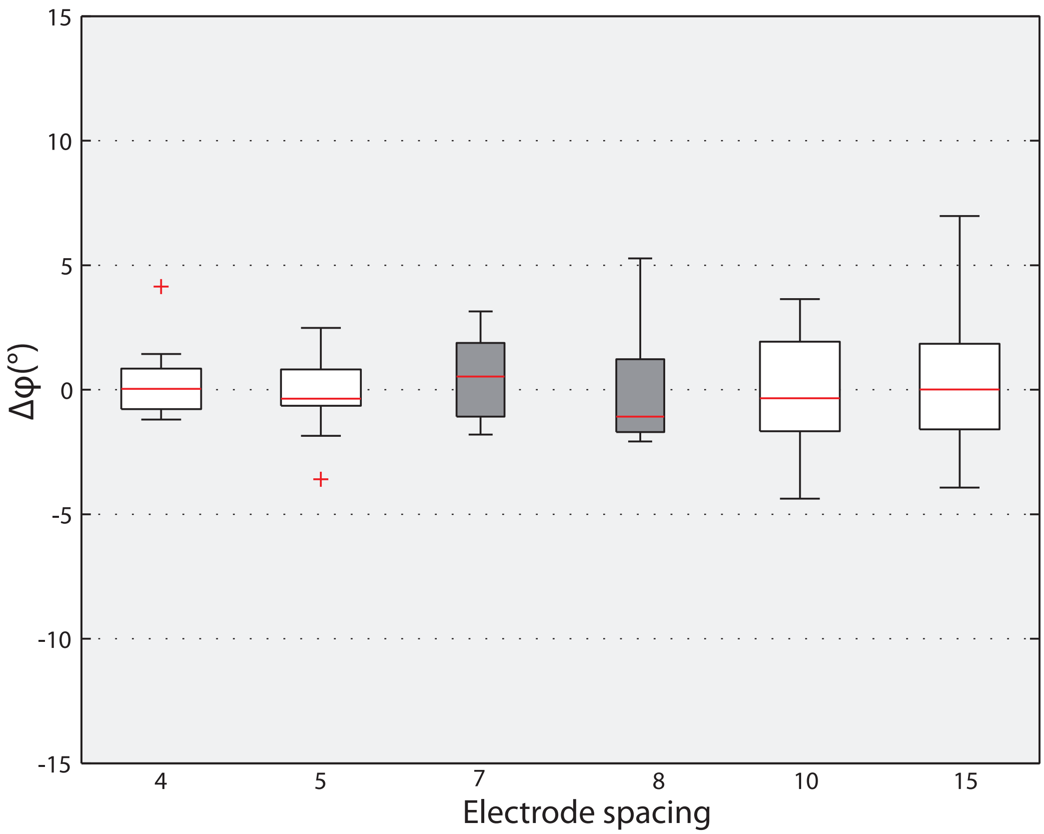

Figure 3.6: Phase angle in degrees at 46.4 kHz relative to its value for a spacing of one electrode as a function of electrode spacing expressed in number of electrodes, data from all CI subjects. Empty boxes comprise 16 data points while grey boxes only comprise 8 data points. Whiskers represent the ranges, boxes the 25^{th} and 75^{th} percentiles, and horizontal lines within the boxes the medians.

Among the 112 transimpedance spectroscopy measurements carried out in CIs in this experiment [14 conditions*8 subjects], 23 recordings in four subjects (S5, S6, S7 and S8) not only exhibited a high frequency phase shift due to the presence of C_p but also an unexpected *low frequency phase shift* associated with an increase in amplitude. Figure 3.7 compares regular and distorted spectroscopy data measured with subject S5 for different electrode pairs.

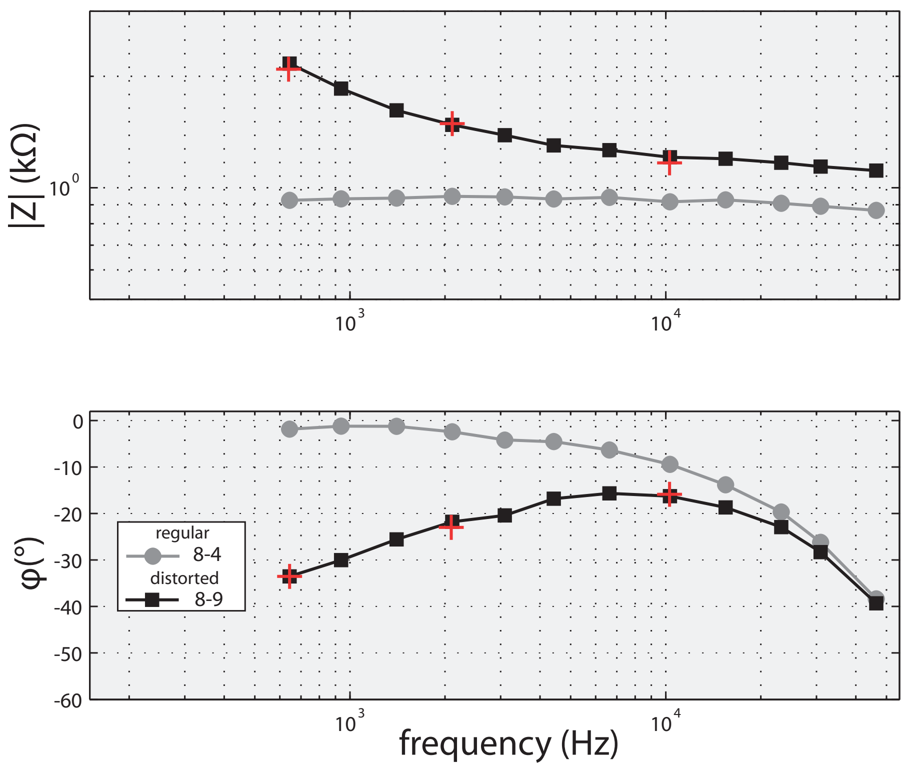

Figure 3.7: Bode diagram from transimpedance spectroscopy with 10 μA stimuli transimpedance measured in S5. Regular data (grey circles) were recorded using stimulating-recording electrodes 8-4 and distorted data (black squares) were recording using electrodes 8-9. Red + symbols represent additional data recorded using electrodes 8-9, with an amplitude of 5 μA

This suggests a capacitive charging of the inactive recording electrodes. This phenomenon was also visible on transimpedance recordings with biphasic pulses, as displayed in figure 3.8.

It is also worth noting that this distortion is associated with specific pairs of stimulating-recording electrodes and not to individual electrode interface. In other words, it could occur when stimulating electrode X and recording on electrode Y but not necessarily when stimulating electrode X and recording on electrode Z or when stimulating electrode Z and recording on electrode Y. To quantify the conditions where distorted signals occurred, the entire transimpedance matrix was measured with 50-μA biphasic pulse and 100-μs phase duration using the maximum sampling rate of the present device (55.6-kHz). Impedance waveforms were normalized and fitted with a biphasic pulse with exponential transients. We arbitrarily defined waveforms showing a sum of squared error higher than 0.015 as distorted. As a result, 18% of the 1920 [16$\times$15 electrode combinations$\times$8 subjects] waveforms could be reported as distorted. Possible explanations for this phenomenon are discussed in section 3.6.

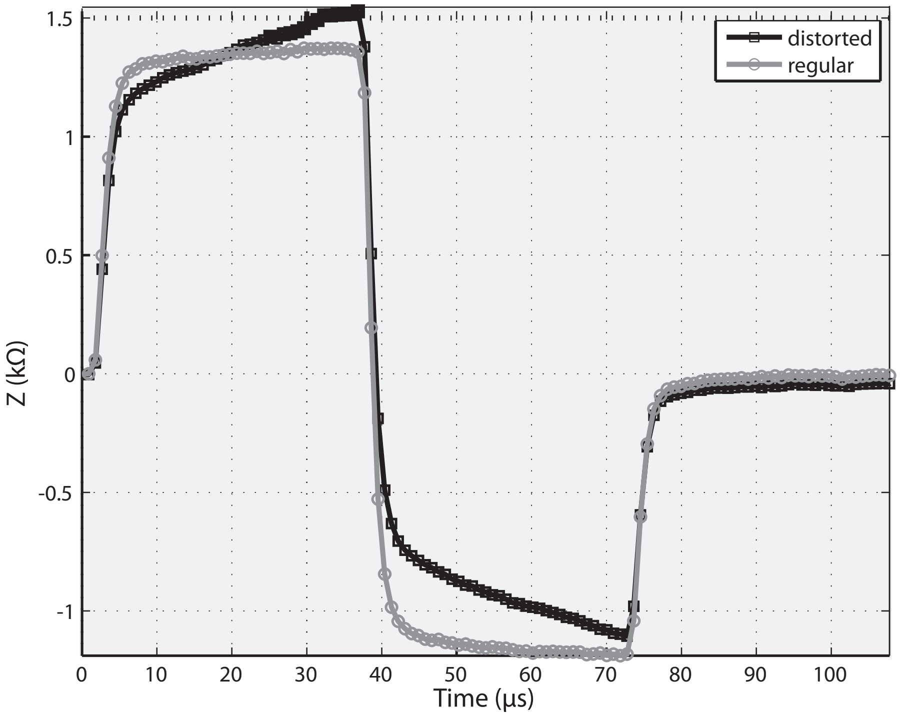

Figure 3.8: Up-sampled transimpedance waveforms for 50-μA biphasic pulse input measured in S5. Regular data (grey circles) were recorded using stimulating-recording electrodes 1-2 and distorted data (black squares) were recording using electrodes 8-9.

3.3.2 Linearity

3.3.2.1 Rationale and Method

In the PA strategy, the spatially-selective electrical pattern results from the linear sum of the electrical fields produced by each individual electrode. To efficiently control channel interactions it is thus necessary to make sure that no distortion is induced by electrical field summation. A series of measurement were carried out to investigate the linearity of current summation in vitro and in CI users. Those measurements consisted in activating a pair of electrodes in BP+1 or BP+2 stimulation mode using biphasic pulses and 50 μA amplitude, and measuring the voltage between one inactive electrode located in between the stimulating electrodes and the ground. For each subject, different electrode pairs were chosen in the apical, middle and basal sections of the array. All recordings were up-sampled [1]. The amplitude of the recorded waveform was then compared to the value inferred from the linear sum of transimpedance measurements made in MP mode.

[1] The combination of BP stimulation and a full up-sampling up to 1.1 MHz exceeds the performance of the device. To run these measurements, fs was reduced to 557 kHz

3.3.2.2 Results

Figure 3.9 shows a typical resulting waveform measured in subject S2. Assessing the linearity of current summation was not straightforward not only because of the peaky artifacts located at the onset and offset, but also because some waveforms were affected by the same distortion as in section 3.3.1.

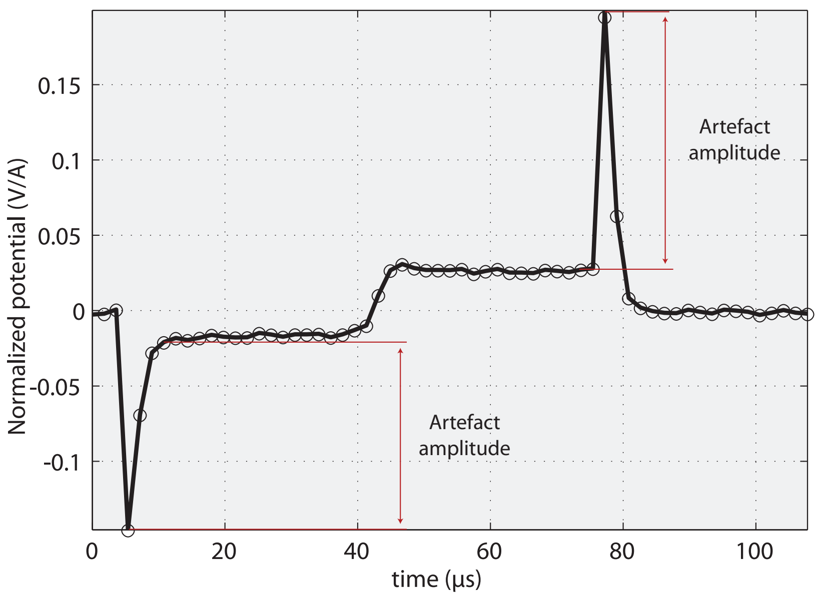

Figure 3.9: Current summation from the bipolar stimulation of electrodes 7 and 9 measured on electrode 8, in subject S2.

The amplitude of the recorded waveforms was thus arbitrary defined as half the difference between the amplitudes at $t_1 = 7.2\mu s$ (three samples after the peak of the onset artifact) and $t_2 = 50.3\mu s$ (six samples after the peak of the phase reversal artifact). This estimation was then compared to the theoretical amplitude inferred from the transimpedance matrix. Overall the amplitude of the electrical field superimposition could be predicted from transimpedance data with an average error of 31 V/A [2] ($s.d. = 30V/A$). The marked artifacts at onset and offset can be explained by an imperfect superimposition of individual electrical fields due to transient time constants discrepancies. These differences in time constants arise from the different values of the resistive paths between each electrode and the ground coupled to the parasitic capacitance. Similar patterns were obtained in all subjects and also in vitro even with time constant differences lower than 0.2 μs. The amplitude of the onset and offset artifacts was measured relative to the following or preceding phase respectively ($i.e.$ relative to the expected amplitude). For all recordings carried out in CIs the mean amplitude was estimated at 192 V/A ($s.d. = 84V/A$). Since those artifacts arise from simultaneous interactions, their amplitude will increase with the amplitude of the original stimuli.

[2] Even though V/A units are equivalent to Ohms, it seemed more physically relevant to express the amplitude of the recorded waveforms in terms of normalized potential in V/A.

Here, recordings were made at a very low level (50 μA) and none of the eight participants reported an auditory percept. It is however complicated to predict if such artifacts might become audible at higher levels.

Consequences of the artifacts as well as possible solutions to reduce them are discussed later in this chapter (section 3.6).

3.4 Experiment 2: Tetrapolar measurements

3.4.1 Rationale and methods

Despite the low frequency distortion observed in section 3.3.1, biological materials composing the inner ear are often described by their electrical resistivity whose three dimensional variations drive the electrical spread within the cochlea. The validity of this assumption is discussed in section 3.6.

As previously mentioned, the increasing knowledge about the cochlear geometry and its composition led to the design of detailed finite-elements models. In the opposite, several studies favored a more practical approach and attempted to describe this current spread with simple resistive networks (Kral et al., 1998; Vanpoucke et al., 2004b). This approach, providing more control on the number of parameters and their physical meaning, was used by Vanpoucke et al. (2004b) with networks consisting of a ladder of resistors connected by nodes corresponding to the measured transimpedances. In the most simple case (called order one in their study), this ladder is made of longitudinal resistors modeling the resistance in the ST between two electrodes and transversal resistors modeling the current pathways through the bony wall. In Vanpoucke et al. (2004b), the output of the model yielded transversal values being two orders of magnitude higher than longitudinal ones. This would mean that, first, only a small portion of the current lines run through the osseous spiral lamina, second, intra-cochlear electrical stimulation is poorly dependent on stimulation site.

Herein, a 4-point measurement procedure (Suesserman and Spelman, 1993a; Grill and Mortimer, 1994; Binette, 2004; Kumar et al., 2010) was used to estimate the pattern of resistivity in the vicinity of the electrode array. Such measurements consist in activating a pair of electrodes using a BP+X (X = 2, 3, 4 and 5) stimulation mode and recording the voltage difference between adjacent electrodes among the 2, 3, 4 or 5 left inactive.

Stimuli were biphasic pulses with 100 μA amplitude and 100 μs phase duration. For each configuration current lines will spread from one electrode to the other and the resistance measured across the X-1 recording pairs supposedly represents local resistance along the current path. For large values of X, current lines will spread deeper into the medium and impedance recordings will give an average resistance of the surrounding tissues and/or fluids (Binette, 2004; Grimnes and Martinsen, 2008). Such a protocol thus theoretically provides information on the longitudinal pattern of resistivity but can also be used to reveal contrasts of resistivity at different depth. Figure 3.10 illustrates the four-point measurement configuration for a simplified medium composed of two layers with different resistivities. In this configuration, current lines produced by the BP+2 stimulation (Panel A) will spread as if in a homogeneous medium, while with BP+3 stimulation (Panel B) current lines will be refracted by the presence of a higher density layer.

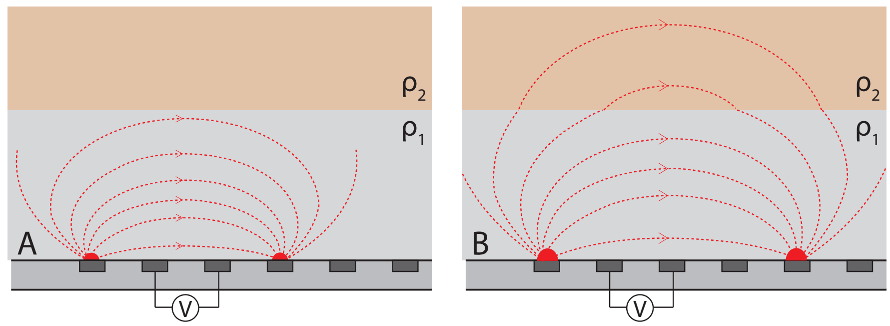

Figure 3.10: Illustration of the four-point measurement configuration for a two-layer medium, $\rho_1 < \rho_2$. A) BP+2 stimulation; B) BP+3 stimulation. Current lines are depicted by dotted lines.

To quantify the leak induced by shifting stimulating electrodes, we calculated the difference in dB relative to the BP+2 configuration, referred to as Δ_{BP+X}.

3.4.2 Results

3.4.2.1 In vitro data

This recording protocol was applied in vitro. All recordings yielded flat across-electrode patterns ($s.d < 4\Omega$), which is consistent with a homogeneous medium (data not shown here). In free field, where current lines are not constrained at all, Δ_{BP+3} was 3.96 dB on average across the array. The electrode array was then inserted in a 2.2-mm diameter straight cylinder, perfectly isolating, opened at both extremities. In this configuration, the difference between BP+2 and BP+3 was reduced to 0.9 dB. These outcomes suggest that in the presence of the isolating tube, current lines were forced to be similar for both BP+2 and BP+3 stimulation configurations.

3.4.2.2 CI data

Figure 3.11 represents the estimated resistance measured for BP+2 (circles in fig.3.11A) and BP+3 (triangles in fig. 3.11A) stimulation modes as a function of the recording electrodes pair for subject S1.

In contrast to the recordings made in vitro, the across-electrode patterns were strongly irregular which supposedly results from variations of resistivity in the vicinity of the electrodes. It was observed that changing the stimulation mode by increasing the spacing between stimulating electrodes yielded consistent patterns with decreasing amplitude for all subjects (right- and left-pointing triangles in fig. 3.11A) meaning that a part of the electrical current is no longer "visible" by the recording electrodes. Figure 3.11B represents Δ_{BP+3}, for the most apical (left-pointing triangles in fig 3.11B) and the most basal (right-pointing triangles in fig 3.11B) pair of electrodes. One can note that both configurations yielded symmetrical patterns resulting in a flat average pattern (dotted line in fig 3.11B) suggesting the pattern along the array essentially arises from local resistivity changes but that a few millimeters deeper through the modiolus, the resistivity is relatively homogeneous along the cochlea. In the present configuration, shifting one stimulating electrode toward the base or toward the apex by 1.1 mm (ie. BP+3 vs BP+2) induced a current leakage of several dB ([1.99 – 3.85 dB], mean = 2.8 dB).

Considering the average dimensions of the first turn of the cochlea (≈2.1 mm; Ericson et al., 2008), the confrontation of the in vitro and CI recordings suggests that a large portion of the current passes through the bony wall thanks to its porous structure revealed by Küçük et al. (1991) and Shepherd and Colreavy (2004). While several studies suggested the presence of a large ratio of resistivity between the perilymph and the modiolar wall (eg. 1:100, or higher, (Vanpoucke et al., 2004b; Whiten, 2007; Malherbe et al., 2015)), the present findings would suggest a much lower contrast (Kalkman et al., 2014). However, many parameters such as the recording configuration, fibrosis, ossification, current pathways, or the size of the cochlea, may also influence these data.

3.5 Experiment 3: Contact impedance

3.5.1 Rationale and methods

3.5.1.1 Rationale

As previously mentioned, the contact impedance is defined as the voltage measured between an active electrode and the ground electrode. It thus theoretically provides information on the path between one stimulating electrode and the ground. Unfortunately, the polarization of the electrode-fluid interface distorts the recorded waveforms which prevents a straightforward estimation of the resistance between the electrode surface and the ground referred to as the access resistance. A modeling approach, as described in the next paragraph is thus often necessary.

In the field of neural prostheses (eg. CI or retina implants), being able to estimate the access resistance is a crucial challenge for several reasons. First, it can be used as a clinical follow-up to make sure all electrodes are normally functioning. Second, some studies investigated the possibility to use impedance changes as a predictor of electrode placement (Majdi et al., 2015). Finally, for the PA strategy, knowing the access resistance would provide an estimation of the diagonal terms of the impedance matrix which relates to the electrical field produced in the vicinity of a stimulating electrode.

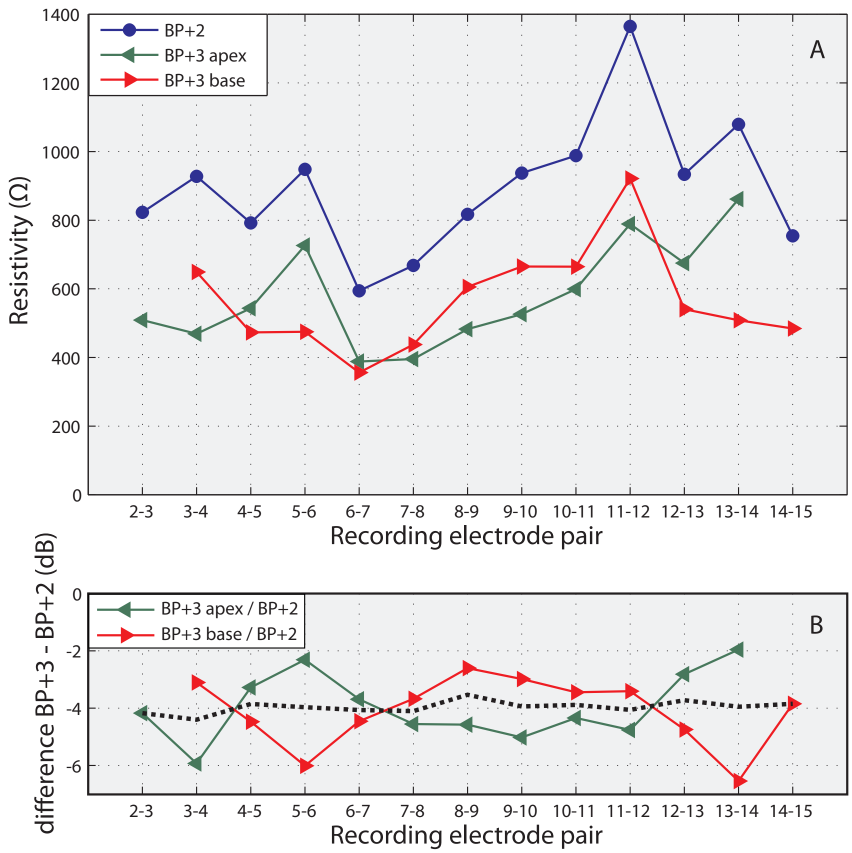

Figure 3.11: A) Four-points measurements for subject S1, for BP+2 (circles) and BP+3 stimulation (right- and left-pointing triangles for the most basal and apical configuration respectively), B) difference in dB between BP+2 and BP+3 measurements.Dotted line represents the mean difference.

3.5.1.2 Equivalent electrical circuit

Polarization of stimulating electrodes is a well-known phenomenon which has been investigated in many studies. The commonly used approach to model electrode polarization is by means of equivalent electrical circuits. In human CI recipients, few studies proposed a simple description of this phenomenon including the resistance of the current path from the electrode to the ground in series with the polarization impedance composed of a capacitance in parallel with a charge transfer resistance. (Vanpoucke et al., 2004b; Tykocinski et al., 2005).

However, several in vitro and animal studies provided a good account of this phenomenon using more advanced equivalent electrical circuits and recording systems (e.g. Duan et al. (2004); Franks et al. (2005)). Herein we used a simple phenomenological model derived from those studies to describe contact impedance. This model (figure 3.12) consists of five components including a known blocking capacitor, C_b ($C_b = 100$ nF), a constant phase element, CPE, modeling a non-perfect capacitor whose impedance is given by equation 3.1, R_f is a Faradaic resistance associated with the transition from electrical to ionic charge carriers, R_a is the access resistance modeling the overall resistance of current pathways, and C_p is the parasitic capacitance introduced in section 3.3.1.

$$Z_{CPE} = \frac{1}{Y_0.(j\omega)^\alpha} \tag{3.1}$$

Unlike other models used in human CI studies (Vanpoucke et al., 2004b; Tykocinski et al., 2005), the capacitive element of the polarized interface was modeled by estimating both the amplitude and the α coefficient. The method described in Appendix 7.4 (Lario-García and Pallàs-Areny, 2006) was used to determine the analytical solution for the overall equivalent impedance in the time domain considering biphasic current pulses. Model parameters (R_a, R_f, Y_0, α, C_p) were estimated by fitting (nonlinear least-squares method) normalized potential waveforms with this analytical solution.

Spectroscopy data were also used to estimate model parameters using EIS Spectrum Analyzer software (Bondarenko and Ragoisha, 2005) and the Nelder-Mead simplex algorithm (Nelder and Mead, 1965).

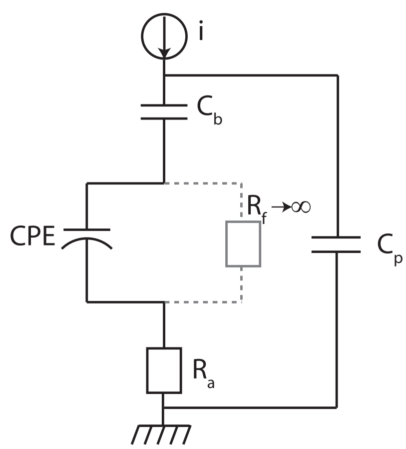

Figure 3.12: Electrical model of the electrode-electrolyte interface.

In CIs, many different conditions were tested in the same session. All contact impedances were measured using the up-sampling procedure for 50-μA biphasic pulses with a 35.92-μs phase duration. This condition is referred to as the *default condition* in the following paragraphs. Additional conditions were tested on a subset of electrodes (electrodes 1, 4, 8, 12, and 16) to evaluate the robustness of the parameters' estimation. This included varying the level (25 and 100-μA), the phase duration (17.96-μs and 67.35-μs), and leading polarity of the pulses. Contact impedance spectroscopy was also measured for all contacts on the entire frequency range ([0.2-46.4]-kHz) As in the experiment 1, for CI listeners, the amplitude of sinusoids was chosen depending on the comfortable level obtained at 200-Hz.

3.5.2 Results: In vitro data

The present electrical model shown in fig.3.12, as well as the classic R-C model (Vanpoucke et al., 2004b; Tykocinski et al., 2005), were first tested in vitro to test their ability to fit the data in ideal conditions. In vitro measurements yielded very high estimation for R_f ($> 10^{15}\Omega$) suggesting that no current passes through this resistor. To limit the number of relevant parameters of the present model, R_f was removed and another analytical solution (Appendix 7.4, eq. 7.15) was used to fit the data which did not affect the estimation of other parameters.

Figure 3.13 represents the impedance waveforms and the present model output for $R_e = 2.2$-$k\Omega$ and $R_e = 5.6$-$k\Omega$. For each case, the estimation of the access resistance was 2.85 $k\Omega$, and 6.18 $k\Omega$ respectively. Figure 3.14 displays the residual of three different models: R-C, CPE with and without C_p, applied on the same data as in figure 3.13, for $R_e = 2.2$ $k\Omega$. Those preliminary measurements suggested that, first, a CPE is more appropriate to model polarization impedance, and second, including C_p is absolutely necessary for the fitting of the entire impedance waveform and especially for an accurate estimation of R_a.

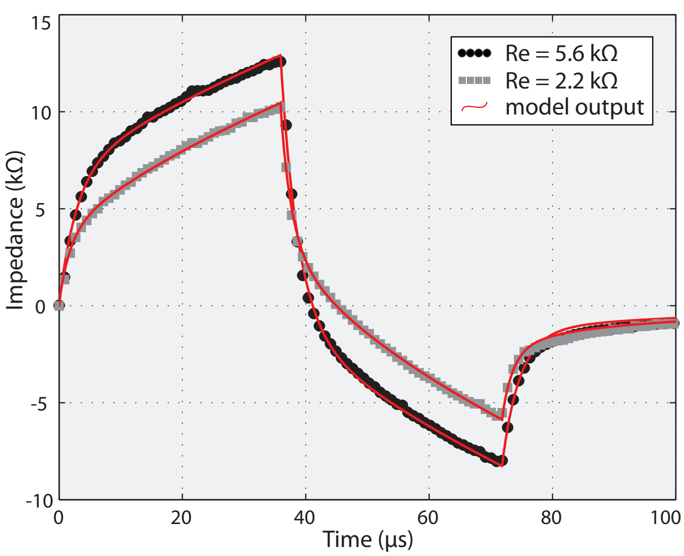

Figure 3.13: Contact impedance waveforms recorded in vitro for $R_e = 2.2$ $k\Omega$ (grey squares) and 5.6 $k\Omega$ (black dots) and model output.

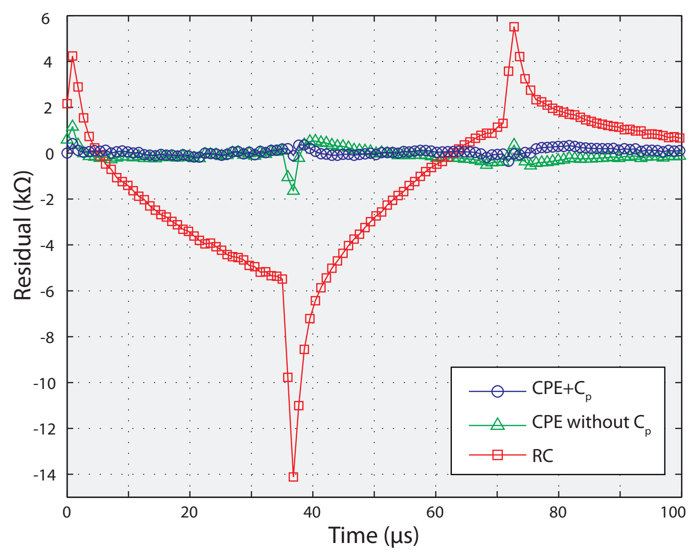

Figure 3.14: Residual of different contact impedance models: RC (squares), CPE without C_p (triangles), CPE + C_p (circles).

Theoretically, R_a accounts for three main elements: the resistance due to the device (switches, wires, amplifier, etc. R_{device}), the spreading resistance ($R_{spreading}$) and the actual resistance of the current path to the ground. The spreading resistance for a rectangular electrode (one-side exposed) can be estimated using the equation 3.2, where ρ is the resistivity of the medium in $\Omega.cm$, l and w represent the length and with of the electrode (Kovacs, 1994; Franks et al., 2005). In the present experimental conditions, $R_{spreading}$ should be approximately 565 Ω. If this equation is still valid for a recessed electrode, this would suggest that, in the present experiment, R_{device} is negligible.

$$R_{spreading} = \rho.\frac{ln(4.l/w)}{\pi.l} \tag{3.2}$$

3.5.3 Results: CI users data

Contact impedances were measured for all available electrodes and all CI users. All waveforms could be described by the present model ($r^2 > 0.98$ for all electrodes).

Figure 3.15 shows an example of contact impedance waveforms for four different electrodes measured in subject S2 (circles in fig 3.15) and the corresponding model outputs (red solid lines).

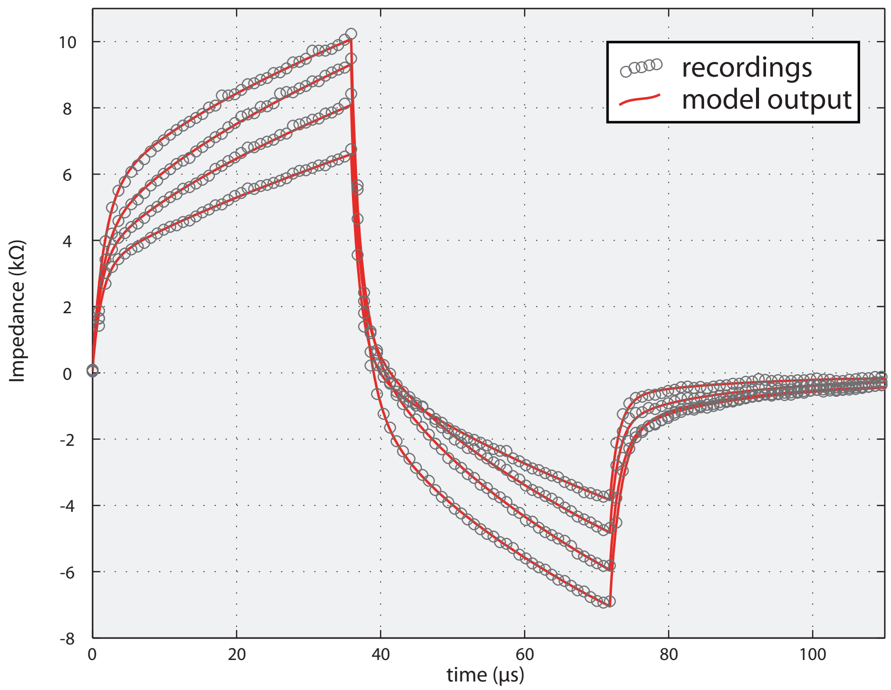

Figure 3.15: Four examples of contact impedance waveforms (circles) and model output (solid lines) measured for S2 in the default condition.

The overall dataset for CI users yielded very subject-specific across-electrode patterns for R_a. Table 3.3 gives a summary of the averaged fitted parameter values as well as the minimum and maximum values across the array for each subjects in the default condition.

The robustness of the model was investigated by varying the amplitude, phase duration, and leading polarity of the pulses for a subset of electrodes, resulting in five estimations of the model parameters obtained from independent measurements. For each subject, each electrode within this subset, and each parameter, the coefficient of variation (CV) across the five conditions was calculated. Figure 3.16 displays the individual CVs expressed in percentage. Each data point relates to one of the electrodes measured in a given subject and different symbols are for different subjects. Averaged

	R_a (kΩ)		$Y_0(\Omega^{-1}.j\omega^{\alpha}).10^{-9}$		α		C_p (nF)	
	mean	range	mean	range	mean	range	mean	range
S1	5.76	[4.73-7.29]	712	[319-1010]	0.58	[0.53–0.67]	0.23	[0.20-0.25]
S2	3.20	[2.40-4.55]	427	[95-770]	0.64	[0.56–0.78]	0.39	[0.32–0.46]
S3	3.62	[2.46-5.06]	533	[74-928]	0.64	[0.56–0.83]	0.35	[0.24–0.45]
S4	4.54	[3.30-6.37]	558	[223-891]	0.62	[0.54–0.71]	0.28	[0.23–0.32]
S5	3.55	[1.63-6.93]	258	[91-601]	0.66	[0.54–0.77]	0.44	[0.30–0.60]
S6	3.35	[2.53-4.79]	245	[46-564]	0.73	[0.60–0.87]	0.39	[0.31–0.47]
S7	4.63	[3.12-5.56]	672	[354-1119]	0.59	[0.55–0.64]	0.29	[0.23–0.37]
S8	4.14	[2.15-6.42]	442	[86-891]	0.64	[0.54–0.81]	0.36	[0.26–0.60]
average	4.01		481		0.64		0.34	

Table 3.3: Model parameters for all CI subjects estimated from anodic first biphasic pulses with 50 μA amplitude and 35.92 μs phase duration.

across subjects and electrodes, the mean CV was: 7.2% for R_a, 40.3% for Y_0, 7.3% for alpha, and 17. 5% for C_p.

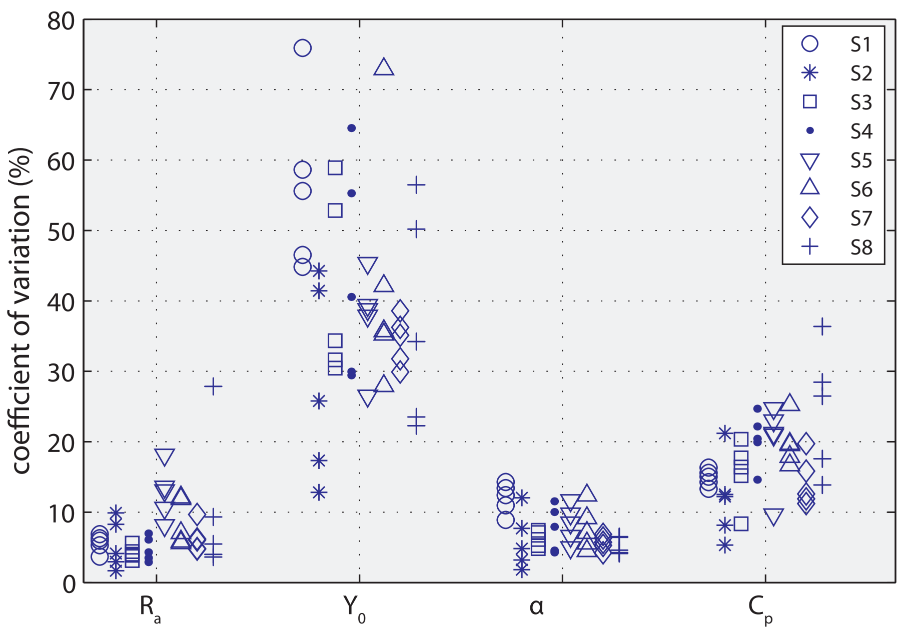

Figure 3.16: Coefficient of variation of model parameters estimates using different stimuli. Different symbols are for different subjects.

The model parameters were also estimated from impedance spectroscopy data for all electrodes. Figure 3.17 represents the individual estimation of model parameters obtained in the spectral domain versus those obtained in the time domain. Here again, each data point relates to one electrode and different symbols are for different subjects. Data points located above the diagonal indicate a higher estimation using spectroscopy data than using biphasic pulses. Overall, one can note that the values of R_a and C_p

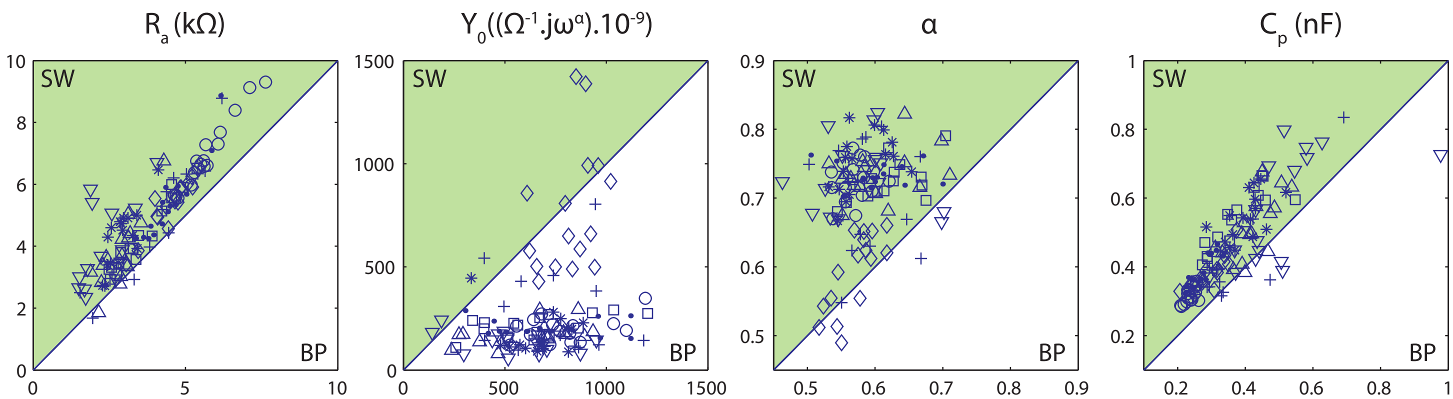

Figure 3.17: Spectral domain estimation versus time domain estimation of model parameters. From left to right, R_a, Y_0, α, C_p. Each data point corresponds to one electrode for one subject, different symbols are for different subjects as is figure 3.16.

were very consistent across all conditions in both the spectral and temporal domain while Y_0 and α exhibited much more variation across the different conditions.

In figure 3.17, it is worth noting that the range of Y_0 was smaller using the spectroscopy data than the biphasic pulse data,, except for one subject who showed surprisingly high values for Y_0 associated with very low α.

Possible explanations for the variability of the estimation observed between different stimuli will be discussed in section 3.6.

3.6 Discussion

3.6.1 Experiment 1:

3.6.1.1 Parasitic capacitance, C_p

In the experiment 1, impedance spectroscopy enabled to assess the presence of a parasitic capacitance, C_p, which resulted in a low-pass filtering of all stimuli. To our knowledge in previous in vitro, in vivo or model studies, pulsatile stimuli were always considered as perfect square pulses. Franks et al. (2005), pointed out a comparable phase drop at high frequency ($f > 100kHz$) in their in vitro spectroscopy data but attributed this to the measurement system. In vitro, the influence of C_p on electrical stimuli might not be an issue when the access resistance is very low, for instance when the ground is located in the saline solution, which seems to be the case for Ifukube and White (1987); Suesserman et al. (1991); Franks et al. (2005); Tognola et al. (2007). In this situation, its effect would be constrained to the very high frequency domain. However, the present results suggest that C_p must not be neglected when using this device in CIs and it is likely that other devices also show a similar parasitic capacitance.

We have seen in the present study that the presence of C_p is responsible for the smoothing of biphasic pulses stimuli. Because of the across-electrode variations of

C_p combined with variations in the access resistance, each source generates current pulses with slightly different transients. When different electrical fields superimpose this mismatch yields current summation artifacts as shown in Fig 3.9. As a consequence, such artifacts may occur with all multipolar stimulation modes (eg. TP and BP). It might be especially problematic for the PA strategy since the residual electrical field would present unwanted voltage peaks. As these artifacts result from an imperfect cancellation of two (or several) stimuli, their amplitude is thus proportional to the amplitude of the original stimuli. We may thus expect high-amplitude artifacts to occur in the vicinity of the stimulating electrode. It might be beneficial to consider using single-cycle sinusoids or Gaussian-shaped pulses as alternative pulse shapes to restrain the spectral content of the stimulus waveform to lower frequencies. Recordings similar to those carried out in section 3.3.2 were done in CIs, using single-cycle sine waves. Figure 3.18 shows typical signals recorded in subject S7 on electrodes 8 (black curves) and 14 (grey curves) resulting from the bipolar stimulation of electrodes 7-9 and 13-15 respectively. One can note that summation artifacts located at the onset, offset and phase reversal are removed when using single-cycle sine waves.

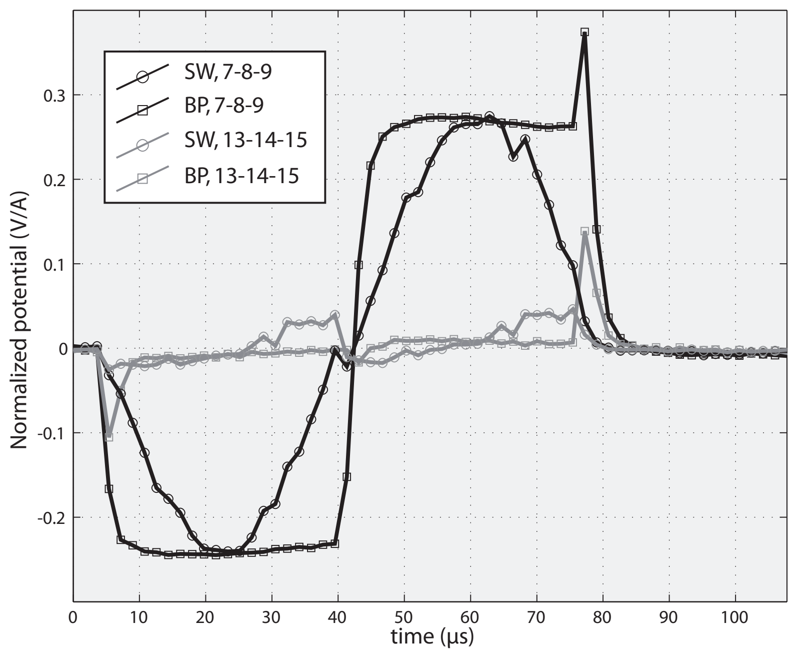

Figure 3.18: Normalized potential resulting from current summation using biphasic pulses (BP) and single cycle sine waves (SW) measured in subject S7. Electrode pairs 7-9 and 13-15 were stimulated in bipolar mode and voltage was recorded on electrode 8 and 14 respectively.

3.6.1.2 Resistivity and Partial polarization

While the present measurements enabled to verify the resistive behavior of the inner ear at high frequency, it also revealed the presence of another parasitic phenomenon.

Since distorted waveforms showed similarities with polarized electrodes' impedance, it is possible that this distortion results from the partial polarization of inactive electrodes. This partial polarization might be explained by the combination of several factors.

Non-resistive biological materials.

It is first possible that current lines pass through biological materials that are not purely resistive over this frequency range. Grill and Mortimer (1994), reported that a layer of macrophages, foreign body giant cells, loose collagen, and fibroblasts could form around epoxy electrode arrays. They observed that the electrical impedance of this layer showed a frequency-dependency suggesting a capacitive behavior. However, the effect was limited to very low frequencies ($< 100Hz$) and was not obtained with silicon carriers. Furthermore, the analysis of transimpedance recording seems to contradict this theory. If one considers electrode 2 as the stimulating electrode, one might expect the voltage recorded on electrodes 14, 15 and 16 to reflect the influence of comparable current pathways. However, in the case of S8, in this specific configuration electrodes 14 and 16 yielded distorted patterns but not electrode 15.

Charge deposition on the recording electrode.

It is possible that this polarization arises because of a charge deposition on the recording electrodes. This might first occur within the device, if the proximity of wires within the silicon carrier creates a stray capacitance and that few electrical charges deposit on the metallic surface of recording electrodes (Fridman and Karunasiri, 2010). Charge deposition might also occur in the cochlear medium because of a deviation of current lines towards the electrodes when passing in the very vicinity of the highly conductive platinum surface (Grimnes and Martinsen, 2008). Even though the use of recessed contacts supposedly limits this phenomenon, it might be facilitated if the electrodes are constrained in fibrous tissues or even bone due to a traumatic insertion. Consequently, current stimuli delivered by one of those electrodes would be forced to pass along other inactive electrodes. This phenomenon is illustrated in figure 3.19, where electrode A is deeply recessed in the silicon carrier and electrode B is not. The presence of electrode A deviates current lines from their theoretical path while electrode B not only deviates current lines but becomes polarized by the passage of current though its surface.

Electrode surface modifications.

Finally, the presence of this distortion seemed at least partially related to patients fitting history and especially the way the device was (or was not) used.

For S7, all electrode pairs yielded distorted waveforms. Interestingly, it happens that this patient had troubles to adapt to the implant and relied on residual hearing of the contralateral ear. She had barely used her implant for about 8 years before reactivating it after the loss of her residual hearing.

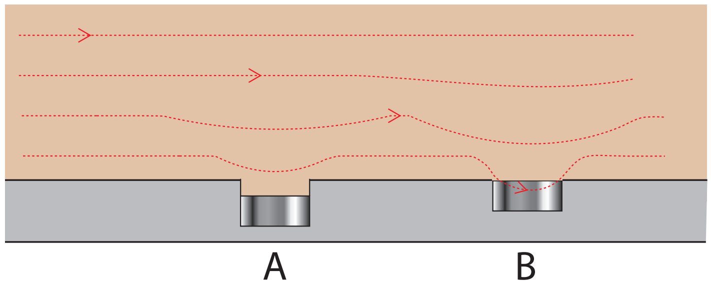

Figure 3.19: Schematic illustration of deviation of current lines induces by the presence of highly conductive electrodes along the current pathway. Electrode A deviates current lines but is not polarized, electrode B deviates current lines and enables the passage of current through its surface leading to its polarization.

For S8, measurements involving even electrodes yielded distorted signals and it seems that this patient was using an early strategy where every other electrode was turned off. Figure 3.20 represents normalized transimpedance patterns recorded in S8. Panel A displays the recordings obtained with all odd stimulating electrodes, panel B displays the recordings obtained with even stimulating electrodes and odd recording electrodes and panel C displays the recordings obtained with even stimulating electrodes and even recording electrodes. We can note that no distortion at all is observed with odd stimulating electrodes, while almost all waveforms are distorted when both the stimulating and recording electrodes are even electrodes.

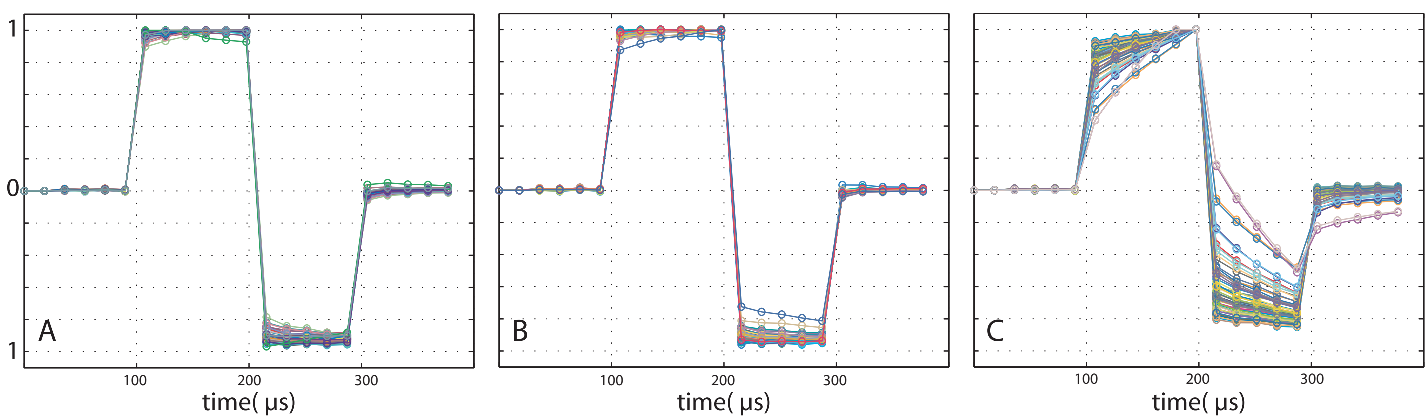

Figure 3.20: Normalized transimpedance recording made with S8 and single cycle sine waves (SW) measured in subject S7. Electrode pairs 7-9 and 13-15 were stimulated in bipolar mode and voltage was recorded on electrode 8 and 14 respectively.

For both cases, this period of inactivity might have induced two possible phenomena yielding reduction of the electrode's active surface.

First, the reaction between the perilymph and the metallic surface might create an oxidation layer, known as the passivation layer (López et al., 2008). Reactivating the electrodes is expected to induce the partial removal of this layer but the electrode may still have a smaller active area (Topalov et al., 2014).

Second, a similar reduction of the free surface of the electrode might be due to the growth of resistive fibrous tissues on its surface. For a given amount of charge deposit induced by the phenomenon introduced in the previous paragraphs, partial polarization might be facilitated by such a reduction of the active metallic surface.

Our recordings revealed different levels of distortion (see figure 3.20, panel C) which could be related to different levels of polarization. Neglecting this phenomenon could provide irrelevant estimations of the transimpedances and thus yield a misinterpretation of the electrical spread patterns. To obtain a fully determined transimpedance matrix a simple electrical model derived from the one used for contact impedances was used to estimate the resistive part of the impedance (see appendix 7.4).

3.6.2 Experiment 2:

3.6.2.1 Tetrapolar measurements

As previously mentioned, the present data showed that the across electrode patterns for R_a or tetrapolar measurements are strongly subject-dependent and thus induce very specific patterns of electrical diffusion.

Figure 3.21 represents the log-transformed individual access resistances and four-point impedance patterns normalized by their mean. Normalization enables to remove the influence of the absolute amplitude and thus to focus on the overall patterns. It is worth noting that R_a and tetrapolar measurements patterns were significantly correlated ($p < 0.01$) for subjects S1-2-3 and S6. However, the data from S5, S7 and S8 were analyzed using the same procedure as other subjects but their interpretation might be affected by the strong distortion of 4-points waveforms. This suggests that across-electrode patterns for R_a partly arise from the local variation of resistivity in the vicinity of the electrode plus an unavoidable error term due to the device itself.

Determining the depth of sounding is complicated since it varies with the electrode spacing but also with the medium resistivity and the contrast of resistivity between different layers (Mussett and Khan, 2000). In tetrapolar measurement theory, it is often assumed that the order of magnitude of the depth of sounding is approximately {0.3*electrode separation} (Mussett and Khan, 2000), being 1-mm for the present device in BP+2 configuration. We could thus hypothesize that 4-point measurements account for the influence of the perilymph, the presence of fibrosis within the inner ear and current pathways out of the ST. The rest of the access resistance variance might arise from near-field factors of the electrode surface (tissue-encapsulation, Grill and Mortimer (1994)) or far field factors such as current pathways to leave the otic capsule and estimation error induced by the device itself. In the case of subjects for which correlation coefficient are very low (S4, S5, S7, and S8), it might be possible that the sources of variation cannot be quantified using the present protocol.

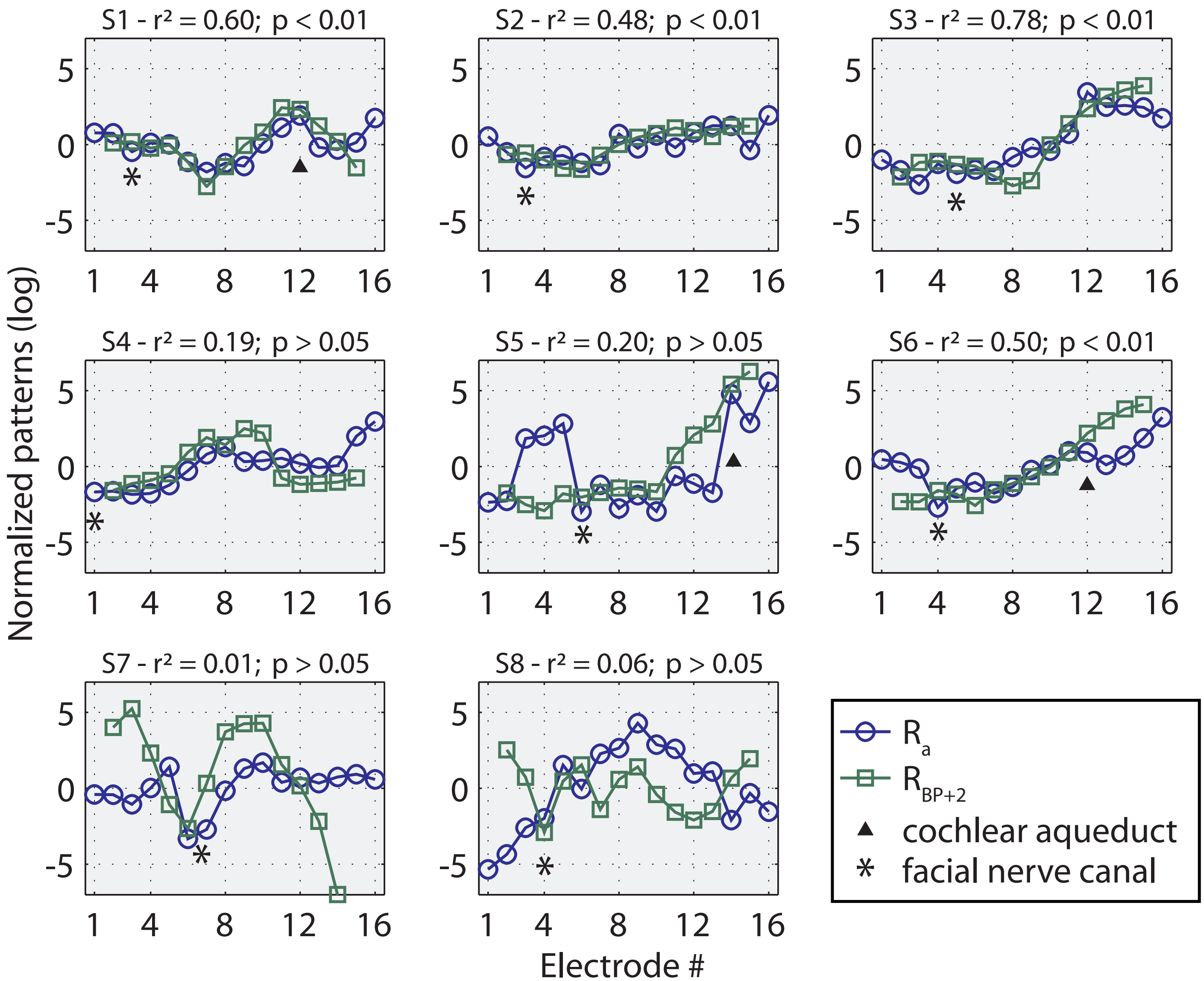

Figure 3.21: Normalized 4-points measurement pattern (squares) and normalized access resistance pattern (circles) for all CI subjects. r indicates the correlation coefficient between R_a and R_{BP+2}. Triangles and asterisks indicate the location of the cochlear aqueduct and the FNC respectively.

3.6.2.2 Current pathway

Current pathways from intracochlear electrodes to the ground are still not clearly identified. Indeed, they appear to be highly dependent on individual cochlear anatomy, electrodes position, insertion technique and insertion depth.

Several studies suggested that different cochlear features could influence current pathways, such as the round window, and the facial nerve canal (FNC) (Vanpoucke et al., 2004b; Duan et al., 2004). Cone beam CT scans were analyzed for all participants using Onis Viewer® (Onis Pro. v2.5) to investigate the presence of anatomical singularities that could be related to impedance measurements and identify possible current pathways. Vanpoucke et al. (2004a) suggested, based on model outcomes that a significant portion of the current could leave the cochlea through the FNC. This hypothesis seems supported by the fact that the location of the FNC on CT scans (fig.3.22) coincided with the global minimum, or at least a local minimum, of the access resistance across-electrode pattern for all subject except S8 (asterisks in fig. 3.21). However, subject S8 was implanted using a positioner which maintains the array close to the modiolus. In this configuration, it is possible that the modiolus provides a dominant current pathway, limiting the influence of the presence of the FNC. This pathway seems even more efficient when the FNC and what we think might be the greater petrosal nerve canal meet in the vicinity of the cochlea.

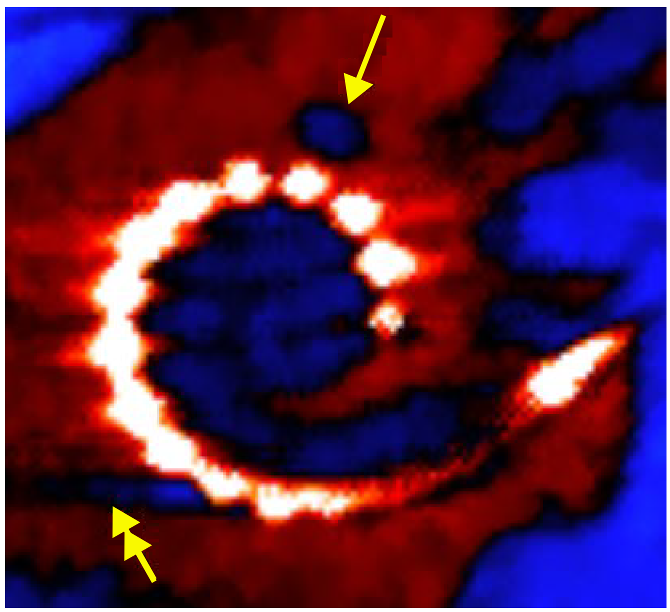

Figure 3.22: CT scan images for subject S4.Single arrow: passage of the facial nerve canal in the vicinity of the first turn of the cochlea. double arrow: cochlear aqueduct connecting with the Scala tympani.

The cochlear aqueduct (fig 3.22) could be clearly identified in four subjects. It is difficult to conclude as for its actual influence since neither the function nor the dimensions of the cochlear aqueduct have been conclusively demonstrated (Gopen et al., 1997). However, it seems that the connection of the cochlear aqueduct with the base of the cochlea induces an increase of R_a for electrodes at proximity. This might be related to the fact that after implantation, the cochlear aqueduct carries perilymph within the ST to restore pressure balance. The intense activity in this region might be associated with a strong immune reaction and tissue growth.

3.6.3 Experiment 3: Contact impedance model

The model presented here provided a good description of all contact impedance waveforms recorded both in vitro and in CI users. Model parameters estimates slightly varied

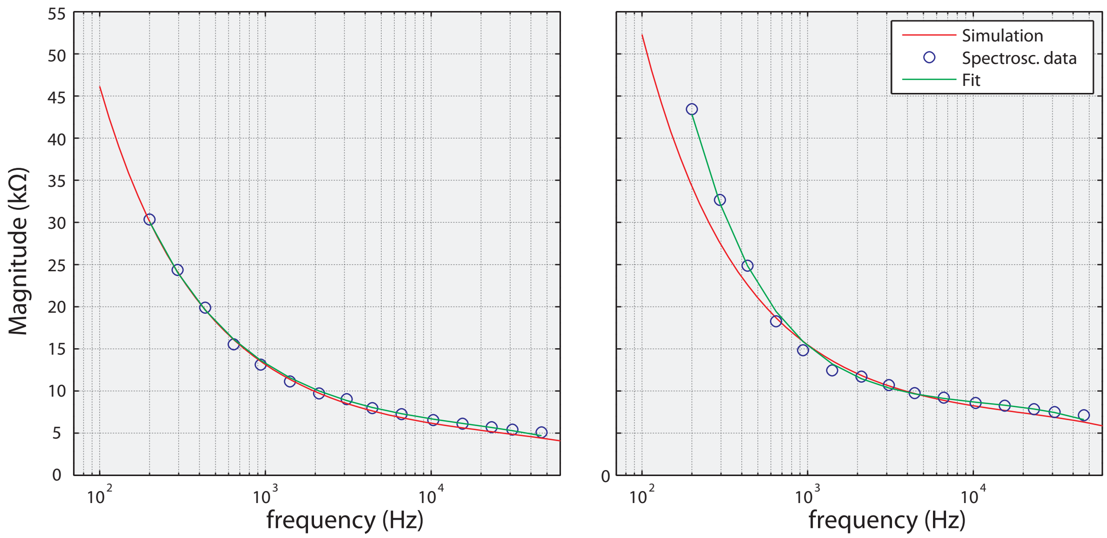

Figure 3.23: Magnitude diagram of contact impedance. Circles indicate the spectroscopy data points, green curves represent the output of the contact impedance model applied on spectroscopy data and Red curves represent the simulated spectrum based on the model estimations using biphasic pulses. Subject S7, left panel and S1, right panel

depending on the stimulus waveform. The differences observed between biphasic pulses and sine wave stimuli might be partly explained by differences in their spectral content. While C_p reduces the high frequency content of biphasic pulses it is likely that when the product $R_a \times C_p$ is not too high, pulses contain higher frequency components than 46.4 kHz. In contrast, the spectrum of biphasic pulses contains less energy in the low frequency region. Figure 3.23 displays the magnitude spectrum of contact impedance recorded in two CI subjects (circles, S7 left panel, and S1 right panel). Green curves indicate the output of the contact impedance model applied on these data. Red curves represent the simulated magnitude spectrum based on the model parameters estimation using biphasic pulses. One can see on the right panel that, as expected, spectral and temporal model estimations are especially consistent between 600-Hz and 10-kHz, bellow and beyond this range spectral and temporal estimations diverge. On the left panel, both estimations were surprisingly consistent over the entire frequency range.

These observations demonstrate that impedance spectroscopy provides more information than biphasic pulses and thus represent a relevant way of estimating contact impedance. Unfortunately, the protocol used here would require further optimization to reduce the duration of the measurement (approximately 25 minutes for 16 electrodes) for a clinical use.

Acknowledgments

Experiments carried out with CI users were approved by the local ethics committee. The authors sincerely thank Paddy Boyle, Leo Litvak, Yves Cazals, CHU Montpellier, for their help, CI subjects for their participation. This work was partly funded by AB.

Chapter 4

Investigating the Determining Factors of Neural Responsiveness.

The efficiency of electrical stimulation in terms of transmission of sound information depends on several factors that may vary between subjects. The most influent factors of the periphery of the auditory system can be modeled by the electrode-neuron interface.

This basic model accounts for the electrode, the distance to the neurons and the health of the stimulated neural population. Here, we investigate the electrode-neuron interface in a total of 16 CI subjects and evaluate the polarity sensitivity of nerve fibers as a potential correlate of neural survival. Detection thresholds were measured in partial tripolar mode for symmetric biphasic, triphasic-anodic and triphasic-cathodic pulses. The electrode-to-modiolus distance (EMD) was estimated from CT images for a subset of subjects. Speech recognition and SMRT (Aronoff and Landsberger, 2013) were tested in free field with the CI users' own processor.

We first show that an important part of the *within-subject* variance in detection threshold is explained by the EMD. Besides, we observed a polarity effect using triphasic pulses. Detection thresholds for anodic triphasic stimuli were lower than for cathodic stimuli in 78% of the tested electrodes. The difference between cathodic and anodic thresholds (referred to as the *polarity effect*) varied from less than -4dB to more than +4dB. If, as suggested by computational models, cathodic stimulation is more likely to generate action potentials at the level of the peripheral processes, we hypothesize that the polarity effect may be a correlate of neural survival. A partial correlation analysis revealed that part of the *within-subject* variance in detection threshold that cannot be explained by the EMD can be explained by the polarity effect. Furthermore, a significant across-subject correlation was observed between SMRT scores and the mean polarity effect across the electrode array. Speech recognition scores, however, did not show any relationship with the polarity effect. The present results suggest that the polarity effect may be used to picture the neural health along the electrode array.

4.1 Introduction

To restore an auditory percept to profoundly deaf patients, a cochlear implant (CI) initiates action potentials in the remaining auditory nerve fibers using direct electrical stimulation. In most CI devices, each intracochlear electrode is activated with reference to a remote return electrode located in the temporal muscle area. Using this monopolar (MP) stimulation mode, each electrode generates an electrical field in its vicinity which spreads along the cochlea and creates a presumably wide excitation pattern at the level of the auditory nerve. This MP configuration presents the advantage of requiring relatively low current levels to recruit a large population of neurons. However, as shown in the acoustic simulation study presented in chapter 2, activating adjacent electrodes induces the superimposition of different electrical fields which distorts the sound information present in each frequency channel. This poor spatial selectivity has been pointed out as one of the main limitations of present devices (Friesen et al., 2001) and has consequently been the topic of many research projects. Spatially-selective stimulation can be achieved using multipolar stimulation modes such as tripolar, partial tripolar (sometimes called quadrupolar) or phased-array stimulation (Litvak et al., 2007; van den Honert and Kelsall, 2007). These focused stimulation strategies enable to limit the electrical spread along the cochlea and, thus, to recruit narrower populations of neurons (Zhu et al., 2012; Fielden et al., 2013; Smith et al., 2013). Highly-focused stimulation should improve the transmission of sound information contained in each frequency channel. However, spatially selective stimulation is also likely to be more sensitive to dead regions in the neural population (Zhu et al., 2012; Marozeau et al., 2015). Typically, if an electrode faces a dead region, then higher stimulation currents may be needed to generate a clear auditory percept, thereby widening the extent of the stimulated region. To ensure an efficient transmission of sound information at the level of the auditory nerve fibers, it appears important for the design of alternative stimulation strategies not only to consider the electrical field generated by the electrodes, but also the entire electrode-neuron interface (Bierer, 2010).

A simple model of the electrode-neuron interface involves three sources of inter-subject variability, (1) the electrode position and insertion depth, (2) the current path and electrical properties from the electrode to the neurons and finally (3) the distribution of the neural population. The first two points can respectively be investigated directly by analyzing CT images (Saunders et al., 2002; Cohen et al., 2006; Long et al., 2014; Venail et al., 2015) and by performing electrical measurements (see chapter 3, Vanpoucke et al. (2004b,a); Micco and Richter (2006a)).

However, assessing neural survival and identifying its influence on CI performance is more complicated.

Following the loss of sensory hair cells and of the organ of Corti, the peripheral processes of auditory nerve fibers progressively degenerate up to the spiral ganglion cells (SGCs) which can secondly degenerate (see figure 4.1) (Leake and Hradek, 1988; Shepherd and Javel, 1997; Stankovic et al., 2004; Glueckert et al., 2005; Liu et al., 2015). Some studies investigated neural survival in CI recipients retrospectively by counting the remaining cells in cadaver cochleas (Nadol et al., 1989; Linthicum and Anderson, 1991; Glueckert et al., 2005). They demonstrated that it is complicated to predict neural survival especially since the speed of neural degeneration depends on numerous factors such as the duration of hearing loss, the duration of profound deafness, and the cause of deafness. In addition, those three main factors are sometimes unknown as we will see with the present group of participants. Besides, rather surprisingly, the influence of the number of remaining neural fibers on CI users' speech performance has not been clearly established and has yielded largely inconsistent results across studies (Khan et al., 2005a; Nadol and Eddington, 2006; Kamakura and Nadol, 2016).

Unfortunately, despite the continuous improvement of imaging techniques, it is still technically impossible to objectively estimate the extent of neural survival in CI users. As a result, several studies attempted to identify indirect correlates of neural survival using electro-physiological and psychophysical measures.

Measuring detection thresholds (T-levels) is commonly used to study the electrode-neuron interface (Bierer et al., 2015). The T-level is defined as the minimum current level required to create an auditory percept. Assuming that this T-level is reached when a certain fixed number of neurons is activated, the across-electrode pattern of detection thresholds may be interpreted as reflecting the distribution of neural responsiveness to a given stimulus. With the MP configuration, the across-electrode pattern of threshold tends to be flat, thereby providing little information. Focused stimulation modes can be used instead and generally exhibit more variability across the electrode array. Some studies reported that the within-subject variance in threshold across the electrode array correlates with speech performance (Pfingst et al., 2004; Long et al., 2014). It was also shown in animals that the sensitivity in threshold as a function of the electrical pulse rate is dependent on neural health (Pfingst et al., 2011). Zhou and Pfingst (2014) measured this rate sensitivity, called *multipulse integration*, in human CI users. They hypothesized that a large decrease of the T-level associated with a doubling of the pulse rate could be a psychophysical correlate of neural health. They reported that the amplitude of the multipulse integration was positively correlated with the performance in consonant recognition in noise, and transmission of place of articulation of consonants which corroborated their hypothesis.

Electrically evoked compound action potentials (eCAPs) can also be measured by intracochlear electrodes to provide information about the neural responsiveness to a given stimulus by recording the early response of the auditory nerve. Recording eCAPs has the advantage of being an objective measure in the sense that it does not rely on subjects' perception. It is however sometimes impossible to record eCAP responses and the interpretation of eCAP amplitude has yet to be clarified. Prado-guitierrez et al. (2007) evaluated the influence of both the inter-phase gap and the phase duration on the amplitude of eCAP recordings in animals. The SGCs counts revealed that the increase in eCAP amplitude as a function of either the inter-phase gap or the phase duration was larger in cochleas with a good neural survival.

Nevertheless, the outcome of both eCAPS and detection thresholds account for a combination of numerous parameters including neural survival, and the spread of excitation.

Long et al. (2014) recently measured detection thresholds, electrode-modiolus distance and speech recognition in a group of CI users. For seven of their ten subjects, a significant linear relationship was found between the electrode-modiolus distance and the detection threshold, referred to as the *distance model*. Interestingly, speech recognition scores were correlated with the residual of the distance model, meaning that when the distance cannot explain the variation in threshold across electrodes, speech performance tends to be poorer. They hypothesized that this correlation might reflect the state of neural survival and that subjects with better neural survival are better performers.

A first aim of this chapter was to replicate the experiment of Long et al. (2014). In addition, we evaluate another way to assess neural survival using a psychophysical measure of polarity-sensitivity.

Clinical electrical stimuli are symmetric biphasic pulses (figure 4.2, CA). Using this pulse shape, both the anodic (positive) and the cathodic (negative) phases of the pulse can produce action potentials at the level of the auditory nerve. However, animal studies usually demonstrated a higher sensitivity to negative current phases, meaning that neural threshold is reached at a lower current level for negative than for positive currents (Hartmann et al., 1984; Miller et al., 2001; Macherey and Cazals, 2016).

Even though monophasic pulses are not used in human CI users for safety reasons, various pulses shapes can be designed to investigate polarity effects while maintaining electrical charge balance. This can be done using triphasic pulses (Bonnet et al., 2004; Eddington et al., 2004) or pseudo-monophasic pulses composed of a short phase of one polarity followed by a longer and lower-amplitude phase of the opposite polarity. Unlike clinical pulses, such an asymmetric pulse shape is supposed to induce a domination of the short, high-amplitude phase over the long, lower-amplitude one. Using the latter pulse shape, Macherey et al. (2008), and Undurraga et al. (2012) investigated polarity sensitivity in human CI users. Rather surprisingly, both studies showed that human auditory nerve fibers exhibit a higher sensitivity to positive current (*ie.* anodic phase). The mechanism of nerve fiber stimulation has been intensively investigated in numerous studies and two main factors have been proposed to explain this difference in polarity sensitivity: the degree of myelination and the site of excitation (van den Honert and Stypulkowski, 1984; Rattay, 1989; Rubinstein, 1993; Rattay, 1999; Mcintyre and Grill, 2002). In particular, Miller et al. (1999) observed longer latencies of neural responses for cathodic stimulation compared to anodic stimulation in cat's fibers. They hypothesized that cathodic stimuli initiate action potentials at the level of the peripheral processes and are delayed by the presence of the cell body (see figure 4.1). In contrast, the shorter latencies for anodic stimulation may result from a more central site of excitation. These results were corroborated in humans by Undurraga et al. (2013) who observed longer latencies for cathodic stimulation in the eABRs (Electrical Auditory Brainstem

Responses).

While the first aim of the present study was to replicate the findings of Long et al. (2014) using comparable methods, the second aim was to better characterize the contribution of neural survival to both detection thresholds and speech perception. If the variations in the effect of polarity across the electrode array reflects the presence or absence of healthy peripheral processes, we would expect that it also reflects the extent of degeneration of the local neural population. In particular, we would expect lower cathodic thresholds to be associated with a healthy neural population and lower anodic thresholds to be associated with a partially-degenerated population.

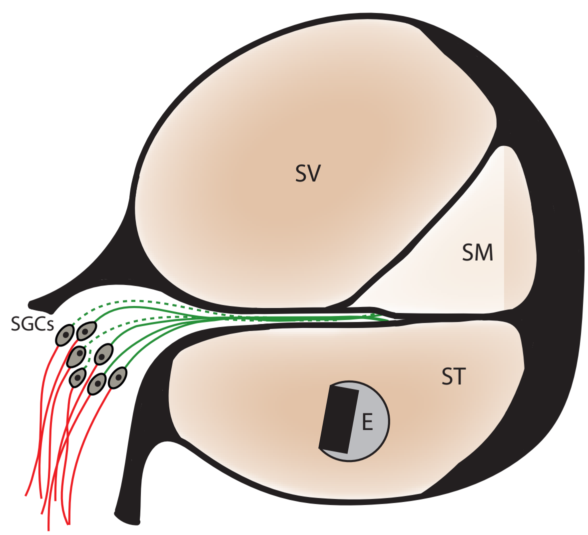

Figure 4.1: Illustration of the organization of auditory nerve fibers. Healthy and degenerated peripheral process are represented by solid and dotted green lines, respectively. Central processes are represented by red solid lines. Spiral ganglion cells (SGCs) are depicted in blue. ST, scala tympani; SM, scala media; SV, scala vestibuli; E, electrode.

4.2 Methods.

4.2.1 Subjects

Experiments were conducted both in France and in the United Kingdom with a total of 15 adult CI users (16 ears). Ten subjects (11 ears) were tested in France, six of them already participated in the previous experiments described in chapter 3. Five additional subjects were tested in the United Kingdom. One subject (S8) wore a CII device and all the others wore the HiRes 90k device (Advanced Bionics) with either the HiFocus 1J or Mid scala electrode array. Subjects were paid for their participation and their details are reported in table 4.1.

Subjects	Duration of deafness prior to CI (years)	Etiology	CI use (years)	Age (years)	Deactivated electrodes
S1	20	Unknown progressive	12	38	/
S2	7	Unknown progressive	7	62	/
S21	1	Unknown progressive	1	62	/
S4	10	Unknown progressive	13	52	/
S6	6	Usher syndrome	13	20	/
S7	24	Pendred syndrome	12	39	/
S8	2	Unknown progressive	15	87	/
S10	47	Ototoxic drug following meningitis	12	61	E15
S11	34	Congenital	0.5	42	/
S17	10	Viral	11	63	/
S18	20	suspected ototoxicity	1.5	35	/
C12	/	/	/	73	E8
C13	/	/	7	71	E15
C14	/	/	2	71	/
C15	/	/	/	57	/
C16	33	Otosclerosis	8	70	/

Table 4.1: Subjects details. Subjects labelled with the letter $S-$ were tested in France, and those labelled with the letter $C-$ were tested in the United Kingdom.

4.2.2 Detection thresholds

Detection thresholds (T-levels) were measured for all subjects using the Bionic Ear Data Collection System (BEDCS, Advanced Bionics, Litvak (2003)) and custom Matlab interfaces.

Stimuli

Electrical stimuli were 300-ms long pulse trains with a rate of 100-Hz. Three pulse shapes were tested. Cathodic-first symmetric biphasic pulses (CA) were considered as baseline pulses. Triphasic ACA and CAC pulses were also tested. These pulse shapes consist of a central phase of a given polarity and amplitude preceded and followed by phases of the same duration, opposite polarity and half the amplitude. ACA and CAC pulses are supposed to enhance the influence of the cathodic and anodic phase respectively (Eddington et al., 2004; Macherey et al., 2006). For more clarity, ACA and CAC thresholds are referred as *cathodic* and *anodic* thresholds respectively. For all pulse shapes, the duration of each phase was 97 μs. Figure 4.2 gives a schematic representation of the three pulse shapes used in this experiment. Herein, we are not only interested in the absolute thresholds but also the inter-electrode variability. In monopolar stimulation, detection thresholds tend to yield flat across electrodes patterns (Long et al., 2014; Marozeau et al., 2015). To maximize the range of threshold values across the array, stimuli were presented using partial tripolar (pTP) stimulation with 75% of the current returning to the flanking electrodes and 25% to the ground (i.e. $\sigma = 0.75$, Jolly et al. (1996); Litvak et al. (2007), see figure 1.7 in section 1.2.2). In pTP stimulation mode, the most apical and most basal electrodes cannot be stimulated because they do not have two neighboring electrodes, thereby limiting the maximum number of available tripolar channels to test to 14 from E2 to E15. Electrodes that were deactivated in patients' clinical map (see table 4.1) were not tested (neither as stimulating electrodes nor as return electrodes). As a result, the number of conditions per subject varied between 33 (for C12) and a maximum of 42 ($\{14$ electrodes$\}\times\{3$ pulse shapes$\}$ = 42 conditions).

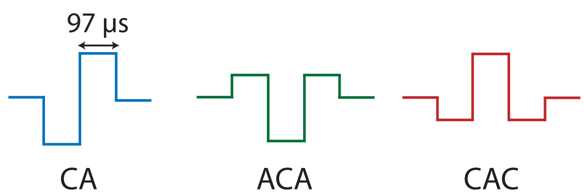

Figure 4.2: Electrical pulse shapes used for T-level estimations. From left to right: cathodic-first biphasic pulse (CA), triphasic cathodic (ACA) and triphasic anodic (CAC).

Procedure

Even and odd electrodes were tested independently yielding two subsets of 7 electrodes and 21 testing conditions. For each subset, one electrode was selected in randomized order and for this electrode, the three pulse shapes were tested successively, also in a randomized order. The most comfortable level (C-level) was then estimated for each specific condition.

Subjects were asked to report the perceived loudness using a loudness chart ranging from 0 to 10, where level 1 corresponds to the first just noticeable sound, 6 is the estimated C-level and level 10 corresponds to sounds that are too loud. The stimulation level was manually increased starting at sub-threshold level with an amplitude step of 1-dB. Typically, when the loudness reached level 2, the amplitude steps was reduced to 0.5-dB up to level 4 and then 0.2-dB until the C-level was reached. Before each stimulation it was checked that the current level did not exceed the compliance limit of the device (≈ 7 volts for the present devices, see Appendix 7.3). If compliance limit was reached before the C-level, the procedure was stopped and the maximum allowed current level was recorded instead.

After the estimation of all the C-levels for all 21 conditions, thresholds were estimated for each of them using a one-up/one-down procedure. The initial level was set to 90% of the C-level (or 90 % of the maximum level below the compliance limit). Subjects were asked to press the space bar of a computer keyboard each time they heard a sound. If a percept was reported within a 3-s time window, the timer was stopped and a lower amplitude stimulus was played after a random delay between 2 and 3s. In the absence of a response after 3s, a higher amplitude stimulus was played after a shorter random delay (between 0.1s and 0.6s). As a result, with or without a response, the duration between two consecutive stimuli varied between 2s and 6s.

During this automatic procedure, the incremental step in level was ± 0.5 dB until the first reversal and ± 0.2 dB afterwards with a minimal current resolution of 4 μA. The procedure stopped after eight reversals and each T-level was calculated as the average of the last six reversals.

4.2.3 Speech recognition

Speech recognition was tested in a sound insulated booth or in an anechoic chamber, using the subjects' own speech processor and clinical map. Two lists of single words (ie. 100 words in total) from the French (N=9) or English (N=5) versions of the Phonetically Balanced Kindergarten corpus (PBK, Haskins, 1949) were tested. S2 is an American English speaker and thus did not participate in this task. Acoustic stimuli were played in free field through a Fostex 6301B loudspeaker without masking noise. Subjects sat one meter away from the loudspeaker, where the sound level was calibrated to be 65 dB SPL. They were asked to repeat each word they heard. Correct and incorrect responses were determined by an experimenter sitting next to the subject. Scores are given in percentage correct for both lists.

4.2.4 Spectro-temporally Modulated Ripple Test, (SMRT)

In this study, apart from the native language, CI users had a wide variability of experience with speech and with their device. CI experience varied from 0.5 to 15 years and some of them were prelingually deaf. To limit the effect of CI experience (Blamey et al., 2013) and of native language, a spectro-temporally modulated ripple test (SMRT, Aronoff and Landsberger (2013)) which reflects the ability of subjects to receive and integrate spectro-temporal cues, was also carried out with all 16 subjects. Such tests have been found to correlate to speech recognition performance when testing homogeneous groups of CI users (Won et al., 2007).

This test is implemented as a 3-intervals, 3 alternative forced choice adaptive procedure. Two of the intervals contain a reference stimulus and the third one contains the target stimulus. The reference has always a density of 20 *ripples per octave (rpo)* and the target initially has a density of 0.5 *rpo*. A one-up/one-down adaptive procedure runs with steps of 0.2 *rpo* until the subject cannot differenciate the target from the reference. Thresholds are given based on the average of the last six reversals and are expressed in terms of *rpo*. For this test, subjects also used their own processor and clinical map. Stimuli were presented in the same experimental conditions as for the speech recognition experiment (i.e. free field acoustic stimulation at a level of 65-dB SPL). After one first run of training with feedback, two additional runs were carried out without feedback and the outcome measure is given as the average of both runs.

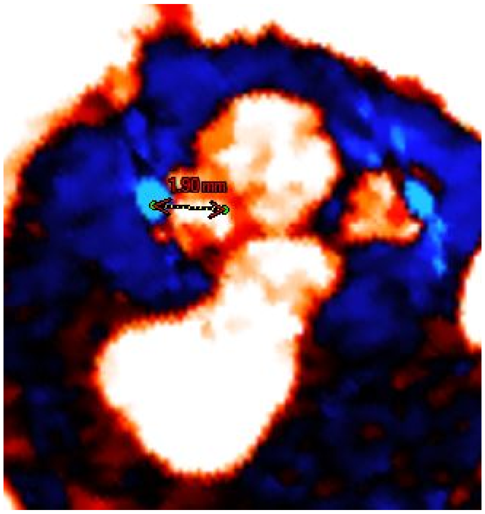

Figure 4.3: Sagittal-section view of a CT scan from subject S4.

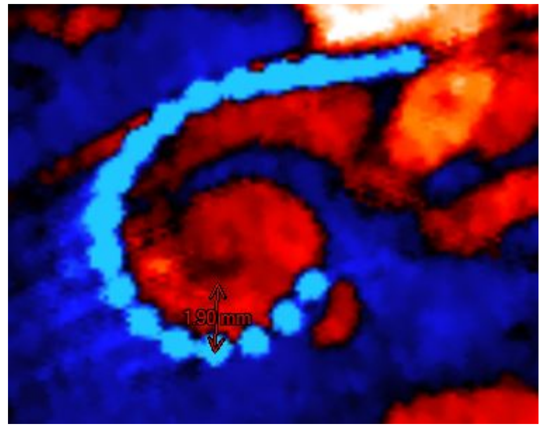

Figure 4.4: Transversal-section view of a CT scan from subject S4.

4.2.5 Electrode to modiolus distance

The cone beam CT scans ($125\mu m \times 125\mu m \times 125\mu m$ voxels) from 9 subjects (S1-2-21-4-5-7-8-11-17), were analyzed using Onis Pro software (v2.5 DigitalCore®, Co. LTD) in order to estimate the electrode-to-modiolus distance, (EMD). The location of the electrodes was assumed to be in the center of the contact artefact. This position was estimated using the 3D rendering of the multiplanar reconstruction. The EMD was then measured on a plane orthogonal to the modiolar axis and was defined as the radial distance between the electrode and the modiolar wall (see figure 4.4). When possible, the distance estimation was validated by measuring it in the sagittal plane (see figure 4.3). Since, in humans, SGCs are clustered in Rosenthal's canal, this measurement gives a first approximation of the distance between the electrodes and the SGCs. Unfortunately, the modiolar wall could not be identified in CT images from S7 due to a possible cochlear malformation. While this malformation had apparently no direct influence on the psychophysical results, its influence on the intracochlear electrical field was dramatic and will be discussed in chapter 5.

4.2.6 Session

T-levels, speech recognition test and SMRT were carried out in the same session lasting approximately three hours and organized as follows:

- Clinical impedance measurement with SoundWave software (Advanced Bionics®)

- C-level estimation for even (or odd) electrodes in randomized order, for three pulse shapes which were also randomly selected. Then T-levels estimation for all conditions

- Speech recognition test and SMRT

- C-level estimation for odd (or even) electrodes in randomized order for three pulse shapes which were also randomly selected. Then T-levels estimation for all conditions

- Clinical impedance measurement with SoundWave software.

4.3 Results

4.3.1 Detection thresholds

T-levels exhibited different patterns across subjects. Figure 4.5 displays individual T-level estimates for the three pulse shapes, expressed in dB relative to 1μA. One can note that several T-level patterns exhibit sudden and localized increase or decrease.

The effect of distance

Across the 8 subjects for whom Cone-beam CT scans were available, EMD estimates ranged between 0.13 and 2.27 mm. To analyze the *between-subject* variance in threshold, we calculated the mean threshold (across the array) and mean EMD (across the array) for these 8 subjects. For all three polarities, a significant positive correlation was found between the EMD and the detection thresholds ($p < 0.05$). This basic model enables to describe 63, 65 and 68% of the *between-subject* variance in thresholds for CA, ACA and CAC stimuli respectively. Figure 4.6 reports the variation of the mean threshold as a function of the mean EMD. Each symbol is for one subject.

For each subject, the EMD and the T-level patterns were then normalized by their mean value across the electrode array. This allowed us to remove the between-subject variance in threshold and in distance and to pool the data from all subjects together to perform a within-subject correlation analysis (Bland and Altman, 1995). Figure 4.7 represents the normalized thresholds as a function of the EMD for the three pulse shapes.

It results that on average, only 5.7% of the within-subject variance in threshold can be explained by the EMD ($p < 0.02$). This poor relationship may be due to small within-subject variability in EMD values. In other terms, for any given subject, the EMD was relatively constant across the electrode array but it could differ across subjects. For each subject, the difference in EMD between electrodes was smaller in our subject group (between 0.43 mm and 0.99 mm depending on the subject, 0.75 mm on average) than in Long et al.'s study (0.75mm to 1.45mm, 1.20mm on average). This discrepancy will be discussed in paragraph 4.4.

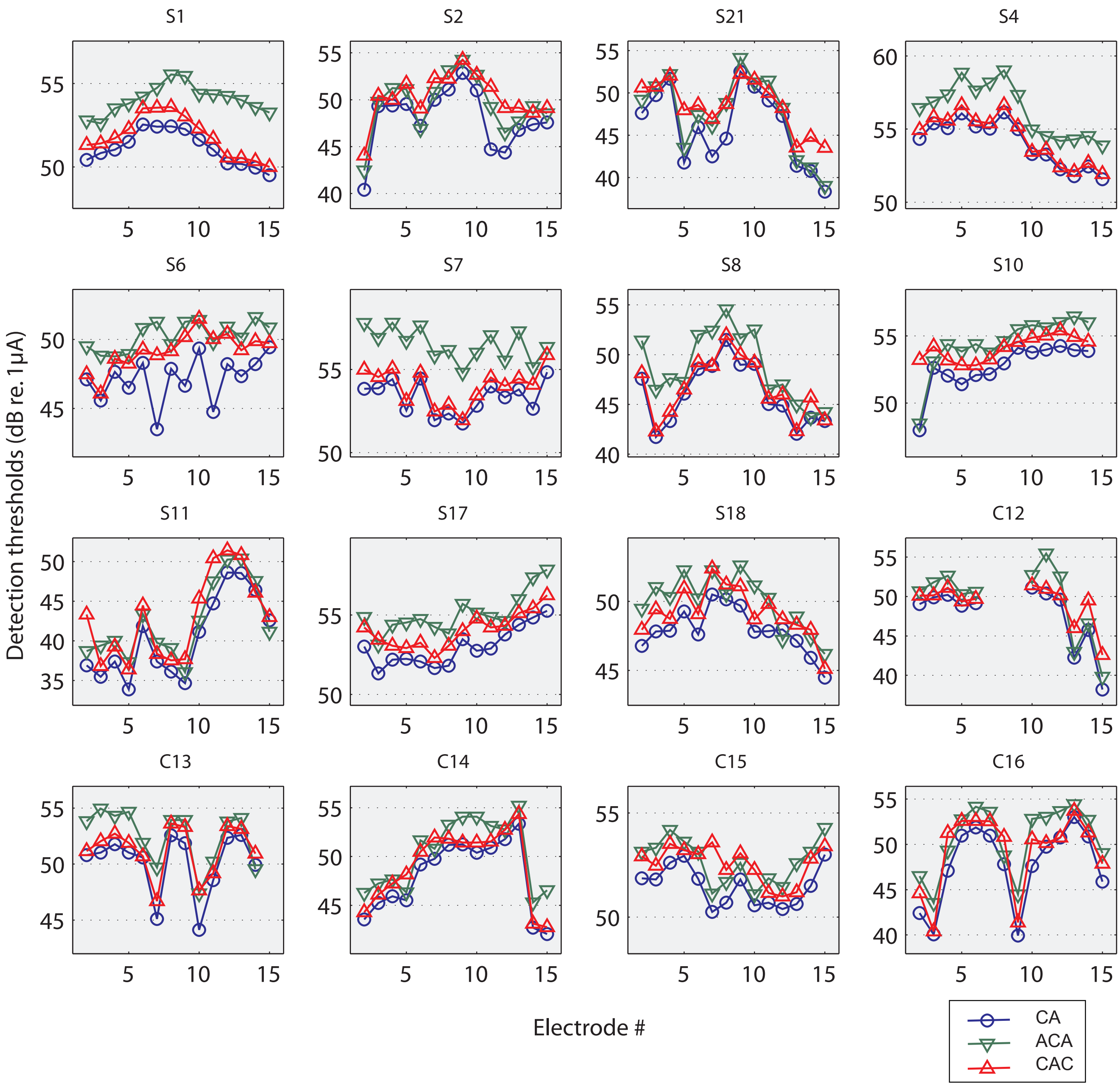

Figure 4.5: Detection threshold patterns in dB relative to 1 μA. Each panel is one subject. Blue circles represent CA stimuli, up-pointing red triangle represent CAC stimuli and down-pointing green triangles represent ACA stimuli.

Polarity effect

The ACA and CAC pulse shapes used in this experiment are supposed to reflect an effect of a polarity. Symmetric biphasic stimulation (CA) was used as a baseline as

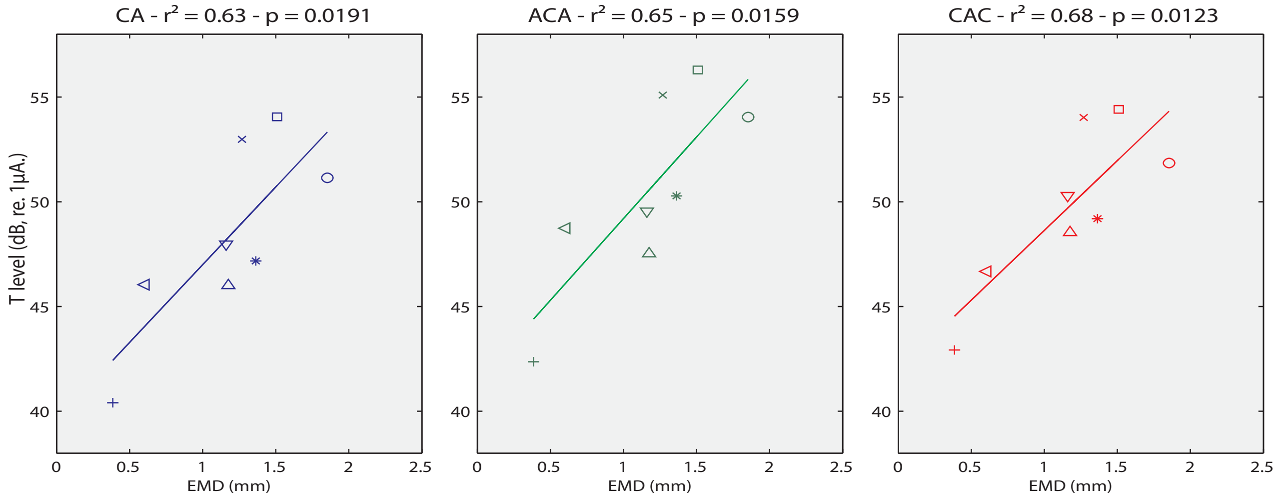

Figure 4.6: Mean detection threshold as a function of the mean EMD. Each symbol is for one subject. N=8

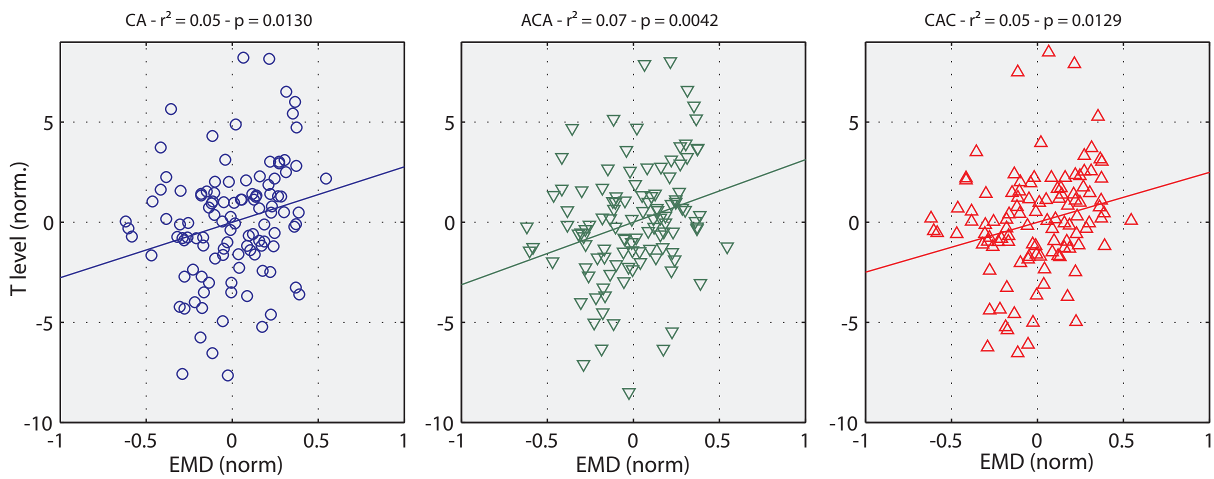

Figure 4.7: Normalized thresholds as a function of the normalized EMD. Each symbol is for one subject, N=8

both phases of this pulse are likely to initiate action potentials. As expected, CA-thresholds were always lower or equal to anodic (CAC) and cathodic (ACA) thresholds. The polarity effect was quantified as by calculating Δ_{C-A}, defined as the difference in dB between cathodic thresholds and anodic thresholds. As a result, negative values of Δ_{C-A} indicate that, for a given electrode, the cathodic threshold is lower than the anodic threshold. Figure 4.8 displays the individual across electrode patterns for Δ_{C-A}. We can note that overall, out of 219 electrodes, 48 yielded negative Δ_{C-A} (see figure 4.8).

If it is the case that cathodic stimulation preferentially generates action potentials at

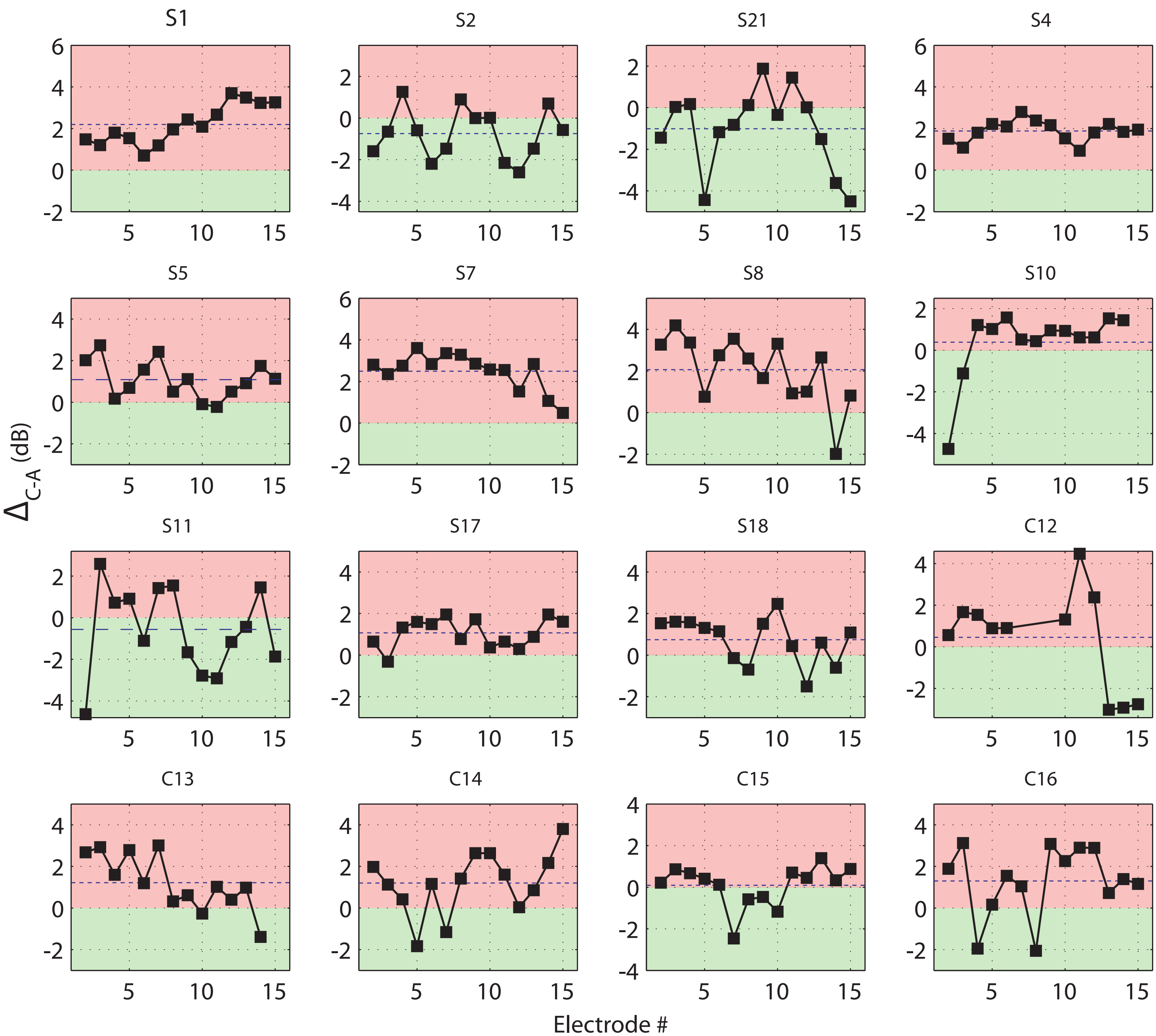

Figure 4.8: Difference between cathodic threshold and anodic threshold, Δ_{C-A} (dB).Red and green areas represent positive and negative difference respectively. Dashed lines represent the mean Δ_{C-A}.

the level of the peripheral processes, the negative Δ_{C-A} obtained for those 48 electrodes may indicate that peripheral processes are present and more likely to be stimulated for these specific electrodes. By extension, it may also mean that neural survival is overall better near these electrodes.

We would therefore hypothesize that both the EMD and Δ_{C-A} have an influence on T-levels.

Pearson's correlations revealed a significant but weak correlation between Δ_{C-A} and T-levels ($r^2 = 5.3\%, p = 0.015$) which indicates that Δ_{C-A} might also explain a small part of the within subject variance in thresholds (between-subject: $r^2 = 14\%, p = 0.36$).

To be able to conclude as for the contribution of EMD and Δ_{C-A} on T-levels, partial correlations were analyzed and the outcomes are reported in table 4.2. This confirmed the relationships of both the EMD and Δ_{C-A} with T-levels. Furthermore, the fact that the partial correlation $[EMD \times \Delta_{C-A}]$ controlling for the influence of T-levels was not significant suggests that both the EMD and Δ_{C-A} contribute to explain the across-electrode patterns of T-levels.

controlling for	*Variables*	*r*	*p*	*df*
EMD	$\Delta_{C-A} \times T-level$	0.209	0.027	109
Δ_{C-A}	$EMD \times T-level$	0.214	0.024	109
T-level	$\Delta_{C-A} \times EMD$	0.069	0.471	109

Table 4.2: Partial correlations statistics

4.3.2 Multilevel model (MLWin)

We have seen that both the EMD and the Δ_{C-A} might contribute to the variance in thresholds across the electrode array. To investigate the combined contribution of both parameters, we fitted our data using a multilevel regression model (with MLWin software, Rasbash et al. (2009)).

We first fitted the baseline model composed of a simple subject-dependent random intercept ($\beta_{0,subject} = 48.22(var.1.16), degree\ of freedom = 0$).

$$T_{subject,electrode} = \beta_{0,subject} \tag{4.1}$$

We then found that incorporating the distance improves significantly ($p < 0.001$) the estimation of thresholds ($\beta_{0,subject} = 44.9(var.2.14), \beta_{1,subject} = 3.89(var.1.97), degree\ of freedom = 1$).

$$T_{subject,electrode} = \beta_{0,subject} + \beta_{1,subject} \times EMD_{subject,electrode} \tag{4.2}$$

Then, adding the polarity effect enabled to further improve the model fit in a significant way ($p < 0.05$, see equation, where $\beta_{0,subject} = 44.94(var.2.08), \beta_{1,subject} = 3.64(var.1.90), \beta_{2,fixed} = 0.49(var.0.19), degrees\ of freedom = 2$).

$$T_{subject,electrode} = \beta_{0,subject} + \beta_{1,subject} \times EMD_{subject,electrode} + \beta_2 \times \Delta_{CA_{subject,electrode}} \tag{4.3}$$

The results of the multilevel model are therefore consistent with the partial correlation analysis.

4.3.3 Speech recognition and SMRT.

Word recognition scores ranged from 20% to 68% with an average score of 43.2% for French speaking participants and 66.6% for English speaking participants. The test/retest reliability, expressed in percentage of variation between the two lists, ranged between 0 and 24% (12% on average for French subjects and 7% for English subjects). Across the population of subjects, numerous factors might have affected speech recognition performance. For instance, subjects S10 and S11 performed very poorly in the speech recognition task which can probably be explained by the fact that S10 was prelingually deaf and implanted at the age of 49, while S11 had only 6 months of experience with the device after 34 years of auditory deprivation. For subject S17, the duration of deafness prior to CI was "only" 10 years. However, she reported a reduction in speech performance after reimplantation due to a device failure. In contrast, subject S5 who was one of the best performer was prelingually deaf but implanted before 6 years old. The scores for the SMRT carried out with all subjects ranged between 0.66 and 4.01 *rpo* with an average score of 1.84 *rpo*. Figure 4.9 reports the individual scores for both speech and SMRT tests. It is worth noting that the outcome of both tests were not correlated. This may relate to the fact that our population of subjects was more heterogeneous than in previous studies (Won et al., 2007).

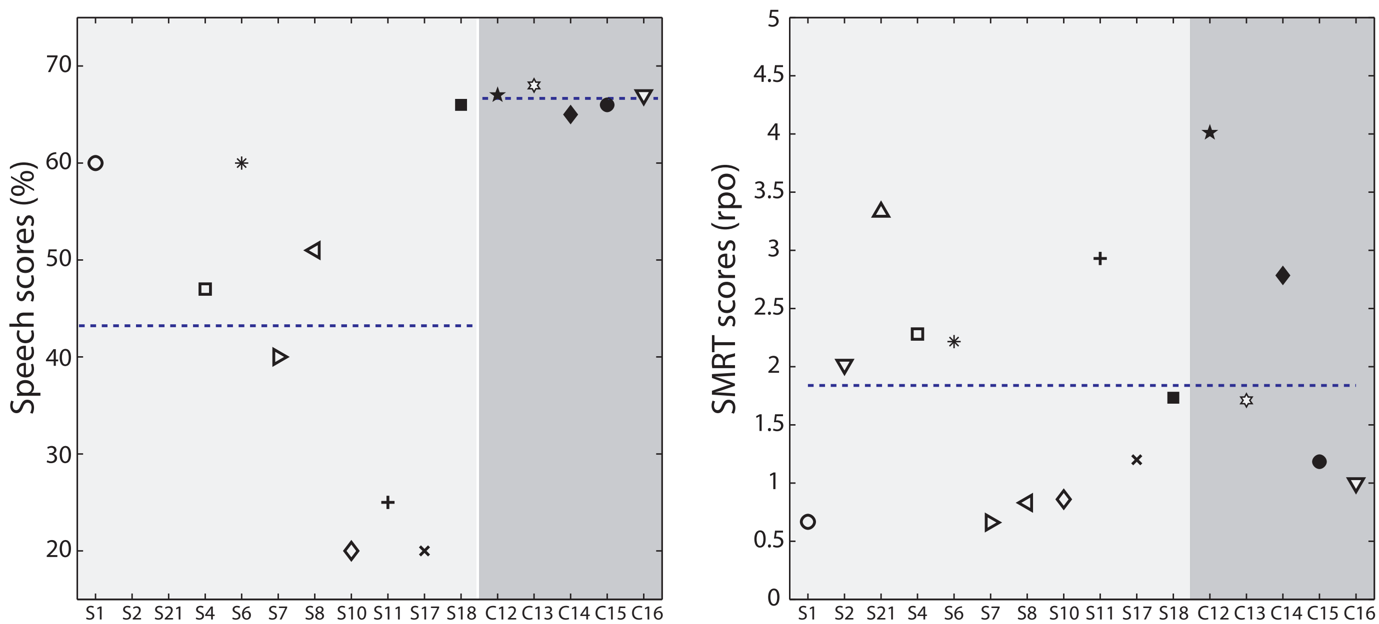

Figure 4.9: Left panel: individual speech recognition scores in percentage, dotted lines represent the mean score for the french speaking and english speaking subgroups. Right panel: individual SMRT scores in *rpo*, dotted line represents the mean score.

Contrary to previous studies by Pfingst et al. (2004) and Long et al. (2014), in the present data, the *within-subject* variance in thresholds was not correlated to the logit of speech recognition. Furthermore, rather counter-intuitively, the *within-subject* variance in thresholds was positively correlated to the SMRT scores ($r^2 = 0.38, p < 0.01$) which suggests that subjects with an important variance in thresholds tend to perform better in spectro-temporal modulation discrimination.

Long et al. (2014) reported that neither mean T-levels alone nor mean EMD alone predicted speech recognition scores. However, in their study, the root mean square error (RMSE) of the distance model was significantly correlated with the results of speech understanding. As a result, they proposed the RMSE as a metric for the prediction of CIs performance. For each subject, the RMSE to the global distance model presented in figure **??** was calculated. However, no such correlation was observed in the present study.

If, as suggested by the correlation between Δ_{C-A} and detection threshold, Δ_{C-A} relates to neural health, we would expect better performance in SMRT and Speech recognition when the mean value of Δ_{C-A}, referred to as $\bar{\Delta}_{C-A}$, is low. This mean value of $\bar{\Delta}_{C-A}$ may be seen as a global measure of neural survival across the electrode array. Figure 4.10 displays SMRT scores in *rpo* as a function of $\bar{\Delta}_{C-A}$. We can note that SMRT scores show a significant negative relationship with $\bar{\Delta}_{C-A}$ (Pearson correlation: $r^2 = 0.31$, $p < 0.05, N = 16$) which corroborates our hypothesis. In contrast, no such trend was observed between $\bar{\Delta}_{C-A}$ and speech recognition scores for none of the two groups of subjects.

This suggests that, first, speech recognition and spectral ripple sensitivity rely on different processes among which CI experience may play a major role (Blamey et al., 2013). Second, while the measure of Δ_{C-A} seemed to relate to neural survival, this is the first time this polarity effect is investigated as a correlate neural health. This result thus remains to be reproduced to confirm our hypothesis. Besides, to assess the robustness of this *global* measure of neural survival, the same analysis was carried with all possible combinations of even and odd subsets of electrodes (for 16 subjects, 216 permutations were possible). Overall 88% of the combinations yielded a significant correlation (p¡0.05) between SMRT scores and $\bar{\Delta}_{C-A}$. Even though this global polarity effect, $\bar{\Delta}_{C-A}$ removes the information of the across-electrode differences in Δ_{C-A}, this relationship seems relatively robust. Here again those results seem to corroborate the hypothesis that Δ_{C-A} relates to the level of neural survival.

4.4 Discussion and conclusion

The linear distance model could explain 65% of the between-subject variance in thresholds. However, the within-subject correlation between distance and threshold were much smaller, yielding an R-square value of only 5.7%. These relationships indicate that the distance to the modiolar wall (i.e. near where the neurons lie) has an influence on detection threshold which is consistent with several previous studies. However, in the present study its effect was limited at the individual level. This might arise from the fact that in Long et al. (2014) all subjects were users of the Nucleus® perimodi-

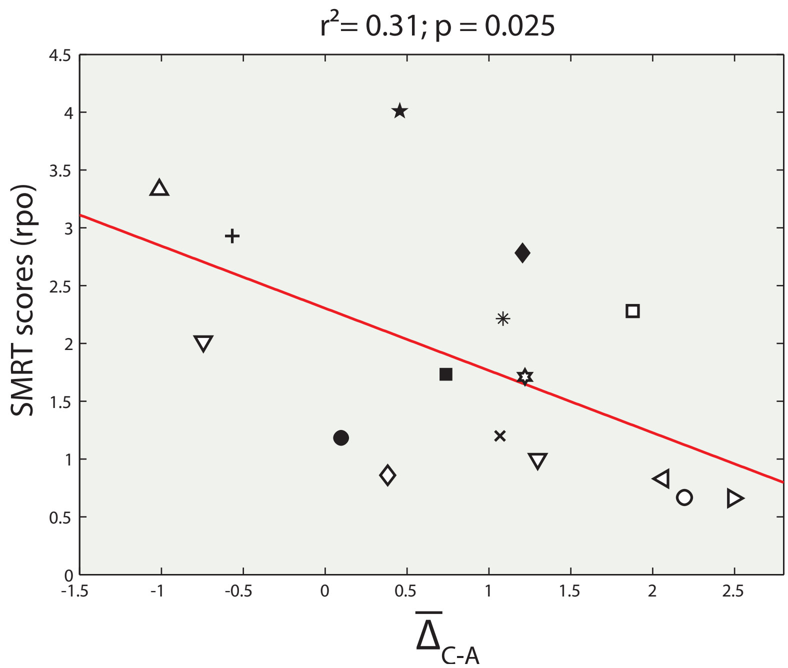

Figure 4.10: SMRT scores (in ripple per octave) as a function of the difference between cathodic threshold and anodic threshold (in dB). N=16

olar electrode array while in the present study, only S21,S8 and S11 were implanted with either a positionner or a mid-scala electrode array which theoretically result in a position of the array closer to the modiolus. Indeed, the effect of distance is likely to be greatest close to the electrode where electrical potential quickly decreases. In contrast, few millimeters away, electrical potential flattens and the effect of distance is no longer visible. Besides, we could not replicate the finding that speech scores correlate with the RMSE of the distance model. This might be due to the fact that Long et al. (2014) used a more advanced procedure for the estimation of the EMD which may have improved the relevance of the RMSE especially in the apical region where it is more difficult to localize the modiolar wall. First, the resolution of CT images was slightly poorer here compared to Long et al. (2014) ($125-\mu m$ cubic voxels versus $100\mu m$ in their study). Second, they had access to either pre-operative scans that are not affected by the electrodes' artifacts or a scalable cochlear model.

Speech test outcomes in the present experiment did not enable to replicate the findings of previous studies that speech performance is correlated with the within-subject variance in threshold. This may be due to the fact that our subjects group was heterogeneous compared to that of Long et al. (2014). In particular, speech tests were carried out with subjects' own processor and stimulation settings and their experience with their device varied from 0.5 to 15 years. In contrast, in Long et al. (2014), all speech recognition tests were carried out at 12 months post-activation and using the same external processor providing the exact same stimulation strategy (MP ACE). This might have dramatically reduced the number of subject-specific parameters that may potentially influence speech recognition.

The subjects/electrodes tested in this study exhibited a marked polarity effect. Absolute values of T-levels showed a higher sensitivity to anodic stimulation for 78% of tested electrodes. While previous studies in humans reported a higher sensitivity to anodic stimulation almost exclusively at C-level (Macherey et al., 2006), the present results extend these findings at threshold level.

Several hypotheses have been proposed to explain this higher sensitivity to anodic stimulation. At threshold, the main factor may be related to the level of degeneration of the peripheral processes as previously stated (Rattay et al., 2001) or to their level of demyelination as suggested by Rattay (1999). However, the present results are in accordance with previous studies showing that even when cathodic threshold are lower than anodic threshold due, possibly, to the presence of healthy peripheral processes, this difference tends to disappear at higher current levels. This phenomenon might be partly explained by investigating electrical stimulation at the level of a single neuron. The activating function (Rattay, 1989) represents the pattern of polarization of a single neuron in response to electrical stimulation. In this simple model, cathodic stimulation creates a main lobe of depolarization responsible for the generation of action potentials and two side lobes of hyperpolarization while anodic stimulation produces the opposite pattern. Based on this theory, the presence of the side lobe of hyperpolarization located more centrally might disturb or even prevent the propagation of action potentials along the fibers and through the cell body in the case of cathodic stimulation. This phenomenon, referred to as *cathodal block*, illustrated in figure 4.11 was predicted by a computational model of the guinea pig cochlea (Frijns et al., 1996). Recently, Macherey et al. (2015) observed a possible psychophysical correlate of this cathodal block in a group of human CI users. In their study, loudness growth functions were accurately measured using quadraphasic pulses which yield similar polarity effect as the triphasic pulses used in the present experiment. Using cathodic quadraphasic pulses, loudness ranking sometimes revealed a non-monotonic loudness growth function which never occurred with anodic quadraphasic pulses. This unexpected outcome was attributed to the cathodal block.

Herein, the procedure used to obtain the C-levels seemed to reveal several non-monotonic loudness growth functions (at least 28 out of 205). Indeed, some CI patients reported a clear decrease in loudness with an increase in the stimulating current. As for Macherey et al. (2015), these non-monotonic loudness growth functions only occurred with cathodic pulses (triphasic ACA).While the exact understanding of this phenomenon remains unclear, these non-monotonic loudness growth functions seem to be more frequent than expected. Although they only represent 12.8% of the present data, it is possible that either some subjects did not report it because they thought they misjudged previous sounds or the current step was too large to make it clearly emerge.

The difference between cathodic and anodic thresholds, Δ_{C-A} was assumed to reflect the degree of degeneration of peripheral processes. In particular, high values of

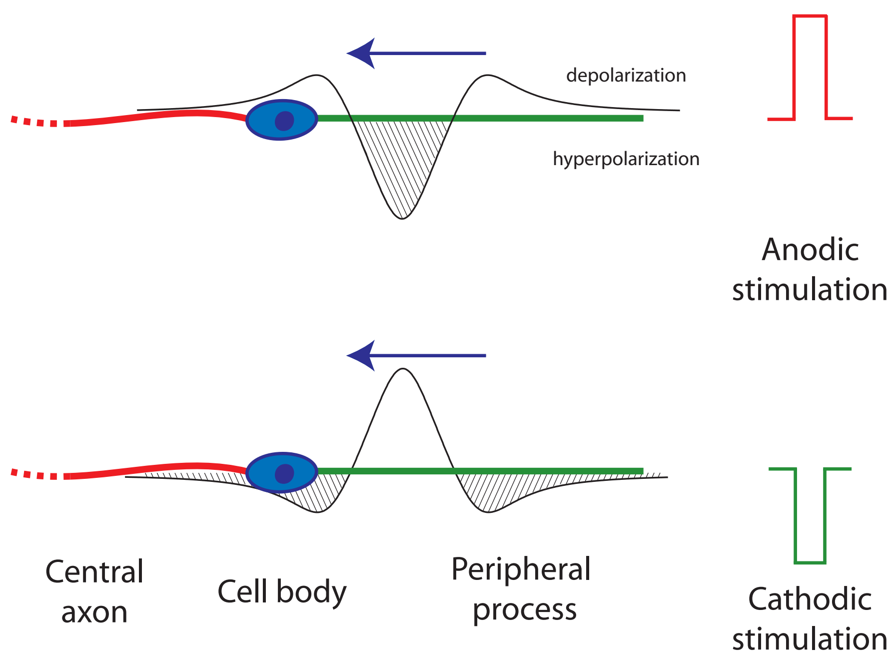

Figure 4.11: Schematic illustration of the cathodic blocking phenomenon. Dashed areas represent hyperpolarization

Δ_{C-A} may relate to a place where peripheral processes cannot be stimulated or are degenerated. Interestingly, SMRT scores and $\bar{\Delta}_{C-A}$ showed a significant negative relationship.

Even though only 31% of the variance of SMRT scores could be explained by $\bar{\Delta}_{C-A}$, this may suggest that Δ_{C-A} relates to neural survival. This idea was strengthened by the analysis of partial correlations, which suggest that both EMD and Δ_{C-A} play a role in neural responsiveness, as well as by the multilevel model analysis which demonstrated the significant contribution of both parameters in the description of detection thresholds variations. On the other hand, our findings have to be tempered by the counter-intuitive positive relationship between the across-electrode variance in threshold and the SMRT scores which is inconsistent with previous studies. Besides, even though we found that both the EMD and the polarity effect might contribute to explain this variance in threshold, the correlations were weak. Additional factors still need to be identified to better explain those results, these might for instance include the amount of fibrosis and/or ossification.

CT-scan analysis only enabled to estimate the distance between the electrodes and the modiolar wall. A higher resolution might have enabled to measure not only the EMD but also the distance to the osseous spiral lamina. This distance may better represent the location of existing peripheral processes. In this case it would have been interesting to test the *distance model* first, between the EMD and anodic thresholds and, on the other hand, between the distance to the OSL and cathodic thresholds.

Although further investigation is required to strengthen the observation made in the present study, Δ_{C-A} might provide an indirect measure of the distribution of neural survival along the electrode array. Being able to picture the places where healthy neurons lie would be extremely beneficial for the optimization of stimulation strategies. In particular, current focusing and current steering techniques using multipolar strategies have been investigated in the past to create spatially selective virtual channels and thus improve spectral resolution (Berenstein et al., 2008; Bonham and Litvak, 2008). While it was demonstrated that the locus of excitation might be slightly translated by manipulating the amplitude of different electrodes, the benefits in terms of speech recognition were poor or inconsistent across studies and/or subjects. Δ_{C-A} might provide relevant information to further improve such strategies. It might be used to select specific electrodes in order to target regions of the cochlea where the neural population is expected to be healthy. However, this would also require a good understanding of electrical diffusion in the implanted ear which is investigated in chapter 5.

Acknowledgments

We sincerely thank Alan Archer-Boyd, Bob Carlyon and John Deeks (MRC CBU), Debbie Vickers (UCL), Jean-Pierre Piron and Marielle Sicard from the University Hospital of Montpellier, and CI participants for their work. This work was partly funded by Advanced Bionics.

Chapter 5

Perspectives for an Optimized Multipolar Strategy: in vitro and in vivo study

In this study we evaluate different ways to improve the spatial selectivity of the electrical field produced by a cochlear implant using multipolar stimulation. We show, in vitro, the possibility to achieve current focusing using a multipolar stimulation based on recordings at the level of the electrodes. This finding was corroborated in one CI user by a psychophysical metric of channel interactions. However, the efficiency of multipolar stimulations might be improved by considering the voltage distribution at the level of the neural fibers.

Electrical field recordings were carried out both in vitro and in vivo to better understand the dominant factors of the electrical diffusion in the implanted ear in order to propose a method to infer the voltage at the modiolus based on recordings on the electrodes. Our results suggest that the electrical field produced by a single electrode can be divided in two distinct regions. In a far field region (more than 2 mm away from a stimulating electrode) the across-subject differences mainly arise from an amplitude offset due to differences in the access resistance of the stimulating electrode. The normalized patterns were very consistent across subjects despite possible electro-anatomical differences. We observed a significant influence of the direction of propagation along the scala tympani. Here again the decay rate patterns were very consistent across subjects, and suggested that the asymmetry of the electrical field in the cochlea is due to a dominant current pathway towards the base. However, in this far field region the estimations of the voltage at the electrodes could provide a reasonable approximation of the voltage at the modiolar wall. In the near-field region, in the vicinity of the stimulating electrode, numerical models may be necessary to provide a relevant estimation of the voltage at the modiolar wall. The analysis of electrical field imaging in the implanted cochlea suggested that, in this restricted near-field region, (1) the electrical field can be considered as symmetrical in the longitudinal direction and (2) the cross section of the scala tympani can be considered as constant along the array. Such assumptions may reduce the number of parameters of such numerical models.

5.1 Introduction

The wide electrical field produced by the activation of an intracochlear electrode, using the commonly-used monopolar (MP) stimulation mode, is responsible for channel interactions which deteriorate the transmission of sound information, as seen in chapter 2. The Phased-Array strategy (PA) proposed by van den Honert and Kelsall (2007) is the most advanced multi-electrode technique available to narrow the electrical spread along the cochlea and target a restricted neural population. Unfortunately the original strategy suffers from several limitations which have already been exposed in the previous chapters.

The study presented in Chapter 3 tackled some of the main issues of this strategy. Transimpedance measurements together with the contact impedance model enable to fully estimate the impedance matrix, Z, with a satisfying accuracy for all patients. Using this matrix, the original inverse problem of the PA algorithm (equations 5.1) can be solved to define the weights to be applied to each electrode to achieve a highly focused electrical field, V_d. However, the elements of the matrix Z are inferred from transimpedance measurements on the electrodes. As a result, the solution of the inverse problem theoretically enables to compensate the current spread in the longitudinal dimension and thus to focus the electrical stimulation at the level of the electrode array.

$$\begin{cases} Y = Z^{-1} \\ W = \begin{bmatrix} \vdots \\ 1/y_{p,p} \\ \vdots \end{bmatrix} \cdot \begin{bmatrix} \ddots & y_{1,p} & \\ & \vdots & \\ & y_{16,p} & \ddots \end{bmatrix} p = 1:16 \\ Ie = W.V_d \end{cases} \tag{5.1}$$

In chapter 4, we highlighted the fact that detection thresholds quickly increase with the distance separating the electrode from the neural fibers in Rosenthal's canal (approximately 6 dB/mm in partial tripolar stimulation). Furthermore, previous results in accordance with Long et al. (2014) suggest that the slope of this linear relationship is larger with focused stimulation than with MP. This trend might be partly explained by the fact that spatially focused strategies, by definition, generate electrical fields with a steep decay in the vicinity of the stimulating electrode. If one considers an order of magnitude for the electrode-to-modiolus distance (EMD) of approximately 1 mm, the electrical field might be dramatically reduced at the level of the auditory nerve.

With the PA strategy, Long et al. (2014) reported detection thresholds between 0 and 20 dB higher than with MP stimulation. Even though, computational model studies (Frijns et al., 2011; Kalkman et al., 2015) suggested that the PA strategy might produce more narrow neural excitation pattern than MP stimulation, in CIs, the need to increase the stimulation level has been thought to reduce the spatial selectivity of the stimulation. The EMD can also vary between subjects and within subjects for different electrodes. As a result, the electrical field produced at the level of the electrodes might not yield the expected neural excitation pattern. This radial spread from the electrode array to the place where the neural fibers lie has been pointed out as one possible limitation of the PA strategy (Smith et al., 2009).

Early studies by Townshend and White (1987) and von Compernolle (1985) already introduced the need to create a focused electrical stimulation at the level of the nerve fibers to induce an efficient neural stimulation. In order to design efficient stimulation strategies, it is necessary to take into account both the longitudinal and radial voltage spread. However, because of the complexity of the cochlea, the three-dimensional diffusion of electrical potential remains unpredictable and is still the topic of current research projects.

Different approaches have been used in the past to study the electrical spread in the cochlea. Computational models (finite elements or boundary elements models) rely on accurate descriptions of both the structure of the inner ear and the resistivity of different biological materials (Briaire and Frijns, 2000; Hanekom, 2001; Frijns et al., 2011; Kalkman et al., 2014, 2015; Malherbe et al., 2015). Such models provide information on the 3D distribution of the electrical potential and can thus be coupled to neural models to predict the pattern of neural excitation. However, they necessarily rely on numerous assumptions on the electrical properties of the cochlea. For instance, most numerical models rely on tissues and bone resistivity estimations from animal studies (Suesserman, 1992). Besides, the different complex compartments of the living cochlea such as the porous bony structure or neural aggregates in the Rosenthal's canal can only be modeled by homogeneous media. Furthermore, it is not always possible to have access to individual high-resolution cochlear geometries in order to implement subject-specific models .

Another approach consists in considering simplified configurations in which an analytical solution can be expressed. For instance, several early studies modeled the electrical diffusion in the inner ear using lumped-parameters models (Suesserman and Spelman, 1993b; Jolly et al., 1996; Kral et al., 1998), while others proposed an analytical description of the current spread produced by point-source electrodes in an infinite or semi-infinite medium (Litvak et al., 2007; Goldwyn et al., 2010). While limited by the hypothesis that they require, such simple models offer an easier control on the number of parameters and may facilitate the interpretation of the results.

The aim of the present chapter is to further investigate the diffusion of electrical stimuli for both fundamental and practical interests. In vitro and in vivo recordings were carried out using the same cochlear implant device (HiRes 90k) to identify the main factors influencing the electrical field produced by a cochlear implant.

Based on those recordings we attempt to describe the electrical diffusion both along the scala tympani (ST) and radially from the electrode to the nerve fibers. A better knowledge of the diffusion of electrical stimuli produced by the implant might provide valuable insights for further optimization of stimulation strategies. In particular, being able to handle the electrical pattern at the level of the modiolar wall, where the remaining neural fibers supposedly lie, would represent a significant improvement of the original strategy.

5.2 Methods

5.2.1 Device specifications

The present experiments were all carried out with the HiRes 90k device (Advanced Bionics ®) connected to the HiFocus 1J electrode array. This electrode array consists of a silicon carrier with 16 recessed rectangular contacts ($0.5 * 0.4 mm^2$ surface) spaced by 1.1 mm (see description in appendix 7.3).

5.2.2 In vitro experimental setup for electrical field recording

An in vitro setup was designed to investigate the electrical field diffusion in a controlled environment. The stimulating section was identical to the setup used in Chapter 3. Stimuli were monitored using the Bionic Ear Data Collection System (Litvak, 2003) and custom Matlab interfaces. Stimuli were 1-kHz sinusoids with an amplitude of 1-mA.

Electrical field recordings were made by measuring the voltage between the wire mesh and a custom electrode. The tip of the electrode was made of a 75-μm diameter platinum wire soldered to a shielded cable. The position of the recording electrode and the cochlear implant could be adjusted in three dimensions using a micro-manipulator.

The acquired voltage signal first passed through the pre-amplification stage of a SR830m lock-in amplifier (Stanford Research Systems, SRS Inc. CA) and was then sent to the input stage of a digital storage oscilloscope (LeCroy WaveRunner 6 Zi). The voltage measure was defined as the amplitude of the voltage waveform averaged across 100 traces. The synchronization of stimulation and recording as well as data transfer was made using a TCP/IP connection. Stimulating and recording chains are illustrated in figure 5.1.

In the following paragraphs we consider the electrode array located along $\vec{x}, y = z = 0$ in the Cartesian system of coordinates represented in figure 5.1.

5.2.3 Electrical recordings in the implanted ear

Electrical field recordings were carried out in eight adult CI users of the HiRes 90k device (see table 3.1 in Chapter 3). The entire transimpedance matrix was obtained for all stimulating-recording pairs of electrodes and for all subjects. Electrodes were activated in MP mode and stimuli were 50-μA anodic-first biphasic pulses with a phase duration of 100-μs. The voltage waveforms were recorded between intracochlear electrodes and the case ground electrode, averaged across 30 traces. The amplitude was defined as half the peak-to-peak amplitude and finally normalized by the input current amplitude.

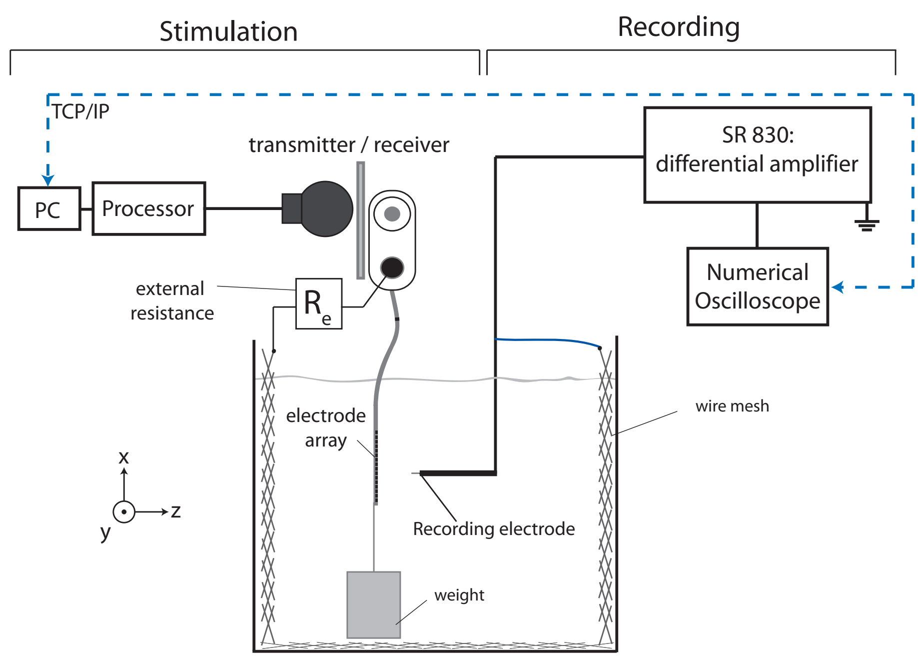

Figure 5.1: Experimental in vitro setup for electrical field recording.

Some transimpedance recordings were distorted by the partial polarization phenomenon observed in chapter 3. To provide relevant spread patterns, impedance values were extracted from distorted waveforms by fitting a partial polarization model (appendix 7.4.2).

Contact impedances were recorded with anodic-first biphasic pulses stimuli with an amplitude of 50-μA and a phase duration of 35.92-μs. All recordings were made using the up-sampling procedure described in section 3.2.5. The access resistance was then estimated using the contact impedance model previously presented. For more details, see Chapter 3.

5.3 Electrical field diffusion in vitro

5.3.1 Monopolar stimulation

In vitro experimental setups enable to study the electrical field produced by the CI in a controlled ideal environment (Ifukube and White, 1987; Kral et al., 1998; Ho et al., 2004). The present setup is considered as equivalent to a homogeneous infinite medium with a resistivity of 55 $\Omega.cm$. However, one important difference between the present setup and most of those described in the literature is that the electrical current was applied by the actual current sources of the implant and not external stimulation devices.

Figure 5.2 represents the recorded voltage distribution, resulting from the MP stimulation of a single electrode (electrode 8 in the middle of the array) and recorded along the $\vec{x}$ axis for $y = 0$ and at three different radial distances z, 200, 500, and 800 μm.

To describe the electrical field produced in the present conditions we consider that the silicon carrier is perfectly insulating. This configuration is thus equivalent to a single-side exposed electrode in a semi-infinite medium. To account for the finite dimensions of the electrode we consider that the voltage at the surface of the stimulating electrode is given by the voltage produced by a point source electrode at the surface of a sphere with a radius a. Voltage distributions could be fitted with the theoretical expression given in equation 5.2 (ρ is the resistivity of the surrounding medium in $\Omega.cm$, I is the electrical current amplitude, dc is the offset voltage). Figure 5.2 displays both the recorded patterns and the fitted curves (solid lines).

$$V = \frac{\rho.I}{2\pi.\sqrt{x^2 + z^2 + a^2}} + dc \tag{5.2}$$

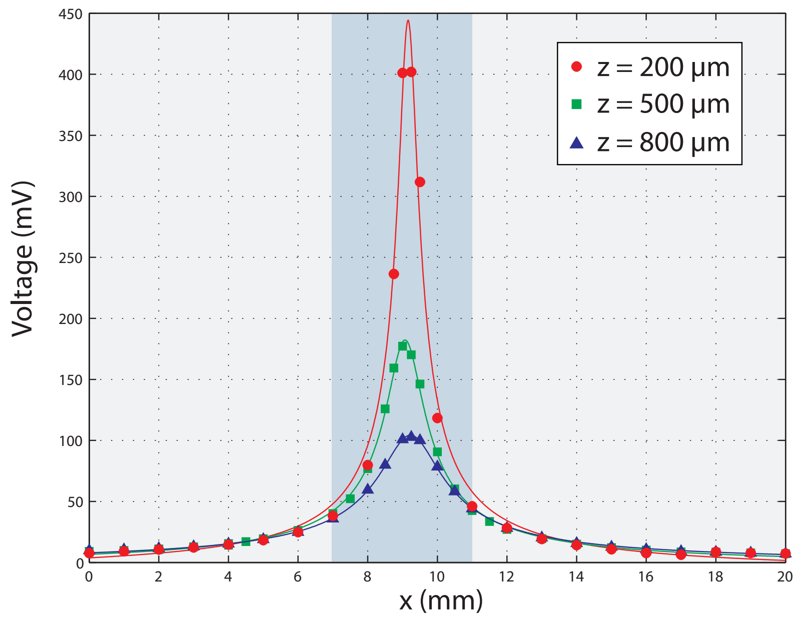

Figure 5.2: Electrical potential fields produced by monopolar stimulation in vitro, measured at z =200, 500, and 800 μm. The shaded area illustrates the near-field region where the radial distance has a major influence.

Overall, experimental data were in good agreement with the model. For $z = 500$ μm and $z = 800$ μm, data could be accurately described with this expression ($r^2 > 0.99$ and *root mean square error*, RMSE = 3.43 and 2.23 mV respectively) all along the $\vec{x}$ axis and the estimations of the resistivity, ρ, were 58 and 62 $\Omega.cm$ respectively, which is consistent with the actual resistivity of the solution measured with a conductimeter, 55 $\Omega.cm$. Additional recordings along the radial axis $\vec{z}$ (not shown here) could also be described using the same theoretical expression. We can however note that for the closest radial distance $z = 200$ μm, the recorded pattern was slightly steeper than $1/r$ model decay (RMSE = 19.84 mV), in the vicinity of the electrode. This might relate the influence of a non-uniform charge density profile above the electrode due to the straight recess in the silicon carrier (Suesserman et al., 1991) or the perturbation of the electrical field induced by the presence of the recording electrode.

Interestingly, in this free field environment, one can distinguish a *near field region* (illustrated by the shaded area in figure 5.2) and a *far field region* along the electrode array. In front of the stimulating electrode, the radial distance has a major influence on the voltage amplitude. However, as one moves away from the stimulating electrode in the apical and basal directions, current lines become more and more parallel and the influence of the radial distance between the array and the recording electrode progressively diminishes. As a result, in the present experiment, approximately 2 mm away from the stimulating electrode, voltage patterns are no longer dependent on z, which corresponds to a far field condition where current lines can be considered as parallel to the electrode array.

5.3.2 Multipolar stimulation

A second aim of the present experiment was to assess the efficiency of multipolar focusing in vitro. The transimpedance matrix was first measured following the methods described in section 5.2.3. Electrode current weights were then calculated following the procedure described in van den Honert and Kelsall (2007) (equations 5.1). As shown in figure 5.2, in free field conditions, the electrical voltage quickly decreases along the array resulting in flat transimpedance patterns. In these conditions, the extrapolation of contact impedances as proposed in the *original* PA strategy is inappropriate to estimate the diagonal terms of the impedance matrix and would highly underestimate the actual peak values yielding inconsistent current weightings. As a result, the strategy based on the estimations of the access resistance (R_a) using the contact impedance model, was implemented here and referred to as the *Contact Phased Array* strategy (CPA). Figure 5.3 displays the electrical field produced by the CPA strategy and measured along the electrode array using the same experimental conditions as previously described.

In those conditions, current focusing was efficiently achieved with a nearly perfect cancellation of the electrical spread each side of the stimulating contact. However, further away a marked negative lobe emerges around $x \approx 17mm$ corresponding to the location of electrode 15. This might be explained by the fact that the weight attached to the extremity of the array could not perfectly compensate for the curvature of the silicon carrier, especially at the base, where the silicon carrier is slightly larger than at the apex. As a result, the distance between the recording and stimulating electrodes might be smaller than in the middle of the array.

To assess the spatial selectivity of both MP and CPA stimulations in the present configuration, the width (in mm) of the electrical patterns was measured 10 dB below the maximum (W_{10dB}, as in Kral et al. (1998)) and the results are reported in table 5.1. Figure 5.4 displays the normalized voltage patterns for MP and CPA stimulations for the smallest and largest radial distances.

Kral et al. (1998) recorded the voltage pattern produced by MP stimulation in com-

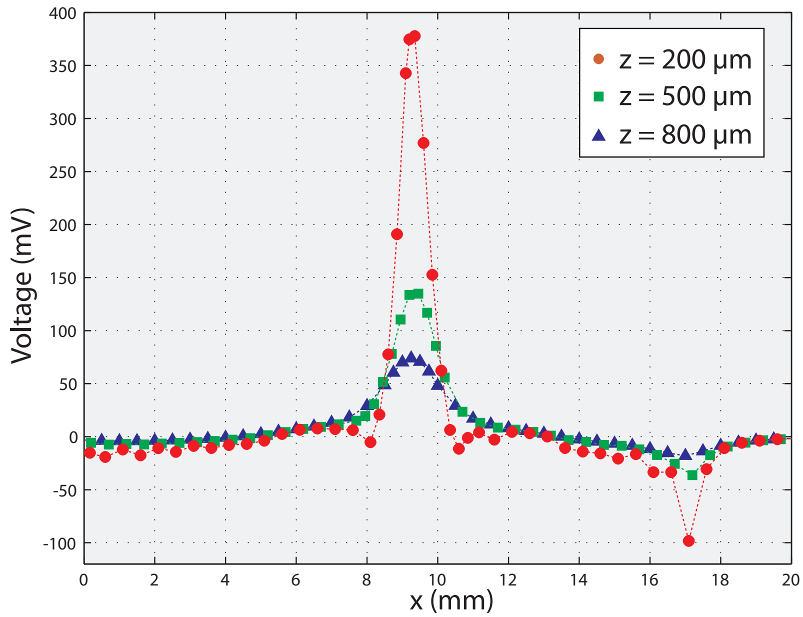

Figure 5.3: Electrical potential fields produced by the Contact Phased Array stimulation of channel 8, measured at 200 (red), 500 (green), and 800 μm (blue)

parable experimental conditions with the Nucleus-22 electrode array (Cochlear ltd.). Their estimation of W_{10dB} at a distance of 200 μm was 3.6 mm while it is only 1.74 mm in the present experiment. Under the assumption of linearity, this difference in the voltage spread cannot be explained by differences in the current amplitude or the resistivity of the solution (100 μA and 62.5 $\Omega.cm$, respectively in Kral et al. (1998)). It might however be explained by the larger available surface of ring-shaped electrodes of the Nucleus-22 device ($\approx 0.47\ mm^2$ vs. 0.2 mm^2 for the HiFocus 1J).

The CPA pattern yielded smaller W_{10dB} than MP stimulation, for all three radial distances. However, the present conditions were very specific. In particular, the fact that the impedance matrix was strongly dominated by its diagonal means that low compensating currents were required to efficiently reduce the lateral spread and limit the attenuation of the main peak. As we will see, in vivo, the wider electrical spread produced by MP stimulation implies higher compensating weights on the flanking electrodes. We could thus expect the presence of more fluctuations off-site and much lower voltage amplitude compared to MP stimulation.

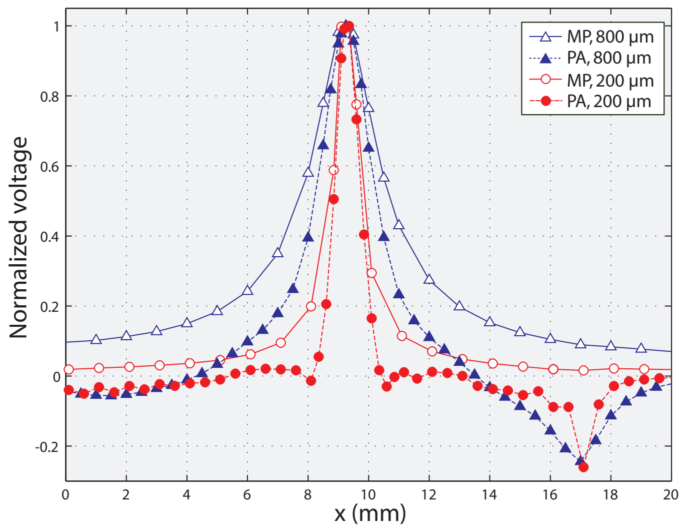

Figure 5.4: Normalized electrical potential fields produced by MP (empty symbols) and CPA (filled symbols) stimulation measured at 200 (red curves), and 800 μm (blue curves).

	W_{-10dB}	
z(μm)	MP	CPA
200	1.74	1.2
500	3.01	2.04
800	4.97	2.95

Table 5.1: W_{10dB} in mm for MP and CPA stimulation.

5.4 Analyzing intra-cochlear recordings

As shown in chapter 3, CI devices offer the opportunity to record the voltage distribution in the implanted ear along the longitudinal dimension (also called EFI for *Electrical Field Imaging*). With the present device this measure gives a discrete description of the electrical decay, on 16 data points spaced by 1.1 mm. Those data enable to, first, visualize and quantify the actual voltage distribution in one specific implanted cochlea and, second, evaluate different models of electrical diffusion based on subject-specific information.

We have seen in vitro that in a homogeneous medium, the voltage distribution generated by the activation of an electrode follows a $1/r$ law. In contrast, intracochlear recordings cannot be described by the same theoretical law. It is often admitted that the electrical diffusion in the human inner ear is affected by two main factors: the geometry of the cochlea, detailed in the General Introduction and the electrical properties of the biological tissues resulting in very specific patterns.

Herein we review and explore different ways to analyze electrical recordings made with each CI participant to better understand and discuss the dominant factors of electrical diffusion. In the perspective of developing a method for a subject-specific optimization of the electrical stimulation, individual data were carefully analyzed. In particular, we will see that S7 represents a interesting clinical case.

5.4.1 Descriptive models

5.4.1.1 Exponential decay

Several early animal studies investigated the electrical diffusion in the implanted ear and modeled it by a leaky transmission line (Suesserman and Spelman, 1993b; Jolly et al., 1996). It was observed that the voltage distribution along the ST could be qualitatively described with decreasing exponential curves.

More recently, several studies fitted EFI data recorded in CI patients with the expression given in equation 5.3 (Berenstein et al., 2010; Vanpoucke et al., 2012). As a matter of comparison, a comparable approach was used here for electrodes 5 to 12. As in Berenstein et al. (2010) different length constants were considered in the apical (λ_{apex}) and basal (λ_{base}) direction, while the extrapolated amplitude A and the offset dc were common in both directions. Estimations were made using the $fminsearch$ algorithm (Matlab).

Figure 5.5 displays a subset of EFI patterns measured in one CI patient and the fitted exponential curves. Peak values of the EFI data are obtained using the contact impedance model introduced in Chapter 3 but were not taken into account in the estimation of parameters. One can note that this approach yields very low peak voltage estimations, and is comparable to the linear extrapolation method proposed by van den Honert and Kelsall (2007). The goodness of estimation was assessed by the sum of squares of the residual error (SSE) which was 0.020 $k\Omega$ on average across all CIs and all electrodes.

$$V = A * e^{-\frac{x}{\lambda}} + dc \tag{5.3}$$

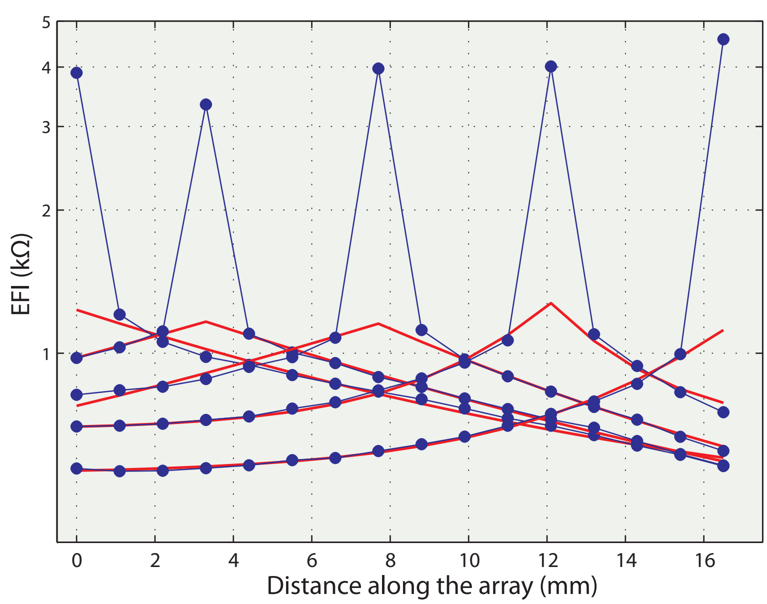

Figure 5.5: EFI patterns measured in S2 (blue dots) and exponential fitting curves (red solid lines) as a function of longitudinal distance in mm, .

Table 5.2 reports the estimated length constants in both the apical and the basal direction for electrode 8 in the middle of the array and for each subject . The order of magnitude of both λ_{base} and λ_{apex} were consistent with the findings of Berenstein et al. (2010).

Subject	S1	S2	S3	S4	S5	S6	S7	S8	Mean
λ_{base}	2.13	8.55	11.29	1.42	16.77	12.96	0.30	2.80	7.03
λ_{apex}	2.71	12.10	16.00	1.40	18.38	17.11	0.24	3.37	8.92

Table 5.2: Length constants estimations in mm obtained from the exponential fit for electrode 8.

Vanpoucke et al. (2004b) pointed out that, even though the slopes of fitted exponential curves seem related to the electrode position, such a model only enables to describe the voltage spread qualitatively. The estimations of length constants cannot be related to the electro-anatomical properties of the inner ear, the interpretation of $\lambda_{apex/base}$ is thus unclear. Moreover, we can see that such a model is unable to fit the electrical decay in the vicinity of the stimulating contact.

5.4.1.2 Two horizontal layers: Ratio of resistivity

Previous numerical models suggested that the presence of a high contrast of resistivity between the perilymph and the bony structures of the cochlea is responsible for the electrical voltage spread along the ST. Whiten (2007) highlighted the importance of the ratio of resistivity between inner ear fluids and the surrounding bone. They suggested that a ratio of approximately 1:100 was appropriate to describe experimental psychophysical measurements. A comparable value is thus often used in computational models with a perilymph resistivity around 70 $\Omega.cm$ and a bone resistivity of approximately 7000 $\Omega.cm$. In a similar way, recent numerical models attempted to find the optimal ratio that could best explain either voltage distribution or neural excitation patterns recorded in human (Kalkman et al., 2014; Malherbe et al., 2015).

Herein we attempt to describe intracochlear recordings using a very simple model geometry. We first assume that the silicon carrier of the present electrode array has an infinite resistivity. To focus on the presence of a contrast of resistivity while neglecting the complex cochlear geometry, we thus consider a semi-infinite medium with two plane layers of different resistivities, ρ_1 and ρ_2. The first layer, in contact with the electrode array models the conductive cochlear fluid while the second medium represents the modiolar bone. As presented in Telford et al. (1990), with this model geometry, and considering point-source electrodes it is possible to compute the voltage distribution in the first medium using an infinite sum of image current sources. Figure 5.6 represents the model geometry and equation 5.4 gives the expression of the voltage in the first medium.

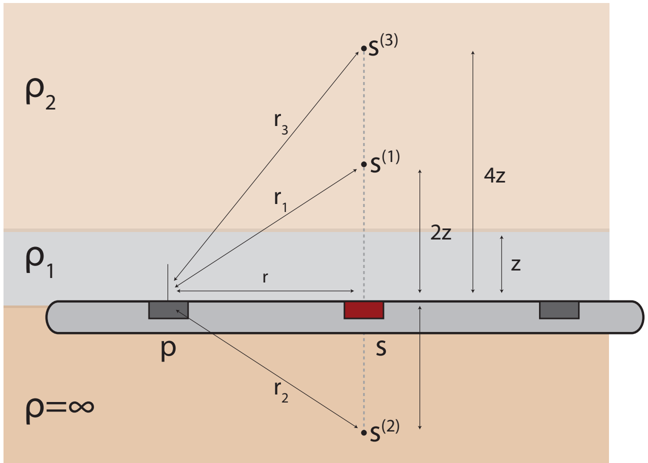

Figure 5.6: Model geometry for a two horizontal layers configuration. S denotes the stimulating electrode and $S^{(j)}$ represent the virtual image sources. P is the point where the voltage is calculated, and r_j represents the distance between the virtual sources and P.

$$\begin{cases} V(p) = \frac{\rho_1 . I}{2.\pi} . \left(\frac{1}{r} + \sum_{j=1}^{\infty} \frac{2k^j}{r_j}\right) \\ k = \frac{\rho_2 - \rho_1}{\rho_2 + \rho_1} \end{cases} \tag{5.4}$$

For patients for which we had access to both the EFI and the EMD estimations (i.e., subjects S1, S2, S4, S6, S8), model parameters were estimated using the $fminsearch$ algorithm (Matlab) for electrodes 5 to 12. Parameters ρ_1 and k were estimated independently in the apical and basal direction. Figure 5.7 represents the same EFI data as in figure 5.5 and the two-layers model outputs. Table 5.3 reports the individual estimations of ρ_1 and the ratio of resistivity for electrode 8.

	Subject	S1	S2	S4	S6	S8	Mean
Apex	ρ_1	328.31	92.94	346.94	139.88	163.15	214.25
	Ratio	140	14444	32	1236	60	48
Base	ρ_1	442.14	165.30	517.67	240.21	1853.05	310.07
	Ratio	31	106	10	60	34	3183

Table 5.3: Fluid resistivity (ρ_1, in $\Omega.cm$) and ratio of resistivity (ρ_2/ρ_1) estimated using the two-layers model for electrode 8.

This model remains strongly limited by the assumptions it relies on. In particular, the model geometry strongly overestimates the current leak in the radial dimension, as a result infinite contrasts of resistivity were sometimes estimated to fit the EFI data. Hence, the amplitude of ρ_1 ($mean = 202\ \Omega.cm$, $s.d = 143\ \Omega.cm$) and the ratio of resistivity ($mean = 415, s.d = 1733$, the three conditions yielding an infinite ratio were note included here) cannot be directly transposed to the real cochlea. It is however interesting to note that EFI data could be fitted with a simple model considering point sources, and only two parameters, while neglecting the influence of the actual geometry

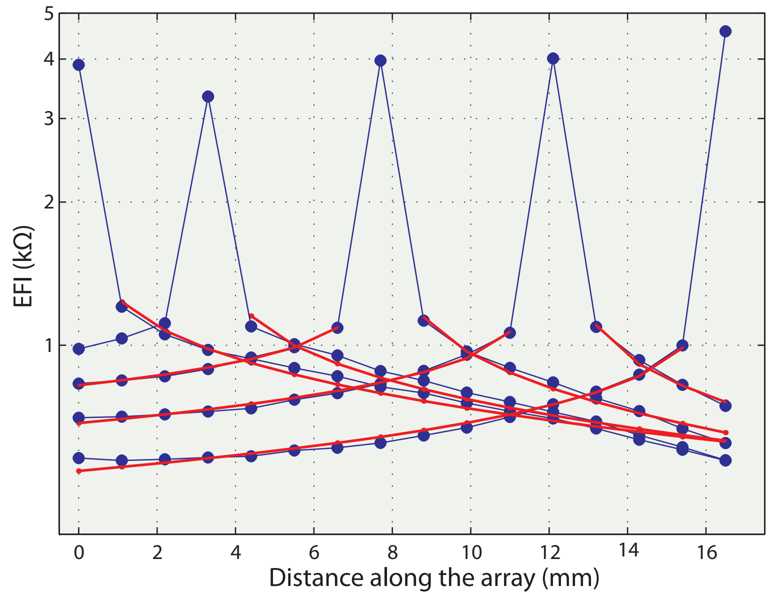

Figure 5.7: Electrical field imaging and layer-model output.

of the cochlea. The SSE for this subset of subjects and for electrode 5 to 12 was 0.008 $k\Omega$, on average while it was 0.019 $k\Omega$ for the exponential decay model on the same subgroup of subjects.

This simple model illustrates the influence of the presence of a contrast of resistivity in the inner ear independently from the coiling, tapering or other anatomical features of the real cochlea.

However, as illustrated in figure 5.7, most EFI recordings reveal an asymmetric pattern with a smooth decay toward the apex (E1) and a steeper decay toward the base (E16). This specific pattern has been reported in numerous studies (Lim et al., 1989; Hanekom, 2001; Vanpoucke et al., 2004a; Berenstein et al., 2010) and has been partly attributed to the coiling and/or tapering of the bony cavity (Lim et al., 1989; Hanekom, 2001; Vanpoucke et al., 2004a; Choi et al., 2006). It is assumed that, towards the apex the section area of the cochlea tends to gradually diminish which makes it behave like a wave-guide, hence sustaining the electrical potential. In the opposite, towards the base, the section of the cochlear cavity monotonically increases making electrical decay faster. To account for this asymmetry, in both descriptive models, fitting parameters had to be estimated independently in the the apical and basal direction which does not enable to propose a clear physical explanation of this phenomenon.

5.4.2 Interpreting EFI data

Individual EFI data were analyzed using different methods to better understand the laws of electrical diffusion in the implanted ear and see whether it is possible to identify the influence of specific features such as the presence of current pathways, inhomogeneous resistivity distribution, or the size of the cochlea.

For each subject, we defined six active electrodes at the very apex and the base of the array (E1, 2, 3, and E13, 14, 15). The six EFI patterns recorded in response to the activation these electrodes were normalized by the amplitude recorded on the electrode 8. Figure 5.8, represents the individual normalized EFI patterns centered between electrode 5 and 11. This representation enables to visualize the spatial electrical spread while minimizing the offset amplitude as well as the influence of the near-field.

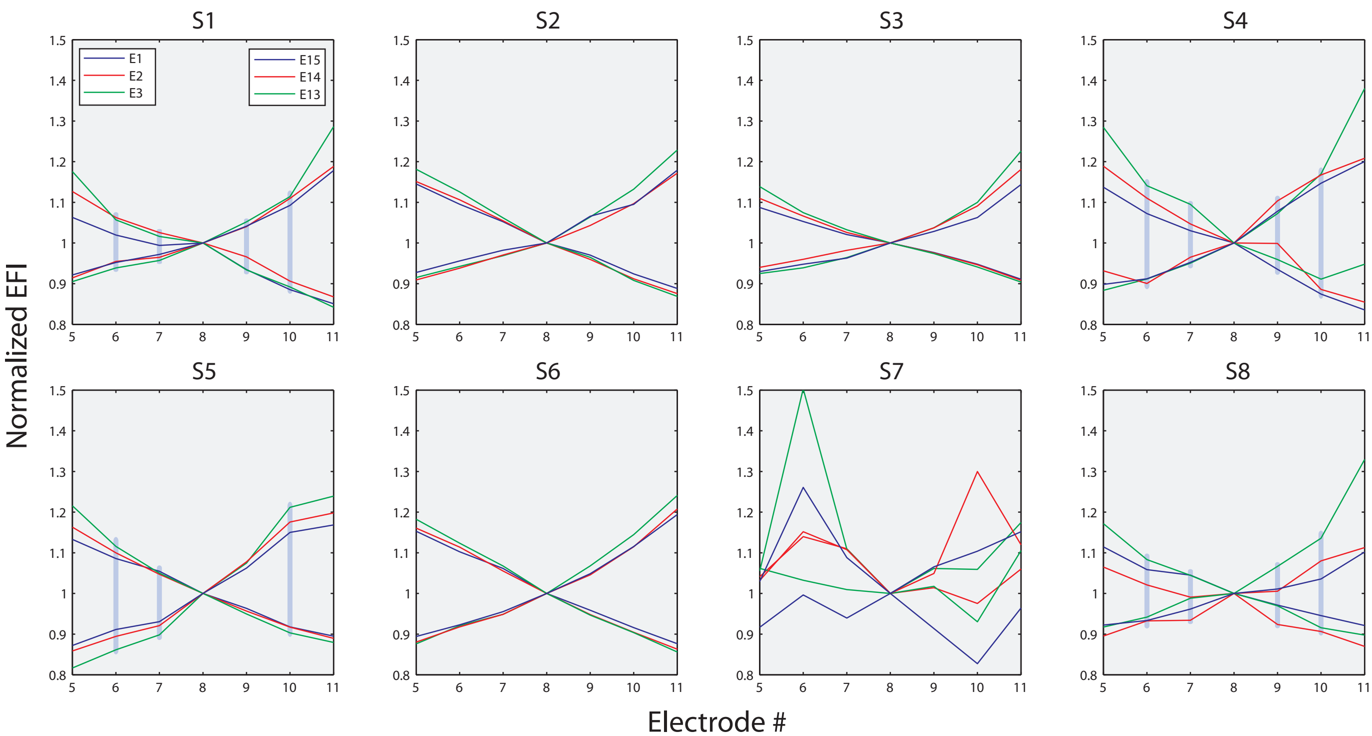

Figure 5.8: EFI patterns resulting from the activation of electrodes 1, 2, 3 and 13, 14, 15. All patterns were normalized by the value recorded on E8. Each panel is for one subject

One can distinguish three sub-groups in figure 5.8. S2, S3 and S6 exhibit very similar linear patterns both in the apical and basal directions. This suggests that, first, at least along this 6.6 mm path, the tapering of the cochlea has few effect on the electrical patterns. This may be explained by the fact that in this region of the cochlea (first turn) the cross-sectional area is almost constant (Hatsushika et al., 1990). Second, at this distance ($\approx 2.2mm$ from the closest active electrode) the influence of the near-field is negligible which corroborates the observation made in vitro.

On the other hand, subjects S1, S4, S5, S8 show more variability in the EFI patterns. In particular, sudden slope variations can be observed. It is worth noting that those singularities are place-dependent and could be observed in different patterns and in both directions, as illustrated by the shaded areas in figure 5.8. This local effect might result from local variations of the surrounding resistivity (fibrosis, ossification) or current pathways. Finally, S7 yielded chaotic patterns which will be discussed later in this chapter.

The previous analysis suggests that an important part of the inter-subject variability in the EFI patterns may be related to an amplitude offset and local singularities due to local changes of the tissue resistivity or of the electrode surface. To further investigate the spatial spread in the implanted ear, we calculated the derivative of the EFI pattern along the electrode array ($\frac{\Delta z}{\Delta x}$) which provides us with an estimation of the rate of the electrical decay in $k\Omega.mm^{-1}$.

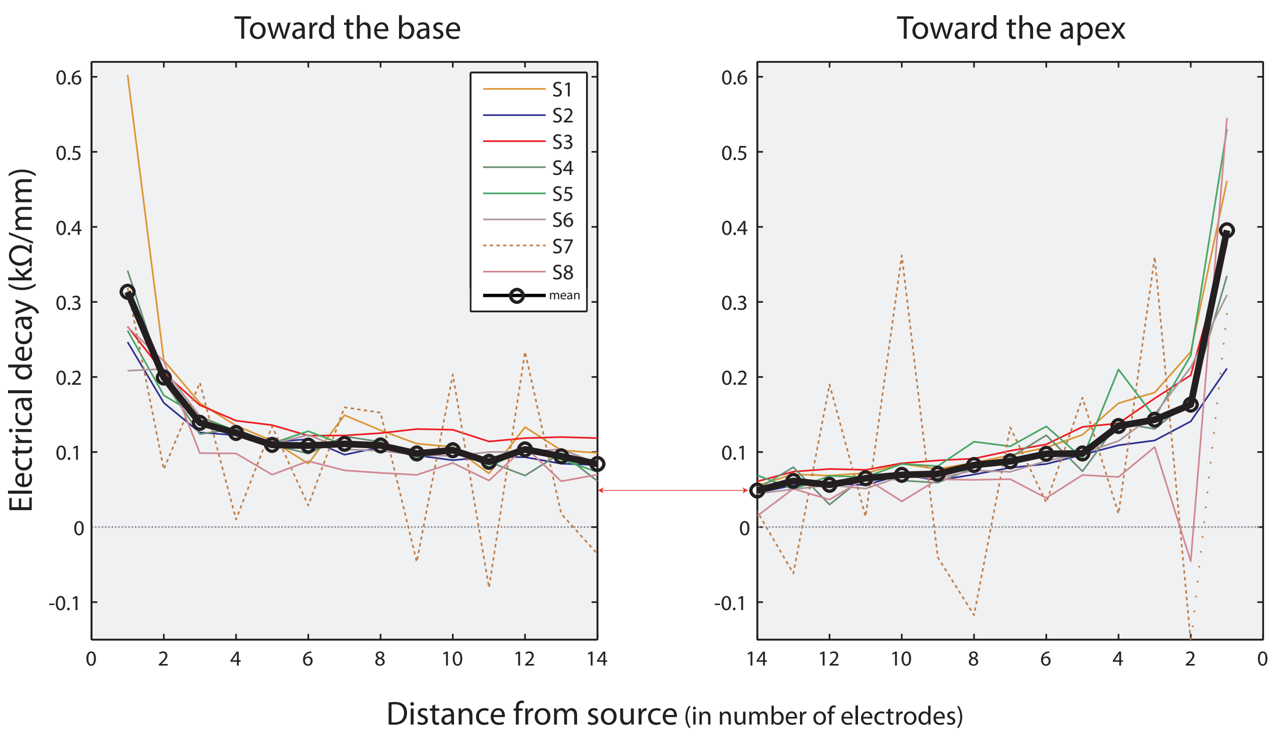

Figure 5.9: Spatial derivative of the EFI pattern (in $k\Omega.mm^{-1}$) resulting from the stimulation of E1 (left panel) and E16 (right panel), as a function of the distance from the active contact. Thin lines represent different subjects, thick black line indicate the mean pattern. The mean pattern did not include the data from S7 which are depicted with dotted lines.

Figure 5.9 represents the derivative of the EFI resulting from the stimulation of E1 (left panel) and E16 (right panel). We can first observe, that the across-subject variations were maximal in the vicinity of the stimulating electrode (0.31 $k\Omega.mm^{-1}$ for E1 and 0.40 $k\Omega.mm^{-1}$ for E16). However, further away, individual patterns were consistent.

In both directions, this representation enables to assess the steep decay in the vicinity of the stimulating electrodes. A repeated-measurements analysis of variance suggests that the decay rate was significantly different in the basal direction and in the apical direction ($F(1,6) = 6.445, p < 0.05$). Qualitatively, we can note that the slope of the decay rate is steeper towards the apex than towards the base. Toward the base the decay rate seems to slowly diminish down to 0.1 $k\Omega.mm^{-1}$ suggesting that the current leak in this direction is homogeneous along the array.

In contrast, in the apical direction, a marked decrease of the decay rate was observed from the stimulating electrode to the second adjacent contact. Beyond this distance, the spatial decay monotonically decreases (down to 0.05 $k\Omega.mm^{-1}$) suggesting that less and less current is dissipated in the apical direction. Interestingly, the same analysis extended to other electrodes of the array yielded similar patterns.

Overall, those results seem to indicate that in all patients, the electrical field decreased following the same spatial law, despite potential differences in the size of the cochlea, electrodes positioning or local resistivity.

The very specific EFI patterns recorded in the implanted ear seem to relate to an electrical field asymmetry imposed by the presence of a preferential current pathway at the base of the cochlea. The across-subject and the across-electrode variability may be explained by, first, the local access resistance, which yields an amplitude offset, and second, local bumps on the EFI patterns may be due to local variations of the resistivity of the medium around the recording electrode. This can, for instance, be induced by different levels of fibrosis on the electrodes.

These observations corroborate the findings of tetrapolar recordings presented in chapter 3 with the same subjects. By stimulating a pair of electrodes in BP+2 and recording the voltage difference across the inactive electrodes located in between, we were able to estimate the across-electrode pattern of resistivity. Besides, increasing the spacing between the stimulating electrodes (BP+3) which theoretically enables to estimate the resistivity of deeper media, yielded a decrease in amplitude but similar across electrode-patterns. This suggested that the ratio of resistivity between the vicinity of the electrode and deeper biological materials (potentially the modiolar bone) was homogeneous along the array.

5.5 Radial diffusion and spatial selectivity at the level of neural fibers

Considering the observations of both the present and previous studies, it seems obvious that the current spread along the cochlea is dominated by the longitudinal dimension. However, understanding the current spread from the electrodes to the modiolus remains critical since it strongly influences the neural excitation pattern. Unfortunately, neither in vivo nor in vitro recordings can be carried out to estimate the electrical field at the level of the auditory nerve fibers.

5.5.1 Psychophysical measurement of selectivity

Level of Interaction

While the electrical field cannot be directly measured at the level of the nerve fibers, the spatial selectivity of a stimulation mode at the level of the auditory nerve fibers can be investigated by measuring the *level of interaction* (Townshend and White (1987)).

This psychophysical measure relates to the influence of the superimposition of two electrical fields on detection thresholds. It thus theoretically accounts for both the spatial selectivity of the electrical field at the level of the nerve fibers and the responsiveness of the neural population.

The estimation of the level of interaction requires the measure of detection thresholds (T-levels) in several configurations. To evaluate a given stimulation mode, we define one *probe* channel and one *perturber* channel and operate the following steps:

- T-level estimation for the perturber channel alone.
- T-level estimation for the probe channel in the presence of the perturber channel at a fixed subthreshold level ($I_{perturber}$) with the same polarity. Θ_{same}
- T-level estimation for the probe channel in the presence of the perturber channel at a fixed subthreshold level ($I_{perturber}$) with the opposite polarity. $\Theta_{opposite}$

Using those measures, two metrics have been proposed in the past to quantify the amount of interactions. Townshend and White (1987) proposed the calculation of the *level of interactions* (LOI) using equation 5.5, while Eddington and Whearty (2001) used the *interaction index* (II) defined by the equation 5.6.

$$LOI = |\frac{\Theta_{opposite} - \Theta_{same}}{\Theta_{opposite} + \Theta_{same}}| \tag{5.5}$$

$$II = \frac{\Theta_{opposite} - \Theta_{same}}{2 * I_{perturber}} \tag{5.6}$$

If both channels are interacting the electrical field produced by the perturber channel should yield low Θ_{same} and high $\Theta_{opposite}$ and thus a large value of LOI and II.

Conversely, if both channels are independent, since the amplitude of the pertuber channel is fixed at a subthreshold level, Θ_{same} and $\Theta_{opposite}$ should be similar and both LOI and II should be close to zero. Figure 5.10 illustrates this paradigm for interacting channels.

Smith et al. (2009) applied a similar method to optimize the PA strategy by changing the value of the diagonal terms of the impedance matrix. They assumed that the optimal values were obtained when the II was close to zero. Herein, the amount of interactions was assessed in a preliminary experiment with only one subject (S4) to evaluate the selectivity of three stimulation modes: MP, PA and CPA. However, with the original PA strategy, T-levels for individual channels could not be reached before the charge density safety limit was reached (see the description of safety recommendations in appendix 7.3.4). As a result we tested an alternative configuration where diagonal terms of the impedance matrix were defined as the average of those of PA and CPA (i.e., average between R_a and the extrapolation estimation). This configuration is referred to as $PA_{average}$ thereafter. Channel 8 was defined as the probe and channel 9 as the

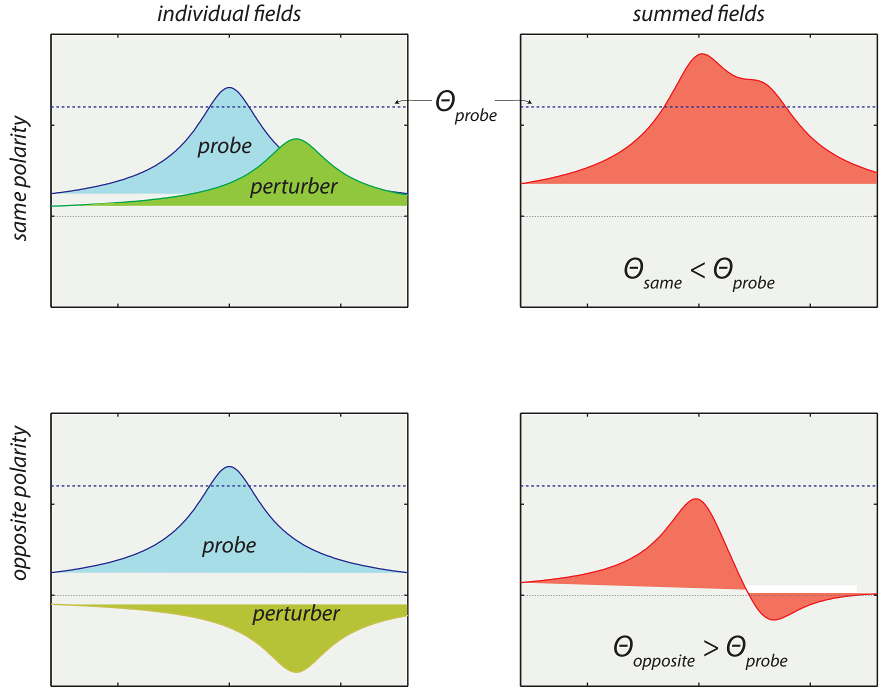

Figure 5.10: Illustration of the Interaction Index paradigm

perturber channel. Stimuli were 300 ms long trains of cathodic-first biphasic pulses presented at a rate of 150 pps and with a phase duration of 130 μs.

The T-level estimation procedure was identical to the one used in chapter 4. The different measurements were organized as follows:

- C-level estimation for the pertuber channels in both polarities.
- T-level estimation for the pertuber channels in both polarities ($\times 2$).
- C-level estimation for three different conditions $[probe; probe + perturber; probe - perturber]$.
- T-level estimation for three different conditions $[probe; probe + perturber; probe - perturber]$, in randomized order. ($\times 3$).

The T-level of the pertuber was estimated in both polarities and $I_{perturber}$ was set to -2 dB below the mean estimate.

Results

Figure 5.11 displays the detection thresholds estimated in all different configurations. We can note that, for the individual probe and perturber channels, MP thresholds were on average, 11.15 dB lower than $PA_{average}$ thresholds and 9 dB lower than CPA thresholds. The perturber levels for MP, $PA_{average}$, and CPA were: 101-, 329-, and

240 μA, respectively. For all stimulation modes, Θ_{same} were much lower than the individual channels while $\Theta_{opposite}$ were higher. Unfortunately, $\Theta_{opposite}$ could not be reached without exceeding the charge density limit for $PA_{average}$.

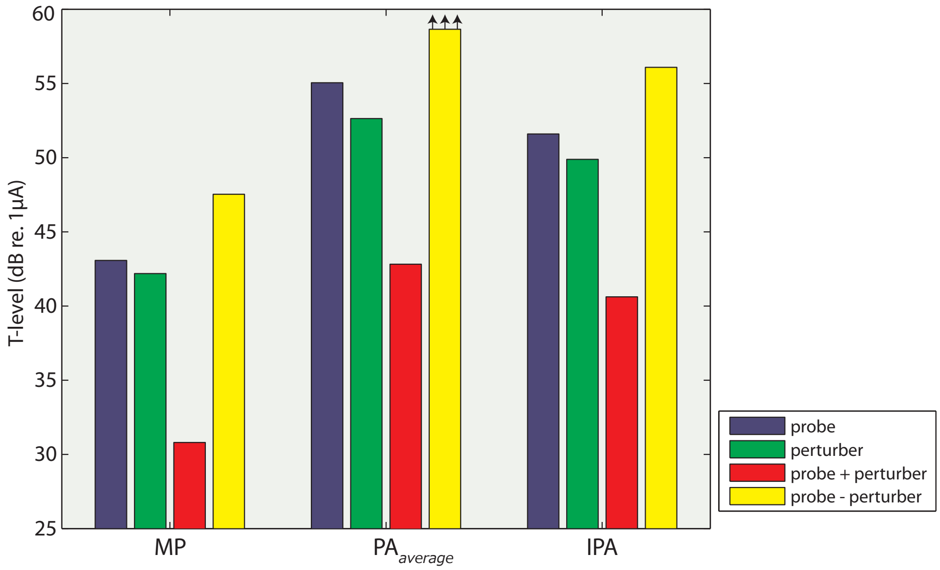

Figure 5.11: Detection thresholds measured for the perturber and the probe channels, for MP, $PA_{average}$ and CPA stimulation modes.

	MP	$PA_{average}$	CPA
Level of Interaction	0.21	$>$ 0.16	0.16
Interaction Index	0.21	$>$ 0.16	0.16

Table 5.4: Interactions metrics for MP, $PA_{average}$ and CPA calculated in dB

Table 5.4 reports both LOI and II for the different configurations, calculated in dB. Overall, those results seem to suggest that the amount of interactions was larger with MP and slightly lower for both $PA_{average}$ and CPA. Unfortunately, the fact that $\Theta_{opposite}$ could not be measured for $PA_{average}$ only enables to say that the amount of interactions, as calculated by those metrics was at least equal or larger using $PA_{average}$ than using CPA.

Assuming that our estimation of the contact impedance provides a relevant estimation of the voltage at the surface of the electrodes, we can estimate the voltage distribution at T-level for the different configurations. Figure 5.12 displays those estimated patterns. We can first note that in the different measurement configurations it is likely that different populations of neurons were recruited. Besides, the small difference in threshold between Θ_{same} and $\Theta_{perturber}$, suggest, that both channels strongly overlapped at the level of the nerve fibers. Further improvement is thus needed to create independent neural excitation patterns.

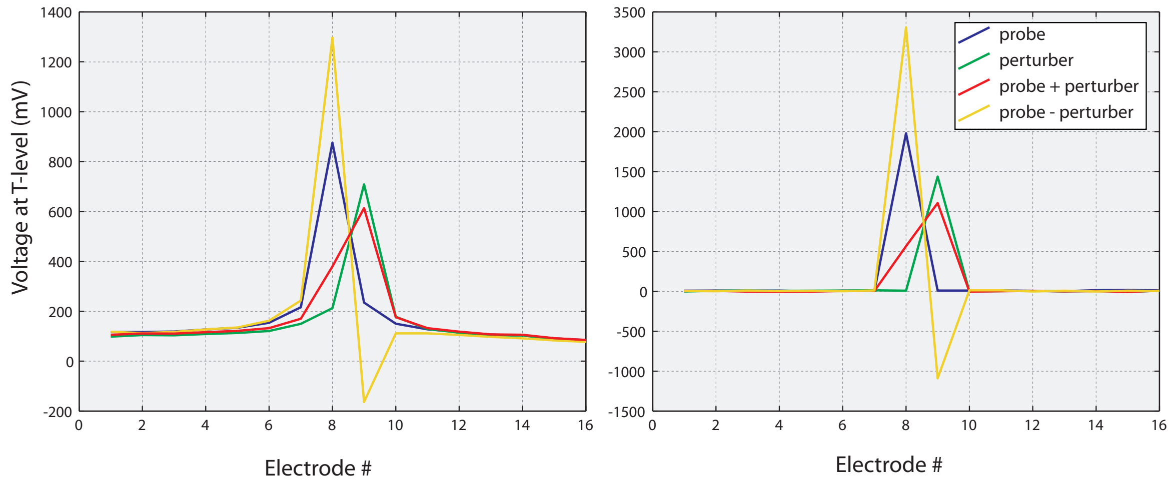

Figure 5.12: Estimated voltage patterns at T-level (in mV), on the electrode array, for MP (left panel) and CPA (right panel).

5.5.2 Electrical field at the modiolar wall

We have seen in vitro, that the influence of the radial spread on the voltage distribution along the electrode array was most influent in a *near-field region* in the vicinity of the stimulating electrode. Beyond approximately 2 mm each side of the stimulating electrode, the voltage patterns recorded at 200-, 500-, 800-μm along the array were similar, suggesting that current lines could be considered as parallel to the array. In the implanted cochlea, because of the presence of a barrier of higher resistivity we would expect current lines to bend in the longitudinal direction. As a result, this near-field region should be even smaller in the implanted ear than in free field. To understand the radial spread toward the modiolar wall we can thus limit our investigation to this specific region.

Based on the outcome of a computational model of the guinea pig's cochlea, Briaire and Frijns (2000) proposed a description of the electrical spread in two distinct regions. In the vicinity of the stimulating electrode ($r_c < 0.2mm$) the electrical voltage would not be affected by the presence of different biological materials and thus decrease as if in a free field homogeneous medium, following a $\frac{1}{r}$ law. Beyond this region, the electrical field would progressively deviate from this hypothesis due to the presence of the bony structure on the cochlea. As a result, the voltage decay would be better described by a decreasing exponential curve (see, equation 5.3). Berenstein et al. (2010) transposed this approach to the human cochlea assuming that the critical radius r_c introduced by Briaire and Frijns (2000) might be larger in humans (≈ 0.4 rather than 0.2 mm) because the size ratio between the human cochlea and the guinea pig cochlea is approximately 2:1. As highlighted by Briaire and Frijns (2000); Vanpoucke et al. (2004a); Berenstein et al. (2010) this transition zone is of major interest for the understanding of the electrode-neurons interface.

Herein, we tried to investigate whether this approach would be affected by the apex-base asymmetry of the electrical field. For each stimulating electrode E_i (from E2 to E15), the difference $\delta z_{apex-base} = \frac{z(i-1,i)-z(i+1,i)}{z(i-1,i)}$ was calculated and the same calculation was reproduced up to a maximum spacing of 7-electrode (for E8). One can thus consider that if $\delta z_{apex-base}$ is close to zero, then the electrical field can be considered as symmetrical in the longitudinal direction. Figure 5.13 displays $\delta z_{apex-base}$ as a function of the spacing between the stimulating electrode and the recording electrodes.

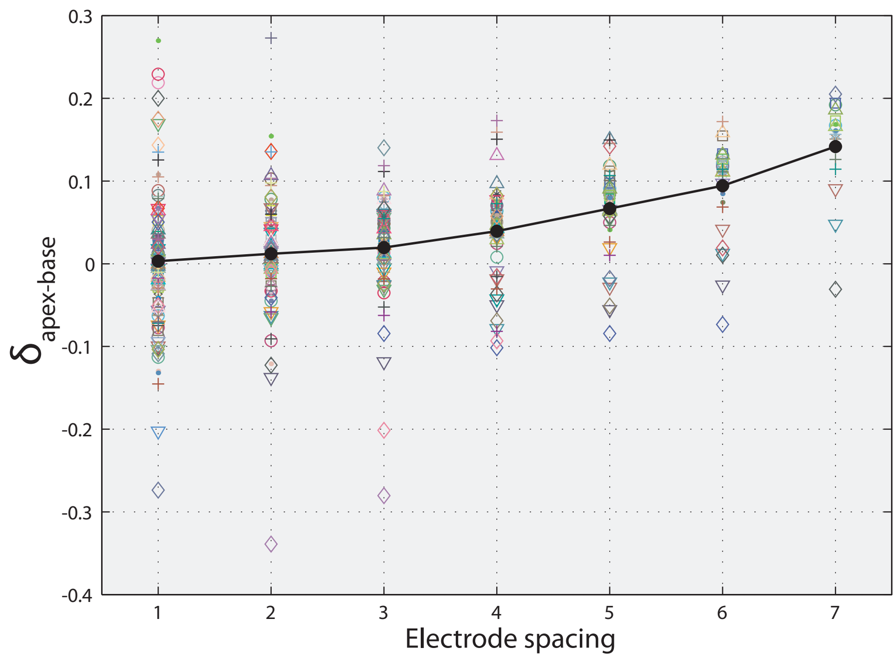

Figure 5.13: Transimpedance difference between the apical and basal direction as a function of electrode spacing. Black line indicates the mean.

Despite an important variability, those data interestingly show that, on average, the apex-base asymmetry is marginally visible one electrode away from the stimulating contact ($\approx 1.1mm$). $\delta z_{apex-base}$ then monotonically increases which might be explained by an increasing influence of the cochlear structures and current pathways. A RM-ANOVA was carried out on the values of $\delta z_{apex-base}$ calculated for E8, in order to assess the influence of the electrode spacing. The analysis revealed a significant effect of the electrode spacing ($F(2.11, 11.64) = 33.77, p < 0.001$, including a Greenhouse-Geisser correction of sphericity). Besides, pairwise comparisons suggest that the apex-base asymmetry was not significant for an electrode spacing varying from 1 to 3.

This suggests that, in the perspective of inferring the voltage at the level of the modiolar wall from EFI recordings, it might be possible to neglect the asymmetry of the electrical field up to the 2^{nd} adjacent electrodes.

5.6 Discussion and Implications for CIs

5.6.1 Longitudinal diffusion

In vitro recordings demonstrated the feasibility of electrical focusing using the PA strategy. However, in the present configuration the electrical fields produced by each electrode were almost similar, symmetrical and very peaky. As a result, the computed weights were homogeneous across the flanking electrodes and low in amplitude to maintain the residual field as low as possible expect at the level of the active electrode.

In the human ear, conditions are more challenging. The analysis of CI data was conducted to better understand these EFI patterns and provided several information.

1. Individual EFI patterns seem to differ mainly due to the variability of the access resistance which yields an amplitude offset.

2. Local bumps in the EFI patterns are likely due to local features which may include: electrode encapsulation, ossification, the proximity of a dominant current pathway.

3. The apex-base asymmetry of the EFI patterns seem to result more from the presence of a dominant current pathway towards the base than from the coiling or tapering of the cochlea.

4. Despite differences in the position of the electrodes, the inner ear resistivity, or the size of the cochlea, all EFI patterns seem to decrease at the same rate.

In the present study, the case of S7 is of particular interest. EFI carried out with this subject, displayed in figure 5.14, reveal a unexpected patterns. Interestingly, these patterns are comparable to those measured in free field using the in vitro setup, which suggests the absence of a marked contrast of resistivity. The analysis of CT images for this subject was complicated since the bony structure could only be identified up to approximately $5mm$ from the round window. As shown in figure 5.15, beyond this distance no bony intracochlear structure is visible. We may speculate that this reveals a Mondini dysplasia which can be associated with Pendred Syndrome (Johnsen et al., 1986). This syndrome is known to induce a cochlear deformity, in particular, a collapse of the scala media and/or an endolymphatic duct enlargement (Gulya, 2013; Wangemann, 2006).

5.6.2 Radial diffusion towards the modiolar wall

While the psychophysical metrics of interaction used here suggested an improvement in the spatial selectivity of the neural excitation pattern using the CPA stimulation compared to MP, the benefit remained limited. Further improvement could potentially be achieved by taking into account the electrode to modiolus distance.

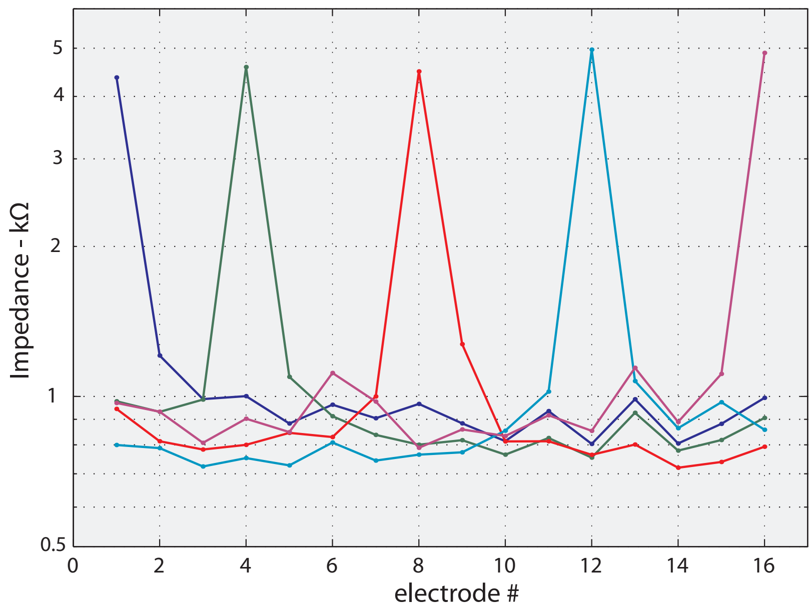

Figure 5.14: EFI recorded with S7. Peak values were obtained using the contact impedance model. For this subject, all transimpedances had to be estimated using the partial polarization model.

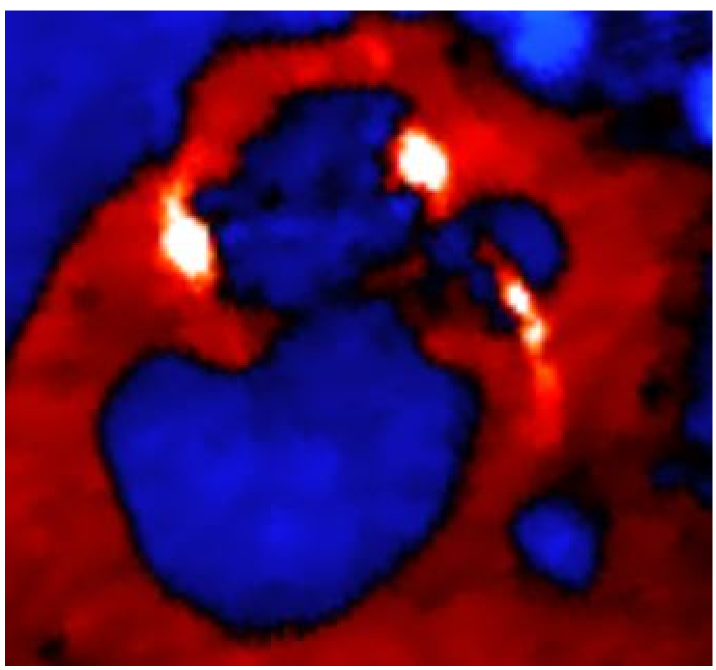

Figure 5.15: Saggital cross-section from CT images of S7.

The present results suggest that, the voltage distribution at the level of the modiolar wall could be inferred from EFI recordings by modifying the peak voltage and the voltage recorded at the level of the first (or two-first) adjacent electrodes. Beyond this distance ($\approx 2.2mm$), we may assume that the voltage recorded at the level of the electrodes will not significantly differ from the voltage that would be measured on the modiolar wall.

In the perspective of developing a neural-focusing strategy this would involve a modification of the first two subdiagonals and first two superdiagonals of the impedance matrix, as illustrated in figure 5.16.

However, using numerical models seems necessary to determine those values. These models should include an accurate description of the shape of the electrode and the electrode array. However, a complex cochlear geometry might not be necessary for this specific objective. Indeed, the analysis of CT images suggests that from the most basal to the most apical electrode, the section of the cochlea does not dramatically decrease, at least for the relatively shallow insertions of this electrode array. This might not hold for longer arrays or deeper insertion depths (Hatsushika et al., 1990). Furthermore, the results presented in the section 5.5.2 suggest that, in this restricted near-field region, the electrical field could be reasonably considered as symmetrical.

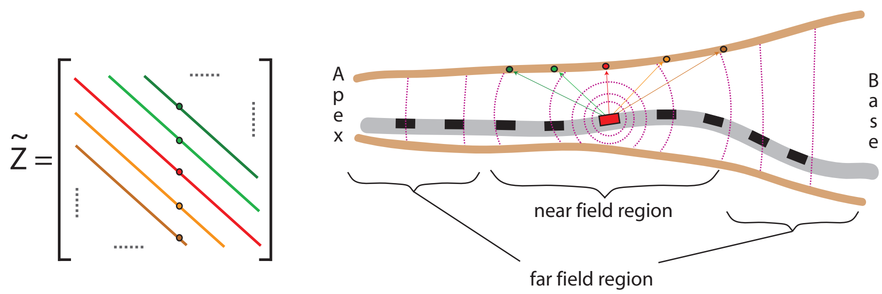

Figure 5.16: Schematic illustration of the hypothetical description of the electrical field diffusion in the implanted cochlea considered for neural focusing paradigm.

5.6.3 Feasibility of neural focusing

Being able to estimate the impedance matrix at the level of nerve fibers might theoretically enable to transpose the methods of the PA strategy to design a neural focusing technique. Recently, Saba et al. (2014) investigated this approach in a computational model. In their study, a numerical model of the implanted cochlea was used to compute the voltage distribution at the level of the modiolar wall. They then generalized the PA algorithm with a non-square neural matrix, Z_n, instead of a transimpedance matrix. The current weights required to theoretically create a single focused channel at the target site were calculated using the pseudo-inverse of Z_n.

However, the voltage distribution at the level of the nerve fibers tend to be shallower than the EFI patterns. As a result, the compensating current applied on flanking electrodes dramatically reduce the voltage in the vicinity of the target site. In their numerical model, to produce the same voltage amplitude in monopolar and neural-focusing stimulation, the input current level had to be increased by a factor 56. Using real devices, this requirement could not be fulfilled without reaching the device compliance limit. They also pointed out that using a limited number of current sources, one cannot handle the possible oscillations of the electrical field in between electrodes.

While mathematically feasible, it seems that further optimization is thus needed to develop an efficient neural focusing stimulation technique.

Chapter 6

Conclusion and Perspectives

6.1 Summary of findings

The present research project aimed to better understand the Cochlear Implant−Auditory nerve interface focusing on two important limiting factors of present CI devices: channel interactions and subject specificity. A multidisciplinary approach was used to improve our knowledge of this interface. The main findings of the experiments carried out with normal hearing listeners, cochlear implant users and using our in vitro setup are summarized in this chapter. I first summarize the main results and then discuss the potential implications for the improvement of cochlear implant devices and/or alternative stimulation strategies.

6.1.1 Acoustic simulation

Acoustic simulations of CIs are commonly used to investigate the influence of signal processing on speech recognition. It enables to identify the salient cues that need to be conveyed through the processing of a CI while limiting the influence of across-subject variability. However, the reliability of acoustic simulations can be improved by taking into account some specific features of electrical stimulation at the peripheral level of the auditory system. Chapters 2 and the study presented in the appendix 7.1 proposed two main improvements of acoustic simulations of cochlear implants.

Excitation pattern

Channel interaction is unfortunately one of the main characteristics of electrical stimulation. Instead of using identical filters for both the analysis and the synthesis stages of vocoder simulations, it is possible to simulate channel interactions by imposing an overlap between synthesis filters (Bingabr et al., 2008; Strydom and Hanekom, 2011a). The model of synthesis filter design introduced in Chapter 2 enabled simulation of the spread of excitation produced by different stimulation modes based on the activating function patterns (Rattay, 1989). In this chapter, the electrical interactions created by MP, BP and virtual stimulation modes were simulated by the superimposition of different portion of the input signal spectrum. The dual-peak excitation pattern produced by bipolar stimulation was simulated and the outcomes in terms of speech intelligibility demonstrated an improvement with increases in the number of channels up to 8 channels. Above 8 channels, performance tended to plateau or even drop because of strongly deleterious interactions introduced by the presence of two peaks. Those results were consistent with those obtained with CI listeners.

The results of experiment 3 in this study also suggested that the deleterious influence of channel interactions might be increased when remote parts of the signal's spectrum overlap. This observation was explained by the fact that adjacent spectral channels carry well correlated modulation information but that this correlation decreases when interacting channels are spectrally remote (Crouzet and Ainsworth, 2001). Finally, the superimposition of poorly correlated signals highly deteriorates the transmission of information conveyed in both frequency channels. This kind of interactions might also occur in tripolar stimulation in the vicinity of the flanking electrodes. This observation motivated the need to create focused unimodal electrical fields which can theoretically be obtained with multipolar stimulation.

Carrier signal

In appendix 7.1, we focused on the waveform of the carrier signal used in acoustic simulations. Most acoustic simulations are based on pure tone or noise-band carriers. However, we believed that an important step to further improve the reliability of acoustic simulations involves the use of a more realistic signal carrier. The *Pulse Spreading Harmonic Complex* signal used in appendix 7.1 presents the advantage of being temporally AND spectrally more similar to the electrical pulse trains clinically used in CI. Hilkhuysen and Macherey (2014) demonstrated that PSHCs can be designed and optimized to elicit less intrinsic fluctuations after auditory filtering than other broadband signals. In the present study, PSHCs were optimized for each frequency channel. Sentence-in-noise recognition was assessed by measuring the speech reception threshold (SRT) with pure-tone, noise and PSHC vocoders. These simulations yielded better performance with PSHC carriers (SRT= 3.8 dB) than with broadband noise carriers (SRT = 4.9 dB) but lower than with pure-tones (SRT = 1.5 dB). This result confirmed the hypothesis that intrinsic fluctuations of the carrier signal affects the transmission of speech modulations. This study presented the PSHC as a valuable alternative acoustic signal carrier.

6.1.2 Cochlear electrical properties and Electrode impedance

Recent cochlear implant devices offer the opportunity to realize intracochlear electrical measurements using implanted electrodes as recording electrodes. In chapter 3, a large interest was given to impedance measurements and analysis. We made the most of the recording capabilities of the Advanced Bionics HiRes 90k device to develop several complementary recording protocols (tetrapolar measurements, impedance spectroscopy, upsampled recordings, etc) to be able to investigate the electrical properties of both the device itself and of the inner ear. The in-vitro setup involving the entire implant greatly helped develop these protocols and in interpreting CI data.

Resistivity

One of the most fundamental assumptions involved in multipolar stimulation strategies is that biological materials are purely resistive. As a result with the activation of one or several electrodes, no frequency dependency or phase delays are introduced. Several studies demonstrated this hypothesis up to 12.5 kHz. Considering the major importance of this assumption for the scope of multipolar strategies, a specific attention was given to extend the range of validity to a higher frequency. To investigate this aspect, an impedance spectroscopy protocol was developed using the clinical device. Sinusoidal stimuli were generated and recorded on the [0.2-46.4]-kHz frequency range. The magnitude and phase of recorded signals were analyzed in Bode diagrams. A purely resistive medium theoretically yields flat magnitude and phase diagrams. However, the presence of a parasitic capacitance, C_p, due to the device, induced a drop of both the magnitude and the phase at high frequency in all measurements. This capacitive behavior due to the device could consequently mask a potential capacitive behavior of the inner ear tissues and fluids in CI users' data. To overcome this issue, for a given electrode, impedance spectroscopy was measured on different recording electrodes. It was assumed that an increasing phase drop at high frequency associated with a longer distance between the stimulating and the recording electrodes would reveal the presence of additional capacitive elements along the current pathway. For all CI subjects, no effect of distance emerged from spectroscopy data in the high-frequency region.

However, in this study, several spectroscopy recordings revealed an unexpected low-frequency ($< 1\ kHz$) non-resistive behavior. This behavior also affected 18% of the transimpedance waveforms recorded with biphasic pulses, which exhibited similar patterns as polarized electrodes.

Based on the literature, a possible explanation was that recording electrodes were partially polarized by the activation of another intracochlear electrode. This might arise from (1) an unexpected internal charge transfer between the wires of the device, or (2) the passage of current from the perilymph to the recording electrode due to its very high conductivity. Besides, the influence of both phenomena might be emphasized by modifications of the surface of the electrodes. This hypothesis was corroborated by the fact that deactivation of electrodes for a certain period of time seemed to accentuate the partial polarization phenomenon.

As mentioned in Micco and Richter (2006b), the local variations of resistivity due to the presence of tissues or bone, might play an important role in the current flow within the cochlea. Tetrapolar measurements were thus carried out in CI users to see whether it was possible to estimate the pattern of resistivity changes along the electrode array. While this measure was also sometimes affected by partially polarized electrodes, the pattern of resistivity could be estimated along the electrode array and yielded very subject-specific patterns. It is known from geophysics studies that increasing the spacing between the electrodes in tetrapolar measurements can provide information on the presence of singularities in the resistivity distribution at a certain depth. Herein, increasing the spacing between electrodes only affected the amplitude of the recordings but yielded comparable across-electrode patterns which suggest that first, a significant portion of the current spreads radially through the biological tissue and bone, and second, that the across-electrode differences are dominated by differences in resistivity close to the array. In other words, this suggests that the resistivity few millimeters away from the electrode (i.e., possibly in the modiolus) may be relatively homogeneous along the scala tympani.

Contact impedance model

While the electrical field produced by a given intracochlear electrode can be estimated by recording transimpedances on inactive electrodes, the voltage peak at the surface of the stimulating electrode cannot be directly measured because of the polarization of the electrode-fluid interface. The electrode impedance has been studied for a long time in numerous studies reviewed in this manuscript, however, in the field of human CIs, polarization impedance had so far only been described by a basic R-C model. The present study proposed an alternative phenomenological model derived from animal and electrochemistry studies. The equivalent electrical circuit used to model the electrode-fluid interface involved a known blocking capacitor in series with a constant phase element instead of a pure capacitance and the access resistance, R_a. The presence of C_p, previously introduced, was also included by considering biphasic pulses with smooth exponential transients as current input. The in-vitro setup enabled to implement and validate the recording and estimation procedure for the polarized electrodes impedance. It could then be used to estimate model parameters from CI impedance data. The value of R_a theoretically provides an estimation of the resistance between the surface of a stimulating electrode and the remote ground electrode. This model, while being more realistic due to the presence of the aforementioned parasitic capacitance and of the constant phase element, requires the same number of parameters as previous models but yields a better fit of the data.

The parallel analysis of tetrapolar measurements and contact impedances revealed some similarities in the across-electrode patterns. This result suggests that across-electrode differences in R_a may arise from differences in the local resistivity along the electrode array. This also corroborates the findings that the local resistivity is a dominant factor in the overall pattern of resistivity.

6.1.3 Neural responsiveness

Using the electrode-neuron interface model, we tried to account for the most peripheral sources of inter-subject variability of performance. Such a model includes the electrodes, as previously investigated in chapter 3, the distance between the electrodes and the neural elements and finally the neural responsiveness. In chapter 4 we tried to assess the influence of the distance and of neural survival on perceptual outcomes (detection thresholds, speech recognition and SMRT scores). Since the state of the neural population cannot be directly estimated using objective techniques, several studies attempted to define indirect correlates of neural survival. We tried to reproduce the findings of previous studies and also to evaluate another potential correlate of neural survival based on the polarity sensitivity of nerve fibers.

Distance

In the present study, the electrode-to-modiolus distance (EMD) was estimated using Cone-beam CT images. Consistent with previous studies, the estimated EMD and detection thresholds revealed a significant positive linear relationship (6 dB/mm on average using pTP stimulation). As a result, the EMD explained 40% of the within-subject variance in threshold using symmetric biphasic pulses. However, at the individual level, this relation was only observed for 3 out of 8 subjects. This might be due to the fact that most subjects were implanted with a lateral-wall electrode array which may reduce the influence of the EMD. We could not reproduce the findings of previous studies showing that speech recognition scores are correlated to, first, the within-subject variance of thresholds, and second, to the RMS error of the distance model.

Polarity effect

Previous studies investigated the polarity sensitivity of auditory nerve fibers. In particular, it is assumed that anodic stimulation is more likely to initiate neural spikes at the level of the central axon while cathodic stimulation should be more likely to stimulate the peripheral processes. In this chapter, detection thresholds were measured with three different pulse shapes: biphasic pulses, charged balanced triphasic anodic and cathodic pulses to induce a polarity effect.

A strong polarity effect was found in CI users which confirmed that in most cases (78% of the tested electrodes) anodic stimulation is more effective than cathodic stimulation. However, the difference in threshold between cathodic and anodic stimulation (Δ_{C-A}) varied both across- and within subjects.

If we consider the assumption that anodic and cathodic phases are more likely to stimulate central and peripheral processes respectively (Miller et al., 1999; Undurraga et al., 2013), then, by extension, the difference in threshold between both stimuli might relate to the level of degeneration of peripheral processes. A partial correlation analysis revealed that both the EMD and Δ_{C-A} contributed to explain the within-subject variance in detection threshold, which strengthens this assumption.

Besides, this polarity effect, averaged across electrodes, was significantly correlated to subjects performance in SMRT in the sense that people with cathodic thresholds lower that anodic thresholds tended to perform better in the SMRT task. This result suggests that $\bar{\Delta}_{C-A}$ may be interpreted as a global measure of neural survival. However, no such correlation was observed with speech recognition scores.

6.1.4 Electrical diffusion in the cochlea

The last element of the Cochlear Implant – Auditory Nerve interface, as described in the present study relates to the electrical diffusion within the implanted ear. The measurements and analysis carried out in chapter 5 attempted to provide relevant information for a better understanding of the determining factors of electrical diffusion in the implanted ear and discuss possible implications for alternative stimulation strategies.

Longitudinal diffusion

While in vitro, the electrical field produced by the CI can be described by a $1/r$ law, EFI patterns recorded in the implanted ear cannot. A simple model considering point source electrodes and a two-layers model geometry suggested that the presence of a contrast of resistivity in front of the stimulating electrode is a determining factor of the EFI patterns recorded in CIs. However, the analysis of these patterns suggested that, in the present study, they mainly varied across-subject and across-electrode due to differences in R_a which influences the near-field (in the vicinity of the stimulating electrode).

Besides, we investigated the decay rate of the electrical voltage in the implanted ear (expressed in $k\Omega.mm^{-1}$) and found that: (1) it is maximal in the vicinity of stimulating electrodes due to a near-field behavior, (2) further away the evolution of the decay rate as a function of the distance from the stimulating electrode is significantly dependent on the direction of propagation (towards the apex or towards the base), (3) regardless of the electrode position or of the size of the cochlea, the patterns of decay rate were very consistent across subjects.

Radial diffusion

A psychophysical measure of channel interactions was evaluated in this chapter to compare MP stimulation with multipolar stimulations. Not surprisingly MP yielded the lowest detection thresholds. The interaction metrics used here suggested little improvement of the spatial selectivity for both multipolar strategies (PA_{R_a} and $PA_{Average}$, cf chapter 5).

However, we think that further optimization could be possible if one could infer the voltage distribution at the level of the nerve fibers from EFI recordings.

In vitro and in vivo recordings first suggested that it may be possible to consider that beyond approximately 2 mm from a stimulating electrode, the voltage at the level of the modiolar wall will not significantly differ from the voltage measured by the implanted electrodes. This would thus simplify the problem to a modification of the diagonal, the first two subdiagonals and the first two superdiagonals of the impedance matrix.

To estimate these values, a numerical model seems necessary. However, further investigation enabled to propose several simplifications. As a result, such a model should account for: the presence of the electrode array, the fluid filled cavity and the bony structure. A cylindrical geometry might provide a reasonable approximation since neither the place of the electrode nor changes in the section of the cochlea seemed to have the biggest effect. Finally, in this restricted region around the stimulating electrodes, we may assume that the electrical field is symmetrical in the longitudinal dimension (i.e., the apex-base asymmetry is not significant within this region).

Focused stimulation

While it is mathematically possible to compute an inverse problem to focus the electrical field at the level of the modiolar wall, the efficiency of the stimulation seems limited by several factors. First, the voltage pattern at the modiolar wall is necessarily shallower than the EFI pattern. As a result, the solution of the inverse problem yields large amplitude weights on the flanking electrodes. The overall electrical field is thus dramatically reduced and one may face compliance limit issues. To avoid both technical and safety issues associated with the use of very high amplitude it seems that further optimization will be needed.

6.2 Short-term implications

Simulations

Past research studies have already demonstrated the utility of acoustic simulations to assess the influence of signal processing on the transmission of speech cues. The present results suggest that the reliability of CI simulations can be enhanced by including more realistic excitation patterns and carrier signals. However, in chapter 2, the synthesis filters were designed based on the activating function theory (Rattay, 1989) for a very simple model geometry (Litvak et al., 2007). We may think that being able to estimate the voltage distribution at the modiolar wall in several CI patients, could also help design more realistic synthesis filters.

An additional study is also running in our research team with unilaterally deaf listeners in order to compare electrical hearing in the deaf ear and acoustic simulations in the healthy ear. From a "social" point of view, realistic acoustic simulations may also be useful to help normal-hearing listeners (eg. family members) understand and comprehend the auditory perception of CI users.

Recording capacities

The present research project has demonstrated the important recording capabilities of this device. The up-sampling technique presented in Chapter 3 does not require additional equipment and can be implemented with all Advanced Bionics devices. Being able to record voltage waveforms with this precision and run impedance spectroscopy might be a relevant tool for further investigation of the electrical properties of the inner ear.

In Chapter 3, we also demonstrated the possibility to realize tetrapolar measurements using this device. However, our recording procedure, as well as our interpretation, remained relatively direct and basic.

Numerous studies in biomedical sciences, as well as in geophysics, developed advanced tetrapolar recording protocols. In particular, different stimulating and recording configurations (e.g. *Wenner*, *Schlumberger*, *Dipole-dipole*, Mussett and Khan (2000)) have been proposed in the past and can be used depending on the type of investigation, the depth of penetration and also the technical convenience.

This knowledge could be transposed in the CI field to design more advanced experimental protocols. For instance, *electrical profiling* protocols should be used to investigate the distribution of resistivity along the electrode array (i.e, in the scala tympani), while *vertical electrical sounding* protocols should be used to study the electrical properties of the inner ear in the radial dimension (i.e, modiolus, Rosenthal's canal). Such measures may provide relevant information for the improvement of numerical models.

Parasitic capacitance

The presence of C_p affects all stimuli produced by the device and is thus present in all recordings. To avoid misinterpretation of CI data, and especially of spectroscopy data, it seems necessary to take this parameter into account.

Partial polarization

While the physics of the partial polarization phenomenon has yet to be clarified, ignoring it may yield an over-estimation of the transimpedance. This might thus explain irregular (non-monotonous) electrical field imaging data. In the present study, the contact impedance model could be adapted to describe transimpedance waveforms an provide a more accurate estimation of transimpedance values. Figure 6.1 represents an example of distorted waveform recorded in subject S5, and the partial polarization model output. In this case, estimating the transimpedance by measuring half the peak-to-peak amplitude would yield a value of 1355 Ω while the present model predicts an actual transimpedance of 1142 Ω.

Contact impedance model

Both in vitro and in vivo measurements demonstrated that the present CPE-model together with the up-sampling technique provide a better description of the polarization impedance than a R-C model. We showed that the model parameters could be estimated either by fitting the CPE-model in the time domain or in the spectral domain, using impedance spectroscopy. However, the simulation presented in the figure 3.23, in Chapter 3 suggested that the limited spectral content of biphasic pulses stimuli may induce an small uncertainty in the estimation of the model parameters. The spectral approach should thus be preferred.

This may have two direct implications. In clinics, the SoundWave software enables to measure the impedance of Advanced Bionics devices. To provide a quick estimation, the procedure used in this software is very basic. Electrodes are stimulated with biphasic pulses stimuli and the impedance is obtained by measuring the voltage 6-μs after the onset. A model-based estimation might provide a more accurate clinical follow-up. In particular, we may expect our estimations of contact impedance (R_a) to be slightly lower than those estimated with the SoundWave clinical software. As a result, a proper

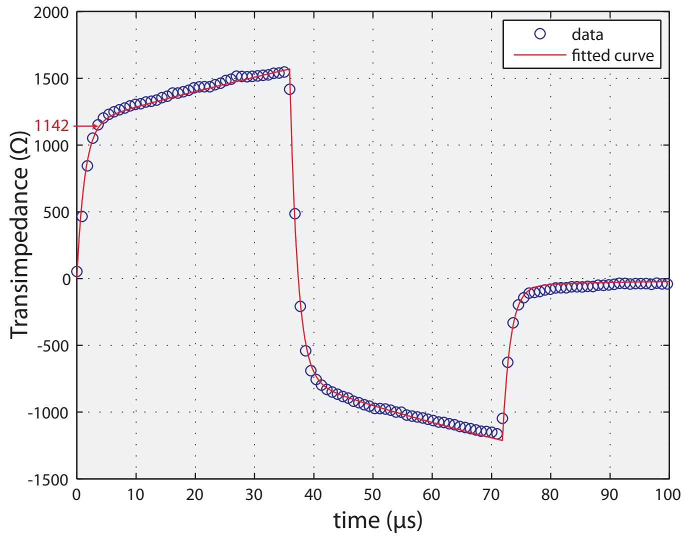

Figure 6.1: Partially-polarized transimpedance recording. Circles indicate samples and red curve represents the model output. The arrow indicates the estimated transimpedance.

estimation of impedances would decrease the risk of exceeding the device compliance limit and thus increase the current sources' dynamic range.

The resistive part R_a is definitely the most interesting parameter since it is assumed to represent the resistive path from one electrode to the ground. However, a better understanding of the polarization phenomenon would enable to interpret the other parameters which may provide valuable information. In particular, the interpretation of both the amplitude and the exponent of the CPE (Y_0, α) has been thought to relate to the electro-chemical properties of the surface of the electrode. However, it is still unclear whether the origin of these electro-chemical changes is geometric (roughness of the electode's surface, Rammelt and Reinhard (1990)) or energetic (energetic heterogeneities at the atomic scale, Cordoba-Torres et al. (2015)). Secondly, the most interesting application of this model may be the optimization of the original Phased-array strategy. The present contact impedance model as well as the adapted version for partial polarization of recording electrodes enable to fully estimate the impedance matrix Z.

6.3 Longer-term implications

Stimulus waveform

All clinical devices stimulate the auditory nerve with charge-balanced biphasic pulses. This has been validated as a safe and efficient stimulus. However, the present study together with previous research suggest that the pulse shape might be optimized.

We have seen that the presence of a parasitic capacitance acted as a low-pass filter resulting in smooth exponential transients. Because both the access resistance and this parasitic capacitance may vary across electrodes, the time constant of these transients changes across electrodes. We have shown that small differences in the transients time constant could yield current summation artifacts. Being able to generate smoother transients might avoid the residual artifacts and may thus be beneficial in multipolar stimulations where electrodes are activated simultaneously. This could be achieved, for example, by using Gaussian-shaped pulses or single-cycle sine-waves. The present Hires90k device enables to create various stimulus waveforms, however, all waveforms necessary result from the concatenation of monophasic pulses which will not solve this problem. It seems that the only way to achieve this would be to modify the device electronics.

Artefact-free eCAPS

Most devices enable to record electrically evoked compound action potentials (eCAPS) using intracochlear electrodes. However, because of the very short latency between the electrical stimulus and the auditory nerve response, the early response of the auditory nerve is masked by a strong electrical artifact. Different techniques have been proposed to compensate for this artifact and are implemented in most research platforms (Forward-masking subtraction method, alternating polarity) but do not enable to analyze the entire eCAP response. However, being able to record the entire neural response without artifact would be highly beneficial for fundamental perspectives. The identification of the parasitic capacitance as well as current summation protocol used in section 3.3.2 in Chapter 3 might be combined to develop an artifact-free eCAP measurement procedure. When stimulating a pair of intracochlear electrodes in bipolar mode (eg. BP+1), the electrical fields generated by each contact add within the cochlea. Somewhere in between the electrodes the overall electrical field is zero. It may then be possible to adapt the current weight of one stimulating electrode to shift the position where the potential is zero until it coincides with the location of an inactive electrode (this configuration would be equivalent to a *partial bipolar* stimulation). This electrode should be used to record the eCAP. Figure 6.2 illustrates such a recording configuration.

However, because of the presence of the parasitic capacitance it is basically impossible to create a perfect zero voltage. Here again, using smooth edge pulses or single-cycle sine waves should enable to overcome this issue.

Optimized multipolar stimulation & Remaining limitations

All along this manuscript, we presented several results that may represent relevant hints for the design of alternative stimulation strategies.

Even though further investigation is required to develop a complete and reliable method to achieve current focusing at the level of the nerve fibers, the present work suggests that it is theoretically feasible.

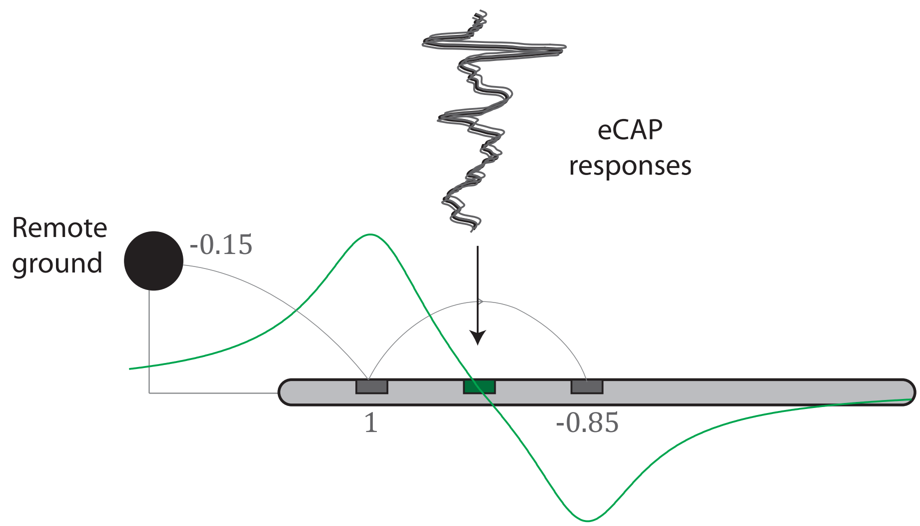

Figure 6.2: Schematic illustration of the artifact-free eCAP configuration with a partial bipolar stimulation where 15% of the current returns to the ground electrode.

If we also consider that the measure of polarity sensitivity introduced in Chapter 4 enables to picture the distribution of neural survival, this hypothetical neural-focusing strategy could then be further optimized to target cochlear regions where the neural population is supposedly healthy by means of current steering techniques.

One important technical limitation pointed out in the present work relates to the compliance limit of the current sources to use such a strategy. However, providing the future devices with more powerful current sources would emphasize another important limitation of the contemporary devices: the battery life. Indeed, one major foreseeable limitation of such an advanced strategy would be the much higher power consumption.

Chapter 7

Appendices

7.1 Pulse-spreading harmonic complex as an alternative carrier for vocoder simulations of cochlear implants.

Adapted from:
Mesnildrey, Q., Hilkhuysen, G. and Macherey, O. (2016). "Pulse-spreading harmonic complex as an alternative carrier for vocoder simulations of cochlear implants", J. Acoust. Soc. Am. 139, 986–991

7.1.1 Introduction

Channel vocoders as the one presented in chapter 2 are commonly used to simulate the amount of information transmitted by a cochlear implant (CI; Shannon et al. (1995)). In a vocoder, the input speech signal is split into various audio channels by a bank of band-pass filters. The time-varying envelope of the signal in each channel is extracted and used to modulate an acoustic carrier. Most previous vocoder studies have used sine-wave or noise-band carriers which likely produce different temporal and spatial patterns of auditory-nerve excitation than the electrical pulse trains delivered by a CI. Sine waves presumably induce a narrower spread of excitation across the tonotopic axis than monopolar stimulation of an intracochlear electrode and, therefore, cannot mimic the channel interactions that CI listeners experience (e.g., Snyder et al. (2004)). In contrast, noise-bands may be filtered to simulate different spreads of excitation. It has been shown, for example, that simulating channel interactions in a noise-band vocoder could account for the lack of improvement of CI listeners on speech perception tasks when the number of channels is increased beyond about 8 to 10 (Bingabr et al., 2008; Strydom and Hanekom, 2011b; Mesnildrey and Macherey, 2015). But noise-bands contain intrinsic modulations possibly interfering with the modulations of the speech signal that each channel aims to transmit. Because these intrinsic modulations are absent in a real CI, there is a need to use alternative acoustic carriers to improve the realism of CI vocoder simulations (Whitmal et al., 2007; Stone et al., 2008; Souza and Rosen, 2009; Gaudrain and Başkent, 2015). Whitmal et al. (2007) used narrowband low-noise noises as carriers in their vocoder and found better speech perception scores than for narrowband Gaussian noises. However, a low-noise noise may only reduce intrinsic modulations compared to a Gaussian noise when its bandwidth is smaller than an auditory critical band. If larger, auditory filtering reintroduces modulations (Hartmann and Pumplin, 1988; Kohlrausch et al., 1997). In consequence, low-noise noise carriers suffer from the same limitation as sine wave carriers, because they may not be able to represent the broad spread of excitation produced by a CI while, at the same time, maintaining few intrinsic modulations. Hilkhuysen and Macherey (2014) recently introduced a class of acoustic signals termed pulse-spreading harmonic complexes (PSHCs). The phase relationship between the harmonics of a PSHC can be adjusted so that its envelope repetition rate, referred to as *pulse rate*, can be varied independently of its fundamental frequency (f_0). The principle of the generation of PSHCs is further explained and illustrated in section 7.2 of the Appendices. Simulations using a gamma-tone filterbank suggested that for a given auditory filter, there is an optimal pulse rate at which the intrinsic modulations of the PSHC *after auditory filtering* are lowest. Figure 7.1 illustrates how this optimal pulse rate, defined as the pulse rate for which the Crest factor is minimal, varies as a function of the center frequency of the auditory filter. As additional information, a second-order polynomial equation relating the optimal pulse rate to the center frequency is also provided [1].

Similarly to Hilkhuysen and Macherey (2014), the amount of intrinsic modulations was estimated by calculating the Crest factor of PSHCs passed through different gamma-tone filters simulating auditory filtering. Hilkhuysen and Macherey (2014) showed that a broadband PSHC presented at its optimal pulse rate yielded higher modulation detection thresholds (MDTs) than a sine wave, but lower MDTs than the other broadband signals tested, including pseudo-random and low-noise noises. Assuming that the MDT reflects the amount of intrinsic modulations present in a signal, this suggests that PSHCs can be tuned to exhibit less intrinsic modulations than other broadband signals previously considered in the literature. It makes these signals appealing carriers for vocoders that attempt to simulate CIs. To that end the present study compares the intelligibility of speech in noise for three different vocoders that use sine waves, noise bands and PSHCs as carriers, hypothesizing that carriers showing lower MDTs will lead to a higher intelligibility when used in a vocoder.

7.1.2 Method

7.1.2.1 Subjects

The study included twelve naïve normal-hearing listeners with ages ranging from 18 to 34 years. They were paid for their efforts as approved by the local ethics committee.

7.1.2.2 Vocoders

Noisy speech was processed by a noise-, sine- or PSHC-vocoder. The analysis stage in these vocoders followed the description provided by Whitmal et al. (2007) as much as possible. The broadband signal was divided into six audio channels, using 6th-order Butterworth filters with widths of 201, 331, 546, 901, 1487 and 2453 Hz, geometrically centered at 0.150, 0.414, 0.841, 1.544, 2.703 and 4.613 kHz, respectively. The subsequent envelope extraction after half-wave rectification used channel-dependent 2$^{\text{nd}}$-order Butterworth low-pass filters with cut-off frequencies at 29, 49, 79, 135, 217 and 360 Hz,

[1] Gaudrain and Başkent (2015) gave an equation relating the optimal order of the PSHC to the center frequency for the particular case of a fixed f_0 of 1 Hz. They acknowledged a typo in their text: the first coefficient of their equation should read 0.0459 and not 0.459. With this corrected value, the values of optimal rates obtained with their equation are similar to those derived from the equation given in figure 7.1 of the present article.

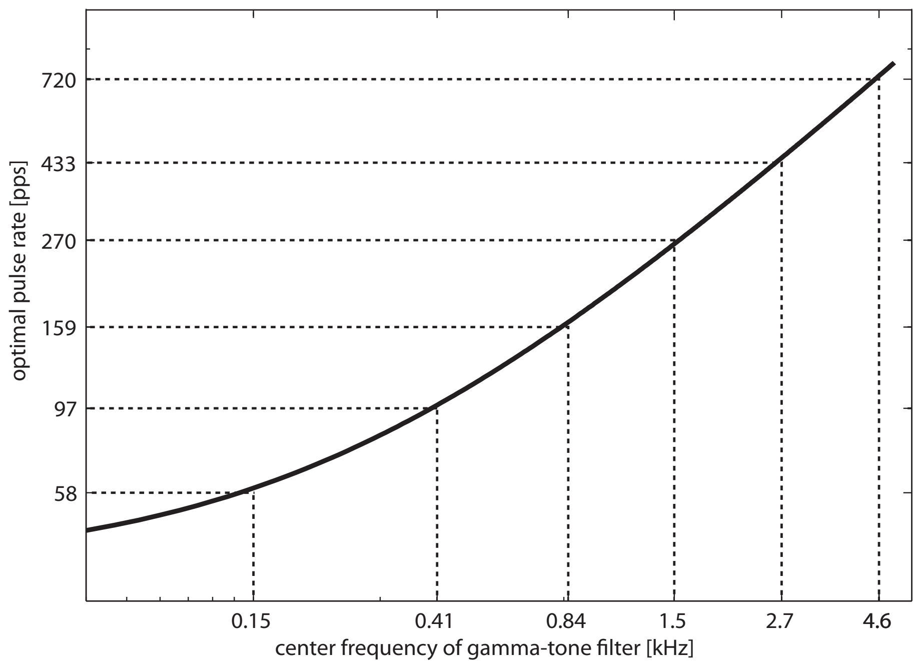

Figure 7.1: Optimal pulse rates as a function of a gammatone filter's center frequency. This function was obtained by generating broadband PSHCs having f_0s of 0.3 Hz and different rates. Each PSHC was then passed through a bank of 100 gammatone filters with center frequencies ranging from 70 to 15000 Hz regularly spaced on an ERB scale. For each gammatone filter, the PSHC's rate that produced the lowest Crest factor at the output of the filter was selected as the optimal rate. The curve shows a second-order polynomial fitted on the optimal rate values found in these simulations. Dotted lines indicate the center frequencies of the PSHC carriers used in the current study.

respectively. The reason for the channel-dependence of these cut-off frequencies is described later in this section.

The synthesis stage varied across vocoders. In the noise-vocoder, each envelope was multiplied with a broadband white noise and the resulting broadband signal was spectrally restricted by convolution with the matching analysis band-pass filter. To create sine-vocoded speech, sine waves at the center frequencies of the audio channels were modulated with their corresponding envelopes without subsequent band-pass filtering. Carriers in the PSHC-vocoder all had an f_0 of 0.3 Hz. Their pulse rates were optimised per audio channel, such that the Crest factors after auditory filtering, as approximated by gammatone filters, were minimal (c.f. figure 7.1; Hilkhuysen and Macherey (2014)). Gammatone filters at the center frequencies of the audio channels suggested optimal pulse rates of 58, 97, 159, 270, 433 and 720 pulses per second (pps) for the lowest through to the highest audio channel, respectively. These pulse rates limited the highest modulation rates that could be transmitted. Consequently, the low-pass filters in the envelope extraction restricted modulation rates to half the optimal pulse rates and below. Because intrinsic modulations can vary between PSHCs with equal f_0s and pulse rates, sets of 50 PSHC exemplars per pulse rate were generated. While generating a stimulus, one exemplar per audio channel was randomly selected from each corresponding set. After multiplying the envelope with the PSHC carrier, band-pass filters spectrally restricted the resulting broadband signals, comparable to the noise-vocoder. In the final synthesis stages of all vocoders the levels of the six audio channels were equalized to the corresponding levels after the analysis band-pass filters, and the six signals were added.

7.1.2.3 Intelligibility testing

Intelligibility of vocoded speech was measured with the French Matrix test (Jansen et al., 2012). A best-of-three adaptive procedure (Levitt and Rabiner, 1967) estimated the SNR for speech in long-term average speech-shaped steady-state noise resulting in 50% sentence correct scores, an outcome measure known as the speech reception threshold (SRT). A response was scored as correct only when the listener reported all five words forming the uttered sentence. Following two consecutive correct responses or two correct out of three consecutive responses, the SNR was reduced by one step. This ratio was increased after two consecutive errors, or two errors in three consecutive responses. Starting the measurement at 20-dB SNR, the step size was initially 4 dB up to the first reversal and then set to 2 dB. A measurement stopped after ten reversals. The SRT was defined as the average across the last six reversals. During an SRT measurement, sentences were selected randomly without replacement from the set of 320 recorded sentences available in the speech corpus.

Listeners heard vocoded sentences presented monaurally to the right transducer of a pair of Sennheiser HD650 headphones connected to a Focusrite Saffire PRO24 D/A converter. Signal processing and test procedures were controlled by custom software written in Matlab (Mathworks, 2010). The signal level was fixed at 65 dB SPL. Listeners sat in a sound-attenuated booth facing a computer screen that showed a matrix of ten by five words. They responded by selecting one out of the ten alternatives for each of the five words in the sentence.

7.1.2.4 Sessions

Training and data collection took place in two sessions, each lasting about two hours. The first session started with passive listening, i.e., sentences of vocoded speech were presented with the correct words highlighted in the matrix on the computer screen. After twenty such sentences, ten sentences were presented that required responses. The SNR and the vocoder type were fixed during these thirty presentations. Starting at 20-dB SNR, listeners were trained on all three vocoders. This procedure was repeated twice, each time decreasing the SNR by 5 dB. The first session finished with a training on the SRT test: each listener providing one SRT per vocoder.

The second session started with passive listening to 20 sentences per vocoder. The SNRs were set at the SRTs obtained from training. The session finished with the actual data-collection blocks, during which SRTs for all three vocoders were measured in a randomized order. Three such blocks were presented to each listener. Each SRT measurement started with passive listening to two sentences presented at 20-dB SNR, to accommodate the listeners to a change in vocoder. Listeners received no feedback during data collection, in contrast to the training.

7.1.3 Results

108 SRTs were measured according to a $Block[1,2,3] \times Vocodertype[noise, sine, pshc] \times Listeners[1..12]$ full factorial experimental design. Differences in SRT scores were addressed with an analysis of variance for repeated measurements (RM-ANOVA). When necessary, nonsphericity corrections were made using Greenhouse-Geisser adjustments. The RM-ANOVA showed significance only for the main effect of VOCODER TYPE with mean SRT scores of 1.5, 4.9 and 3.8 dB for sine, noise and PSHC vocoders respectively ($F(1.1, 12.5) = 19.2, p < 0.05$). To inspect this effect further, we averaged the SRTs across blocks and subtracted per listener the mean SRTs obtained with the PSHC-vocoder from the mean SRT for noise-vocoding. A similar difference was calculated for the contrast of the PSHC-vocoder with the sine-vocoder. The distribution of the resulting ΔSRTs is visualised in figure 7.2. The average ΔSRT for noise- and sine-vocoding were 1.2 and -2.3 dB, respectively. Two Bonferroni adjusted t-tests addressed the statistical significance of these ΔSRTs. SRTs with noise-vocoding were higher than those for PSHC-vocoding ($t(11) = 3.9, p < 0.05$). SRTs with sine-vocoding were lower than the SRTs for PSHC-vocoding ($t(11) = -4.2, p < 0.05$). In summary, intelligibility was worst for noise-vocoding, better with PSHC-vocoding and best with sine-vocoding.

7.1.4 Discussion

7.1.4.1 Effect of intrinsic modulations on speech intelligibility

The difference in SRT between noise- and sine-vocoders averaged 3.4 dB, which comes close to the 4.5-dB difference observed by Whitmal et al. (2007) using similar processing conditions. The result is also consistent with several studies reporting higher intelligibility for sine- than for noise-vocoders (reviewed in Souza and Rosen (2009)). These intelligibility differences have been attributed to the intrinsic modulations present in noise carriers that interfere with the transmission of speech envelope modulations (Whitmal et al., 2007; Stone et al., 2011). The current finding that the SRTs obtained with the PSHC-vocoder are lower than those obtained with the noise-vocoder may reflect the reduced intrinsic modulations present in the PSHC carrier. This explanation corresponds with the results of Hilkhuysen and Macherey (2014) showing that a PSHC yields lower MDTs than pseudo-random noise, which is similar to Gaussian noise. The SRTs obtained with the PSHC-vocoder were, however, higher than the SRTs obtained

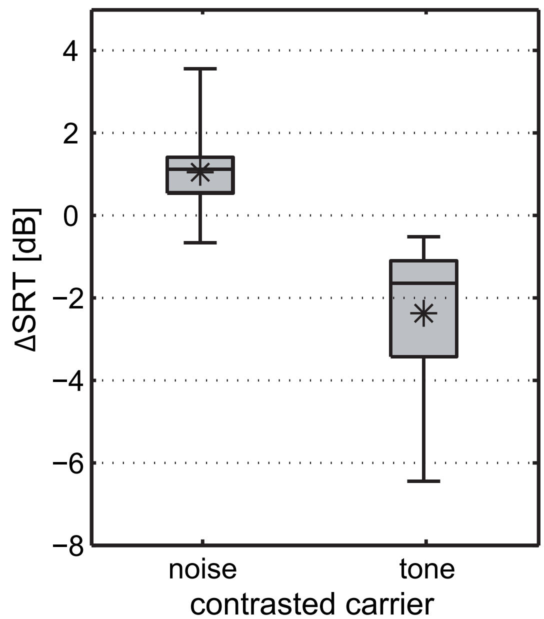

Figure 7.2: SRT differences obtained by comparing performance with the PSHC-vocoder to performance with the other two carriers. Left and right boxes with whiskers indicate the distributions of differences in SRT scores between PSHC-vocoding and noise- and sine-vocoding, respectively. Whiskers represent the ranges; boxes the 25th and 75th percentiles; and horizontal lines within the boxes the medians. Asterisks indicate the mean. SRTs were averaged across blocks; differences were calculated within listeners.

with the sine-vocoder, probably because optimized PSHCs still exhibit more intrinsic modulations than sine waves. The fact that the pulse rates of the PSHC carriers were only optimized within each audio channel could provide an additional explanation. Because all carriers were presented simultaneously, intrinsic modulations occurring at frequencies between the audio channels may have contributed to the intelligibility difference between PSHC and sine vocoding. This explanation is explored further in figure 7.3 showing the Crest factor of gammatone filter's outputs for three input signals as a function of the filter's center frequency. The gammatone filters simulate the auditory filters; the internal Crest factor expresses the amount of intrinsic modulations after auditory filtering. Each input signal is the sum of six unmodulated carriers corresponding to the different bands of our vocoder. Carriers were equated in level before summation. The Crest factor is lowest for the sine-vocoder, highest for the noise-vocoder and intermediate for the PSHC-vocoder, consistent with the results of the speech intelligibility experiment. It is also worth noting that the Crest factor for the PSHC-vocoder increases between audio channels, due to interactions between carriers from adjacent channels. Although this effect is also present for the sine-vocoder, it should have a much lower influence on the speech scores because the output of filters located at the cross-over frequency between adjacent channels is about 30 dB lower than the output of filters centered in each audio channel.

So far only intrinsic modulations present in noisy signals were considered. These can be referred to as *random intrinsic modulations*. However, some signals can also exhibit *periodic intrinsic modulations*. Churchill et al. (2014) used a harmonic complex with an f_0 of 100 Hz and harmonics summed with an equal sine starting phase. The resulting carrier was a peaky signal repeating at a rate of 100 pps. The presence of this periodic intrinsic modulation produces a temporal pitch percept corresponding to the f_0 (Houtsma and Smurzinski, 1990). While jittering the starting phase of the harmonics by different amounts, the authors flattened the peaky envelope, thereby diminishing the regular intrinsic modulations and reducing the pitch salience. They found that this flattening improved intelligibility. A PSHC carrier at its optimal rate should produce a relatively flat envelope at the output of auditory filters, therefore reducing both random and periodic intrinsic modulations.

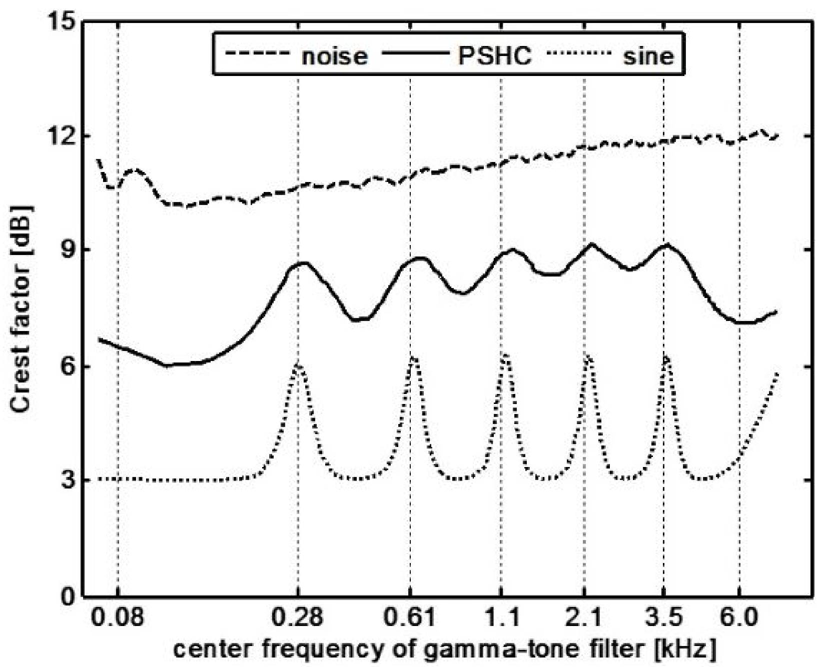

Figure 7.3: Crest factors after gammatone filtering resulting from channel interaction. Crest factors were obtained from the outputs of ERB-spaced gamma-tone filters with center frequencies ranging from 70 to 8000 Hz. Input signals were the unmodulated carriers used during vocoding mixed at a level constant across channels. The Crest factors for both the noise and PSHC signals were averaged across 100 exemplars. Dotted lines indicate the cross-over frequencies of the vocoder's bandpass filters.

7.1.4.2 Comparison with other vocoders

Other alternatives to sine- and noise-vocoders have been proposed, including modulated sine-waves and harmonic complexes with different phase relationships. Strydom and

Hanekom (2011a) multiplied their sine-wave carriers with a 250-Hz half-wave-rectified sinusoid during vocoding, while Lu et al. (2010) imposed Gaussian-shaped envelopes on their sine carriers, hence creating blips to mimic electrical pulses. While evaluating the relevance of different carriers to simulate CI stimulation, it may be necessary to distinguish whether the aim of the vocoder is to simulate low-rate or high-rate electrical stimulation. When using modulated sine-waves as carriers, the rate of the modulator affects the carrier's spectral content. At high rates, side bands will be resolved by the auditory periphery and will provide a salient pitch percept that is absent in CIs. Therefore, modulated sine-wave carriers may only be appropriate to simulate low-rate CI stimulation. In contrast, most contemporary CI strategies stimulate at relatively high rates of 900 pps or more per channel. Although it is clearly not possible to reach such rates on all channels with our vocoder carrier, producing a relatively flat envelope at the output of auditory filters by using PSHCs at their optimal rates may come closer to the electrical signals delivered by real CIs.

Harmonic complexes summed with a fixed sine starting phase can also produce acoustic pulse trains of various rates. Their periodic intrinsic modulation rate equals f_0, hence increasing f_0 increases the pulse rate, and one could envision optimizing these rates to flatten the output of the auditory filters. However, above a certain f_0 that covaries with frequency region, the auditory periphery will resolve individual harmonics, once more creating a salient pitch percept that is absent in CIs. For example, the lower three bands of the vocoder used by Churchill et al. (2014) contained harmonics 2 to 9 which were probably resolved. Similarly, if the PSHC carriers used here were replaced by sine-phase complexes presented at f_0s equal to the PSHC optimal rates, the individual harmonics of all carriers would be resolved. This can be illustrated by considering the pass-band of the highest frequency channel of our vocoder with cut-off frequencies of 3.5 and 6.1 kHz. Using a sine-phase complex with an f_0 of 720 Hz would imply that harmonics 5 to 8 are present in the pass-band.

Assuming one wants to avoid the presence of resolved harmonics in a vocoder, there is a trade-off between the lowest audio channels that can be included and the highest pulse rates that can be obtained. To partially overcome this trade-off, Deeks and Carlyon (2004) used a vocoder based on harmonic complexes with an alternating sine-cosine starting phase. The envelope of this carrier signal repeats at $2f_0$, thus can yield higher pulse rates than a sine-phase complex whilst keeping all harmonics unresolved. However, this may only be true when three or more harmonics interact in a given auditory filter. The output of an auditory filter capturing only two unresolved harmonics of an alternating-phase complex will show a periodic intrinsic modulation at the f_0 (Macherey and Carlyon, 2014). For example, the highest band of the current vocoder corresponds approximately to the HIGH frequency region of Macherey and Carlyon (2014). Their results show that for an alternating-phase complex with an f_0 of 360 Hz, whose rate equals our PSHC optimal rate in the highest audio channel, the outputs of some auditory filters will beat at f0 while some others will beat at $2f_0$. While this effect of different auditory filters beating at different rates may also be present for PSHCs having a high f_0, it seems unlikely to happen in the case of PSHCs with a very dense harmonic spacing as used here, because many components interact in each auditory filter.

7.1.4.3 Implications for simulating CI

Several studies have tried to infer the amount of information available to CI listeners by investigating the vocoder processing parameters that would best match the performance of CI listeners on speech recognition tasks. These approaches are limited by the different excitation processes at stake in acoustic and electrical hearing. The information delivered by a vocoder to an NH subject will be different from a real CI because the synthesized signal is further filtered by the peripheral auditory system instead of being delivered to discrete portions of the auditory-nerve array. Nevertheless, these studies can provide information on the amount of signal degradation that CI listeners experience. For example, Fu and Nogaki (2005) showed that their noise-vocoder needed to have between 8 and 16 spectrally-smeared channels to yield speech scores similar to those obtained with real CI listeners. We would expect a PSHC-vocoder to yield better overall scores than their noise-vocoder and, thus, to require an even lower number of channels to match the performance of their CI listeners. This illustrates the importance of developing vocoders that can produce similar patterns of neural activity as real CIs.

Finally, it is worth noting that the electrical pulse-train carriers used in CIs probably also introduce modulations at the level of the auditory nerve. In other terms, the firing pattern produced by a constant-amplitude high-rate electrical pulse train is not a constant train of action potentials. Refractoriness, spike-rate adaptation, accommodation and facilitation may produce temporal interactions between consecutive electrical pulses (Boulet et al., 2015), thereby creating modulations in the auditory nerve's firing pattern that interact with the modulations of the speech signal envelope. Nevertheless, these effects, probably also present to some extent in normal acoustic hearing, are introduced at the level of the auditory nerve or more centrally but not peripherally, as is the case for noise carriers used in channel vocoders with normal-hearing subjects. Therefore, it appears to us that minimizing the intrinsic modulations present at the periphery of a normal-hearing ear is a first step to bring acoustic simulations closer to CI perception. While the PSHC-vocoder seems an appropriate tool to achieve this goal, Hilkhuysen and Macherey (2014) noted that it may benefit from further tuning by taking into account the phase curvature of the auditory filters and the fact that auditory filters usually broaden with sound level. This implies that a more optimal pulse rate, different from that predicted by a gamma-tone filterbank, may give rise to even better SRTs with PSHC-vocoding.

To conclude, we have shown that a PSHC-vocoder yields different speech intelligibility scores than sine- and noise-carrier vocoders. Although finding the carrier that can best simulate CIs will eventually require a direct comparison of acoustic and electrical stimulation in CI subjects with residual hearing, we note that a PSHC carrier appears to combine several advantages over other acoustic carriers to simulate contemporary CI strategies with a vocoder. It is a wide band signal and can thus be shaped in the spectral domain to simulate different spatial spreads of excitation and it can be tuned to exhibit less intrinsic modulations than Gaussian noise. Furthermore, it is pulsatile and provides a way to investigate pulse-rate effects without modifying the long-term spectral content of the sound.

7.2 Complementary informations on Pulse Spreading Harmonic Complexes, PSHC

This section aims to provide further information on the generation of PSHC stimuli. Considering a harmonic series with a fundamental frequency f_0, adding all different harmonics with the same starting phase yields a pulsatile acoustic signal with a rate of f_0. This time, if one adds only odd terms of the harmonic series, the resulting signal will have a rate $2 * f_0$ while the fundamental frequency remains equal to f_0. The same process can be done with even harmonics. Finally if we impose a delay of half the period between those two peaky signal and add them together we end up with a peaky signal with a fundamental frequency equal to f_0 but a rate of $4 * f_0$. This concept is used in the generation of high rate PSHCs and can be expressed in the mathematical form as in equation 7.1, where k is referred to as the *order* of the PSHC and defines the number of sub-complexes. The rate of the resulting PSHC is k^2.

$$s(t,k) = \sum_{i=m}^{N} sin(2\pi.f_0.i.t + \phi(i,k)) \tag{7.1}$$

Figure 7.4 illustrates the generation of a PSHC stimulus with an order $k = 7$. Each line represents a given sub-harmonic series in the spectral domain (left panels) and the sum of harmonics in the time domain (right panels).

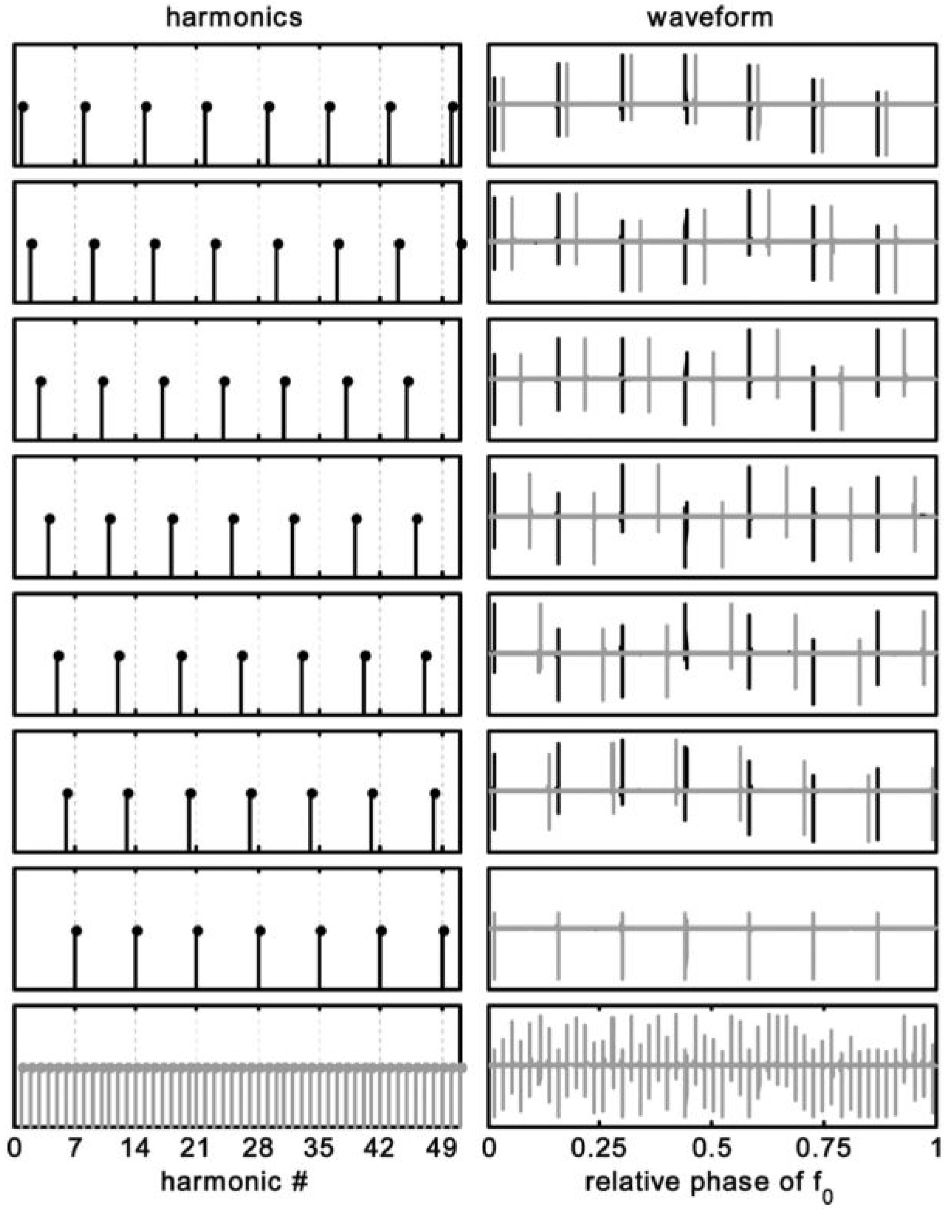

Figure 7.4: Composition of a seventh order PSHC. The harmonic series is decomposed in mutually exclusive sub-complexes that have harmonic spacing equal to the order of the PSHC (left top-seven panels). Mixing the harmonics within a sub-complex with a fixed phase results in a waveform with seven pulses per period (black lines in right top-seven panels). Waveforms of sub-complexes are delayed such that the pulses are spread evenly within a period of the PSHC (gray lines in right top-seven panels). Gray and black lines overlap in the seventh subpanel. Adding the waveforms of the sub-complexes results in a PSHC with a waveform showing 72 pulses per period (bottom-row panels).from Hilkhuysen and Macherey (2014)

7.3 Device characteristics

7.3.1 The HiFocus 1j electrode array

In this thesis, all experiments involving CI stimulation were carried out using the HiRes 90k device (Advanced Bionics). Figures 7.5 and 7.6 represent the internal part of this device. The electrode array HiFocus 1J is composed of 16 rectangular contacts ($0.5 \times 0.4mm^2$) spaced by 1.1mm and two remote ground electrodes, one large case electrode (represented in figure 7.5) and one ring electrode.

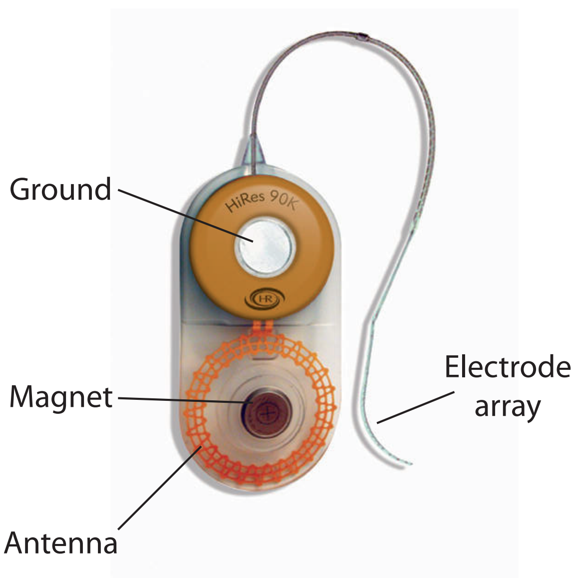

Figure 7.5: Internal part of the HiRes 90k device.

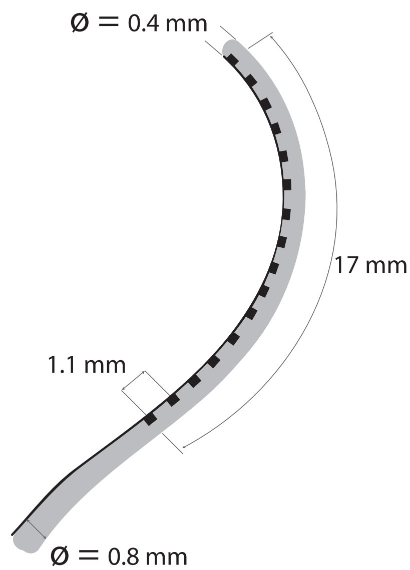

Figure 7.6: Illustration and dimensions of the HiFocus 1J electrode array.

7.3.2 Compliance limit

The compliance limit defines the maximum voltage that can be delivered by the current sources across a given electrode and the ground. Below the compliance limit, the voltage output is linearly proportional to the current input, while above the compliance limit the voltage output plateaus. In CI experiments one wants to make sure that this limit is never reached. The compliance limit of an experimental HiRes 90k device was measured by connecting the sources output to a 10 kΩ resistive load. Figure 7.7 displays the voltage output as a function a the input current level for all 16 sources. Voltage output grows linearly with the current input up to 7V and then reaches an asymptote. This value was used in all experiments in this study as the device compliance limit.

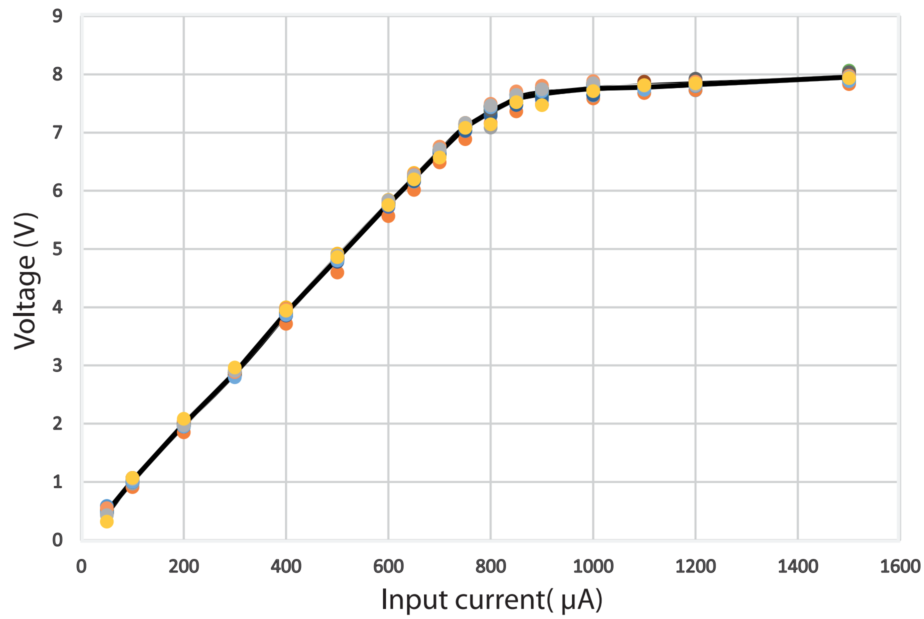

Figure 7.7: Source output voltage across a resistive load of 10 kΩ as a function of the current level. Black line indicates the average voltage output.

7.3.3 Communication with the implant

In both in vitro and in vivo experiments, stimuli and recording were made using Matlab custom softwares that serve as an interface for the BEDCS software (Bionic Ear Data Collection System, Litvak (2003)) which controls the device. All stimuli are defined by concatenating monophasic square pulses. For instance, the sequence [-1,1] generates a cathodic-first biphasic pulse. The duration of each phase is defined as a multiple of the smallest clock-step, 0.898 μs. The amplitude is defined in μA and is applied to the entire stimulus sequence. One important feature of the Advanced Bionics HiRes device is that it is provided with 16 independent current sources which enables to create 16 independent stimulation sequences.

Recordings can be made either between one intracochlear electrode and one of the ground electrodes or between two intracochlear electrodes. The sampling rate can be set to 9-, 28- or 56 kHz and the internal amplifier gain can be 1, 3, 6, 18, 33, 100, 300 or 1000dB. Stimulation sequences and recording must be designed keeping in mind that the recording buffer depends on both the stimulus complexity (length of the sequence) and the sampling rate.

7.3.4 Safety

During all experiments, a careful attention was given to ensure CI users comfort and safety.

1. All stimuli were charge-balanced to avoid damages on the electrode and inner ear biological tissues.

2. A maximum charge density limit was fixed at $100\mu C/cm^2$, considering the surface of the electrode $S = [0.05 * 0.04]cm^2$

3. Before each experiment with CI participants, stimuli waveforms were visualized and checked on an oscilloscope.

4. Because of an important inter- and within-subject variability of perception it is almost impossible to predict the loudness of a given stimulus. In chapters 3, 4, 5, to avoid any discomfort for CI participants, all stimuli were first tested at the lowest level and increased to reach the desired amplitude depending subjects feedback.

7.4 Implementation of the polarization impedance model

7.4.1 Contact impedance model equations

Complete model

The polarization impedance was modeled using the equivalent electrical circuit of figure 7.8. Chapter 3 enabled to identify the presence of a parasitic capacitance C_p. In the present model, the effect of C_p was included by changing the current input waveforms. We now consider a biphasic current pulse with exponential transients (time constant τ, defined as $R_a \times C_p$) as the input signal. If we consider the input current waveform in figure 7.9, its mathematical expression can be written as in equation 7.9, where $H(t)$ is the Heaviside step function.

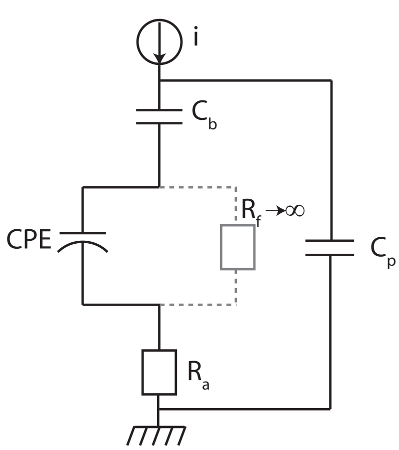

Figure 7.8: Equivalent electrical circuit used to model the polarization impedance.

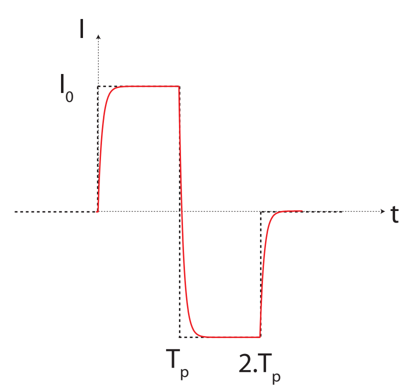

Figure 7.9: Illustration of the input current waveform. I_0 is the current amplitude and T_p is the phase duration.

To be able to compute an analytical solution, this problem is converted in Laplace domain. Equation 7.2 becomes equation 7.3.

$$I(t) = I_0.\left[(1 - e^{-\frac{t}{\tau}}) - 2.(1 - e^{-\frac{(t-T_p)}{\tau}}).H(T_p) + (1 - e^{-\frac{(t-2.T_p)}{\tau}}).H(2.T_p)\right] \tag{7.2}$$

$$\mathscr{L}(I(t)) = I_0.\left[(\frac{1}{s} - \frac{1}{s+\frac{1}{\tau}}) - 2.e^{-T_p.s}(\frac{1}{s} - \frac{1}{s+\frac{1}{\tau}}) + e^{-2.T_p.s}(\frac{1}{s} - \frac{1}{s+\frac{1}{\tau}})\right] \tag{7.3}$$

$$Z(s) = R_a + \frac{1}{C_b.s} + \frac{1}{Y_0}.\left(\frac{1}{s^\alpha + \frac{1}{R_f.Y_0}}\right) \tag{7.4}$$

The voltage across the entire circuit in the Laplace domain (eq. 7.5) is obtain by multiplying equation 7.3 and the overall circuit impedance (without C_p) whose Laplace transform is given by the equation 7.4.

$$U(s) = I_0.\left[Z(s).\frac{1}{s} - 2.e^{-Tp.s}.Z(s).\frac{1}{s} + e^{-2Tp.s}.Z(s).\frac{1}{s}\right]...$$

$$... - I_0.\left[Z(s).\frac{1}{s+1/\tau} - 2.e^{-Tp.s}.Z(s).\frac{1}{s+1/\tau} + e^{-2Tp.s}.Z(s).\frac{1}{s+1/\tau}\right] \tag{7.5}$$

Rearranging the terms of this expression and after transformation back in the time domain, one distinguish in this solution the contribution of a perfect square pulse and the contribution of the transients. The exact solution in the time domain can thus be written as in equations 7.6.

$$\begin{cases} U(t) = I_0.\left[f(t).H(0) - 2.f(t).H(T_p) + f(t).H(2.T_p)\right]... \\ ... - I_0.\left[\tilde{f}(t).H(0) - 2.\tilde{f}(t).H(T_p) + \tilde{f}(t).H(2.T_p)\right] \\ with, \\ f(t) = \mathscr{L}^{-1}(Z(s).\frac{1}{s}) \\ \tilde{f}(t) = \mathscr{L}^{-1}(Z(s).\frac{1}{s+\frac{1}{\tau}}) \end{cases} \tag{7.6}$$

To obtain an analytical solution, one needs to solve both $f(t)$ and $\tilde{f}(t)$. Let us start with $f(t)$ whose expression can be developed as in equations 7.7.

$$\begin{cases} f(t) = \mathscr{L}^{-1}\left(R_a.\frac{1}{s} + \frac{1}{C_b.s^2} + \frac{1}{Y_0.s}.\frac{1}{s^\alpha + \frac{1}{R_f.Y_0}}\right) \\ f(t) = R_a + \frac{t}{C_b} + g(t) \\ with, \\ g(t) = \mathscr{L}^{-1}\left(\frac{1}{Y_0.s}.\frac{1}{s^\alpha + \frac{1}{R_f.Y_0}}\right) \end{cases} \tag{7.7}$$

$g(t)$ can then be expressed involving a geometric series (equation 7.8).

$$\begin{cases} g(t) = \mathscr{L}^{-1}\left(\frac{1}{Y_0.s}.\frac{1}{s^\alpha + \frac{1}{R_f.Y_0}}\right) \\ g(t) = \frac{1}{Y_0}.\mathscr{L}^{-1}\left(\frac{1}{s^{\alpha+1}}.\sum_{k=0}^{\infty}\left(\frac{-1}{R_f.Y_0.s^\alpha}\right)^n\right) \\ g(t) = \frac{1}{Y_0}.\mathscr{L}^{-1}\left(\frac{1}{s^{\alpha+1}}.\sum_{k=0}^{\infty}\left(\frac{-1}{R_f.Y_0}\right)^n.\frac{1}{s^{\alpha n}}\right) \\ g(t) = \frac{1}{Y_0}.\mathscr{L}^{-1}\left(\sum_{k=0}^{\infty}\left(\frac{-1}{R_f.Y_0}\right)^n.\frac{1}{s^{\alpha n+\alpha+1}}\right) \end{cases} \tag{7.8}$$

At this stage, to be able to solve this expression, one needs to involve the Γ function as in equations 7.9 which introduces a known Laplace function, $\Gamma(x)/s^x$.

$$g(t) = \frac{1}{Y_0}.\sum_{k=0}^{\infty}\left(\frac{-1}{R_f.Y_0}\right)^n.\mathscr{L}^{-1}\left(\frac{\Gamma(\alpha n+\alpha+1)}{s^{\alpha n+\alpha+1}}.\frac{1}{\Gamma(\alpha n+\alpha+1)}\right) \tag{7.9}$$

We can then write:

$$\begin{cases} g(t) = \frac{1}{Y_0}.\sum_{k=0}^{\infty}\left(\frac{-1}{R_f.Y_0}\right)^n.t^{\alpha n+\alpha}.\frac{1}{\Gamma(\alpha n+\alpha+1)} \\ g(t) = \frac{1}{Y_0}.\sum_{k=0}^{\infty}\left(\frac{-1}{R_f.Y_0}\right)^n.\frac{t^{\alpha n}}{\Gamma(\alpha n+\alpha+1)}.t^\alpha \end{cases} \tag{7.10}$$

A final analytical solution can be written using the $Mittag-Leffler$ function, whose general expression is given by the equation 7.11 and by including the expression of $f(t)$ (equation 7.14) in the equation 7.6.

$$E_{\gamma,\beta}(t) = \sum_{k=0}^{\infty}\frac{t^k}{\Gamma(\gamma.k+\beta)} \tag{7.11}$$

$$g(t) = \frac{t^\alpha}{Y_0}.E_{\alpha,\alpha+1}(\frac{-t^\alpha}{R_f.Y_0}) \tag{7.12}$$

Following the same procedure one can solve $\tilde{f}(t)$.

$$\begin{cases} \tilde{f}(t) = \mathscr{L}^{-1}\left(R_a.\frac{1}{s+1/\tau} + \frac{1}{C_b.s}.\frac{1}{s+1/\tau} + \frac{1}{Y_0}.\frac{1}{s^\alpha+\frac{1}{R_f.Y_0}}.\frac{1}{s+1/\tau}\right) \\ \tilde{f}(t) = R_a.e^{-\frac{1}{\tau}} + \frac{\tau}{C_b}.(1-e^{-\frac{t}{\tau}}) + \frac{1}{Y_0}.(\tilde{g}(t) * e^{-\frac{1}{\tau}}) \\ \tilde{g}(t) = \mathscr{L}^{-1}(\frac{1}{s^\alpha+\frac{1}{R_f.Y_0}}) \end{cases} \tag{7.13}$$

$$\tilde{g}(t) = t^{\alpha-1}.E_{\alpha,\alpha}(\frac{-t^\alpha}{R_f.Y_0}) \tag{7.14}$$

Simplification

In Chapter 3, the parameter R_f was removed from the model. In this case the overall solution can be simplified by replacing $f(t)$ and $\tilde{f}(t)$ in equation 7.7 by $f_{simplified}(t)$ and $\tilde{f}_{simplified}(t)$as in equation 7.15.

$$\begin{cases} f_{simplified}(t) = R_a + \frac{t}{C_b} + \frac{1}{Y_0.\Gamma(\alpha+1)}.t^{\alpha} \\ \tilde{f}_{simplified}(t) = R_a.e^{-\frac{1}{\tau}} + \frac{\tau}{C_b}.(1 - e^{-\frac{t}{\tau}}) + \frac{1}{Y_0}.t^{\alpha}.E_{1,\alpha+1}(\frac{-t}{\tau}) \end{cases} \tag{7.15}$$

7.4.2 Partial polarization model

Based on the observations in both the spectral and temporal domain, it is likely that the parasitic phenomenon identified in section 3.3.1 can be described using an alternative polarization model. For transimpedance measurements, the equivalent electrical circuit has to be slightly modified as in figure 7.10 and the analytical solution (eq. 7.16) can be obtained following the same procedure as for the contact impedance.

$$\begin{cases} f_{partial}(t) = Z + \frac{1}{Y_0.\Gamma(\alpha+1)}.t^{\alpha} \\ \tilde{f}_{partial}(t) = Z.e^{-\frac{1}{\tau}} + \frac{1}{Y_0}.t^{\alpha}.E_{1,\alpha+1}(\frac{-t}{\tau}) \end{cases} \tag{7.16}$$

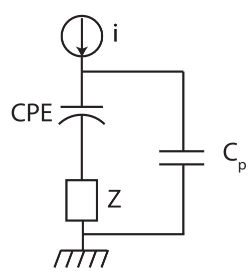

Figure 7.10: Equivalent electrical circuit for partially polarized transimpedances

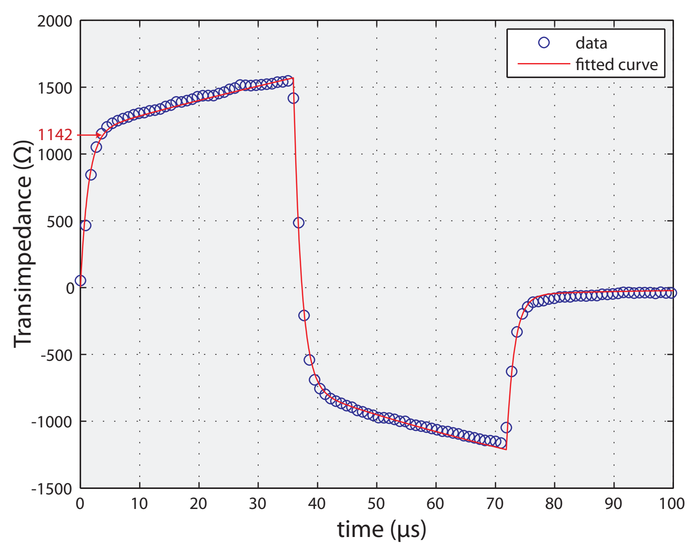

Figure 7.11: Partially polarized transimpedance recording. Circles indicate samples and red curve represents the model output. The arrow indicates the estimated transimpedance.

Figure 7.11 represents an example of distorted waveform recorded in subject S5, and the partial polarization model output. Estimating the transimpedance by measuring half the peak-to-peak amplitude would yield a value of 1355 Ω while the present model predicts an actual transimpedance of 1142 Ω.

Contributions

Publications

- Q. Mesnildrey, and O. Macherey, (2015). “Simulating the dual-peak excitation pattern produced by bipolar stimulation of a cochlear implant: Effects on speech intelligibility”, *Hear. Res.* 319, 32–47.

- Q. Mesnildrey, G. Hilkhuysen and O. Macherey, (2016). “Pulse-spreading harmonic complex as an alternative carrier for vocoder simulations of cochlear implants”, *J. Acoust. Soc. Am.* 139, 986–991

Conferences

- Q. Mesnildrey and O. Macherey. Simulations Acoustiques de l’Implant Cochléaire : modélisation de la configuration géométrique des électrodes et effets sur la perception de la parole. Journées des Jeunes Chercheurs en Acoustique Audio et Signal (JJCAAS), December 2012, Marseille, France (poster)

- Q. Mesnildrey and O. Macherey. Simulating the bimodal excitation spread produced by bipolar stimulation : Effect on speech intelligibility. Conference on Implantable Auditory Prosthese (CIAP), July 2013, Lake Tahoe, CA, USA (poster)

- Q. Mesnildrey and O. Macherey. Simulation Acoustique de l’Implant Cochléaire : Influence des patterns d’excitation bimodaux (stimulation bipolaire) sur l’intelligibilité de la parole, Congrès Français d’Acoustique (CFA), April 2014, Poitiers, France (poster)

- Q. Mesnildrey, O. Macherey and P. Herzog. Optimisation du codage spatio-temporel de l’information sonore dans l’implant cochléaire : Vers une caractérisation sujet-spécifique de l’interface électrode/neurones. Journées des Jeunes Chercheurs en Acoustique Audio et Signal (JJCAAS), July 2014, Lyon, France (poster)

- Q. Mesnildrey and O. Macherey. Simulating the bimodal spread of excitation produced by bipolar stimulation in cochlear implant: Effects on speech intelligibility. 6^{th} Speech In Noise Workshop (SPIN), January 2014, Marseille, France (talk)

- Q. Mesnildrey, O. Macherey, F. Venail and P. Herzog. Impedance measures for subject-specific optimization of spatial selectivity. Conference on Implantable Auditory Prosthese (CIAP), July 2015, Lake Tahoe, CA, USA (poster)

- Q. Mesnildrey, O. Macherey, F. Venail and P. Herzog. Mesures d'impédances pour l'optimisation de la sélectivité spatiale de la stimulation électrique par l'implant cochléaire. Congrès Français d'Acoustique (CFA), April 2016, Le Mans, France (talk)

- Q. Mesnildrey, O. Macherey, F. Venail and P. Herzog. Objective measures for subject-specific optimization of spatial selectivity. 9^{th} International Symposium on Objective Measures in Auditory Implants (OMAI), June 2016, Szeged, Hungary (talk)

Bibliography

F. Apoux and S.P. Bacon. Differential contribution of envelope fluctuations across frequency to consonant identification in quiet. *J. Acoust. Soc. Am.*, 123(5):2792, 2008a. doi: 10.1121/1.2897916.

F. Apoux and S.P. Bacon. Selectivity of modulation interference for consonant identification in normal-hearing listeners. *J. Acoust. Soc. Am.*, 123(3):1665–1672, 2008b. doi: 10.1121/1.2828067.

J.M Aronoff and D.M. Landsberger. The development of a modified spectral ripple test. *J. Acoust. Soc. Am.*, 134(2):EL217–22, 2013. ISSN 1520-8524. doi: 10.1121/1.4813802.

B. Barbour. Electronics for electrophysiologists. 2014.

D. Baskent and R.V. Shannon. Speech recognition under conditions of frequency-place compression and expansion. *J. Acoust. Soc. Am.*, 113(4 Pt 1):2064–2076, 2003. ISSN 00014966. doi: 10.1121/1.1558357.

D. Baskent and R.V. Shannon. Interactions between cochlear implant electrode insertion depth and frequency-place mapping. *J. Acoust. Soc. Am.*, 117(3):1405–1416, 2005. doi: 10.1121/1.1856273.

S.B. Baumann, D.R. Wozny, S.K. Kelly, and F.M. Meno. The electrical conductivity of human cerebrospinal fluid at body temperature. *IEEE Trans. Biomed. Eng.*, 44 (3):220–225, 1997. ISSN 00189294. doi: 10.1109/10.554770.

C.K. Berenstein, L.H.M. Mens, J.J.S. Mulder, and F.J. Vanpoucke. Current Steering and Current Focusing in Cochlear Implants : Comparison of Monopolar , Tripolar , and Virtual Channel Electrode Configurations. *Ear Hear.*, 29(2):250–260, 2008.

C.K. Berenstein, F.J. Vanpoucke, J.J.S. Mulder, and L.H.M. Mens. Electrical field imaging as a means to predict the loudness of monopolar and tripolar stimuli in cochlear implant patients. *Hear. Res.*, 270(1-2):28–38, 2010. ISSN 03785955. doi: 10.1016/j.heares.2010.10.001. URL http://dx.doi.org/10.1016/j.heares.2010.10.001.

J.A. Bierer. Probing the electrode-neuron interface with focused cochlear implant stimulation. *Trends Amplif.*, 14(2):84–95, jun 2010. ISSN 1940-5588. doi: 10.1177/1084713810375249.

J.A. Bierer and K.F. Faulkner. Identifying cochlear implant channels with poor electrode-neuron interface: partial tripolar, single-channel thresholds and psychophysical tuning curves. *Ear Hear.*, 4(164):247–258, 2010. ISSN 15378276. doi: 10.1126/scisignal.2001449.Engineering.

J.A. Bierer and J.C. Middlebrooks. Auditory cortical images of cochlear-implant stimuli: dependence on electrode configuration. *J. Neurophysiol.*, 87(1):478–492, 2002. ISSN 0022-3077. doi: 10.1152/jn.00212.2001.

J.A. Bierer, S.M. Bierer, and J.C. Middlebrooks. Partial tripolar cochlear implant stimulation: Spread of excitation and forward masking in the inferior colliculus. *Hear. Res.*, 4(164):134–142, 2011. ISSN 15378276. doi: 10.1126/scisignal.2001449.Engineering.

J.A. Bierer, S.M. Bierer, H.A. Kreft, and A.J. Oxenham. A Fast Method for Measuring Psychophysical Thresholds Across the Cochlear Implant Array. *Trends Hear.*, 19: 1–12, 2015. doi: 10.1177/2331216515569792.

J.S. Binette. Tetrapolar Measurement of Electrical Conductivity and Thickness of Articular Cartilage. *J. Biomech. Eng.*, 126(4):475, 2004. ISSN 0148-0731. doi: 10.1115/1.1785805.

M.G. Bingabr, B. Espinoza-Varas, and P.C. Loizou. Simulating the Effect of Spread of Excitation in Cochlear Implants. *Hear. Res.*, 241:73–79, 2008. doi: 10.1016/j.heares.2008.04.012.SIMULATING.

M.G. Bingabr, B. Espinoza-varas, and S. Sigdel. Measurements of monopolar and bipolar current spreads using forward-masking with a fixed probe. *Cochlear Implant Int.*, 15(3):166–172, 2014.

P. Blamey, F. Artieres, D. Başkent, F. Bergeron, A. Beynon, E. Burke, N. Dillier, R. Dowell, B. Fraysse, S. Gallégo, P.J. Govaerts, K. Green, A.M. Huber, A. Kleine-Punte, B. Maat, M. Marx, D. Mawman, I. Mosnier, A.F. O'Connor, S. O'Leary, A. Rousset, K. Schauwers, H. Skarzynski, P.H. Skarzynski, O. Sterkers, A. Terranti, E. Truy, P. Van De Heyning, F. Venail, C. Vincent, and D.S. Lazard. Factors affecting auditory performance of postlinguistically deaf adults using cochlear implants: An update with 2251 patients. *Audiol. Neurotol.*, 18(1):36–47, jan 2013. ISSN 1421-9700. doi: 10.1159/000343189.

J.M Bland and D.G. Altman. Calculating correlation coefficients with repeated observations: Part 1 - correlation within subjects. *BMJ*, 310:446, 1995.

S.E Blumstein, E. Isaacs, and J. Mertus. The role of the gross spectral shape as a perceptual cue to place articulation in initial stop consonants. *J. Acoust. Soc. Am.*, 72(1):43–50, 1982.

C. Boëx, M. Kós, and M. Pelizzone. Forward masking in different cochlear implant systems. *J. Acoust. Soc. Am.*, 114(4 Pt 1):2058–2065, 2003. ISSN 00014966. doi: 10.1121/1.1610452.

A.S. Bondarenko and G.A. Ragoisha. EIS Spectrum Analyser. In Pomerantsev A. L., editor, *Prog. Chemom. Res.*, pages 89–102. Nova Science Publishers, New York, 2005.

B.H. Bonham and L.M. Litvak. Current Focusing and Steering. *Hear. Res.*, 242((1-2)): 141–153, 2008. doi: 10.1016/j.heares.2008.03.006.

R.M. Bonnet, J.H.M. Frijns, S. Peeters, and J.J. Briaire. Speech recognition with a cochlear implant using triphasic charge-balanced pulses. *Acta Otolaryngol.*, 124(4): 371–375, 2004. ISSN 0001-6489. doi: 10.1080/00016480410031084.

J. Boulet, M.W. White, and I.C. Bruce. Temporal Considerations for Stimulating Spiral Ganglion Neurons with Cochlear Implants. *JARO - J. Assoc. Res. Otolaryngol.*, 17 (1):1–17, 2015. ISSN 14387573. doi: 10.1007/s10162-015-0545-5.

J.J. Briaire and J.H.M. Frijns. Field patterns in a 3D tapered spiral model of the electrically stimulated cochlea. *Hear. Res.*, 148(1-2):18–30, 2000.

J. Campbell and A. Sharma. Cross-modal re-organization in adults with early stage hearing loss. *PLoS One*, 9(2), 2014. ISSN 19326203. doi: 10.1371/journal.pone.0090594.

R.P. Carlyon, O. Macherey, J.H.M. Frijns, P.R. Axon, R.K. Kalkman, P. Boyle, D.M. Baguley, J. Briggs, J.M. Deeks, J.J. Briaire, X. Barreau, and R. Dauman. Pitch comparisons between electrical stimulation of a cochlear implant and acoustic stimuli presented to a normal-hearing contralateral ear. *J. Assoc. Res. Otolaryngol.*, 11(4): 625–640, dec 2010. ISSN 1438-7573. doi: 10.1007/s10162-010-0222-7.

M. Chatterjee, J.J. Galvin, Q.J. Fu, and R.V. Shannon. Effects of stimulation mode, level and location on forward-masked excitation patterns in cochlear implant patients. *JARO - J. Assoc. Res. Otolaryngol.*, 7(1):15–25, mar 2006. ISSN 1525-3961. doi: 10.1007/s10162-005-0019-2.

C. T M Choi, Wei Dian Lai, and Sih Sian Lee. A novel approach to compute the impedance matrix of a cochlear implant system incorporating an electrode-tissue interface based on finite element method. *IEEE Trans. Magn.*, 42(4):1375–1378, 2006. ISSN 00189464. doi: 10.1109/TMAG.2006.872461.

T.H. Churchill, A. Kan, M.J. Goupell, A. Ihlefeld, and R.Y. Litovsky. Speech perception in noise with a harmonic complex excited vocoder. *J. Assoc. Res. Otolaryngol.*, 15

(2):265–278, apr 2014. ISSN 1438-7573. doi: 10.1007/s10162-013-0435-7. URL http://www.ncbi.nlm.nih.gov/pubmed/24448721.

B.M. Clopton and F.A. Spelman. Neural mechanisms relevant to the design of an auditory prothesis. Location and electrical characteristics, 1982. ISSN 00034894.

L.T. Cohen, E. Saunders, M.R Knight, and R.S.C. Cowan. Psychophysical measures in patients fitted with Contour and straight Nucleus electrode arrays. *Hear. Res.*, 212 (1-2):160–75, feb 2006. ISSN 0378-5955. doi: 10.1016/j.heares.2005.11.005.

A. Coordes, A. Ernst, G. Brademann, and I. Todt. Round Window Membrane Insertion With Perimodiolar Cochlear Implant Electrodes. *Otol. Neurotol.*, 34(6):1027–1032, 2013. ISSN 1531-7129. doi: 10.1097/MAO.0b013e318280da2a. URL http://content.wkhealth.com/linkback/openurl?sid=WKPTLP:landingpage{&}an=00129492-201308000-00010.

P. Cordoba-Torres, T.J. Mesquita, and R. P. Nogueira. On the Relationship between the Origin of Constant- Phase Element Behavior in Electrochemical Impedance Spectroscopy and Electrode Surface Structure. *J. Phys. Chemestry*, 119(8):4136–4147, 2015. doi: 10.1021/jp512063f.

J.D. Crew, J.J. Galvin III, and Q.J. Fu. Channel interaction limits melodic pitch perception in simulated cochlear implants. *J. Acoust. Soc. Am. Express Lett.*, 132 (October 2012):429–435, 2012.

O. Crouzet and W.A. Ainsworth. On the Various Influences of Envelope Information on the Perception of Speech in Adverse Conditions: An Analysis of Between-Channel Envelope Correlation. In *Eurospeech'2001*, pages 2–5, 2001.

M.H. Davis, I.S. Johnsrude, A. Hervais-Adelman, K. Taylor, and C. McGettigan. Lexical information drives perceptual learning of distorted speech: evidence from the comprehension of noise-vocoded sentences. *J Exp Psychol Gen*, 134(2):222–241, 2005. ISSN 0096-3445. doi: 2005-04168-006[pii]\n10.1037/0096-3445.134.2.222.

T.J. Davis, D. Zhang, R.H. Gifford, B.M. Dawant, R.F. Labadie, and J.H. Noble. Relationship Between Electrode-to-Modiolus Distance and Current Levels for Adults With Cochlear Implants. *Otol. Neurotol.*, 37(4):31–37, 2015.

J.M. Deeks and R.P. Carlyon. Simulations of cochlear implant hearing using filtered harmonic complexes: implications for concurrent sound segregation. *J. Acoust. Soc. Am.*, 115(4):1736–1746, 2004. ISSN 00014966. doi: 10.1121/1.1675814.

G. Desmadryl, S. Gaboyard-Niay, A. Brugeaud, C. Travo, A. Broussy, A. Saleur, J. Dyhrfjeld-Johnsen, E. Wersinger, and C. Chabbert. Histamine H 4 receptor antagonists as potent modulators of mammalian vestibular primary neuron excitability. *Br. J. Pharmacol.*, 167(4):905–916, 2012. ISSN 1476-5381. doi: 10.1111/j.1476-5381.2012.02049.x.

Y.Y. Duan, G.M. Clark, and R.S.C. Cowan. A study of intra-cochlear electrodes and tissue interface by electrochemical impedance methods in vivo. *Biomaterials*, 25(17): 3813–28, 2004. ISSN 0142-9612. doi: 10.1016/j.biomaterials.2003.09.107.

A.M. Dymond. Characteristics of the Metal-Tissue Interface of Stimulation Electrodes. *IEEE Trans. Biomed. Eng.*, 23(4):274–280, 1976. doi: 10.1109/TBME.1976.324585.

D.K. Eddington and M. Whearty. Electrode interaction and speech reception using lateral-wall and medial-wall electrode systems. In *Conf. Implant. Audit. Prostheses*, Pacific Grove CA, 2001.

D.K. Eddington, J. Tierney, V. Noel, B. Hermann, M. Whearty, and C.C. Finley. Speech processors for auditory prostheses. Ninth quarterly progress report, NIH contract N01-DC-2-1001,Neural Prosthesis Program, National Institutes of Health, Bethesda, MD. Technical report, NIH, 2004.

E. Erixon, H. Hogstorp, K. Wadin, and H. Rask-andersen. Variational Anatomy of the Human Cochlea : Implications for Cochlear Implantation. *Otol. Neurotol.*, 00(NOVEMBER 2008):14–22, 2008. ISSN 1531-7129. doi: 10.1097/MAO.0b013e31818a08e8.

E. Felder, A. Scholtz, H. Rask-Andersen, and A. Schrott-Fischer. Quantitative evaluation of cochlear neurons and computer-aided three-dimensional reconstruction of spiral ganglion cells in humans with a peripheral loss of nerve fibres. *Hear. Res.*, 105: 183–190, 1997.

C. Fielden, K. Kluk, and C.M. McKay. Place specificity of monopolar and tripolar stimuli in cochlear implants: the influence of residual masking. *J. Acoust. Soc. Am.*, 133(6):4109–23, 2013. ISSN 1520-8524. doi: 10.1121/1.4803909.

C.C. Finley, B.S. Wilson, and M.W. White. Models of Neural Responsiveness to Electrical Stimulation. In *Cochlear Implant. Model. Electr. Stimul. Ear*, chapter 5, pages 55–96. Springer, New York, 1990. doi: 10.1007/978-1-4612-3256-8_5.

K. Fishman, R.V. Shannon, and W.H. Slattery. Speech Recognition as a function of the number of electrodes used in the SPEAK cochlear Implant Speech processor. *J. Speech, Lang. Hear. Res.*, 40:1201–1215, 1997.

W. Franks, I. Schenker, P. Schmutz, and A. Hierlemann. Impedance characterization and modeling of electrodes for biomedical applications. *IEEE Trans. Biomed. Eng.*, 52(7):1295–302, 2005. ISSN 0018-9294. doi: 10.1109/TBME.2005.847523.

G.Y. Fridman and R.T. Karunasiri. REMOVING ARTIFACT IN EVOKED COMPOUND ACTION POTENTIAL RECORDINGS IN NEURAL STIMULATORS, 2010.

L.M. Friesen, R.V. Shannon, D. Baskent, and X. Wang. Speech recognition in noise as a function of the number of spectral channels: Comparison of acoustic hearing and cochlear implants. *J. Acoust. Soc. Am.*, 110(2):1150, 2001. doi: 10.1121/1.1381538.

J.H.M. Frijns, S. L. De Snoo, and J. H. Ten Kate. Spatial selectivity in a rotationally symmetric model of the electrically stimulated cochlea. *Hear. Res.*, 95(1-2):33–48, 1996. ISSN 03785955. doi: 10.1016/0378-5955(96)00004-4.

J.H.M. Frijns, D.M.T. Dekker, and J.J. Briaire. Neural excitation patterns induced by phased-array stimulation in the implanted human cochlea. *Acta Otolaryngol.*, 131 (4):362–370, 2011. ISSN 0001-6489. doi: 10.3109/00016489.2010.541939.

Q.J. Fu and G. Nogaki. Noise susceptibility of cochlear implant users: the role of spectral resolution and smearing. *J. Assoc. Res. Otolaryngol.*, 6(1):19–27, 2005. ISSN 1525-3961. doi: 10.1007/s10162-004-5024-3.

Q.J. Fu and R.V. Shannon. Recognition of spectrally degraded and frequency-shifted vowels in acoustic and electric hearing. *J. Acoust. Soc. Am.*, 105(3):1889–1900, 1999.

C.D. Fuller, J.J. Galvin III, B. Maat, R.H. Free, and D. Başkent. The musician effect: Does it persist under degraded pitch conditions of cochlear implant simulations? *Front. Neurosci.*, 8(8 JUN):1–16, 2014. ISSN 1662453X. doi: 10.3389/fnins.2014.00179.

E. Gaudrain and D. Başkent. Factors limiting vocal-tract length discrimination in cochlear implant simulations. *J. Acoust. Soc. Am.*, 137(3):1298–1308, 2015. ISSN 0001-4966. doi: 10.1121/1.4908235. URL http://scitation.aip.org/content/asa/journal/jasa/137/3/10.1121/1.4908235.

B.R. Glasberg and B.C.J. Moore. Derivation of auditory filter shapes from notched-noise data. *Hear. Res.*, 47(1-2):103–138, 1990. ISSN 03785955. doi: 10.1016/0378-5955(90)90170-T.

R. Glueckert, K. Pfaller, A. Kinnefors, H. Rask-Andersen, and A. Schrott-Fischer. The human spiral ganglion: New insights into ultrastructure, survival rate and implications for cochlear implants. *Audiol. Neurotol.*, 10(5):258–273, 2005. ISSN 1420-3030. doi: 10.1159/000086000.

J.H. Goldwyn, S.M. Bierer, and J.A. Bierer. Modeling the Electrode-Neuron Interface of Cochlear Implants: Effects of Neural Survival, Electrode Placement, and the Partial Tripolar Configuration. *Hear. Res.*, 268:93–104, 2010. doi: 10.1016/j.heares.2010.05.005.Modeling.

Q. Gopen, J.J. Rosowski, and S.N. Merchant. Anatomy of the normal human cochlear aqueduct with functional implications. *Hear. Res.*, 107(1-2):9–22, 1997. doi: 10.1016/S0378-5955(97)00017-8.

M. Gouy. Sur la constitution de la charge électrique à la surface d ' un électrolyte. *Jounral Phys. Théorique Appliquée*, 9(1):457–468, 1910.

D.C. Grahame. The Electrical Double-Layer and the Theory of Electrocapillarity. *Chem. Rev.*, 41(3):441–501, 1947.

D.D. Greenwood. A cochlear frequency-position function for several species–29 years later. *J. Acoust. Soc. Am.*, 87(6):2592–605, 1990. ISSN 0001-4966. doi: 10.1121/1.399052. URL http://www.ncbi.nlm.nih.gov/pubmed/2373794.

W.M. Grill and J.T. Mortimer. Electrical Properties of Implant Encapsulation Tissue. *Ann. Biomed. Eng.*, 22(16):23–33, 1994.

S. Grimnes and O.G. Martinsen. *Bioimpedance & Bioelectricity Basics*. Number 2. AP, Oxford, 2 edition, 2008. ISBN 9780874216561. doi: 10.1007/s13398-014-0173-7.2.

W Gstoettner, P Franz, J Hamzavi, Jr. Plenk H., W Baumgartner, and C Czerny. Intracochlear Position of Cochlear Implant Electrodes. *Acta Otolaryngol.*, 119(2): 229–233, 1999. ISSN 0001-6489. doi: 10.1080/00016489950181729.

A.J. Gulya. *Anatomy of the Temporal Bone with Surgical Implications*, volume 53. 2013. ISBN 9788578110796. doi: 10.1017/CBO9781107415324.004.

T. Hanekom. Three-Dimensional Spiraling Finite Element Model. *Ear Hear.*, pages 300–315, 2001.

R. Hartmann, Ge. Topp, and R. Klinke. Discharge patterns of cat primary auditory fibers with electrical stimulation of the cochlea. *Hear. Res.*, 13:47–62, 1984.

W. M. Hartmann and J. Pumplin. Noise Power Fluctuations and the Masking of Sine Signals. *J. Acoust. Soc. Am.*, 83(6):2277–2289, 1988.

S-I. Hatsushika, R.K. Shepherd, G.M. Clark, Y. C. Tong, and S. Funasaka. Dimensions of the Scala Tympani in the human and cat with reference to cochlear implants. *Ann Otol Rhinol Laryngol*, 99(11), 1990.

V.H. Hernandez, A. Gehrt, K. Reuter, Z. Jing, M. Jeschke, A.M. Schulz, G. Hoch, M. Bartels, G. Vogt, C.W. Garnham, H. Yawo, Y. Fukazawa, G.J. Augustine, and E. Bamberg. Technical advance Optogenetic stimulation of the auditory pathway. *J. Clin. Invest.*, 124(3), 2014. doi: 10.1172/JCI69050DS1.

A. Hervais-Adelman, M.H. Davis, I.S. Johnsrude, and R.P. Carlyon. Perceptual learning of noise vocoded words: effects of feedback and lexicality. *J. Exp. Psychol. Hum. Percept. Perform.*, 34(2):460–474, 2008. ISSN 0096-1523. doi: 10.1037/0096-1523.34.2.460.

G. Hilkhuysen and O. Macherey. Optimizing pulse-spreading harmonic complexes to minimize intrinsic modulations after auditory filtering. *J. Acoust. Soc. Am.*, 136(3): 1281, 2014. ISSN 1520-8524. doi: 10.1121/1.4890642.

S.Y. Ho, R.J. Wiet, and C.P. Richter. Modifying Cochlear Implant Design: Advantages of Placing a Return Electrode in the Modiolus. *Otol. Neurotol.*, 25(4):497–503, jul 2004. ISSN 1531-7129. doi: 10.1097/00129492-200407000-00017.

A.J.M. Houtsma and J. Smurzinski. Pitch identification and discrimination for complex tones with many harmonics. *J. Acoust. Soc. Am.*, 87(1):304, 1990. ISSN 00014966. doi: 10.1121/1.399297.

T. Ifukube and R.L. White. Current Distributions Produced Inside and Outside the Cochlea from a Scala Tympani Electrode Array. *IEEE Trans. Biomed. Eng.*, BME-34(11):883–890, nov 1987. ISSN 0018-9294. doi: 10.1109/TBME.1987.326009. URL http://ieeexplore.ieee.org/lpdocs/epic03/wrapper.htm?arnumber=4122463.

A.D. Izzo, C.P. Richter, E.D. Jansen, and J.T. Walsh. Laser Stimulation of the Auditory Nerve. *Lasers Surg. Med.*, 38:745–753, 2006. doi: 10.1002/lsm.20358.

S. Jansen, H. Luts, K.C. Wagener, B. Kollmeier, M. Del Rio, R. Dauman, C. James, B. Fraysse, E. Vormès, B. Frachet, J. Wouters, and A. van Wieringen. Comparison of three types of French speech-in-noise tests: a multi-center study. *Int. J. Audiol.*, 51(3):164–73, mar 2012. ISSN 1708-8186. doi: 10.3109/14992027.2011.633568.

M. Jeschke and T. Moser. Considering optogenetic stimulation for cochlear implants. *Hear. Res.*, 322:224–234, 2015. ISSN 0378-5955. doi: 10.1016/j.heares.2015.01.005.

A. Jeyakumar, S.F. Peña, and T.M. Brickman. Round window insertion of precurved electrodes is traumatic. *Otol. Neurotol.*, 35(1):52–7, 2014. ISSN 1537-4505. doi: 10.1097/MAO.0000000000000194.

T. Johnsen, M.B. Jørgensen, and S. Johnsen. Mondini Cochlea in Pendred ' s Syndrome A Histological Study. *Acta Otolaryngol.*, 102(3-4):239–247, 1986. doi: 10.3109/00016488609108673.

C.N. Jolly, F.A. Spelman, and B.M. Clopton. Quadrupolar Stimulation for Cochlear Prostheses : Modeling and Experimental Data. *IEEE Trans. Biomed. Eng.*, 43(8): 857–865, 1996.

R.K. Kalkman, J.J. Briaire, D.M.T. Dekker, and J.H.M. Frijns. Place pitch versus electrode location in a realistic computational model of the implanted human cochlea. *Hear. Res.*, 315:10–24, 2014. doi: 10.1016/j.heares.2014.06.003.

R.K. Kalkman, J.J. Briaire, and J.H.M. Frijns. Current focussing in cochlear implants : An analysis of neural recruitment in a computational model. *Hear. Res.*, 322:89–98, 2015. ISSN 0378-5955. doi: 10.1016/j.heares.2014.12.004. URL http://dx.doi.org/10.1016/j.heares.2014.12.004.

T. Kamakura and J.B. Nadol. Correlation between word recognition score and intracochlear new bone and fibrous tissue after cochlear implantation in the human. *Hear. Res.*, 2016. ISSN 0378-5955. doi: 10.1016/j.heares.2016.06.015. URL http://dx.doi.org/10.1016/j.heares.2016.06.015.

A.M. Khan, O. Handzel, B.J. Burgess, D. Damian, D.K. Eddington, and J.B. Nadol. Is Word Recognition Correlated With the Number of Surviving Spiral Ganglion Cells and Electrode Insertion Depth in Human Subjects With Cochlear Implants? *Laryngoscope*, 115(April):672–677, 2005a.

A.M. Khan, D.M. Whiten, and J.B. Nadol. Histopathology of human cochlear implants : Correlation of psychophysical and anatomical measures. *Hear. Res.*, 205:83–93, 2005b. doi: 10.1016/j.heares.2005.03.003.

P.R. Kileny, T.A. Zwolan, S.A. Telian, and A. Boerst. Performance With the 20+2L Lateral Wall Cochlear Implant. *Am. J. Otol.*, 19:313–319, 1998.

A. Kohlrausch, R. Fassel, M. van der Heijden, R. Kortekaas, S van de Par, and A.J. Oxenham. Detection of tones in low-noise noise: Further evidence for the role of envelope fluctuations. *Acta Acust.*, 83,:659–669., 1997.

G.T.A. Kovacs. Introduction to the theory, design, and modeling of thin-film microelectrodes for neural interfaces,. In D. A. Stenger and T. M. McKenna, editor, *Enabling Technolo- gies Cult. Neural Networks*, pages 121–165. Eds. londo edition, 1994.

A. Kral, R. Hartmann, D. Mortazavi, and Y. Rainer Klinke. Spatial resolution of cochlear implants : the electrical field and excitation of auditory afferents. *Hear. Res.*, 121(121):11–28, 1998.

B. Küçük, K. Abe, T. Ushiki, Y. Inuyama, S. Fukuda, and Kazuo I. Microstructures of the Bony Modiolus in the Human Cochlea : A Scanning Electron Microscopic Study. *J. Electron Microsc*, 40(40):193–197, 1991.

G. Kumar, M. Chokshi, and C.P. Richter. Electrical impedance measurements of cochlear structures using the four-electrode reflection-coefficient technique. *Hear. Res.*, 259(1-2):86–94, jan 2010. doi: 10.1016/j.heares.2009.10.010.

B.J. Kwon and C. van den Honert. Effect of electrode configuration on psychophysical forward masking in cochlear implant listeners. *J. Acoust. Soc. Am.*, 119(5):2994–3002, 2006. ISSN 00014966. doi: 10.1121/1.2184128. URL http://scitation.aip.org/content/asa/journal/jasa/119/5/10.1121/1.2184128.

D.M. Landsberger, M. Padilla, and A.G. Srinivasan. Reducing Current Spread using Current Focusing in Cochlear Implant Users. *Hear. Res.*, 284:16–24, 2012. doi: 10.1016/j.heares.2011.12.009.Reducing.

J. Laneau, M. Moonen, and J. Wouters. Factors affecting the use of noise-band vocoders as acoustic models for pitch perception in cochlear implants. *J. Acoust. Soc. Am.*, 119(1):491–506, 2006. ISSN 00014966. doi: 10.1121/1.2133391.

J. Lario-García and R. Pallàs-Areny. Constant-phase element identification in conductivity sensors using a single square wave. *Sensors Actuators A Phys.*, 132 (1):122–128, nov 2006. ISSN 09244247. doi: 10.1016/j.sna.2006.04.014. URL http://linkinghub.elsevier.com/retrieve/pii/S0924424706002998.

D.S. Lazard, C. Vincent, F. Venail, P. Van De Heyning, E. Truy, C. Vincent, O. Sterkers, P.H. Skarzynski, H. Skarzynski, K. Schauwers, S.O. Leary, D. Mawman, B. Maat, A. Kleine-punte, A.M. Huber, and K. Green. Pre- , Per- and Postoperative Factors Affecting Performance of Postlinguistically Deaf Adults Using Cochlear Implants : A New Conceptual Model over Time. *PLoS One*, 7(11):1–11, 2012. doi: 10.1371/journal.pone.0048739.

P.A. Leake and G.T. Hradek. Cochlear pathology of long term neomycin induced deafness in cats. *Hear. Res.*, 33(1):11–33, 1988. ISSN 03785955. doi: 10.1016/0378-5955(88)90018-4.

E. Lehnhardt, D. Gnadeberg, R. D. Battmer, and E. von Wallenberg. Experience with the Cochlear Miniature Speech Processor in Adults and Children Together with a Comparison of Unipolar and Bipolar Modes. *ORL*, 54:308–3013, 1992.

H. Levitt and L.R. Rabiner. Use of a Sequential Strategy in Intelligibility Testing. *J. Acoust. Soc. Am.*, 42(May 1967):609–6012, 1967.

H.H. Lim, Y. C. Tong, and G.M. Clark. Forward masking patterns produced by intracochlear electrical stimulation of one and two electrode pairs in the human cochlea. *J. Acoust. Soc. Am.*, 86(3):971–980, 1989. ISSN 00014966. doi: 10.1121/1.398732.

F.H. Linthicum and W. Anderson. Cochlear Implantation of Totally Deaf Ears : Histologic Evaluation of Candidacy Cochlear Implantation of Totally Deaf Ears. *Acta Otolaryngol.*, 111(2):327–331, 1991. doi: 10.3109/00016489109137395.

L.M. Litvak. BEDCS Bionic Ear Data Collection System. Version 1.16, user manual. Technical report, Advanced Bionics, 2003.

L.M. Litvak, A.J. Spahr, and G. Emadi. Loudness growth observed under partially tripolar stimulation: model and data from cochlear implant listeners. *J. Acoust. Soc. Am.*, 122(2):967–81, aug 2007. doi: 10.1121/1.2749414.

W Liu, F Edin, F Atturo, G Rieger, H. Löwenheim, P. Senn, M. Blumer, A. Scrott-Fischer, H. Rask-Andersen, and R. Glueckert. The pre- and post-somatic segments of the human type I spiral ganglion neurons - structural and functional considerations related to cochlear implantation. *Neuroscience*, 284:470–482, 2015. doi: 10.1016/j.neuroscience.2014.09.059.

P.C. Loizou, M.F. Dorman, O. Poroy, and T. Spahr. Speech recognition by normal-hearing and cochlear implant listeners as a function of intensity resolution. *J. Acoust. Soc. Am.*, 108(5 Pt 1):2377–2387, 2000. ISSN 00014966. doi: 10.1121/1.1317557.

S.G. Lomber, M.A. Meredith, and A. Kral. Cross-modal plasticity in specific auditory cortices underlies visual compensations in the deaf. *Nat. Neurosci.*, 13(11):1421–1427, 2010. ISSN 1097-6256. doi: 10.1038/nn.2653.

C.J. Long, T.A. Holden, G.H. McClelland, W.S. Parkinson, C. Shelton, D.C. Kelsall, and Z.M. Smith. Examining the electro-neural interface of cochlear implant users using psychophysics, CT scans, and speech understanding. *J. Assoc. Res. Otolaryngol.*, 15(2):293–304, apr 2014. doi: 10.1007/s10162-013-0437-5.

D.A. López, A. Durán, and S.M. Ceré. Electrochemical characterization of AISI 316L stainless steel in contact with simulated body fluid under infection conditions. *J. Mater. Sci. Mater. Med.*, 19:2137–2144, 2008. ISSN 09574530. doi: 10.1007/s10856-007-3138-y.

T. Lu, R.Y. Litovsky, and F.G. Zeng. Binaural masking level differences in actual and simulated bilateral cochlear implant listeners. *J. Acoust. Soc. Am.*, 127(3):1479–1490, 2010. ISSN 00014966. doi: 10.1121/1.3290994.

H. Luts, E. Boon, J. Wable, and J. Wouters. FIST: A French sentence test for speech intelligibility in noise. *Int. J. Audiol.*, 47(6):373–374, 2008. ISSN 1708-8186. doi: 10.1080/14992020801887786. URL http://ovidsp.ovid.com/ovidweb.cgi?T=JS{&}PAGE=reference{&}D=psyc6{&}NEWS=N{&}AN=2008-10224-015.

O. Macherey and R.P. Carlyon. Re-examining the upper limit of temporal pitch. *J. Acoust. Soc. Am.*, 136(6):3186, 2014. ISSN 1520-8524. doi: 10.1121/1.4900917. URL http://www.pubmedcentral.nih.gov/articlerender.fcgi?artid=4340596{&}tool=pmcentrez{&}rendertype=abstract.

O. Macherey and Yves Cazals. Effects of Pulse Shape and Polarity on Sensitivity to Cochlear Implant Stimulation : A Chronic Study in Guinea Pigs. *Adv. expe*, 2016. doi: 10.1007/978-3-319-25474-6.

O. Macherey, A. van Wieringen, R.P. Carlyon, J.M. Deeks, and J. Wouters. Asymmetric pulses in cochlear implants: effects of pulse shape, polarity, and rate. *J. Assoc. Res. Otolaryngol.*, 7(3):253–66, sep 2006. ISSN 1525-3961. doi: 10.1007/s10162-006-0040-0. URL http://www.pubmedcentral.nih.gov/articlerender.fcgi?artid=2504608{&}tool=pmcentrez{&}rendertype=abstract.

O. Macherey, R.P. Carlyon, A. van Wieringen, J.M. Deeks, and J. Wouters. Higher sensitivity of human auditory nerve fibers to positive electrical currents. *J. Assoc. Res. Otolaryngol.*, 9(2):241–51, jun 2008. ISSN 1525-3961. doi: 10.1007/s10162-008-0112-4.

O. Macherey, A. van Wieringen, R.P. Carlyon, I. Dhooge, and J. Wouters. Forward-masking patterns produced by symmetric and asymmetric pulse shapes in electric hearing. *J. Acoust. Soc. Am.*, 127(1):326–338, 2010. ISSN 00014966. doi: 10.1121/1.3257231.

O. Macherey, G. Hilkhuysen, R.P. Carlyon, Stephane Roman, and Yves Cazals. Polarity Effects in cochlear Implant Stimulation: Insights from Human and Animal Studies. In *Conf. Implant. Audit. Prostheses*, page 60, Lake Tahoe, 2015.

J.A. Majdi, S. Minnikanti, N. Peixoto, A. Agrawal, and E.D. Cohen. Access resistance of stimulation electrodes as a function of electrode proximity to the retina. *J. Neural Eng.*, 12(1), 2015. doi: 10.1088/1741-2560/12/1/016006.

T.K. Malherbe, T. Hanekom, and J.J. Hanekom. The effect of the resistive properties of bone on neural excitation and electric fields in cochlear implant models. *Hear. Res.*, 327:126–135, 2015. doi: 10.1016/j.heares.2015.06.003.

J. Marozeau, H.J. McDermott, B. Swanson, and C.M. McKay. Perceptual Interactions Between Electrodes Using Focused and Monopolar Cochlear Stimulation. *J. Assoc. Res. Otolaryngol.*, 2015. ISSN 1525-3961. doi: 10.1007/s10162-015-0511-2.

C.C. Mcintyre and W.M. Grill. Extracellular Stimulation of Central Neurons : Influence of Stimulus Waveform and Frequency on Neuronal Output Extracellular Stimulation of Central Neurons : Influence of Stimulus Waveform and Frequency on Neuronal Output. *J. Neurophysiol.*, 88:1592–1604, 2002.

L.H.M. Mens and C.K. Berenstein. Speech Perception with Mono- and Quadrupolar Electrode Configurations: A Crossover Study. *Otol. Neurotol.*, 26(5):957–964, 2005. doi: 10.1097/01.mao.0000185060.74339.9d.

Q. Mesnildrey and O. Macherey. Simulating the dual-peak excitation pattern produced by bipolar stimulation of a cochlear implant: Effects on speech intelligibility. *Hear. Res.*, 319:32–47, jan 2015. ISSN 03785955. doi: 10.1016/j.heares.2014.11.001.

Q. Mesnildrey, G. Hilkhuysen, and O. Macherey. Pulse-spreading harmonic complex as an alternative carrier for vocoder simulations of cochlear implants. *J. Acoust. Soc. Am.*, 139(February):986–991, 2016. doi: 10.1121/1.4941451.

A.G. Micco and C.P. Richter. Electrical resistivity measurements in the mammalian cochlea after neural degeneration. *Laryngoscope*, 116(8):1334–1341, aug 2006a. ISSN 0023-852X. doi: 10.1097/01.mlg.0000231828.37699.ab.

A.G. Micco and C.P. Richter. Tissue resistivities determine the current flow in the cochlea. *Curr. Opin. Otolaryngol. Head Neck Surg.*, 14(5):352–355, 2006b.

J.C. Middlebrooks. Cochlear-implant high pulse rate and narrow electrode configuration impair transmission of temporal information to the auditory cortex. *J. Neurophysiol.*, 100(1):92–107, 2008. ISSN 0022-3077. doi: 10.1152/jn.01114.2007.

J.C. Middlebrooks and R.L. Snyder. Auditory Prosthesis with a Penetrating Nerve Array. *J Neurophysiol*, 279:258–279, 2007. doi: 10.1007/s10162-007-0070-2.

C.A. Miller, P.J. Abbas, B.K. Robinson, J.T. Rubinstein, and A.J. Matsuoka. Electrically evoked single-fiber action potentials from cat : responses to monopolar , monophasic stimulation. *Hear. Res.*, 130:197–218, 1999.

C.A. Miller, B.K. Robinson, J.T. Rubinstein, P.J. Abbas, and C.L. Runge-Samuelson. Auditory nerve responses to monophasic and biphasic electric stimuli. *Hear. Res.*, 151(1-2):79–94, 2001. ISSN 03785955. doi: 10.1016/S0300-2977(00)00082-6.

B.C.J. Moore, M. Huss, D.A. Vickers, B.R. Glasberg, and J.I. Alcàntara. AMSTERDAM A test for the diagnosis of dead regions in the cochlea. *Br. J. Audiol.*, 34: 205–224, 2000.

D.R. Moore and R.V. Shannon. Beyond cochlear implants : awakening the deafened brain. *Nat. Neurosci.*, 12(6):686–691, 2009. doi: 10.1038/nn.2326.

A.E. Mussett and M.A. Khan. *Looking Into the Earth: An Introduction to Geological Geophysics*. Cambridge University Press, 2000.

J.B. Nadol and D.K. Eddington. Histopathology of the Inner Ear Relevant to Cochlear Implantation. *Adv Otorhinolaryngol*, 64:31–39, 2006.

J.B. Nadol, Y.S. Young, and R.J. Glynn. Survival of Spiral ganglion cells in profound Sensorineural hearing Loss : Implications for Cochlear Implantation. *Ann. Otol. Rhinol. Laryngol.*, 98:411–416, 1989.

J.A. Nelder and R. Mead. A simplex method for function minimization. *Comput. J.*, 7 (4):308–313, 1965.

D.A. Nelson and H.A. Kreft. Forward-masked spatial tuning curves in cochlear implant users. *J. Acoust. Soc. Am.*, 123(3):1522–1543, 2008.

D.A. Nelson, J.L. Schmitz, G.S. Donaldson, N.F. Viemeister, and E. Javel. Intensity discrimination as a function of stimulus level with electric stimulation. *J. Acoust. Soc. Am.*, 100(4 Pt 1):2393–2414, 1996. ISSN 00014966. doi: 10.1121/1.417949.

B.E. Pfingst. Comparisons of psychophysical and neurophysiological studies of cochlear implants. *Hear. Res.*, 34(3):243–251, 1988. ISSN 03785955. doi: 10.1016/0378-5955(88)90005-6.

B.E. Pfingst, T.A. Zwolan, and L.A. Holloway. Effects of stimulus configuration on psychophysical operating levels and on speech recognition with cochlear implants. *Hear. Res.*, 112(1-2):247–260, 1997. ISSN 03785955. doi: 10.1016/S0378-5955(97)00122-6.

B.E. Pfingst, K.H. Franck, T.A. Zwolan, E.M. Bauer, and L. Xu. Effects of Electrode Configuration and Place of Stimulation on Speech Perception with Cochlear Prostheses. *J. Assoc. Res. Otolaryngol.*, 02:87–103, 2001. doi: 10.1007/s101620010065.

B.E. Pfingst, L. Xu, and C.S. Thompson. Across-Site Threshold Variation in Cochlear Implants: Relation to Speech Recognition. *Audiol. Neurotol.*, 9(6):341–352, 2004.

B.E. Pfingst, D.J. Colesa, S. Hembrador, S.Y. Kang, J.C. Middlebrooks, Y. Raphael, and G.L. Su. Detection of pulse trains in the electrically stimulated cochlea : Effects of cochlear health a). *J. Acoust. Soc. Am.*, 130(December):3954–3968, 2011. doi: 10.1121/1.3651820.

J. Pile and N. Simaan. Characterization of Friction and Speed Effects and Methods for Detection of Cochlear Implant Electrode Tip Fold-over. In *IEEE Int. Conf. Robot. Autom.*, pages 4409–4414, Karlsruhe, 2013. ISBN 9781467356435.

P. Prado-guitierrez, L.M. Fewster, J.M. Heasman, C.M. McKay, and R.K. Shepherd. Effect of interphase gap and pulse duration on electrically evoked potentials is correlated with auditory nerve survival. *Hear. Res.*, 215:47–55, 2007.

M.K. Qin and A.J. Oxenham. Effects of simulated cochlear-implant processing on speech reception in fluctuating maskers. *J. Acoust. Soc. Am.*, 114(1):446–454, 2003. ISSN 00014966. doi: 10.1121/1.1579009.

U. Rammelt and G. Reinhard. On the applicability of a constant phase element (CPE) to the estimation of roughness of solid metal electrodes. *Electrochem. Acta*, 35(6): 1045–1049, 1990.

J. Rasbash, C. Charlton, W.J. Browne, M. Healy, and B. Cameron. MLwiN Version 2.1. Centre for Multilevel Modelling, University of Bristol., 2009.

H. Rask-Andersen, W. Liu, E. Erixon, A. Kinnefors, K. Pfaller, A. Schrott-Fischer, and R. Glueckert. Human cochlea: Anatomical characteristics and their relevance for cochlear implantation. *Anat. Rec.*, 295(11):1791–1811, nov 2012. ISSN 1932-8494. doi: 10.1002/ar.22599.

F. Rattay. Analysis of models for extracellular fiber stimulation. *IEEE Trans. Biomed. Eng.*, 36(7):676–682, 1989. ISSN 00189294. doi: 10.1109/10.32099.

F. Rattay. The basic mechanism for the electrical stimulation of the nervous system. *Neuroscience*, 89(2):335–346, 1999.

F. Rattay, Richardson Naves Leao, and Heidi Felix. A model of the electrically excited human cochlear neuron. II. Influence of the three-dimensional cochlear structure on neural excitability. *Hear. Res.*, 153(1-2):64–79, 2001.

E.M. Relkin and J.R. Doucet. Is loudness simply proportional to the auditory nerve spike count? *J. Acoust. Soc. Am.*, 101(5 Pt 1):2735–2740, 1997. ISSN 00014966. doi: 10.1121/1.418561.

S. Rosen, A. Faulkner, and L. Wilkinson. Adaptation by normal listeners to upward spectral shifts of speech: Implications for cochlear implants. *J. Acoust. Soc. Am.*, 106(6):3629–3636, 1999. ISSN 00014966. doi: 10.1121/1.428215.

J.T. Rubinstein. Axon Termination Conditions for Electrical Stimulation. *IEEE Trans. Biomed. Eng.*, 40(7):654–663, 1993.

R. Saba, S.J. Elliott, and S. Wang. Modelling the effects of cochlear implant current focusing. *Cochlear Implant Int.*, 15(6):318–326, 2014.

E. Saunders, L.T. Cohen, A. Aschendorff, W. Shapiro, M. Knight, M. Stecker, B. Richter, S. Waltzman, M. Tykocinski, T. Roland, R. Laszig, and R. Cowan. Threshold, comfortable level and impedance changes as a function of electrode-modiolar distance. *Ear Hear.*, 23:28S–40S, 2002. doi: 10.1097/00003446-200202001-00004.

M.C. Schoenecker, B.H. Bonham, O. Stakhovskaya, R.L. Snyder, and P.A. Leake. Monopolar intracochlear pulse trains selectively activate the inferior colliculus. *JARO - J. Assoc. Res. Otolaryngol.*, 13(5):655–672, oct 2012. doi: 10.1007/s10162-012-0333-4.

J. Scholvin, J.P. Kinney, J.G. Bernstein, C. Moore-Kochlacs, N. Kopell, Nancy Kopell, C.G. Fonstad, and E.S. Boyden. Close-Packed Silicon Microelectrodes for Scalable Spatially Oversampled Neural Recording. *IEEE Trans. Biomed. Eng.*, 63(1):120–130, 2016. doi: 10.1109/TBME.2015.2406113.Close-Packed.

H.F. Schuknecht. Further Observations On the Pathology of Presbycusis. *Arch. Otolaryngol.*, 80:369–382, 1964.

H.P. Schwan and F.K. Calvin. Capacitive Properties of Body Tissues. *Circ. Res.*, V (July):439–443, 1957. doi: 10.1161/01.RES.5.4.439.

R.V. Shannon, F.G. Zeng, V. Kamath, J. Wygonski, and M. Ekelid. Speech Recognition with Primarily Temporal Cues. *Science (80-.).*, 270(5234):303–304, 1995.

R.V. Shannon, J.J. Galvin, and D. Baskent. Holes in hearing. *JARO - J. Assoc. Res. Otolaryngol.*, 3(2):185–199, jun 2002. ISSN 1525-3961. doi: 10.1007/s101620020021.

A. Sharma, J. Campbell, and G. Cardon. Developmental and cross-modal plasticity in deafness: Evidence from the P1 and N1 event related potentials in cochlear implanted children. *Int. J. Psychophysiol.*, 95(2):135–144, 2015. ISSN 18727697. doi: 10.1016/j.ijpsycho.2014.04.007.

R.K. Shepherd and M.P. Colreavy. Surface Microstructure of the Perilymphatic Space. *Arch Otolaryngol Head Neck Surg*, 130(May):2–4, 2004.

R.K. Shepherd and E. Javel. Electrical stimulation of the auditory nerve. I. Correlation of physiological responses with cochlear status. *Hear. Res.*, 108(1-2):112–144, 1997. ISSN 03785955. doi: 10.1016/S0378-5955(97)00046-4. URL http://dx.doi.org/10.1016/S0378-5955(97)00046-4.

R.K. Shepherd, S. Hatsushika, and G.M. Clark. Electrical stimulation of the auditory nerve: The effect of electrode position on neural excitation. *Hear. Res.*, 66(1):108–120, 1993. ISSN 03785955. doi: 10.1016/0378-5955(93)90265-3.

S.B. Shibata, C.L. Budenz, S.A. Bowling, and B.E. Pfingst. Nerve Maintenance and Regeneration in the Damaged Cochlea. *Hear. Res.*, 281(734):56–64, 2012. doi: 10.1016/j.heares.2011.04.019.Nerve.

Z.M. Smith and B. Delgutte. Using evoked potentials to match interaural electrode pairs with bilateral cochlear implants. *J. Assoc. Res. Otolaryngol.*, 8(1):134–151, mar 2007. ISSN 1525-3961. doi: 10.1007/s10162-006-0069-0.

Z.M. Smith, C. van den Honert, and C.J. Long. Reduced Simultaneous Channel Interactions with Optimized Focal Electrode Configurations Optimization of Focused Channels. In *Conf. Implant. Audit. Prostheses*, 2009.

Z.M. Smith, W.S. Parkinson, and C.J. Long. Multipolar current focusing increases spectral resolution in cochlear implants. In *Annu. Int. Conf. IEEE Eng. Med. Biol. Soc. EMBS*, pages 2796–2799, 2013.

R.L. Snyder, J.A. Bierer, and J.C. Middlebrooks. Topographic spread of inferior colliculus activation in response to acoustic and intracochlear electric stimulation. *JARO - J. Assoc. Res. Otolaryngol.*, 5(3):305–322, 2004. ISSN 15253961. doi: 10.1007/s10162-004-4026-5.

R.L. Snyder, J.C. Middlebrooks, and B.H. Bonham. Cochlear Implant Electrode Configuration Effects on Activation Threshold and Tonotopic Selectivity. *Hear. Res.*, 235:23–38, 2008.

P. Souza and S. Rosen. Effects of envelope bandwidth on the intelligibility of sine- and noise-vocoded speech. *J. Acoust. Soc. Am.*, 126(2):792–805, aug 2009. ISSN 1520-8524. doi: 10.1121/1.3158835. URL http://www.pubmedcentral.nih.gov/articlerender.fcgi?artid=2730710{&}tool=pmcentrez{&}rendertype=abstract.

F.A. Spelman, B.M. Clopton, and B.E. Pfingst. Tissue Impedance and Current Flow in the Implanted Ear Implications for the Cochlear Prosthesis. *Ann. Otol. Rhinol. Laryngol.*, suppl(98):3–8, 1982. URL http:

//www.ncbi.nlm.nih.gov/pubmed/?term=Tissue+Impedance+and+Current+Flow+in+the+Implanted+Ear+Implications+for+the+Cochlear+Prosthesis.

A.G. Srinivasan, M. Padilla, R.V. Shannon, and D.M. Landsberger. Improving Speech Perception in Noise with Current Focusing in Cochlear Implant Users. *Hear. Res.*, 299:29–36, 2013. doi: 10.1016/j.heares.2013.02.004.Improving.

R.C. Stafford, J.W. Stafford, J.D. Wells, P.C. Loizou, and M.D. Keller. Vocoder simulations of highly focused cochlear stimulation with limited dynamic range and discriminable steps. *Ear Hear.*, 35(2):262–70, 2014. URL http://www.ncbi.nlm.nih.gov/pubmed/24322978.

O. Stakhovskaya, D. Sridhar, B.H. Bonham, and P.A. Leake. Frequency map for the human cochlear spiral ganglion: Implications for cochlear implants. *JARO - J. Assoc. Res. Otolaryngol.*, 8(2):220–233, jun 2007. ISSN 1525-3961. doi: 10.1007/s10162-007-0076-9.

K. Stankovic, C. Rio, A. Xia, M. Sugawara, J.C. Adams, C.M. Liberman, and G. Corfas. Survival of Adult Spiral Ganglion Neurons Requires erbB Receptor Signaling in the Inner Ear. *J. Neurosci.*, 24(40):8651–8661, 2004. doi: 10.1523/JNEUROSCI.0733-04.2004.

M. Stone, C. Füllgrabe, and B.C.J. Moore. Benefit of high-rate envelope cues in vocoder processing: effect of number of channels and spectral region. *J. Acoust. Soc. Am.*, 124(4):2272–2282, oct 2008. ISSN 1520-8524. doi: 10.1121/1.2968678.

M. Stone, C. Fullgrabe, R.C. Mackinnon, and B.C.J. Moore. The importance for speech intelligibility of random fluctuations in "steady" background noise. *J. Acoust. Soc. Am.*, 130(5):2874, 2011. ISSN 00014966. doi: 10.1121/1.3641371.

D Strelioff. A computer simulation of the generation and distribution of cochlear potentials. *J. Acoust. Soc. Am.*, 54(3):620–629, 1973.

T Strydom and J.J. Hanekom. An analysis of the effects of electrical field interaction with an acoustic model of cochlear implants. *J. Acoust. Soc. Am.*, 129(4):2213–2226, apr 2011a. ISSN 1520-8524. doi: 10.1121/1.3518761. URL http://www.ncbi.nlm.nih.gov/entrez/query.fcgi?cmd=Retrieve{&}db=PubMed{&}dopt=Citation{&}list{_}uids=21476676.

T Strydom and J.J. Hanekom. The performance of different synthesis signals in acoustic models of cochlear implants. *J. Acoust. Soc. Am.*, 129(2):920–933, 2011b. doi: 10.1121/1.3518760.

G.A Studebaker. A "Rationalized" arcsine transform. *J. Speech Hear. Res.*, 28:455–462, 1985.

M.F. Suesserman. *Noninvasive Microelectrode Measurement Technique for Performing Quantitative, in vivo Measurements of Inner Ear Impedances.* Phd thesis, University of Washington, 1992.

M.F. Suesserman and F.A. Spelman. Quantitative In Vivo Measurements of Inner Ear Tissue Resistivities : I . In Vitro Characterization. *IEEE Trans. Biomed. Eng.*, 40 (October):1032–, 1993a.

M.F. Suesserman and F.A. Spelman. Lumped-Parameter Model for In Vivo Cochlear Stimulation. *IEEE Trans. Biomed. Eng.*, 40(3):237–245, 1993b.

M.F. Suesserman, F.A. Spelman, and J.T. Rubinstein. In Vitro Measurement and Characterization of Current Density Profiles Produced by Nonrecessed , Simple Recessed , and Radially Varying Recessed Stimulating Electrodes. *IEEE Trans. Biomed. Eng.*, 38(9144690):401–408, 1991.

W.M. Telford, L.P. Geldart, and R.E. Sheriff. Resistivity Methods 8.1. In Cambridge University Press, editor, *Appl. Geophys.*, chapter 8. England, 2nd edition, 1990.

K.B. Teufert, F.H. Linthicum, and S.S. Connell. The Effect of Organ of Corti Loss on Ganglion Cell Survival in Humans. *ORL*, 27:1146–1151, 2006.

A.C. Thompson, J.B. Fallon, A.K. Wise, S.A. Wade, R.K. Shepherd, and P.R. Stoddart. Infrared neural stimulation fails to evoke neural activity in the deaf guinea pig cochlea. *Hear. Res.*, 324:46–53, 2015. ISSN 0378-5955. doi: 10.1016/j.heares.2015.03.005. URL http://dx.doi.org/10.1016/j.heares.2015.03.005.

G. Tognola, A. Pesatori, M. Norgia, M. Parazzini, L. Di Rienzo, P. Ravazzani, S. Burdo, F. Grandori, and C. Svelto. Numerical Modelling and Experimental Measurements of the Electric Potential Generated by Cochlear Implants in Physiological Tissues. *IEEE Trans. Instrum. Meas.*, 56(1):187–1993, 2007.

A.A. Topalov, S. Cherevko, A.R. Zeradjanin, J.C. Meier, I. Katsounaros, and K.J.J. Mayrhofer. Towards a comprehensive understanding of platinum dissolution in acidic media. *Chem. Sci.*, 5:631–638, 2014. doi: 10.1039/c3sc52411f.

B. Townshend and R.L. White. Reduction of Electrical Interaction in Auditory Prostheses. *IEEE Trans. Biomed. Eng.*, 11, 1987.

M. Tykocinski, L.T. Cohen, and R.S. Cowan. Measurement and Analysis of Access Resistance and Polarization Impedance in Cochlear Implant Recipients. *Otol. Neurotol.*, 26(5):948–956, sep 2005. doi: 10.1097/01.mao.0000185056.99888.f3.

J.A. Undurraga, R.P. Carlyon, O. Macherey, J. Wouters, and A. van Wieringen. Spread of excitation varies for different electrical pulse shapes and stimulation modes in cochlear implants. *Hear. Res.*, 290(1-2):21–36, 2012. ISSN 03785955. doi: 10.1016/j.heares.2012.05.003. URL http://dx.doi.org/10.1016/j.heares.2012.05.003.

J.A. Undurraga, R.P. Carlyon, J. Wouters, and A. van Wieringen. The Polarity Sensitivity of the Electrically Stimulated Human Auditory Nerve Measured at the Level of the Brainstem. *JARO - J. Assoc. Res. Otolaryngol.*, 14:359–377, 2013. doi: 10.1007/s10162-013-0377-0.

C. van den Honert and D.C. Kelsall. Focused intracochlear electric stimulation with phased array channels. *J. Acoust. Soc. Am.*, 121(6):3703–16, jun 2007. ISSN 1520-8524. doi: 10.1121/1.2722047.

C. van den Honert and P.H. Stypulkowski. Physiological properties of the electrically stimulated auditory nerve . II . Single fiber recordings. *Hear. Res.*, 14:225–243, 1984.

F.J. Vanpoucke, A.J. Zarowski, J. Casselman, J.H.M. Frijns, and S. Peeters. The Facial Nerve Canal: An Important Cochlear Conduction Path Revealed by Clarion Electrical Field Imaging. *Otol. Neurotol.*, 25(3):282–289, may 2004a. ISSN 1531-7129. doi: 10.1097/00129492-200405000-00014.

F.J. Vanpoucke, A.J. Zarowski, and S. Peeters. Identification of the impedance model of an implanted cochlear prosthesis from intracochlear potential measurements. *IEEE Trans. Biomed. Eng.*, 51(12):2174–83, dec 2004b. ISSN 0018-9294. doi: 10.1109/TBME.2004.836518.

F.J. Vanpoucke, P. Boermans, and J.H.M. Frijns. Assessing the Placement of a Cochlear Electrode Array by Multidimensional Scaling. *IEEE Trans. Biomed. Eng.*, 59(2):307–310, 2012.

F. Venail, C. Mathiolon, S. Menjot de Champfleur, J.P. Piron, M. Sicard, F. Villemus, M.A. Vessigaud, F. Sterkers-Artieres, M. Mondain, and A. Uziel. Effects of Electrode Array Length on Frequency-Place Mismatch and Speech Perception with Cochlear Implants. *Audiol. Neurotol.*, pages 102–111, 2015. ISSN 1420-3030. doi: 10.1159/000369333.

D. von Compernolle. A Computational Model of the COchlea used with Cochlear Prothesis Patients. In *Acoust. Speech, Signal Process. IEEE Int. Conf. ICASSP '85.*, pages 427–429, 1985. doi: 10.1109/ICASSP.1985.1168244.

P. Wangemann. Supporting sensory transduction: cochlear fluid homeostasis and the endocochlear potential. *J. Physiol.*, 576(Pt 1):11–21, oct 2006. ISSN 0022-3751. doi: 10.1113/jphysiol.2006.112888. URL http://www.pubmedcentral.nih.gov/articlerender.fcgi?artid=1995626{&}tool=pmcentrez{&}rendertype=abstract.

R.M. Warren, K.R. Hainsworth, B.S. Brubaker, J.A. Bashford, and E.W. Healy. Spectral restoration of speech: intelligibility is increased by inserting noise in spectral gaps. *Percept. Psychophys.*, 59(2):275–83, 1997. ISSN 0031-5117. doi: 10.3758/BF03211895.

J. Wells, C. Kao, K. Mariappan, J. Albea, E.D. Jansen, P. Konrad, and A. Mahadevan-jansen. Optical stimulation of neural tissue in vivo. *Opt. Lett.*, 30(5):504–506, 2005.

G.I. Wenzel, S. Balster, H.H. Lim, K. Zhang, U. Reich, H. Lubatschowski, W. Ertmer, T. Lenarz, and G. Reuter. Stimulation of the cochlea using green laser light. In *Photonic Ther. Diagnostics V*, volume 7161, pages 1–7, 2009. doi: 10.1117/12.817049.

D.M. Whiten. *Whitten, These.* PhD thesis, Harvard-MIT, 2007.

N. Whitmal, S.F. Poissant, R.L. Freyman, and K.S. Helfer. Speech intelligibility in cochlear implant simulations: Effects of carrier type, interfering noise, and subject experience. *J. Acoust. Soc. Am.*, 122(4):2376–2388, oct 2007. ISSN 1520-8524. doi: 10.1121/1.2773993.

J.H. Won, W.R. Drennan, and J.T. Rubinstein. Spectral-Ripple Resolution Correlates with Speech Reception in Noise in Cochlear Implant Users. *JARO - J. Assoc. Res. Otolaryngol.*, 8:384–392, 2007. doi: 10.1007/s10162-007-0085-8.

F.G. Zeng and J.J. Galvin III. Amplitude Mapping and Phonem Recognition in Cochlear Implant Listeners. *Ear Hear.*, 20:60–74, 1999.

N. Zhou and B.E. Pfingst. Relationship between multipulse integration and speech recognition with cochlear implants. *J. Acoust. Soc. Am.*, 136(September):1257–1268, 2014. doi: 10.1121/1.4890640. URL http://dx.doi.org/10.1121/1.4890640.

Z. Zhu, Q. Tang, F.G. Zeng, T. Guan, and D. Ye. Cochlear Implant Spatial Selectivity with MOnopolar, Bipolar and Tripolar Stimulation. *Hear. Res.*, 283:45–58, 2012. doi: 10.1016/j.heares.2011.11.005.Cochlear.

T.A. Zwolan, P.R. Kileny, C. Ashbaugh, and S.A. Telian. Patient performance with the Cochlear Corporation "20 + 2" implant: bipolar versus monopolar activation. *Am. J. Otol.*, 17(5):717–723, 1996. ISSN 0192-9763.